Dissertation

submitted to the
Combined Faculties of Natural Sciences and for Mathematics
of the Ruperto-Carola University of Heidelberg, Germany
for the degree of
Doctor of Natural Sciences

Put forward by
BSc. Edna Loredana Ruiz Velasco
born in Mexico City, Mexico
Oral examination: June 15th, 2021

University of Heidelberg

Department of Physics and Astronomy

Search and first detection of very-high-energy photons in gamma-ray bursts: an analysis with HAWC and H.E.S.S.

1. Referee Prof. Dr. James A. Hinton
Particle Physics and High-Energy Astrophysics
Max Planck Institute for Nuclear Physics

2. Referee Prof. Dr. Stefan Wagner
ZAH, Landessternwarte
University of Heidelberg

Supervisors James A. Hinton and Harm Schoorlemmer

Edna Loredana Ruiz Velasco

Search and first detection of very-high-energy photons in gamma-ray bursts: an analysis with HAWC and H.E.S.S.

PhD Thesis, 15$^{\text{th}}$ June, 2021
Reviewers: Prof. Dr. James A. Hinton and Prof. Dr. Stefan Wagner
Supervisors: James A. Hinton and Harm Schoorlemmer

University of Heidelberg
Particle Physics and High-Energy Astrophysics, div. Hinton
Max Planck Institute for Nuclear Physics
Department of Physics and Astronomy
Saupfercheckweg 1
69117 and Heidelberg

Abstract

This thesis is devoted to the study of extremely energetic short-timescale astrophysical events, Gamma-ray bursts (GRBs). GRBs exhibit broad-band bright non-thermal emission, which was analysed using two major experiments: the High Altitude Water Cherenkov observatory (HAWC) and the High Energy Stereoscopic System (H.E.S.S.). The two experiments are in many respects complementary for the observation of very high energy (VHE) gamma-ray emission from GRBs, and in this work the respective advantages were exploited to maximise the sensitivity to VHE signals. After the analysis of several tens of GRBs observed using H.E.S.S. until 2017, where no significant emission was detected, improvements in the observation strategy of H.E.S.S. allowed the detection of GRB 180729B and GRB 190829A. These detections are presented in context with multi-wavelength data, proposing plausible emission mechanisms, thus concluding a decade-long search for these elusive phenomena at VHE. In the second part, novel methods to improve the accuracy of the HAWC detector simulation are presented, including better modelling of the detector efficiencies and electronics. A model that accounts for the detector response and the GRB flux evolution has been developed to estimate the optimal integration time for VHE searches with HAWC. Thanks to these improvements, it is possible to exploit the wide field of view and high duty cycle of HAWC for the search of VHE emission in several tens of GRBs. Preliminary evidence for emission is found in one of the GRBs studied, and upper limits are obtained for all the GRBs analysed and placed in context of the X-ray properties of these events. Finally, the limits and detections presented in this work are placed within the framework of the current understanding of GRBs and prospects for future and present VHE gamma-ray detectors are presented.

Zusammenfassung

Diese Arbeit widmet sich der Untersuchung von extrem energiereichen, kurzzeitigen astrophysikalischen Ereignissen, den Gammastrahlenblitzen (GRBs). GRBs weisen eine breitbandige, helle nicht-thermische Emission auf, die in dieser Arbeit anhand der Daten zweier großer Experimente analysiert wurde: dem High Altitude Water Cherenkov Observatory (HAWC) und dem High Energy Stereoscopic System (H.E.S.S.). Die beiden Experimente sind in vielerlei Hinsicht komplementär für die Beobachtung von sehr hochenergetischer (VHE) Gammastrahlenemission von GRBs – in dieser Arbeit wurden die jeweiligen Vorteile ausgenutzt, um die Empfindlichkeit für VHE-Signale zu erhöhen. Nach der Analyse von mehreren Dutzend GRBs, die bis 2017 mit H.E.S.S. beobachtet wurden und bei denen keine signifikante Emission festgestellt wurde, ermöglichten Verbesserungen in der Beobachtungsstrategie von H.E.S.S. den Nachweis von GRB 180729B und GRB 190829A. Diese Entdeckungen werden im Zusammenhang mit Multi-Wellenlängen-Daten vorgestellt, wobei plausible Emissionsmechanismen vorgeschlagen werden, um so eine jahrzehntelange Suche nach diesen schwer fassbaren Phänomenen im VHE-Bereich abzuschließen. Im zweiten Teil der Arbeit werden neuartige Methoden zur Verbesserung der Genauigkeit der HAWC-Detektorsimulation vorgestellt, einschließlich einer verbesserten Modellierung der Detektoreffizienz und -elektronik. Es wurde ein Modell entwickelt, das die Detektorantwort und die zeitliche Entwicklung des GRB-Flusses berücksichtigt, um die optimale Integrationszeit für VHE-Suchen mit HAWC abzuschätzen. Dank dieser Verbesserungen ist es möglich, das breite Sichtfeld und den nahezu ununterbrochenen Betrieb von HAWC für die Suche nach VHE-Emission in mehreren Dutzend GRBs zu nutzen. In einem der untersuchten GRBs wurden vorläufige Hinweise auf Emission gefunden; für alle analysierten GRBs wurden Obergrenzen ermittelt und in den Kontext der Röntgen-Beobachtungen dieser Ereignisse gesetzt. Abschließend werden die in dieser Arbeit vorgestellten Grenzen und Nachweise im Rahmen des aktuellen Verständnisses von GRBs diskutiert und Perspektiven für zukünftige und aktuelle VHE-Gammastrahlendetektoren vorgestellt.

Contents

1

Introduction

Contents

The observation and study of astronomical objects and phenomena demand the understanding of those techniques that allow us to detect galactic and extragalactic sources of photons. These comprise methods for the detection of emissions in the whole electromagnetic spectrum, starting from the lowest energies in the radio regime, continuing with optical, infrared and finishing with the highest energies; the X-ray and gamma-ray band (Fig. 1.1). These observations are complemented by other astrophysical messengers such as gravitational waves and neutrinos.

An astrophysical source can emit VHE ($\sim 100\,\mathrm{GeV}$ to $\sim 100\,\mathrm{TeV}$) cosmic rays and photons. Cosmic rays, consisting of protons, electrons, heavy ions, positrons and other anti-particles are charged particles. On their travels, they are deflected by magnetic fields and reach the Earth with an almost isotropic distribution, thereby losing information on their origin. Photons and neutrinos, instead, arrive straight from their source and can be used to study particle acceleration in astrophysical sources.

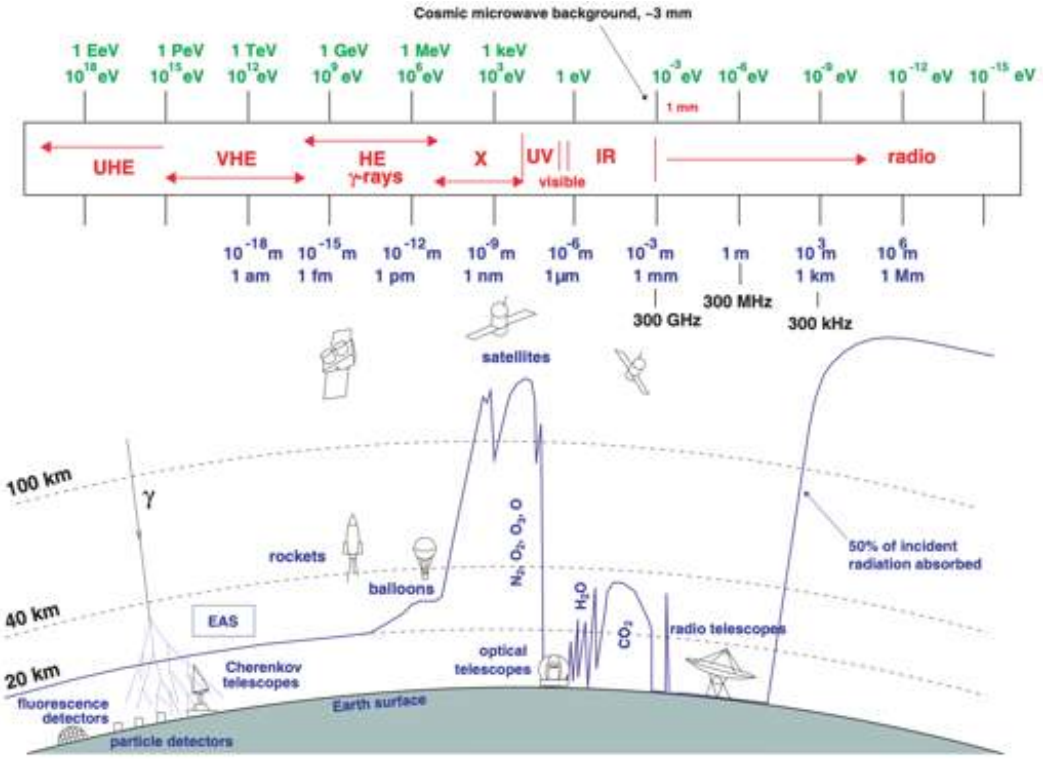

Fig. 1.1.: Typical observational methods in the whole electromagnetic spectrum. At the top, in green, the energy in eV is shown for their equivalent wavelength in blue. In red the name of the frequency band used to refer to them is indicated for each energy range. Figure obtained from Wagner, 2006.

The radiated emission observed at VHE is the consequence of non-thermal processes (where astrophysical sources can not be modelled as black bodies) in which magnetic fields, photon fields, charged particles, and matter accelerated to relativistic speeds come into play (Fig. 1.2).

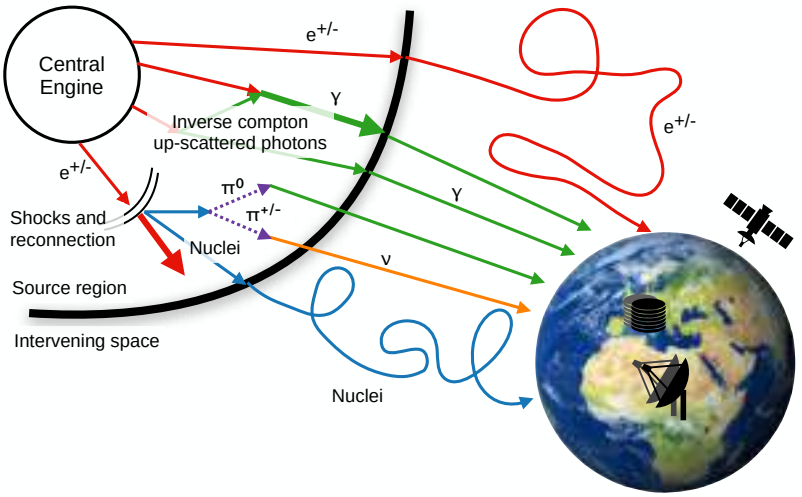

Fig. 1.2.: Illustration of the trajectories of different particle types from their origin (central engine), up to their detection on Earth by different types of instruments. Neutrinos (ν, in orange) and gamma rays (γ, in green), have no charge and therefore travel to the Earth without disturbance in their trajectories. Cosmic rays, such as ionised atomic nuclei (indicated with blue colour) and electrons/positrons (e^+,e^-) are electrically charged and their trajectories suffer from distortions due to the presence of electromagnetic fields throughout their travel to the Earth. Image modified from Pretz, 2016.

For high and very-high-energy photons and cosmic rays, the atmosphere can be used as a calorimeter. These particles interact with the atoms in the air and trigger the development of electromagnetic showers consisting of secondary particles travelling at relativistic speeds. The modern methods of ground-based cosmic and gamma-ray astrophysical observations (see Ch. 3) use the detection and reconstruction of these atmospheric showers to study the universe at VHEs.

In this chapter, the understanding of the non-thermal universe and how we explore it is summarised. Cosmic-ray and gamma-ray physics is introduced, as well as atmospheric showers and Cherenkov radiation. These are the main components used for the detection of VHE radiation of astrophysical origin and are used in the two gamma-ray observatories considered in this work and presented in Ch. 3.

1.1 Cosmic Rays

The discovery of cosmic rays is already more the one hundred years old. Theodor Wulf designed an electrometer to measure ionising radiation of terrestrial origin. In 1909, he placed his electrometer on top of the Eiffel tower and noted that the detected flux decreased but did not vanish completely, hinting at an atmospheric origin for the detected radiation (Hörandel, 2013). In 1911, Domenico Pacini performed experiments by taking electrometers to the surface of the sea and underwater, concluding that the ionisation was originated from penetrating radiation in the atmosphere (De Angelis, 2010). Victor Hess performed more studies from 1911 to 1913. In balloon flights, he measured the flux of ionising radiation and provided evidence that it increased with altitude, demonstrating a cosmic origin for it. For this work, he was awarded the 1936 Nobel Prize together with Carl D. Anderson for the discovery of positrons in cosmic radiation.

In 1929, Walter Bothe and Werner Kohloerster determined that cosmic rays were composed of electrons, protons and light-element nuclei (Bothe et al., 1929). Ten years later, a paper by Pierre Auger reported on the detection of showers with as much as 300 m of extension and noted that primary particles of energies of $\sim 10^{15}$ eV are required for producing those extensive air showers (Auger et al., 1939). These historical observations have inspired tens of experiments, developing novel techniques to understand the origin and physical processes behind cosmic radiation and its sources of acceleration.

The cosmic-rays differential flux as a function of energy is the so-called cosmic-ray spectrum (Fig. 1.3). In general, this distribution follows a power law $\mathrm{d}N/\mathrm{d}E \propto E^{-\alpha}$ where α, the spectral index, has an approximate value of 2.7. This relation is applicable for protons and nuclei with energies

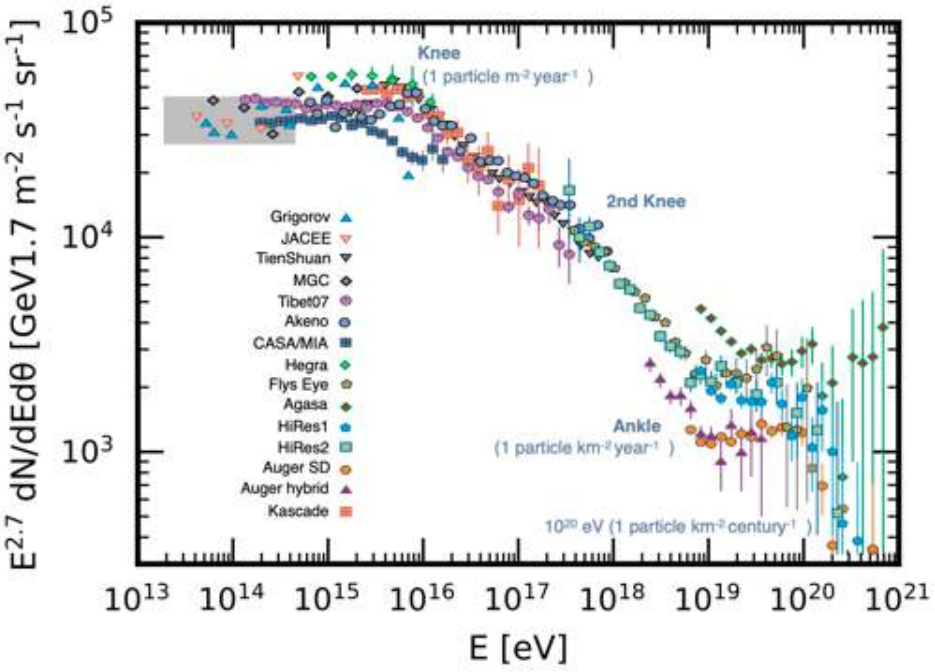

Fig. 1.3.: The cosmic-ray spectral-energy distribution detected by many experiments spanning over nine logarithmic decades in energy. The differential flux is scaled by $E^{2.7}$. The spectrum can be pictured as leg with two knees and one ankle. Figure adapted from Amsler et al., 2008 and Cronin et al., 1997.

between $10^9 - 10^{14}$ eV. The exact proportion of these particle species is energy-dependent (see Amsler et al., 2008 for details). The cosmic-ray spectrum is characterised by several *breaks* in the spectral index, widely attributed to the different scale or process responsible for their origin.

Low energy cosmic rays (up to 10^9 eV) are known to be modulated by the solar wind, since the solar magnetic field shields most of the cosmic rays coming from the outside of the solar system. For higher energies, between $10^9 - 10^{14}$ eV, the spectrum of electrons, protons and nuclei is described by $\alpha \sim 2.5 - 2.7$. At around 10^{15} eV (1 PeV) the spectrum presents a break called the *knee* where α changes to a value of 3.1 (the exact location of the *knee* depends on the particle species). Cosmic rays up to the *knee* are believed to be of galactic origin. Cosmic rays with energies above 10^{15} eV cannot be confined within the galaxy and can escape. The region between $\sim 5{\times}10^{15}$ to $1{\times}10^{17}$ follows a value $\alpha \sim 3.0$. It is widely believed –yet not concluded– that this region corresponds to the transition between cosmic-ray production

from galactic and extragalactic origin (see for example discussion in Bell, 2013).

From 1×10^{17} up to 5×10^{18}, α becomes $\sim$3.3, feature called the *second knee*, associated with the steepening of the spectrum of heavy nuclei. Hardening of the spectrum is seen above these energies up to 4×10^{19} with α returning to a value of 2.6. The transition region at 5×10^{18} is called *ankle*. The origin of the cosmic rays in this region is believed to be extragalactic. At above 4×10^{19} a hard cut-off is observed. This behaviour is believed to be explained by the theoretical model GZK (Greisen–Zatsepin–Kuzmin) for resonant interaction of the cosmic rays with the cosmic microwave background limiting the maximum distance that cosmic-rays can travel (Berezinsky, 2013).

As seen in Fig. 1.3, above 10^{20} eV, cosmic rays are extremely rare. The flux of cosmic rays above these energies is estimated to be less than 1 particle per km^2 per 100 years. To efficiently study these phenomena, detectors with effective areas of several hundred or thousands km^2 are needed (see eg. He, 2019; The Pierre Auger collaboration, 2015).

1.1.1 Particle Acceleration

Astrophysical environments are capable of generating non-thermal particle populations. Non-linear disturbances in the medium, such as shocks, are thought to be a very efficient place for particle acceleration. This was first proposed by Enrico Fermi in 1949 (Fermi, 1949). A complete review on these topics can be found in Longair, 2011.

In diffusive shock acceleration (DSA) or *first order* Fermi acceleration, particles gain energy as they are scattered repeatedly back and forth across the shock. As pictured in Fig. 1.4, in the reference frame of the shock front, the upstream (region where the shock has not interacted with the medium) is approaching the shock front with a speed of U. Starting with the continuity equation for conservation of matter one has $\rho_1 v_1 = \rho_2 v_2$ where ρ_1, v_1 and ρ_2, v_2 are the mass density and velocity of the upstream and downstream (the shocked part of the medium) respectively. Applying conservation of momentum and conservation of enthalpy, and assuming a strong shock $v_1/c_1 >> 1$ where c_1 is the sound speed in the upstream medium, the compression factor

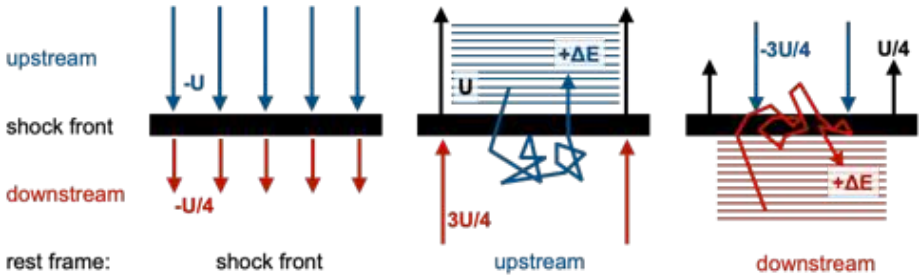

Fig. 1.4.: Schematic of the Diffusive Shock Acceleration. The left panel illustrates the flow of gas in the frame in which the shock front is at rest. Here, the shock front sees the upstream approaching with a velocity U and the downstream leaving with a velocity $U/4$. In the middle panel, the rest frame of the upstream is shown. The particles in the upstream see the downstream advancing with a velocity of $3U/4$. By scattering, they become isotropic and return to the upstream with an energy gain ΔE. In the right panel, the rest frame of the downstream is shown. Particles traversing the shock front encounter the gas in the upstream approaching with velocity $3U/4$. Under the same scenario as the upstream rest frame, particles return to the downstream gaining an energy ΔE. Figure adapted from Funk, 2005.

is $r = \rho_1/\rho_2 \approx (\gamma+1)/(\gamma-1)$ whith γ the specific heat capacity of the shock. For a fully-ionized shock, or one composed by a mono-atomic gas, $\gamma = 5/3$. Therefore, $r = 4$ and the speed of the downstream v_2 is smaller than the upstream speed by a factor of four $v_2 = v_1/4 = U/4$. In the rest frame of the upstream, the particle is approached by the ambient gas in the downstream region with a speed $|v_1 - v_2| = 3U/4$. This situation is similar when considering the rest frame of the downstream. This means that a particle that is being isotropised or scattered, is always gaining energy irrespective of the direction of crossing, acquiring on each crossing an average energy of:

$$\left\langle \frac{\Delta E}{E} \right\rangle = \frac{2}{3}\left(\frac{V}{c}\right). \tag{1.1}$$

Here $V = 3U/4$ is the velocity of the gas approaching the particles. This value is doubled ($2\langle \Delta E/E \rangle$) for a round trip.

After each crossing, $\langle E \rangle = \beta \langle E_0 \rangle$, where β is the energy gain factor and E_0 the initial energy. Let P be the probability that a particle will return to the upstream from the downstream region. After k crossings, the final energy will be $\langle E \rangle = \beta^k \langle E_0 \rangle$, and the number of particles that will have returned to the shock k-times will be $N = P^k N_0$, where N_0 is the initial number of particles within the system. The resulting energy spectrum of particles accelerated under this scenario is a power-law of the form:

$$N(E)\mathrm{d}E \propto E^{-1+\frac{\ln P}{\ln \beta}}\mathrm{d}E. \tag{1.2}$$

From Eq. 1.1, $\beta = 1 + U/c$. The number of relativistic particles crossing the shock front is $nc/4$ (with c the speed of the particle and n the number density of particles) and the number of particles advected away in the downstream region is $nU/4$. Additionally, the probability of escaping the system is $P' = U/c$ and the probability of remaining $P = 1 - P'$. For non-relativistic shocks we have that $U \ll c$ and $\ln P / \ln \beta = -1$, Eq. 1.2 becomes $N(E)\mathrm{d}E \propto E^{-2}$. Therefore, this process naturally produces a power-law that is consistent with emission from many non-thermal astrophysical sources. By allowing for energy-dependent escape the power-law index is close to that required for sources of galactic cosmic rays.

1.1.2 Cosmic-ray Accelerators

In supernova environments, the diffusive shock mechanism can accelerate cosmic rays up to energies of $\sim 10^{15}$ eV (1 PeV). Beyond this limit, other factors, such as the presence of magnetic fields in the shock region, allow to contain the particles for a longer time and therefore accelerate them to even higher energies. Another limitation is the size of the system; the Larmor radius[1] of gyration of particles in the magnetic field needs to be smaller than the acceleration region. Thus, the maximum energy that a particle can reach in the confinement of a source of size $R = l\Gamma$ (with l the co-moving size and Γ the Lorentz factor of the source) and magnetic field strength B is

[1]The Larmor radius is given by $rL = \gamma mc^2/qcB$, where c is the speed of light, γ, m and q are the Lorentz factor, mass and charge of the particles respectively submerged in a magnetic field strength B.

$E_{max} = eBR$. The Lorentz factor correction is significant for active galactic nuclei (AGNs) where it is estimated that $\Gamma \sim 10 - 50$, and GRBs where $\Gamma \sim 10 - 1000$ (Alves Batista et al., 2019). If the acceleration happens in a shock of velocity β_{sh}, the maximum energy achievable, usually known as the Hillas criterion, reads:

$$E_{max} = \eta^{-1} \beta_{sh} eBR \tag{1.3}$$

where η parametrises the efficiency of acceleration.

Potential sources of very-high and ultra-high energy cosmic-rays emission are plotted in Fig. 1.5 as a function of their magnetic field and radial size R in the ideal limit where $\eta = 1$. The solid and dashed lines show the BR product for which protons (red) and iron nuclei (blue) with energy of 10^{20} eV can be confined in the fast shock ($\beta_{sh} = 1.0$) and slow shock ($\beta_{sh} = 0.1$) case respectively. Objects placed to the left of these lines do not satisfy the Hillas criterion for cosmic-ray acceleration.

1.2 Gamma Rays

Gamma rays are produced by accelerated cosmic rays (mainly electrons and protons). A process is required to accelerate cosmic-rays up to relativistic speeds and that at the same time can reproduce the spectrum of cosmic and gamma-ray sources.

1.2.1 Emission Mechanisms

The most common mechanisms to explain the presence of HE and VHE and photons involves their interaction with surrounding matter, magnetic, and photon fields. Gamma rays can be produced via leptonic or hadronic processes. (see F. A. Aharonian, 2004; Schönfelder, 2001, for detailed descriptions). The main mechanisms of gamma-ray emission are:

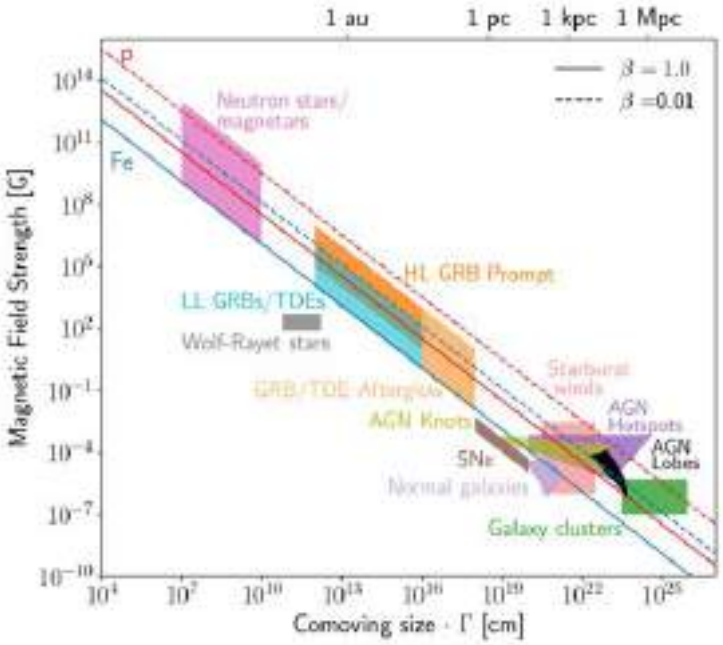

Fig. 1.5.: The Hillas diagram. Astrophysical source classes are shown as a function of their characteristic size, R, and magnetic field strength, B. The values are quoted in the co-moving frame of the source. The acronym LL GRBs/TDEs stands for low-luminosity GRBs and Tidal Disruption Events, HL GRBs prompt for the prompt emission of high-luminosity GRBs, AGN stands for Active galactic nuclei, SNe for supernovae. The figure is taken from Alves Batista et al., 2019

Bremsstrahlung : Charged particles passing very close to an atomic nucleus are accelerated or decelerated by their electric fields. The trajectory of the moving particle is substantially modified and radiation along the velocity vector is emitted. Bremsstrahlung energy loss is predominant over ionisation losses for high-energy electrons. The energy loss rate due to Bremsstrahlung is proportional to the electron incident energy E_e:

$$-\frac{\mathrm{d}E_e}{\mathrm{d}t} = \frac{cm_p n}{X_0} E_e,$$

where c is the speed of light, m_p is the proton mass and n the number density of the ambient gas. The radiation length X_0 is the characteristic amount of matter traversed by the electron (measured in g cm^{-2}) and defines the mean distance over which high-energy electrons lose all but $1/e$ of their energy by Bremsstrahlung (Tanabashi et al., 2018). The lifetime of electrons (or cooling time) due to Bremsstrahlung losses is:

$$t_{br} = \frac{E_e}{-\mathrm{d}E_e/\mathrm{d}t} \approx 4 \times 10^7 n^{-1}\,\mathrm{yr\,cm^{-3}}.$$

Since the energy loss rate is proportional to E_e, t_{br} is independent of E_e and therefore the spectral shape of electrons is not modified due to bremsstrahlung losses. Bremsstrahlung is the most important radiation mechanism for gamma-rays with energies below 100 MeV. It is also responsible for the diffuse galactic gamma-ray emission of up to 100 MeV, caused by electrons interacting with the interstellar medium.

Synchrotron radiation: In the presence of a magnetic field, particles get accelerated in circular motion and emit synchrotron radiation. This acceleration happens perpendicular to their velocity. The energy loss due to synchrotron radiation is proportional to m^{-4} (with m the mass of the particle), therefore synchrotron emission in astrophysical environments is mainly observed in electrons. The average radiated power, or energy-loss rate, due to synchrotron radiation for an isotropic electron population is:

$$P_{sync} = -\frac{\mathrm{d}E_e}{\mathrm{d}t} = \frac{4}{3}\sigma_T c U_B \beta^2 \gamma^2 \tag{1.4}$$

with $U_B = B^2/2\mu_0$ the magnetic energy density of a magnetic field B and magnetic permeability of vacuum μ_0, γ the Lorentz factor of the electron and $\sigma_T = \frac{8\pi}{3} r_e^2 \approx 6.7 \times 10^{25}\mathrm{cm}^2$ the Thomson cross-section with r_e the electron radius. The radiated power is proportional to γ^2 and B^2. In the particle frame, the emission is bipolar and with the relativistic motion of the particle, the emission in the laboratory frame happens in a cone with an opening angle $1/\gamma$. The cooling time for electrons with $\beta \approx 1$ is given by:

$$t_s = \frac{E_e}{-\mathrm{d}E_e/\mathrm{d}t} \propto B^{-2} E_e^{-1}.$$

Electrons of energies of tens of TeV in a magnetic field of $\sim 10^{-4}$G (as estimated for the Crab Nebula), will cool in about 10 years, while the age of the nebula is ~ 1000 years. From this, it can be concluded that the Crab Nebula has still a continuous acceleration of electrons.

The peak of the synchrotron radiation emission occurs at a frequency given by:

$$\nu_{max} = 1.5 \cdot 10^{-5}\mathrm{GeV} \cdot \left(\frac{E}{1\mathrm{TeV}}\right)^2 \cdot \left(\frac{B}{1\,\mathrm{G}}\right). \tag{1.5}$$

Considering an electron of energy of 1 GeV travelling in the interstellar magnetic field (few μG), the resulting synchrotron radiation-emission peaks in the radio-wave regime.

For a power-law distribution of electron energies, $N(E)\mathrm{d}E = \kappa E^{-p}\mathrm{d}E$ one can assume that the emitted radiation comes exclusively from electrons at an energy E such that in a differential interval of energy, ν_{max} can be used. Therefore $\mathrm{d}E \propto v^{-1/2} B^{-1/2} d\nu$. The resulting energy flux per unit frequency is:

$$J(\nu) = -\int \frac{\mathrm{d}E}{\mathrm{d}t} N(E)\mathrm{d}E \propto B^{(p+1)/2} \nu^{(1-p)/2},$$

the exponent of ν is the spectral index $\alpha = (1-p)/2$, determined by the slope of the electron energy spectrum.

Inverse Compton scattering : In this process, a photon of low energy is up-scattered by an electron resulting in an increase of energy of the photon. The cross-section of this process is given by:

$$\sigma_{IC} = \frac{3\sigma_T}{8\epsilon}\left[\left(1 - \frac{2(\epsilon+1)}{\epsilon^2}\right)\ln(2\epsilon+1) + \frac{1}{2} + \frac{4}{\epsilon} - \frac{1}{2(2\epsilon+1)^2}\right],$$

where $\epsilon = \omega_0/E_e$ and ω_0 is the initial energy of the photon in the co-moving frame of the electron, E_e the rest frame electron energy $E_e = m_e c^2$. For non-relativistic electron energies $\epsilon \ll 1$, one has $\sigma_{IC} \approx \sigma_T(1-2\epsilon)$, called the Thomson regime. Considering ultra-relativistic electron energies $\epsilon \gg 1$, the electrons lose a significant portion of energy on each interaction and relativistic effects make the cross-section drop. This is called the Klein-Nishina (KN) regime where $\sigma_{IC} \approx \frac{3}{8}\sigma_T \ln(4\epsilon)/\epsilon$.

The energy-loss rate due to IC scattering for the Thomson regime is:

$$P_{IC} = -\frac{\mathrm{d}E_e}{\mathrm{d}t} = \frac{4}{3}\sigma_T c \omega_0 n_{ph} E_e^2, \tag{1.6}$$

with n_{ph} the photon-field number density. The cooling time in the Thomson regime is similar to the case for synchrotron radiation, $\tau_{IC} \propto 1/E_e$. With an energy loss that depends on E_e^2, the spectrum in the Thomson regime becomes steeper with time, since higher energy electrons will lose energy faster.

For the KN regime the energy loss rate is weakly dependent on the electron energy:

$$P_{IC} = -\frac{\mathrm{d}E_e}{\mathrm{d}t} = \frac{3}{8}\frac{\sigma_T c n_{ph}}{\omega_0}(\ln(4\epsilon\gamma) - 11/6), \tag{1.7}$$

with $\gamma = E_e/mc^2$, making the spectrum become harder with time.

Since synchrotron radiation and inverse-Compton scattering are two closely linked processes, one can conclude from Eq. 1.4 and Eq. 1.6 that the ratio of the radiated power is equal to the ratio of the radiation field U_{rad} over magnetic field energy density U_B:

$$\frac{P_{IC}}{P_{sync}} = \frac{U_{rad}}{U_B} \tag{1.8}$$

Synchrotron self-Compton (SSC) In this process, the photons produced via synchrotron radiation of electrons are also up-scattered by the same population of electrons. This process can in principle happen repeatedly, having SSC of first, second, third, ... order. However, high-order SSC is not commonly treated, since KN effects suppress the process (Zhang, 2018). Defining the left hand side of Eq.1.8 as $Y = P_{IC}/P_{sync} = U_{sync}/U_B$, where U_{sync} is the energy density of the synchrotron photons, higher order of SSC processes can be written as $Y_1 = Y$, $Y_2 = P_{SSC,2}/P_{SSC,1}$ etc. The total emission power of the electron is:

$$P_{tot} = P_{sync}(1 + Y_1 + Y_1 Y_2 + ...).$$

Therefore, the cooling in the SSC process is equal to the synchrotron cooling with additional Y-factors. In the simple and most common case, only the first SSC term is relevant, $P_{tot} = P_{sync}(1+Y)$. If the cases where the KN effect becomes significant, a correction factor $Y_{KN} \leq 1$ is introduced. In principle, Y is independent on γ, since P_{IC} and P_{sync} are proportional to γ^2. A dependency on γ is present when applying the correction factor ($Y(\gamma) = Y \times Y_{KN}$). Where Y_{KN} is given by:

$$Y_{KN}(\gamma) \sim min\left[1, \left(\frac{\Gamma m c^2}{\gamma h \nu_{sync}}\right)^2\right],$$

with Γ and γ the Lorentz factor of the outflow and the electron in the co-moving frame respectively, m the electron mass and ν_{syn} the peak synchrotron frequency in the observer's frame.

Decay and annihilation This involves hadronic processes resulting in gamma rays. The most common is the production of neutral pions π^0 via:

$$p + p \rightarrow X + \pi^0 \tag{1.9}$$

and the photoproduction of π^0 from nucleons N:

$$N + \gamma \rightarrow X + \pi^0, \tag{1.10}$$

where X is typically a proton or a neutron. With a high probability ($\sim$98.8%), the π^0 decays into two photons, $\pi^0 \rightarrow \gamma + \gamma$. The resulting photons have an energy of $\sim$ MeV in the rest frame, which corresponds to half of the rest mass of the pion.

The annihilation of particle-antiparticle pairs can also produce gamma rays. The lightest possible pair ($\mathrm{e}^-\mathrm{e}^+$) produces two photons with energy of 511 keV in the rest frame of the annihilation process.

These mechanisms are responsible for all the non-thermal emission seen in the Universe. Astrophysical sources exhibit the signatures of these acceleration and emission mechanisms throughout their spectrum.

1.2.2 Gamma-ray Sources at VHE

Known sources that emit VHE gamma rays can be split according to their galactic (supernova remnants, pulsars and binary systems) or extragalactic origin (active galactic nuclei, starburst galaxies and GRBs).

A supernova remnant (SNR) is the shell-like structure originated by the explosion of a star. The ejecta during this process interacts with the interstellar medium (ISM) producing shocks where cosmic rays are accelerated and VHE gamma-rays emitted.

Pulsars and pulsar wind nebulae are generated (under certain conditions) after the supernova explosion of a massive star. A pulsar is a highly magnetised rotating neutron star. The magnetic fields in the neutron star can accelerate

particles and give rise to VHE emission. The winds of the pulsar can interact with the supernova shell or ISM and also accelerate particles.

Binary systems are generally composed of a compact object (a neutron star or black hole) and a massive star in the vicinity. One of the scenarios to explain the gamma-ray emission is the accretion of mass from the star into the compact object, giving rise to a jet, where VHE gamma-rays are emitted. In another scenario, a shock is generated when the winds from the neutron star interact with those from the massive star giving rise to particle acceleration and VHE gamma-rays.

In starburst galaxies the star formation, gas density and supernova rate are extremely high. Supernovae can produce cosmic rays that can interact with the highly-dense ambient and produce VHE gamma-rays.

Active galactic nuclei (AGNs) are a type of galaxy hosting a supermassive black hole in its centre. This object generates a collimated jet where matter is accelerated to relativistic speeds giving rise to VHE gamma-rays. Depending on the viewing angle of the jet, AGN can be called BL Lac (if the jet points to the Earth), quasar and Seyfert-1 or 2 when the jet is observed at a certain angle, and radio galaxy if the jet is perpendicular to the Earth.

Gamma-ray bursts are energetic explosions whose origin is believed to be the merger of two compact objects or the explosion of a massive star. Particle acceleration happens within the generated relativistic jets and during the interaction of the outburst with the circumburst medium. They can out-shine any other object in the sky for short periods of time and terminate with a smoothly-fading episode. In Ch. 2, these objects will be presented in more detail.

Since the birth of experimental gamma-ray astrophysics, more than 220 sources of galactic and extragalactic origin emitting VHE gamma-rays have been detected (Wakely et al., 2018). A map with the location of these detected sources is shown in Fig. 1.6.

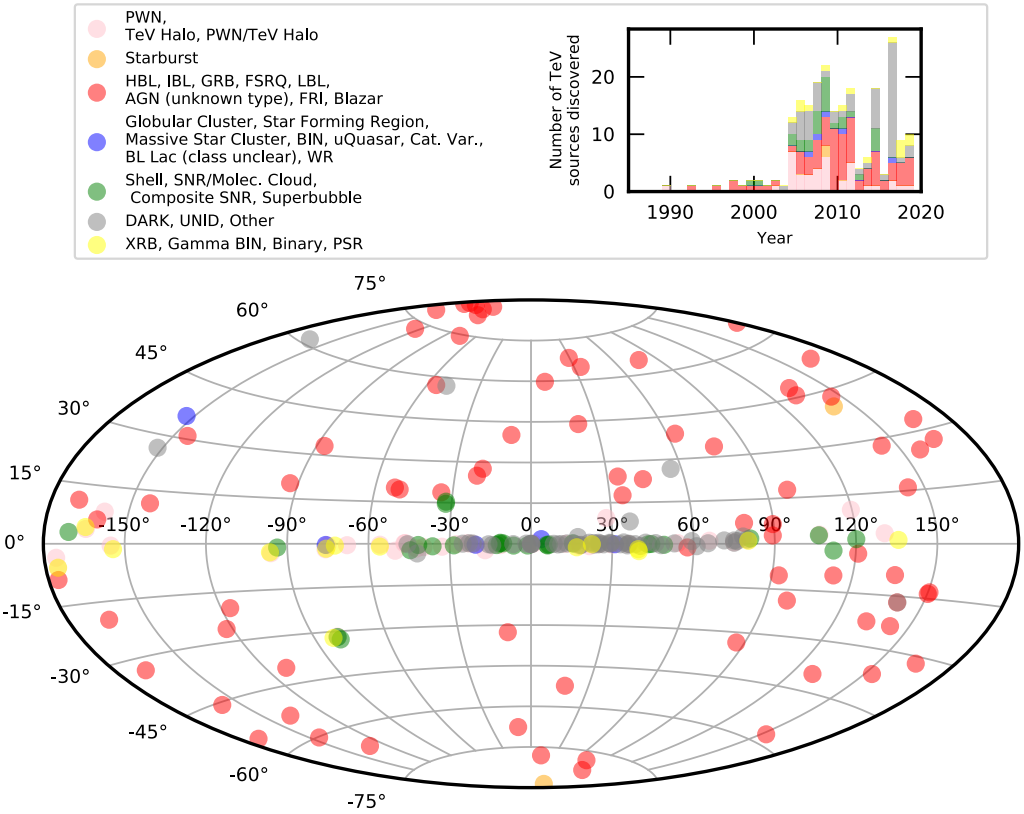

Fig. 1.6.: A compilation of all teraelectronvolt gamma-ray sources detected up to Dec. 2019. The classification scheme is the same as reported in TeVCat (`http://tevcat.uchicago.edu/`). The sub-panel in the upper-right corner shows the number of sources detected per year under the same classification scheme

1.3 Intergalactic Absorption of VHE Gamma Rays

Although gamma rays are undisturbed by magnetic fields through their travel in the Universe, they can interact with background photons (γ_{bkg}) via pair production:

$$\gamma_{bkg} + \gamma_{source} \rightarrow \mathrm{e}^{+} + \mathrm{e}-$$

The cross-section of this process is:

$$\sigma_{\gamma\gamma} = \frac{1}{2}\pi r_0^2(1-\beta^2)\left[2\beta(\beta^2-2) + (3-\beta^4)\ln\left(\frac{1+\beta}{1-\beta}\right)\right] \tag{1.11}$$

where $\pi r_0^2 = 3\sigma_T/8$ (Nikishov, 1961) and σ_T is the Thomson scattering cross-section. In this expression,

$$\beta = \sqrt{1 - \frac{2m_e^2c^4}{E\epsilon(1-\cos(\theta))}} \tag{1.12}$$

carries the dependence on the scattering angle θ. With ϵ the energy of the background photon and E the energy of the source photon.

For an isotropic background of photons $\cos(\theta) \to 0$, $\sigma_{\gamma\gamma} \approx 0.25\sigma_T$ at $\epsilon E \approx 4m_e^2c^4$ and the cross-section is maximised when:

$$\epsilon(E) \approx \left(\frac{1\mathrm{TeV}}{E}\right)\mathrm{eV}.$$

The inverse proportionality of E and ϵ implies that background photons of the lowest energies will scatter preferentially with source photons of the highest energies. For VHE gamma rays, the interaction will happen with the Extragalactic Background Light (EBL) (see Dwek et al., 2013 for a review). The EBL comprises light in the wavelength region of 0.1-1000μm (UV, optical and infrared) originated from all the energy released since the epoch of recombination. As a consequence, the EBL intensity and spectral shape hold key insights into the formation of galaxies through cosmic history. Estimations of the EBL are developed from semi-empirical models or by modelling the stellar light production and re-processing in galaxies at different redshifts (see eg. Domínguez et al., 2011; Franceschini et al., 2017; Gilmore et al., 2012). The EBL spectrum is shown in Fig. 1.7 as a function of background photon wavelength.

For VHE photons emitted from a source, the interaction with the EBL will generate a cutoff in the observed spectrum:

$$F_{\mathrm{int}}(E) = F_{\mathrm{obs}} \times e^{-\tau(E,z)}$$

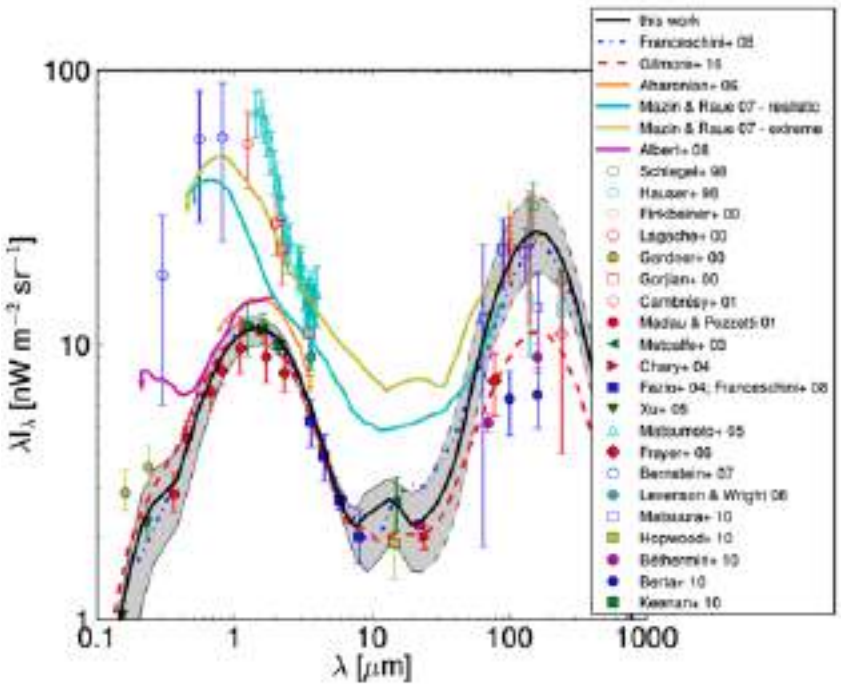

Fig. 1.7.: The EBL spectrum. A compilation of the EBL spectrum measured by many experiments and inferred from models. The figure is taken from Domínguez et al., 2011.

where $F_{\rm int}(E)$ and $F_{\rm obs}$ are the intrinsic and observed spectrum respectively, and the exponential term is the EBL absorption coefficient. The term $\tau(E, z)$ is the optical depth that depends on the cross-section $\sigma_{\gamma\gamma}$ for a source-photon of energy E, the EBL density, and the distance z to the source. In Fig. 1.8 the absorption coefficient for several redshifts as a function of the energy of the source photon is shown. The spectral measurement of extragalactic sources at VHE can be used to probe a substantial part of the EBL spectral distribution (F. Aharonian et al., 2006a) but it also limits the redshift horizon in which VHE observatories can detect extragalactic sources. Overcoming the effect of the EBL absorption requires either extremely bright sources or instruments with good sensitivity.

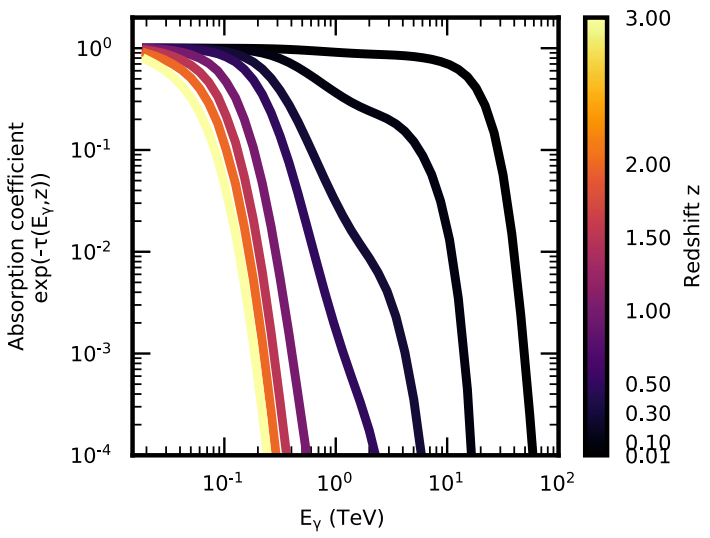

Fig. 1.8.: EBL absorption coefficient. The EBL absorption coefficient is shown as a function of redshift z and energy of the source photon E_γ. At $z = 0.5$ $\sim 99.9\%$ of the emitted photons will get absorbed before arriving to the Earth. The value of $\tau(E_\gamma, z)$ is obtained from Franceschini et al., 2008.

1.4 Atmospheric Showers

The Earth's atmosphere is not transparent to cosmic rays and gammas. When a particle enters the atmosphere, it will eventually interact with a nucleus of an atom in the atmosphere. For energies of few tens of GeV, these particles produce secondary particles travelling at relativistic speeds enclosed in a laterally extended thin-disk geometry, a phenomenon referred to as atmospheric shower. By detecting these secondary particles with terrestrial experiments, it is possible to discriminate between gamma and cosmic-ray induced showers. The discrimination of gamma-rays from cosmic rays allows the study of gamma-rays indirectly, as will be explained in Ch. 3.

The physical extension and particle composition of an atmospheric shower depend principally on the characteristics of its primary particle. For atmospheric showers induced by gamma-rays, a great amount of energy is transferred to secondary electrons and positrons via pair production. These particles will produce gamma rays of lower energies via Bremsstrahlung, resulting in a symmetric distribution of particles (Fig. 1.9). In the Heitler model (Matthews, 2005), particles are considered to be identical and the generation of new

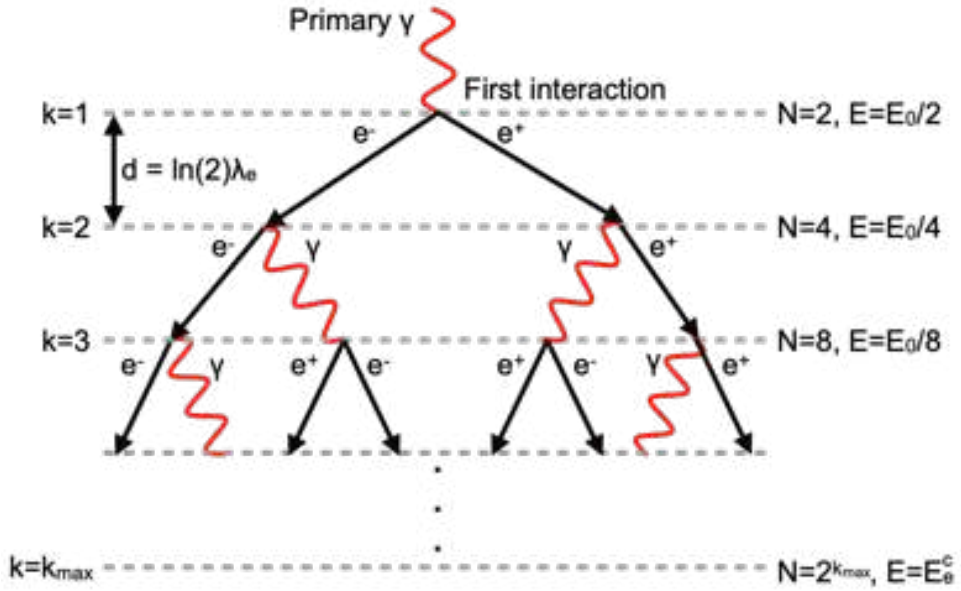

Fig. 1.9.: Electromagnetic shower. Schematic illustration of an electromagnetic shower development under the Heitler approximation. A primary gamma ray interacts with a nucleus in the atmosphere after traversing a length $d = \ln(2)\lambda_e$, $\lambda_e = 37\,\mathrm{g\,cm^{-2}}$ is the characteristic length to produce a pair or a photon by Bremsstrahlung. Therefore, at each layer k the number of secondary particles is multiplied by 2. The binary splitting of the shower continues until the last layer k_{max} where ionisation losses start to dominate.

secondaries occurs at fixed-length intervals. After each interaction length, the number of particles gets doubled. For k radiation lengths the number of particles is $N = 2^k$, each with energy $E = E_0/2^k$. At a given moment, a critical energy E^c where no more particles can be produced is reached. For electrons in air $E_e^c \approx 84\,\mathrm{MeV}$. At this energy, the shower reaches its maximum development k_{max}.

A theoretical description of the lateral distribution of particles was developed by Greisen and by Kamata and Nishimura (Greisen, 1952; Kamata et al., 1958). At each interaction point, the pair production and Bremsstrahlung generate particles that are not exactly aligned to the primary particle direction. Coulomb scattering of the electrons and positrons adds a smearing at

the shower front. The density of particles as a function of distance r from the shower axis is given by the Nishimura-Kamata-Greisen (NKG) function:

$$\rho_e(r) = \frac{N_e}{2\pi R_m^2} C(s) \left(\frac{r}{R_m}\right)^{s-2} \left(1 + \frac{r}{R_m}\right)^{s-\frac{9}{2}}, \tag{1.13}$$

where N_e is the number of electrons in the shower, R_m is the Molière radius that includes the Coulomb scattering effect, $C(s)$ is a normalisation factor equal to $0.366s^2(2.07 - s)^{1.25}$ such that $\int_0^\infty 2\pi r\rho(r)dr = N_e$. The shower age s starts at $s = 0$ when the shower is initiated and reaches $s = 1$ at the shower maximum.

Hadronic showers (initiated by cosmic rays) are produced via the nuclear interaction with the nucleus of a molecule in the atmosphere. This leads to the production of neutral pions (π^0), charged pions ($\pi^\pm$) but also fragments of the target nucleus (N), neutrons (n), and protons (p). Neutral pions decay rapidly into gamma rays and produce sub-electromagnetic showers. Charged pions decay into muons ($\mu^\pm$) and muon neutrinos. With a smaller probability, pions may also decay into electrons or positrons and the respective neutrino (Fig. 1.10).

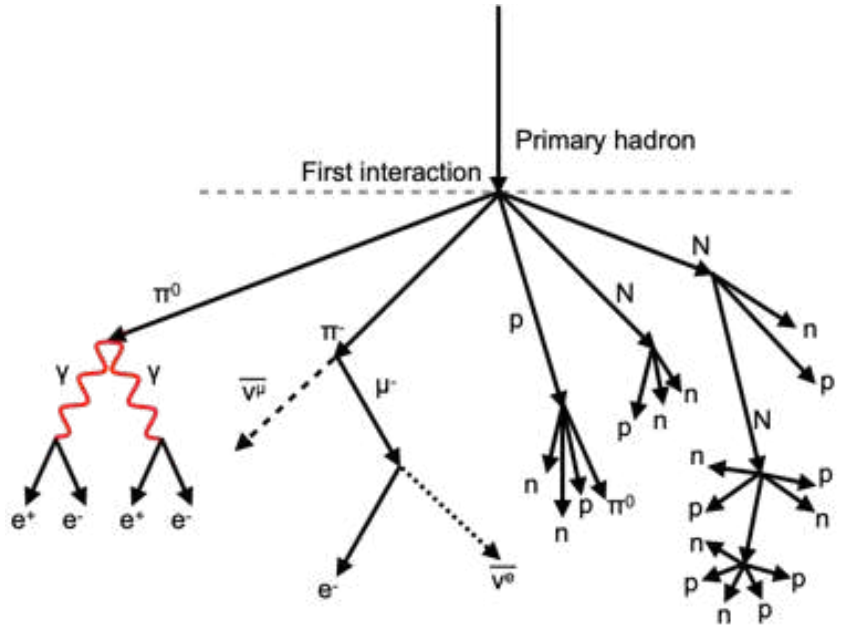

Fig. 1.10.: Hadronic shower. Schematic illustration of the development of an atmospheric shower initiated by a hadron.

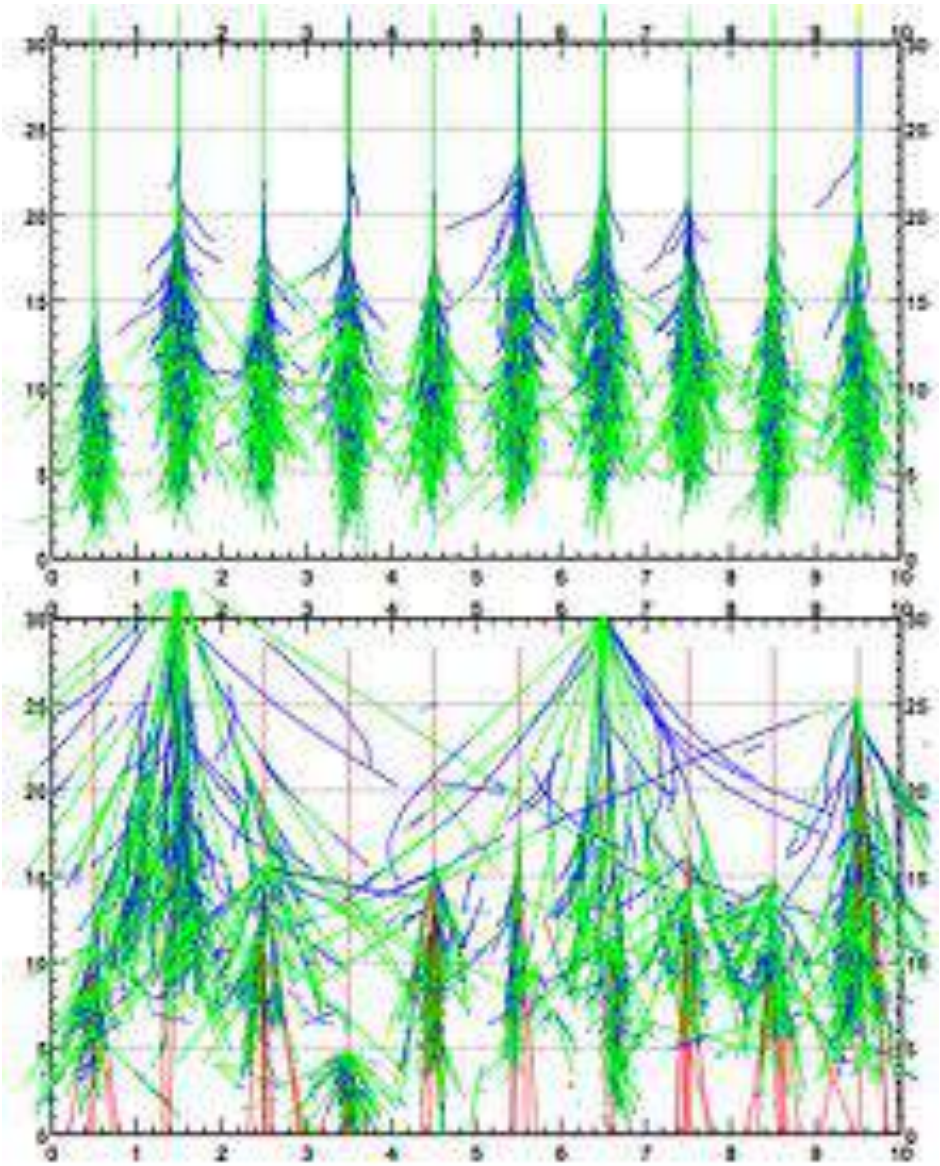

Fig. 1.11.: Development of atmospheric showers. Atmospheric showers simulation with the Monte Carlo package CORSIKA for a primary particle energy of 300 GeV. Blue colours correspond to electrons and positrons, green to photons, red to muons and dark-red to protons. The shower development is tracked from an altitude of 30 km (y-axis) down to ground level 0 km. Top panel: Gamma-induced showers display a well-contained shape with very few fluctuations in each instance. Bottom: Proton-induced showers, by contrast, fluctuate from one another in extension and altitude of first interaction. The figure is taken from De Naurois, 2012.

Fig. 1.11 shows several Monte Carlo simulations of the development of an electromagnetic and hadronic shower with primary particle energy of 300 GeV. Clear differences between them can be seen, principally due to the presence of muons in hadronic showers that tend to swipe out a big fraction of the total energy to the outer parts of the shower. Electromagnetic showers, in contrast, have a collimated and compact geometry with few muons present.

Particles propagating in these atmospheric showers travel at relativistic speeds and can be detected at the Earth's surface or in the atmosphere through the Cherenkov light that they produce as will be discussed in Ch. 3.

1.5 Cherenkov Radiation

Cherenkov radiation is light produced when charged particles travel through a dielectric material faster than the speed of light in that material. This radiation is the consequence of the relaxation from a dipole state induced by the traversing charged particle in the atoms and molecules in the medium (Cherenkov, 1937; Longair, 2011). For particles with a velocity v smaller than the propagation speed of the emitted electromagnetic waves $v_c = c/n$ ($v < c/n$, with c the speed of light and n the refractive index of the medium), the waves will not add coherently. In the case of particles travelling at relativistic speeds where $v > c/n$, according to Huygen's construction, the wave-forms emitted by the medium will add coherently at a given angle relative to the particle trajectory, forming a cone of Cherenkov light (Fig. 1.12). The cone of light will have an opening angle θ_c such that

$$\cos(\theta_c) = c/(vn) = \frac{1}{\beta n}.$$

For Cherenkov radiation in water, the refraction index is $n = 1.33$ and the Cherenkov angle for $v \sim c$ is $41.2°$. In the case of air, the Cherenkov angle is approximately $\sim 1.4°$, although this number varies since the refraction index depends on the atmospheric density. The minimum energy that a particle requires to produce Cherenkov radiation is:

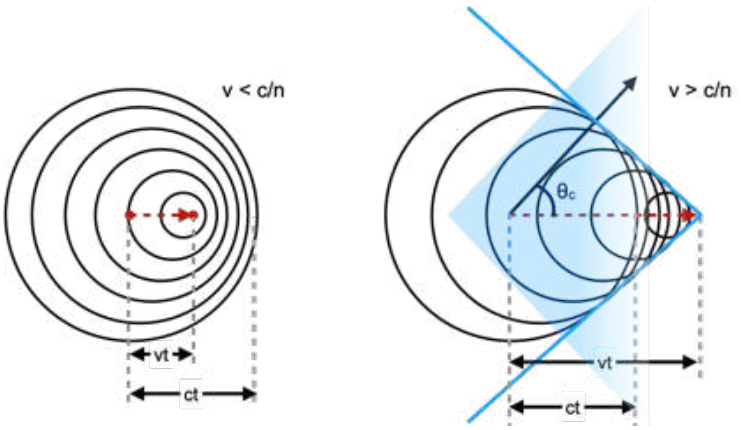

Fig. 1.12.: Diagram illustrating the Cherenkov radiation. The radiation generated by the particle passing through the material forms a coherent wavefront with a conical shape. Adapted from Jackson, 1998.

$$E_{\min} = \gamma_{\min} m_0 c^2 = \frac{m_0 c^2}{\sqrt{1 - n^{-2}}}$$

with γ_{min} the Lorentz factor of the particle of mass m_0. Therefore, particles with low mass (such as electrons) tend to be the dominant source of Cherenkov radiation. For water the energy threshold to emit Cherenkov radiation corresponds to $\sim 775\,\text{keV}$ for an electron, $\sim 1.42\,\text{GeV}$ for a proton and $\sim 160\,\text{MeV}$ for a muon. The number of photons produced at a given wavelength λ per unit length x is given by the Frank-Tamm equation:

$$\frac{\mathrm{d}^2 N}{\mathrm{d}x \mathrm{d}\lambda} = 2\pi\alpha Z^2 \lambda^{-2} \left(1 - \frac{1}{\beta^2 n^2(\lambda)}\right) \tag{1.14}$$

with α the fine structure constant and Z the charge of the particle. Given the λ^{-2} dependence of the spectrum, Cherenkov light will peak at short wavelengths corresponding to the blue to ultraviolet light. In the atmosphere, this radiation will scatter on air molecules and aerosols and be absorbed by ozone, shifting the peak of the spectrum to $\lambda \approx 330\,\text{nm}$.

2

Gamma-ray Bursts

Contents

2.1 Introduction

Luckily, astronomers are sometimes not so imaginative with the naming of astrophysical objects and one instantly imagines what a gamma-ray burst (GRB) is. GRBs are bright flashes of gamma-rays whose bright emission lasts from milliseconds up to thousands of seconds. The emission spectrum is dominated by gamma-rays in the keV to MeV energy range. The burst-like episode of GRBs is called the *prompt* phase that is followed by an *afterglow* episode in which the emission decreases smoothly with time.

The first detection of a GRB was done by the *Vela* satellites in the '60s. This satellite was meant to monitor the use of nuclear weapons after the Cold War when the Partial Test Ban Treaty was signed by the US, USSR and UK governments. The Vela mission, deployed by the US, was a system of orbiting

satellites and ground monitors. The specific mission deployed as a satellite was the *Vela hotel*, sensitive to gamma rays in the energy range from 0.2 to 1.5 MeV.

On the 2nd of July 1967, Vela detected a very bright, yet short, gamma-ray emission with a signature distinct from that expected from a nuclear explosion. The years passed and more of these signals were recorded by Vela. In fact, this first explosion was GRB 670702[1] and the paper "Observations of Gamma-ray burst of cosmic origin" published in 1973 provided the first evidence of the existence of GRBs. In this paper, sixteen bursts detected by Vela were characterised (Klebesadel et al., 1973). The main striking conclusions of that paper was the vastly varying characteristics of these GRBs, with a duration from less than one second up to 30 s, and light curves without any significant structure nor similarities.

T evolution of the understanding of the GRB characteristics can be understood to be the result of the evolution of the satellites and the observatories that were deployed after Vela's discovery to detect them. For a complete description see Zhang, 2018. The most important findings are:

BATSE (1991–1997) The Burst And Transient Source Experiment (BATSE) was onboard the Compton Gamma Ray Observatory, launched in April 1991. BATSE was a wide FoV satellite, equipped with two detectors covering the energy range from 20 keV – 1.9 MeV and 10 keV–100 MeV. It was the first instrument specifically designed for the study of GRBs, having a sensitivity of $\sim 3 \times 10^{-8}$ erg cm^{-2} for a 1 s burst duration. BATSE detected a total of 2704 GRBs and revealed a non-thermal origin for the emission.

The angular distribution of the detected GRBs was found to be isotropic, and the intensity of the bursts was not compatible with a Euclidean geometry; characteristics easily explained if GRBs happened at cosmological distances. BATSE also found a significant bimodal distribution in the GRBs prompt emission duration with a dip at ~ 2 s. As a consequence of this finding, GRBs started to be classified as long and short, based on their prompt emission duration. The emission spectrum

[1] The naming convention of GRBs corresponds to the year, month and day of detection or T_0, adding successive letters of the alphabet if more than one is detected in a day

started to be characterised by the broken power-law function called the "Band function" (Band et al., 1993).

BeppoSAX/HETE Era (1997–2004) BeppoSax, launched in April 1996, was a satellite carrying wide-field cameras (2–30 keV) and narrow and wide FoV instruments including a GRB monitor (40–700 keV). The wide-field cameras would promptly search for counterparts within the localisation uncertainty region of burst detected by its own GRB monitor or by BATSE, improving the localisation measurement. BeppoSAX was the first instrument to measure the X-ray afterglow in GRB 970228 and GRB 970508, also detected in the radio and optical bands. With the localisation of the host galaxy and redshift measurement (z=0.835) of the latter, the cosmological origin of GRBs, first hinted at by BATSE, was established.

The High Energy Transient Explorer 2 (HETE-2) (since the first HETE was lost during launch in 1996), operation between 2000 and 2006. Together with BeppoSAX, the detection of >100 GRB afterglows and measurement of the redshift was achieved. The association of long GRBs with Type Ic supernovae was established with the detection of GRB 980425, spatially consistent with the SN 1998bw in a host galaxy at z=0.0085 and with the association of GRB 030329 with SN 2003dh located at z=0.167. The abundance of multi-wavelength afterglow data in this era allowed a deep understanding of the emission mechanisms is GRBs.

Swift Era (2004–) The *Swift* satellite was launched in November 2004. It is equipped with three instruments, a wide FoV Burst Alert Telescope (BAT), a narrow FoV X-ray Telescope (XRT) and an UV-Optical telescope (UVOT). The BAT (15–350 keV) has a 1.4 sr FoV and serves to locate promptly any new GRB in its field with a localisation uncertainty of few arc-mins. The XRT having a 23.6'×36.6' FoV, slews to these locations, and with a sensitivity of $\sim 2\times10^{-14}$ erg cm^{-2} s^{-1} in $\sim10^4$ s of integration, is capable of detecting the afterglow of most of the GRBs located by BAT. In the same way, UVOT can detect the UV and optical counterpart of most of these GRBs thanks to its 170–650 nm bandpass and sensitivity down to magnitude 23 in white light in 10^3 s of integration.

Swift has been capable of detecting a huge variety of GRBs, from short to ultra-long ones. Thanks to the identification of the host galaxy of several short GRBs, these have been identified as a different population, distinct from long GRBs, originated from the coalescence of compact objects such as binary neutron stars (NS-NS) or a neutron star and a black hole (NS-BH). At the same time, with the detection of many peculiar GRBs, it has been found that the naive classification of GRBs based on their duration is not sufficient to identify their origin. Long-duration GRBs without any SN association or short GRBs exhibiting characteristics of the long-duration population have been detected.

The abundance of afterglow data collected by *Swift*-XRT has allowed the discovery of a canonical afterglow light curve. *Swift* has located the most distant GRBs (GRB 090423 at z=8.2 and GRB 090429B at z=9.4), allowing the use of GRBs as cosmological probes.

Fermi Era (2008–) The Fermi Gamma-Ray Space Telescope (FGST,*Fermi*) was launched in June 2008. It is equipped with a wide-field Gamma-ray burst Monitor (GBM, 8 keV–40 MeV), with a sensitivity of 0.5 $cm^{-2}\,s^{-1}$ in the energy range of 50–300 keV. GBM scans the whole sky (not occulted by the Earth) in the search for GRB events, locating them with a typical uncertainty of few degrees. The Large Area Telescope (LAT, 20 MeV–300 GeV) with a FoV >2 sr searches for the corresponding HE gamma-ray emission of GRBs located by GBM and *Swift*.

Combining observations by GBM and LAT, it is possible to cover roughly 7 decades in energy, which has provided important insights into the spectral characteristics of GRBs. Among the important findings of *Fermi* is the detection of an additional spectral component, besides the Band function, observed in bright GRBs detected by LAT. This points to an external-shock origin for the >100 MeV emission. Generally, only very-bright bursts detected by GBM are also detected by LAT, roughly 4% of the total. The high energy emission (above 100 MeV) is found to be systematically delayed by up to 40 seconds compared to the keV–MeV emission, and it is also seen to last longer, with a characteristic power-law decay of the emission with time ($F \propto t^{-\alpha}$, with F the energy flux). In some GRBs, LAT has detected photons with energies in the GRB rest frame above 100 GeV (GRB 080916C, GRB 090510

and GRB 130427A) posing hard constraints on the particle acceleration and radiation mechanisms of relativistic shocks believed to be present in GRBs, as well as on the effect of the flux attenuation due to the extragalactic background light (EBL).

The Multi-Messenger and VHE Era (2017–) The multi-messenger era comprises the search (and detection) of neutrinos and gravitational waves (GWs), believed to be emitted from GRBs. Up to now, the IceCube neutrino observatory, located in the south pole, has searched for TeV–PeV neutrinos of the three flavours (electron, muon and tau neutrinos) temporally and spatially consistent with GRBs detected by other instruments, without any positive detection. These observations have constrained the production of neutrinos and ultra-high energy cosmic rays in GRBs (Aartsen et al., 2016).

The multi-messenger era began with the detection by Advanced LIGO and Virgo of the NS-NS merger event GW170817 associated with the low-luminosity GRB 170817A (Abbott et al., 2017) detected in X-ray, optical and radio bands and localised in the galaxy NGC 4993 at a distance of $\sim$40 Mpc.

The VHE era began in 2018 with the detection of GRB 180720B by the H.E.S.S. telescopes (see Ch. 5) followed by the detection of GRB 190114C by the MAGIC telescopes (Acciari et al., 2019). These detections confirmed the presence of VHE photons in the afterglow and late-prompt phases and will be discussed in further detail in Sec. 2.6 and Ch. 5.

In the following sections, the fundamental characteristics of GRBs are presented. Important features of the prompt and afterglow phases are summarised in Sec. 2.2 and Sec. 2.3, respectively. Particle acceleration in GRBs is discussed in Sec. 2.4. Notions on GRB classification, origin and important relations, all coming from the evidence of observational data, are given in Sec. 2.5. The HE and VHE emission of GRBs is discussed in Sec. 2.6 and conclusions are given in Sec. 2.7.

2.2 Prompt Emission

In the most accepted picture to describe the emission from GRBs, called the fireball model, the prompt emission phase is assumed to be originated in a central engine, generated during the merger of two compact objects (Piran, 1999). This engine is responsible for producing a relativistic flow of plasma shells (fireballs) of a diverse range of Lorenz factor values. Shells travelling at different speeds eventually collide and produce internal shocks where particle acceleration within magnetic fields takes place. The resulting particles, accelerated and travelling all together within a relativistic bulk of matter, will give rise to the emission of X-rays and gamma-rays.

From an observational point of view, the prompt emission encompasses the episode where 5% to 95% of the total fluence is collected, often called T_{90}. This observational quantity can only be interpreted taking into account the energy range and sensitivity of the instrument measuring it since GRB pulses are wider at lower energies. The prompt emission duration is often measured in the BATSE energy range (25–350 keV). The rest of the multi-wavelength emission detected in the T_{90} interval is often considered as part of the prompt phase.

2.2.1 Temporal Domain

The logarithmic value of T_{90} presents at least two Gaussian components separated at around 2 s. This was first evidenced in the BATSE era (Kouveliotou et al., 1993). In the BATSE energy band (50–300 keV) the ratio of short to long GRBs is 1:3. This relation is not universal and is energy and sensitivity dependant (Y. Qin et al., 2013). For example, *Swift* (15–150 keV) finds a ratio of about 1:9 (Fig. 2.1).

Another basic temporal characteristic of the GRB prompt emission is its notorious irregularity. The light curves are usually composed of fast-rising exponential-decay (FRED) structures and/or pulses of different intensities. Some GRBs may have precursor episodes separated by a quiescent state of several tens to hundreds of seconds of duration. The definition of such

episodes is not well established and the fraction of GRBs presenting such characteristics range from 3% up to 20%. These episodes are often interpreted as erratic GRB central-engine activities (Burlon et al., 2008).

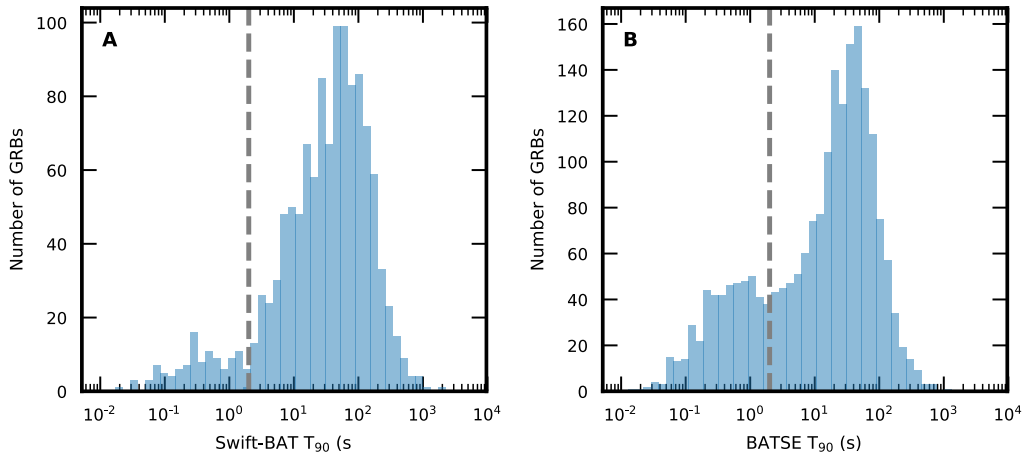

Fig. 2.1.: Illustration of the T_{90} bimodal distribution from the Swift-BAT and BATSE catalogue. For panel A the value of T_{90} is measured in the *Swift*-BAT energy range (15–150 keV). For panel B it is measured in the BATSE energy range (50–300 keV). In both panels, the line at 2 s which usually serves to identify long GRBs (blue) and short GRBs (orange) is shown. The data were obtained from `https://swift.gsfc.nasa.gov/results/batgrbcat/index_tables.html` and `https://heasarc.gsfc.nasa.gov/w3browse/all/batsegrb.html` respectively.

2.2.2 Spectral Domain

Since the BATSE era (see Sec. 2.1), the Band function has been used to describe the prompt GRB photon spectrum. This function of the energy E (in keV) is:

$$N(E) = \begin{cases} A\left(\frac{E}{100\,\mathrm{keV}}\right)^{\alpha} \exp\left(\frac{-E}{E_0}\right), & E < (\alpha-\beta)E_0, \\ A\left[\frac{(\alpha-\beta)E_0}{100\mathrm{keV}}\right]^{-\alpha+\beta} \exp\left(\beta-\alpha\right)\left(\frac{E}{100\,\mathrm{keV}}\right)^{\beta}, & E \geq (\alpha-\beta)E_0, \end{cases}$$

where A is the spectrum normalisation, E_0 the break energy in keV, α and β are the low-energy and high-energy spectral indices respectively. When

α equals β this function reduces to a simple power-law. If β has a large value then the Band function describes an exponential cutoff power-law (sometimes called a Comptonized model). The peak energy (E_p) in the SED ($E^2N(E)$) is related to E_0 through

$$E_p = (2 + \alpha)E_0.$$

The values of E_p range from several keV up to few MeV, centred at around ~ 200 keV. The hard spectral index value α has a normal distribution centred at $\alpha \sim -1 \pm 1$ while the soft index is found to be distributed around $\beta \sim -2^{+1}_{-2}$ (Preece et al., 2000).

As summarised in Ch. 1.2.1, for a synchrotron process, the gamma-ray spectral index for an electron distribution of spectral index $-p$ is $\alpha = (1-p)/2$. In the case of electrons accelerated by shocks (as is thought to be the case for GRBs), $p = -2$ which yields $\alpha = -3/2$, consistent with values found in GRB data. Two bounds can be set for the expected photon-index value. First, where electrons radiate instantaneously all their energy due to synchrotron radiation $\alpha < -2/3$, and second when electrons cool down in timescales shorter than the burst time, $a > -3/2$.

Besides the Band component, another spectral component at high energies is required to fit the broad-band spectra of some GRBs. This additional component has been detected by *Fermi*-LAT and is characterised by a power-law extending above 100 MeV with an index of ~ 2.0. A second E_p is inferred to exist in the 1–100 GeV range to explain the limited number of detections at such energies by the *Fermi*-LAT and by ground-based instruments.

2.3 Afterglow Emission

The afterglow emission is defined as the temporal phase that follows the prompt emission. The presence of the afterglow emission was predicted before its discovery in the framework of the *Fireball model*. In this model, the relativistic flow produced by the central engine will extend away into the circumburst medium and produce strong forward and reverse shocks able

to accelerate particles up to relativistic speeds. The gamma-ray emission is predicted to happen over a wide energy range from optical to TeV.

Another important feature of the afterglow phase is the characterisation of the temporal evolution. When the ejected material starts to *wipe out* the circumburst medium, the deceleration will manifest as a decay in the emission:

$$F_\nu(t,\nu) \propto t^{-\alpha}\nu^{-\beta},$$

where α is the temporal decay and β the photon index. The canonical light curve (Nousek et al., 2006), is an example of this power-law characterisation of the afterglow emission (Fig. 2.2). In general, the X-ray afterglow of GRBs can be decomposed into up to five components (not all GRBs present all five):

I. Steep decay phase. The temporal decay of this phase is steep, with α ranging from 3 to 10, and is usually found to smoothly connect with the end of the prompt emission. This suggests that this component is the natural continuation of the fading prompt episode.

II. Shallow decay phase (plateau). This phase has a typical decay index from 0 to -0.7. Spectral analyses show that there is practically no spectral evolution, suggesting that this segment is of pure geometrical or hydro-dynamical origin. In the forward shock model, this plateau can be predicted when a continuous energy injection into the forward shock is present.

III. Normal decay phase. This segment has the typical decay-value predicted in the forward shock model, from about -1 to -1.2. Similar to the shallow decay, this phase does not present any spectral evolution.

IV. Post jet-break. The temporal decay becomes steeper with a value of $\alpha \sim -2$ or more. This is believed to be an effect of GRB collimation. The visible opening angle of the GRB jet is contracted due to relativistic beaming. In the jet-brake phase, as the jet decelerates, the cone of visible emission becomes wider than the actual GRB jet opening angle.

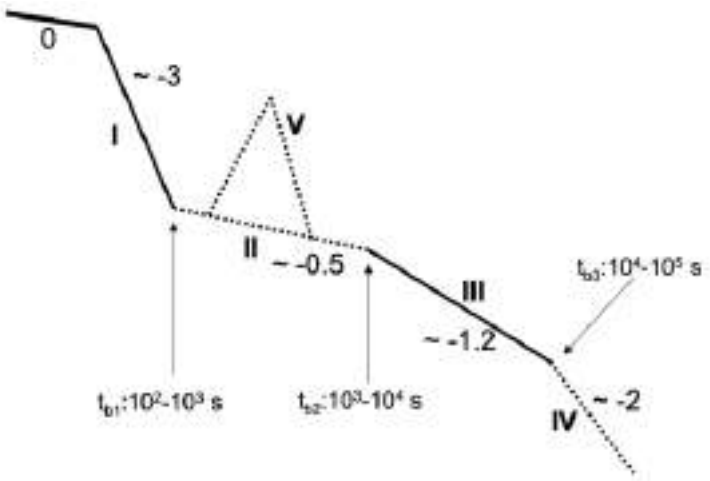

Fig. 2.2.: Illustration of the different segments composing the afterglow light curve of GRBs. Apart from segment V (X-ray flares), each segment can be characterised with a power-law decay with the mean measured decay index indicated in the figure. Figure reproduced from Zhang, 2006

After the jet break, the observed temporal decay corresponds to the actual deceleration of the ejecta without beaming.

V. X-ray flares. This last component is a superposed feature of a power-law decay component (eg. shallow, normal or post jet-break phase). Typically, the temporal decay before and after an X-ray flare remains unchanged, which suggests a different emission site from the power-law segment where it is enclosed. The variety of observed brightness, duration and time of observation seen in these flares suggests that these features are internal events, independent of the afterglow phase, sharing properties observed during the prompt emission.

Examples of these features are shown for a set of GRBs detected by *Swift* in Fig. 2.3.

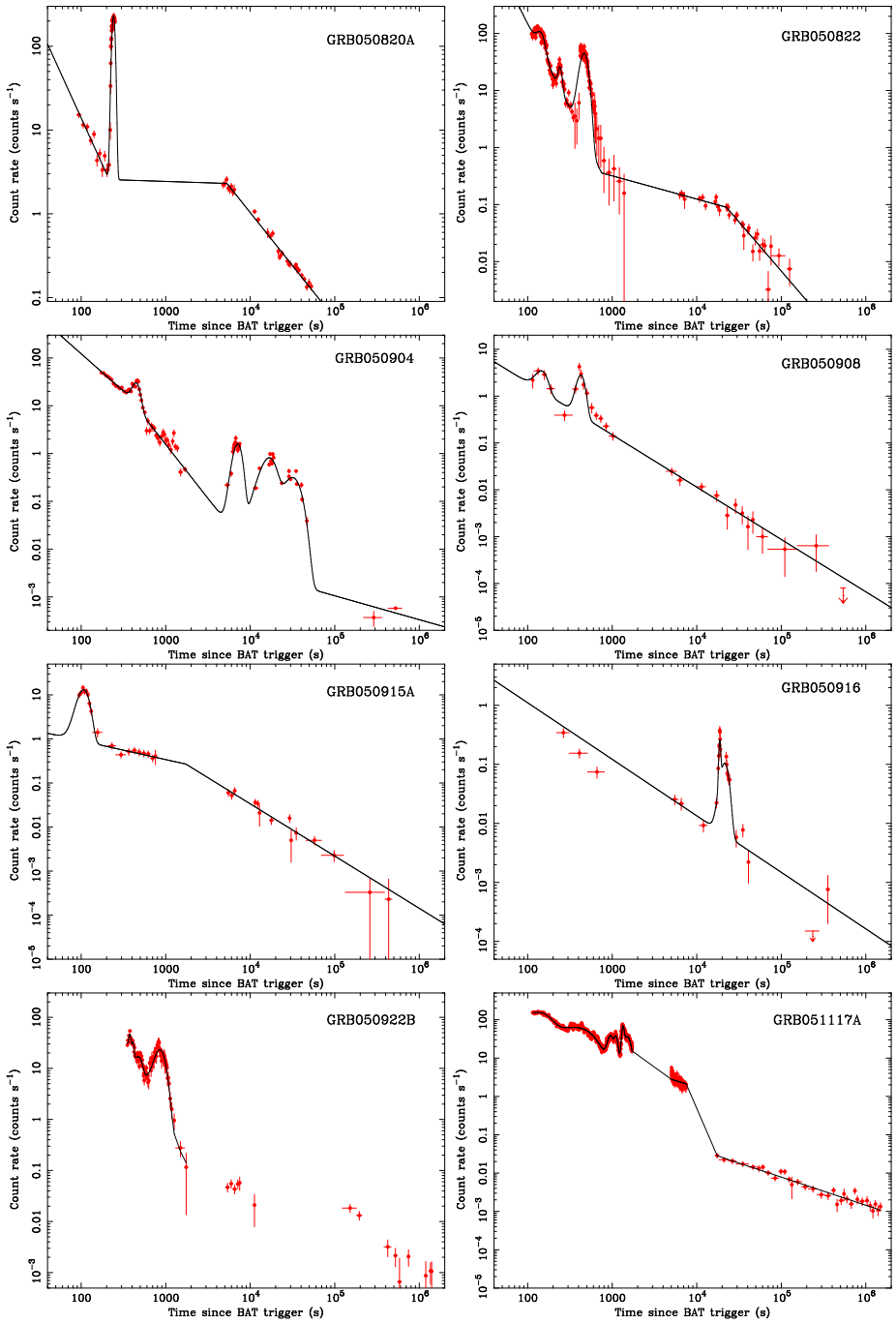

Fig. 2.3.: Examples of GRB light curves in X-rays. These figures show the count rate as a function of time for a set of GRBs detected by the *Swift*-XRT where canonical features are detected. The figure is taken from Chincarini et al., 2007.

2.4 Particle Acceleration in GRBs

Although many aspects of GRB physics remain unknown, there exists strong evidence that the GRB ejecta is beamed and move at relativistic speeds. This ejecta can be interpreted as a relativistic fluid, where shocks can develop. The collision of the ejecta into the circumburst medium generates a forward shock and a reverse shock. In the case of the forward shock, which generates the afterglow phase, efficient acceleration should happen to explain the bright multi-wavelength emission seen in GRBs (see de Gouveia Dal Pino et al., 2015 for a review). The relativistic extension of DSA (see Ch. 1.1.1) is a highly likely mechanism for particle acceleration within the forward shock.

Naturally, the circumburst region, where the forward shock is propagating, should not be highly magnetised, while the afterglow data of some GRBs require high magnetic fields. Therefore, relativistic shocks should feature magnetic instabilities where particles can be accelerated. An example of these is the microscopic Weibel instabilities, where magnetic disturbances in a two-stream plasma system induce an enhanced magnetic field. Other mechanisms suggested are larger-scale instabilities triggering macroscopic turbulence that can also generate magnetic amplification. These instabilities can be generated when the forward shock hits clumps of matter in the circumburst medium. In GRB theory, microphysical parameters are adopted to describe shock acceleration in GRBs. The total shock internal energy is partitioned into a fraction of magnetic energy density $\epsilon_{\rm B}$, another fraction of energy $\epsilon_{\rm p}$ is given to protons/ions and another fraction corresponds to the electron energy $\epsilon_{\rm e}$. A fraction of these electrons is accelerated to the power-law spectra as prescribed by the DSA.

For the prompt emission case, even if the nature and characteristics of the central engine in GRBs are still unknown, the progenitor is likely responsible for the magnetisation required to accelerate particles to high energies during this episode. Scenarios sometimes invoke the presence of internal shocks where constraints on the magnetisation exist to achieve efficient acceleration. Another mechanism that can accelerate particles is magnetic reconnection. The process of acceleration, in this case, can be similar to DSA: trapped particles will bounce back and forth within the regions of re-connection. Inductive magnetic fields in these regions can also accelerate particles.

An alternative scenario for particle acceleration is the shear acceleration (SA, See Rieger et al., 2005). This process has been described in the context of relativistic astrophysical jets of AGNs and GRBs. Velocity shears in the jet trigger Kelvin-Helmholtz instabilities, leading to magnetic field amplification and particle acceleration. In SA, the acceleration is governed by the mean free path of the particles and is favoured for higher energy particles.

2.5 GRB Properties

Thanks to the increased collection of GRB data, some global properties of GRBs have emerged:

Isotropic distribution The spatial distribution of GRBs (Fig. 2.4) is isotropic. No apparent clustering is found along e.g. the galactic centre, nearby galaxies or clusters of galaxies. When measuring the dipole moment ($\langle\cos(\theta)\rangle$, in galactic coordinates where θ is the angle between the burst and the Galactic Centre) or the quadrupole moment ($\langle\sin^2(b)\rangle$, in galactic coordinates where b is the galactic latitude), the values obtained for BATSE bursts are consistent with an isotropic distribution (Meegan et al., 1992).

Non-Euclidean peak flux/fluence distribution For an Euclidean space, the number of objects observed above a fluence (peak flux) S (P) satisfies:

$$N(>S) \propto S^{-3/2}, N(>P) \propto P^{-3/2},$$

and

$$\left\langle \frac{V}{V_{max}} \right\rangle = \frac{1}{2},$$

where V is the volume of a sphere extending to the source distance and $V_{\max}$ is the sphere extending to the maximum distance at which the detector would still detect the source. For GRBs, the fluence and peak flux distributions show a slope harder than $-3/2$ for low S and P values, while the measured $\langle V/V_{\max}\rangle$ ranges between 0.3 to 0.4.

Event rate The detected event rate is sensitivity and energy dependant. For the current GRB detectors (flux sensitivity $\sim 10^{-8}$erg cm^{-2} s^{-1}) it is of

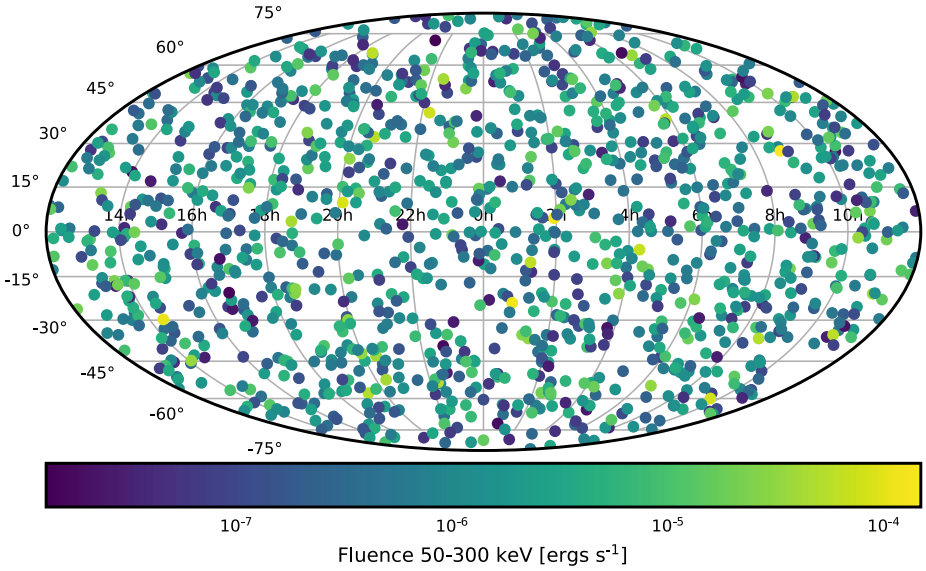

Fig. 2.4.: Spatial distribution of GRBs in the BATSE catalogue. The spatial distribution in the equatorial coordinate system using a Mollweide projection of GRBs in the BATSE 4B catalogue (Paciesas et al., 1999). Each point corresponds to a GRB and the colour encodes the GRB fluence in the 50–300 keV band. Figure reproduced from the catalogue data available in `https://heasarc.gsfc.nasa.gov/W3Browse/all/batsegrb.html`.

roughly 2–3 per day assuming an all-sky coverage (*Swift* field of view is ∼1/7 of the whole sky and it detects 2–3 GRBs per week).

Another relevant quantity is the volumetric event rate. For high-luminosity (HL) long GRBs (long GRBs roughly trace the star formation history of the universe), the observed local rate above a luminosity of $1\times10^{50}\,\mathrm{erg\,s^{-1}}$ is 0.5–1 $\mathrm{Gpc^{-3}\,yr^{-1}}$. Since GRBs are shown to have collimated emission, the measured density can be corrected by a beaming factor ∼500 so the intrinsic event rate is 250–500 $\mathrm{Gpc^{-3}\,yr^{-1}}$. Low-luminosity (LL) long GRBs ($\sim 5\times10^{46}$ – $1\times10^{49}\,\mathrm{erg\,s^{-1}}$) have an observed event rate density of around 100–200 $\mathrm{Gpc^{-3}\,yr^{-1}}$. There is no strong indication of jet collimation in these events, so the beaming factor is $\gtrsim$1 and the rate density remains comparable to the HL long GRBs. For short GRBs, the rate density above $1\times10^{50}\,\mathrm{erg\,s^{-1}}$ is about 0.5–3 $\mathrm{Gpc^{-3}\,yr^{-1}}$. Since short GRBs exhibit collimation with a wide range of values from 0.04 to 25 the total event rate becomes about 13–75 $\mathrm{Gpc^{-3}\,yr^{-1}}$

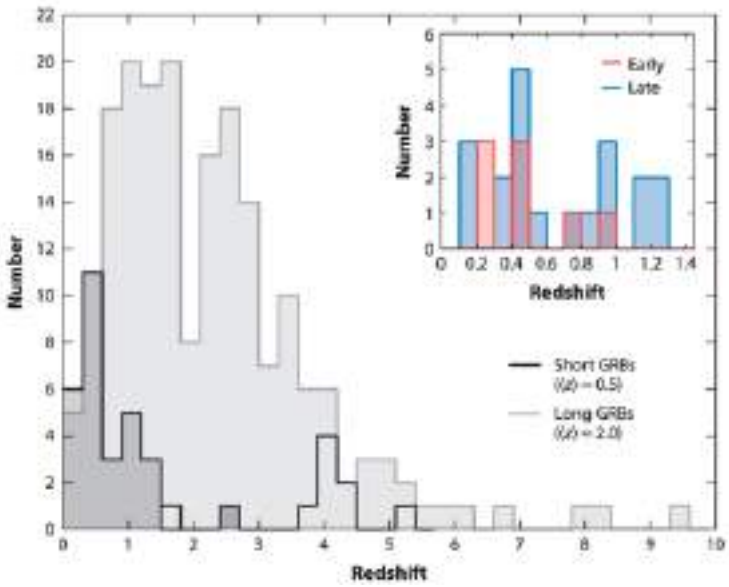

Fig. 2.5.: The redshift distribution of GRBs. GRBs are separated between short and long GRBs having respectively a mean redshift of 0.5 and 2.0. Short GRBs redshifts are separated by their host-galaxy type (early and late) in the inset plot which shows no difference in distribution. Figure reproduced from Berger, 2014.

Redshift distribution The measured redshift distribution of *Swift*-detected GRBs is shown in Fig. 2.5. The redshift distribution for short GRBs is z ∼0.1–1.3. Since most of these values are obtained from the distance of the corresponding host galaxies, this distribution likely spans beyond z≥1 where faint galaxies lack a redshift measurement. From measurements, the mean redshift of short GRBs is $\langle z \rangle$=0.48. As also seen in Fig. 2.5, no clear trend is observed when splitting short GRBs into late-type or early-type host galaxies, which indicates a possible observational bias, since GRB progenitors are expected to be present at a lower redshift for early-type galaxies.

Long GRBs extend up to $z = 9$ with a mean value of $\langle z \rangle \approx 2.0$. Since long GRBs are associated with the core-collapse of massive stars, the redshift distribution is believed to trace the star formation rate of the Universe.

Isotropic Energy The bolometric isotropic energy is defined as:

$$E_{\gamma,\mathrm{iso}} = \frac{4\pi D_L^2 k S_\gamma}{1+z}$$

where D_L is the luminosity distance for redshift z, S_γ is the photon fluence and k is a correction factor used to re-scale the fluence from the instrument energy-band to a fixed co-moving one (Bloom et al., 2001). The distribution of $E_{\gamma,\mathrm{iso}}$ ranges from $\sim 1\times10^{49}$ to $\sim 1\times10^{55}$ erg for long GRBs and from 1×10^{46} to 1×10^{53} erg for short GRBs.

Some relations between different GRB observables have been found (See Zhang, 2018 for an extended review). For example, the Amati relation correlates the rest-frame peak energy and the isotropic energy: $E_{p,z} - E_{\gamma,\mathrm{iso}}$ of long GRBs:

$$\frac{E_{p,z}}{100\mathrm{keV}} = C\left(\frac{E_{\gamma,\mathrm{iso}}}{10^{52}\mathrm{erg}}\right)^m, \tag{2.1}$$

with $C \approx 0.8 - 1$ and $m \approx 0.4 - 0.6$ (Amati, 2006) and indicates that more energetic GRBs tend to have a harder spectrum.

2.6 HE and VHE Emission

In recent years, the GRB detections at VHE have revolutionised the field and increased the number and quality of models to explain the features seen in the HE and VHE domain. The *Fermi*-LAT detects roughly 10 GRBs per year, with some exhibiting energies above 1 GeV. However, with less than a handful of GRBs detected above 100 GeV, the process responsible for accelerating photons up to TeV energies is still a matter of debate. A review on these topics can be found in Inoue et al., 2013 and Nava et al., 2017.

Fermi-LAT observations have constrained the minimal bulk Lorenz factor (Γ) needed to produce the highest energy photons in the pair production threshold, obtaining values for Γ of the order of hundreds. However, these results rely on simplified models of, for example, a homogeneous, time-independent and isotropic photon field, while more detailed models can obtain values for Γ about three times lower. Another important feature seen at HE is a typical delay in the emission, of the order of seconds, relative to the keV signal. In very bright GRBs this delayed HE emission is found to

exhibit the same shape as the keV emission. At late times, the HE emission is found to decay with $\propto t^{-1.2} - t^{-1.5}$ with no significant spectral evolution.

In the prompt phase, the spectrum of several GRBs detected at HE is found to be inconsistent with an extrapolation of the Band function. A second power-law component of photon index ≤ 2 seems required. In some other GRBs, the presence of this second component is not required. The *Fermi*-LAT catalogue of GRB observations (Ajello et al., 2019), finds that in most of the cases, the detected afterglow emission can be modelled by a simple power-law of index ~ -2 which is typically harder than the high-energy spectral index of the Band function.

The most accepted mechanisms to explain the observed HE and VHE emission, for the leptonic scenario, are the synchrotron and synchrotron self-Compton processes:

Synchrotron A major theoretical restriction, for the photons detected at HE, is the so-called synchrotron burnoff limit. This limit is obtained by equating the time scale of electron acceleration and energy loss due to synchrotron radiation. A cutoff in the spectrum is expected to happen at an energy $E_{\rm syn}^{\rm max} \approx 50{\rm MeV}\,\Gamma/(1+z)$. Expected values of Γ for the afterglow phase are of the order of ten, with Γ decreasing with time. This indicates that photons in the GeV range violate the burnoff limit and another emission process might be required to explain the presence of these photons.

Synchrotron Self-Compton In the SSC scenario, the relativistic electrons with $\Gamma \sim$100 can produce Synchrotron radiation in the keV-MeV energy range. Once inverse-Compton scattered by this same population of electrons, these photons can reach energies a factor Γ^2 higher ($\nu_{\rm IC} \approx \Gamma^2 \nu_{\rm syn}$) (Ando et al., 2008). The SSC mechanisms will produce a separate spectral component at high energies. The spectral shape and timescales are modified if the emission happens in the Thomson or Klein-Nishina regime (see Ch. 1.2.1).

Hadronic mechanisms have also been discussed in the context of HE and VHE emission. A proton synchrotron mechanisms could potentially reach the energetic requirements. However, in many GRBs the observed HE emission delay is found to be greater than the width of individual flares. A challenge

faced by the proton-synchrotron scenario is the relatively long variability timescales, increased further in models where the presence of photo-hadronic cascading is evoked to alleviate the low radiation efficiency of proton synchrotron. Therefore, this process is thought to give only a small contribution in the case of HE afterglows (Zhang and Mészáros, 2001).

2.7 Conclusions

Although GRBs were discovered many decades ago and can become one of the brightest objects in the sky during their prompt emission, they are still one of the least understood astrophysical objects. This is mainly due to observational constraints, for example, their transient nature, extragalactic origin, and lack of simultaneous multi-wavelength data. It was shown in this chapter that many of their characteristics have been progressively revealed by observations at different time and energy scales. Thanks to the observation of hundreds of GRBs we can firmly establish an isotropic origin. Observations in the optical band have confirmed the collapse of massive stars as a GRB progenitor. In 2017, the detection of GWs from a binary neutron star merger and its association with GRB 170817A confirmed that GRBs can also be originated by the merger of compact objects. However, there still exists no solid classification scheme based on the observed parameters to securely identify a GRB progenitor. For example, some GRBs are found to contradict the classification scheme based on the burst duration.

The mechanisms capable of explaining the broad-band emission remain unknown, and the search for a unified model continues. In this respect, the fireball model has slowly gained support as a common base, in which microphysical parameters like magnetic and energy density in the acceleration environments, can be fine-tuned to explain the GRB emission on a case-by-case basis.

Observation of GRBs in the HE and VHE range, constitute further challenges to the theoretical framework. The *Fermi*-LAT observations account for a fraction of GRBs detected at lower energies and have provided insights to a likely second emission component. With the recent detections at VHE and the opening of the multi-messenger era, with gravitational waves and

neutrino observatories operating jointly with the second and third generation of VHE gamma-ray observatories, the field will see major steps forward in understanding the GRB processes and their environments.

3

Two Gamma-ray Observatories for the Detection of GRBs: HAWC and H.E.S.S

Contents

3.1 The High Altitude Water Cherenkov Observatory (HAWC)

The High Altitude Water Cherenkov Observatory (HAWC)[1] is a wide field-of-view (FoV) ground-based gamma-ray instrument located in the National Park Pico de Orizaba in the state of Puebla, Mexico at an altitude of 4100 meters above sea level (Fig. 3.1).

Fig. 3.1.: The HAWC Observatory in the National Park Pico de Orizaba in the Sierra Negra of Puebla, Mexico. The array is configured in a hexagonal shape, with avenues that allow access to each unit for maintenance purposes. The Pico de Orizaba seen in the picture is the tallest mountain in Mexico and the tallest volcano of North America. Image credit B. Dingus.

HAWC observes the gamma-ray sky in the TeV energy range, with an instantaneous aperture of $\sim$2 sr and a duty cycle of $\geq$ 98%. It is designed to detect atmospheric showers of secondary particles initiated by cosmic rays and gammas (See Ch. 1.4). These secondary particles are detected at ground level with water Cherenkov detectors (WCDs). A total of 300 WCDs equipped with high-efficiency photo-multiplier tubes (PMTs) compose the HAWC main-array which covers an area of $\sim 22000\,\mathrm{m}^2$. The recently deployed outrigger array, consisting of smaller WCDs sparsely positioned around the main array, increases the instrumented area by a factor of 4 (Marandon et al., 2019).

[1] https://www.hawc-observatory.org/

By detecting the energy deposited and time of arrival of particles in the atmospheric showers, HAWC is capable of reconstructing the arrival time, direction and energy of gamma and cosmic rays from the TeV sky.

3.1.1 Water Cherenkov Detectors

As shown in Fig. 3.2, each WCD in HAWC is a large cylindrical tank of 7.3 m diameter and 5.0 m tall, filled with ultra-purified water. The structure consists of corrugated stainless steel sheets forming a cylinder. A dome on the top protects it from rain and snow. Each WCD is equipped with a light and water-tight plastic lining that serves to contain the $\sim$200,000 litres of water and allows the operation of HAWC during daylight. The inside of the lining is black and prevents light from reflecting on the walls of the tank, improving the HAWC timing. Since a measurement of the time-over-threshold for each PMT signal is performed instead of recording the signal waveform, a black lining also prevents incorrect signal measurements due to late-time photons. Before filling the liner, the water is passed through a purification plant to remove small particles and algae, which can decrease the transparency and increase the scattering of photons. The water level inside the tanks is 4.5 m, ensuring that electrons and positrons from the atmospheric shower are completely absorbed before reaching the bottom of the tank. Thanks to the HAWC modular design, each WCD can be assembled, equipped, and maintained individually, without interrupting the data taking of the full array.

The bottom of the WCDs is equipped with four PMTs placed at about 45 cm above the ground. Three of them are 8" Hamamatusu PMTs (R5912). They surround a high-efficiency 10" Hamamatsu PMT (R7081) located a the centre (see Fig. 3.2). The secondary particles of the atmospheric showers travelling at relativistic speed produce Cherenkov light (see Ch. 1.5) and each PMT records their arrival time and intensity, defined as a PMT hit hereafter. The PMTs are capable of recording single photons at sub-nanosecond resolution. They are equipped with an electronics card that amplifies the signal that is then processed by the on-site electronics farm.

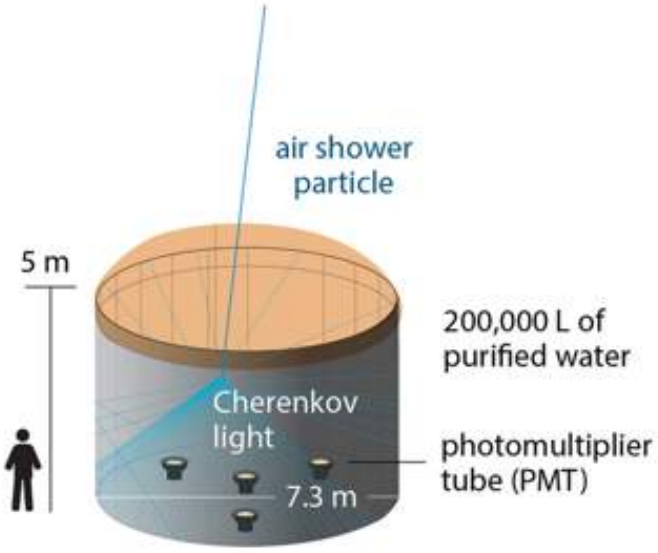

Fig. 3.2.: Diagram illustrating the components of each WCD in HAWC. A metallic cylinder contains 200,000 litres of water within a light and water-tight lining. At the bottom of each WCD, the four PMTs for the detection of the Cherenkov light can be appreciated. Figure credit HAWC/WIPAC.

3.1.2 Data Acquisition and Processing

A dedicated farm of computers and electronics are installed at the HAWC site for the data processing. For each particle radiating Cherenkov light, the time of detection and charge are calibrated based on the pulse captured by the electronics.

In HAWC the complete waveform of each PMT signal is not recorded. Instead, the time-over-threshold (TOT) technique is used to measure the leading and falling edge times at two fixed thresholds (Fig. 3.3). The time a pulse spends above each voltage threshold is correlated to its amplitude (and therefore the Cherenkov-light intensity) through the calibration.

The lowest and highest threshold (LoTOT, HiTOT) are set to the height of a pulse that one would expect from 0.25 PEs ($\sim$ 7.1 mV) and 5 PEs ($\sim$ 113.6 mV) respectively. The digital output of the data acquisition (DAQ) system corresponds to the points in time in which each pulse crosses the corresponding threshold. A weak signal which only crosses the low threshold will generate two time stamps; a leading edge and a falling edge as illustrated

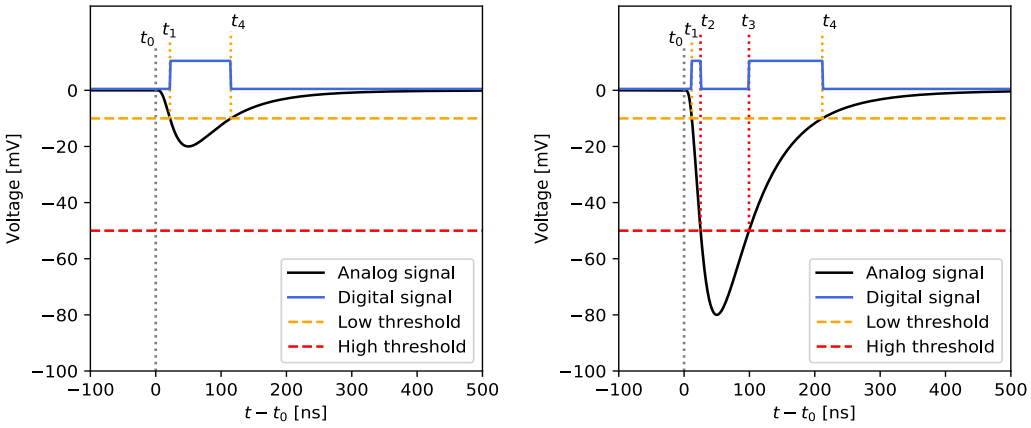

Fig. 3.3.: An illustration of the time over threshold technique. The left panel shows a pulse of low amplitude (analog signal, black) crossing only the low threshold (yellow) and the corresponding digital signal (blue) with two edges. The right panel shows the case of an analog signal of high amplitude, which produces four edges in the digital signal when crossing both thresholds. Figure obtained from Martinez Castellanos, 2019.

in the left panel of Fig. 3.3. Signals that are bright enough will cross first the low threshold, reach the high threshold and fall back crossing again both thresholds, generating a 4-edges hit (Fig. 3.3, right panel). In principle, since the width of the pulse (at a fixed voltage) is unique for a given pulse, only the LoTOT is needed to fully reconstruct the number of PEs detected. However, in reality, one can get hits of multiple PEs with an early or late arrival time which could be misidentified as a big hit rather than small overlapped ones. The HiTOT measurement decreases these type of misidentifications.

The DAQ system continuously performs the processing of all signals. The read-out is done under a simple multiplicity trigger (SMT) criteria; 28 hits in a window of 150 ns are required for an event to be considered a potential atmospheric shower. If this condition is passed, all the hits within 500 ns before the trigger condition is met and 1000 ns after the trigger condition is met, are saved. This results in a SMT rate of $\sim$25 kHz.

3.1.3 Calibration

The calibration procedure consists of extracting the number of PEs and time of arrival of the signals from the LoTOT and HiTOT recorded by the DAQ

system. A detailed description of this procedure can be found in Ayala Solares et al., 2016.

The calibration system consists of a pulsed laser with a wavelength of 532 nm and a set of neutral density filters to regulate the light intensity at the output. The laser light is then directed via optical fibres to each WCDs where a diffuser located at the top of the tank provides uniform illumination to each of the PMTs. Pulses of light are sent to the WCDs for brief periods of time and the Hi/LoTOT are recorded by the DAQ system. When varying the light intensity, a charge calibration is achieved by relating the known number of PEs sent and the TOT values recorded.

A time resolution with sub-nanoseconds precision is required for an accurate reconstruction of the shower directions. The timing calibration takes into account that high amplitude pulses rise faster than low amplitude ones (slewing time), and corrects the time of arrival considering the cable length of each PMT and electronic channel. The slewing time is obtained by measuring the time difference between the laser pulse (considering the light transit time of the optical fibres and geometry of the WCD) and the time of crossing of the two thresholds. Additional sources of timing inaccuracies are corrected for during reconstruction and will be discussed in Sec. 3.1.4.

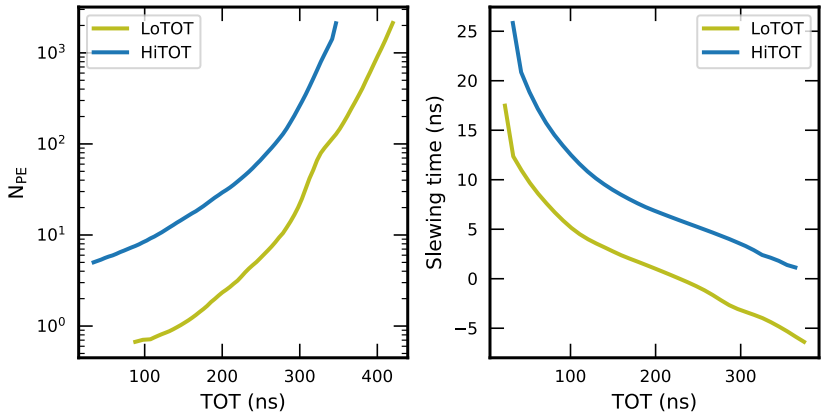

Fig. 3.4.: Calibration curves for HAWC. The left panel shows an example of the calibration curves used to infer the charge of a hit given the high and low TOT. The right panel shows the timing calibration curves used to correct for the effect of fast rising times of high amplitude pulses as explained in the text.

During the reconstruction of the data, the charge is estimated using the calibration curves (Fig. 3.4). With a linear interpolation, the number of photo-electrons (N_{PE}) is computed from the LoTOT, or from the HiTOT if the signal is above the high threshold ($\sim$4 PE in Fig. 3.4). The calibrated charge of the central C-PMTs is scaled by a factor of 0.46 to account for its larger size and efficiency. This scaling normalises the C-PMT effective charge with those of the 8-inches (A, B and D) PMTs and provides a direct relation to the light level in the tank. The time of arrival of each pulse is then shifted using the time calibration curves (Fig. 3.4, right).

3.1.4 Event Reconstruction

Once the data are properly calibrated, the shower parameters are reconstructed. This includes the direction of the primary particle, the energy and the gamma/hadron separation. The HAWC DAQ trigger criteria imply that showers activating at least $\sim$6% of the channels are to be collected. Small events (those with $\lesssim 15\%$ PMT hits) can be highly contaminated by other showers landing near the array. This poses serious limits to the capability of reconstructing their characteristics. High energy showers, above $\sim$10 TeV, can even shine through the whole detector and dominate over the noise, making the reconstruction of their parameters more precise. As a result, events in HAWC can have considerable differences in the quality of their reconstructed parameters, mostly related to the size of the shower footprint.

Since cosmic rays (and most of the astrophysical sources) present a steep energy spectrum, the rate is highest for the lowest trigger threshold and falls rapidly for higher-energy showers. To retain the good quality of high-energy showers, and avoid the loss of sensitivity due to the dominance of small-size events, the data are divided into multiple analysis bins $\mathcal{B}$, based on the number of PMT hits as shown in Tab. 3.1. As a first-order approximation, the size of the event relates also to the energy of the primary particle. In Fig. 3.5, the distribution of energy for simulated showers with this binning scheme is shown. A proportionality between $\mathcal{B}$ and the mean value of the energy distribution is obtained. Considerable overlap between these distributions is generated by the dependency of the event size on the zenith angle and

arrival location of the shower. Therefore $\mathcal{B}$ cannot be used as a direct binning for the energy of the showers.

$\mathcal{B}$	PMTs hit	PINCness cut	Compactness cut
1	6.7–10.5%	<2.2	>7.0
2	10,5–16.2%	<3.0	>9.0
3	16.2–24.7%	<2.3	>11.0
4	24.7–35.6%	<1.9	>15.0
5	35.6–48.5%	<1.9	>18.0
6	48.5–61.8%	<1.7	>17.0
7	61.8–74.0%	<1.8	>15.0
8	74.0–84.0%	<1.8	>15.0
9	>84.0%	<1.6	>3.0

Tab. 3.1.: Table of cuts for the fHit binning scheme. The first column corresponds to the number of bin $\mathcal{B}$. The second column indicates the cut on the percentage of PMT hits used for this binning. The values of PINCness and Compactness cuts for the gamma-hadron separation are shown in the third and fourth column.

Recently, the HAWC collaboration developed two methods to measure the energy of the primary gamma-rays, applicable for energies above $\sim$1.0 TeV. This allows to perform a 2D binning, in energy and shower size $\mathcal{B}$, allowing an improved angular resolution, gamma-hadron separation and spectral reconstruction. The analysis of the Crab nebula under this approach is published in Abeysekara et al., 2019.

Direction Reconstruction

Irrespective of its primary particle type, atmospheric showers are dense along the trajectory of the primary particle. A key parameter to obtain the shower direction is the measurement of the air shower core position. For this, a function that characterises an exponential decrease with distance in the PE distribution of the shower footprint is used. The signal S_i of the i-th PMT is modelled as:

$$S_i = S(A, \vec{x}, \vec{x_i}) = A \left(\frac{1}{2\pi\sigma^2} e^{-|\vec{x_i}-\vec{x}|^2/2\sigma^2} + \frac{N}{(0.5+ \mid \vec{x_i} - \vec{x} \mid /R_m)^3} \right), \quad (3.1)$$

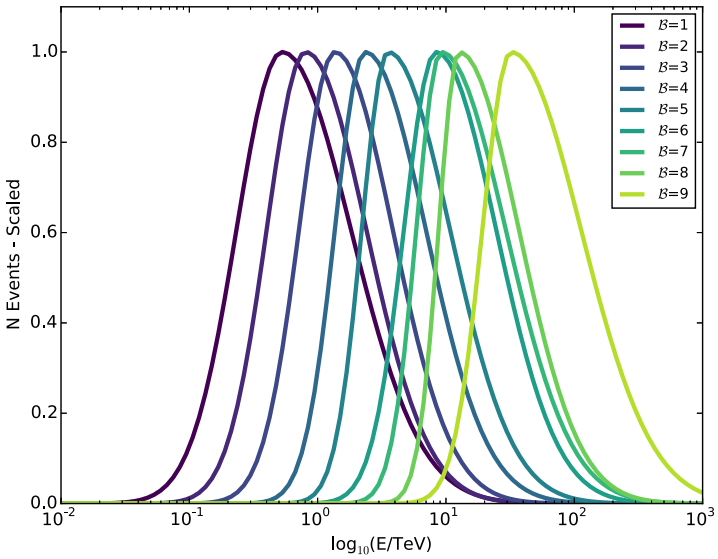

Fig. 3.5.: Energy distribution of simulated showers under the fHit bin scheme. Each curve corresponds to a different value of $\mathcal{B}$ as indicated in the figure label. The mean energy shifts towards higher energies as $\mathcal{B}$ increases. Figure obtained from Abeysekara et al., 2017a.

where $\vec{x}$ and $\vec{x_i}$ are the position of the core and of the i-th PMT signal respectively, A is a normalisation factor, R_m is the Moliere radius of the atmosphere ($\sim 120\,\mathrm{m}$ at HAWC altitude) with $\sigma = 10\,\mathrm{m}$ and $N = 5 \times 10^{-5}$. Eq. 3.1, called SFCF (super-fast core fitter), is an approximation of the Nishimura-Kamata-Greisen (NKG) function (Greisen, 1960). The latter would provide a better estimate of the core location but is more computationally intensive.

Modern approaches for the core reconstruction involve the use of a Monte Carlo template-based likelihood method where the core position and energy of the shower can be obtained simultaneously reducing uncertainties due to the approximations done when employing the fit of the SFCF or NKG function (Joshi et al., 2019).

Once the core position is determined, the reconstruction of the direction is performed using the measured time of arrival of the particles in the shower. Since the shower front is curved, a correction due to this curvature is applied based on data from the Crab Nebula, and the time of each PMT hit is fit to the hypothesis of a flat shower plane. The residuals of this fit are used to correct for curvature. This correction is made using a simple quadratic function of

the distance between a hit and the shower core and it improves the angular resolution of HAWC by a factor of two. After this curvature correction is applied, the direction reconstruction is done with a χ^2 fit to the shower plane, with the normal vector of the plane corresponding to the direction of the primary particle.

Gamma/Hadron Separation

In HAWC two parameters, based on the dominant presence of muons in hadronic showers, are used to perform the gamma/hadron separation. The first one is *Compactness* (C), defined as the ratio between the number of triggered PMTs and the highest number of PEs detected outside a radius of 40 m from the shower core:

$$C = \frac{N_{hit}}{CxPE40} \tag{3.2}$$

Cosmic ray showers tend to contain muons far away from the shower core. Such muons are easily identified, as the amount of Cherenkov light produced when they enter a WCD is high. In this case, *Compactness* will have a high value, far larger than the one expected for gamma-induced air showers, where the PE distribution decreases smoothly from the core. The second variable, Parameter for Identifying Nuclear Cosmic rays (*PINCness*, Fig. 3.6) is defined as the χ^2 of the dispersion of the SFCF function fit (Eq.3.1):

$$P = \frac{1}{N}\sum_{i=0}^{N}\frac{(\zeta_i - <\zeta_i>)^2}{\sigma_{\zeta_i}^2} \tag{3.3}$$

For gamma-induced showers, this parameter is close to one. The dispersion from the expected distribution fitted with SFCF is larger for cosmic ray showers, due to the presence of muons and clustered particles.

A set of cuts is defined for each $\mathcal{B}$ bin to perform the gamma/hadron separation based on P and C as shown in Tab. 3.1.

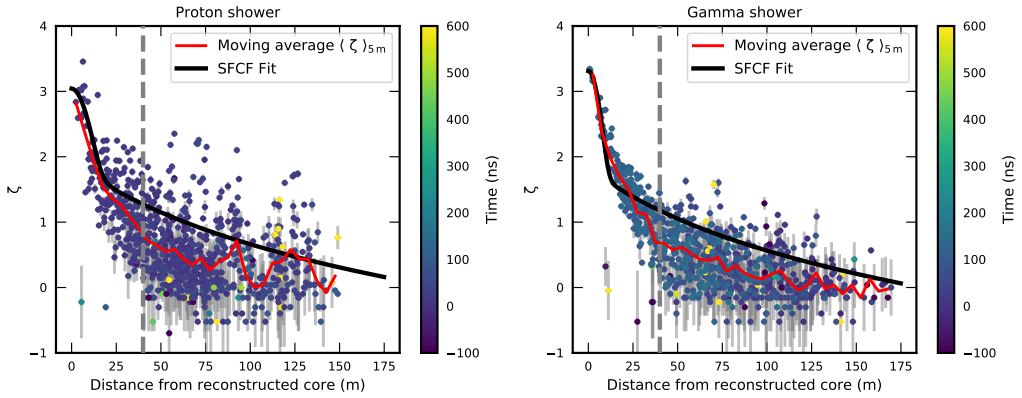

Fig. 3.6.: Recorded effective charge for each PMT as a function of distance from the reconstructed core position. The purple line shows the fit from SFCF (Eq. 3.1) and the mean $< \zeta >$ used to compute the P parameter. Left: Hadronic shower. Right: Gamma shower.

3.1.5 Background Estimation

Hadronic showers that pass the gamma/hadron cuts described in Sec. 3.1.4 constitute the background for the analysis of gamma-ray sources. As the flux of the hadronic background is isotropic and stable, the only factors that affect the determination of the background are variations in atmospheric conditions and the zenith and energy dependency of the detector response.

To produce excess maps, background maps are generated using a background estimation method and subtracted from the count maps. The crudest approach for background estimation is the *declination band averaging*, which accounts for the acceptance of the detector as a function of zenith angle. A more sophisticated method, called *Direct Integration*, considers the distribution of events in zenith and azimuth to be independent of the rate of cosmic rays. The data are split into integration periods Δt, and for each period, the all-sky event rate $R(\tau)$ as a function of sidereal time τ is produced. The angular distribution of events coming from the hour angle h and declination δ is computed to form the efficiency map $\epsilon(h, \delta)$. Then, the background as a function of right ascension α and declination δ is:

$$B(\alpha, \delta) = \int \epsilon(h, \delta) R(\alpha - h) dh \tag{3.4}$$

Finally, the total background is the sum of all the background maps derived for each integration period Δt.

3.1.6 Significance

The method of Li & Ma (Li et al., 1983) is used to compute the significance of emission at a given position in the sky. This method is based on a likelihood ratio test. The statistical significance S is given by:

$$S = \sqrt{-2 \ln (\lambda)} \tag{3.5}$$

Where λ is the likelihood-ratio between the signal hypothesis and the pure background hypothesis. The value of λ is given by:

$$\lambda = \left[\frac{\alpha}{1+\alpha}\left(\frac{N_{ON}+N_{OFF}}{N_{ON}}\right)\right]^{N_{ON}} \times \left[\frac{\alpha}{1+\alpha}\left(\frac{N_{ON}+N_{OFF}}{N_{ON}}\right)\right]^{N_{OFF}} \tag{3.6}$$

where N_{ON} is the number of counts in the region of interest, and N_{OFF} is the number of counts in a nearby region where no signal is expected, and α is the relative exposure. For the direct integration method of background subtraction, a big area of the sky is used to estimate α. The values of α are given by:

$$\alpha = \frac{E}{I - E}$$

where E is the source exposure and I is the total exposure of the background including the source region. This method is ideal for air shower detectors like HAWC since $\alpha \ll 1$, which reduces background fluctuations.

An additional method considers a source hypothesis in the HAWC excess maps with fixed spectral shape and source size, leaving the flux normalisation as a free parameter. The statistical test (TS) compares this source hypothesis over the maps against the background maps, generating maps of TS. With

only one free parameter in this statistical test, the significance is given by $\sqrt{TS}$.

3.1.7 Event Simulation

The simulation of atmospheric showers as detected by HAWC is based on three major components. First, the widely used program CORSIKA (Heck et al., 1998) simulates the propagation of extensive air showers through the atmosphere. The primary particle is followed in its propagation, where it may eventually interact with the molecules of the atmosphere, producing an extensive air shower. The secondary particles are then tracked; decay, energy loss and interaction with further atmospheric molecules are simulated. The energy, distribution, and type of each particle in the shower until it reaches the HAWC altitude is thus estimated. The second element of the simulation chain, called *HAWCSim*, based on the GEANT4 package (Agostinelli et al., 2003), simulates the interaction of the particles propagated by CORSIKA with the detector array (including the metallic walls of each WCD, the PMT quantum efficiency, and the water contained in each of them). The expected number of photo-electrons due to Cherenkov radiation, direction and time of arrival as detected by each PMT are obtained. During this step, the electronics and individual PMTs response are modelled with *DAQSim* (Pretz et al., 2018), a package written by the HAWC collaboration, which mimics the signal transformation through the DAQ system and calibration process.

The *DAQSim* package applies modifications to the timing and number of detected PEs to make the 1 PE and muon peak position match the data. Muons are used since they are minimum ionising particles, thus providing a calibration source of Cherenkov light (see Ch.6.1 for more details):

Acceptance Model In this step the recorded single photo-electron charge is smeared depending on the incident angle of the photons on the PMT surface. This is because the detection efficiency and gain are strongly dependent on the position of the PE production on the PMT's photocathode. The level of spread is determined from the PMT response measured in the laboratory, where the PMT surface is scanned over several impact radius using a light pulse of 1 PE (Fig. 3.7). After

the application of this acceptance model, the single photo-electron distribution peaks at 1.25, since the PMT acceptance curves where generated erroneously. This is corrected with a scaling factor of 0.8, such that the single photo-electron distribution matches the data.

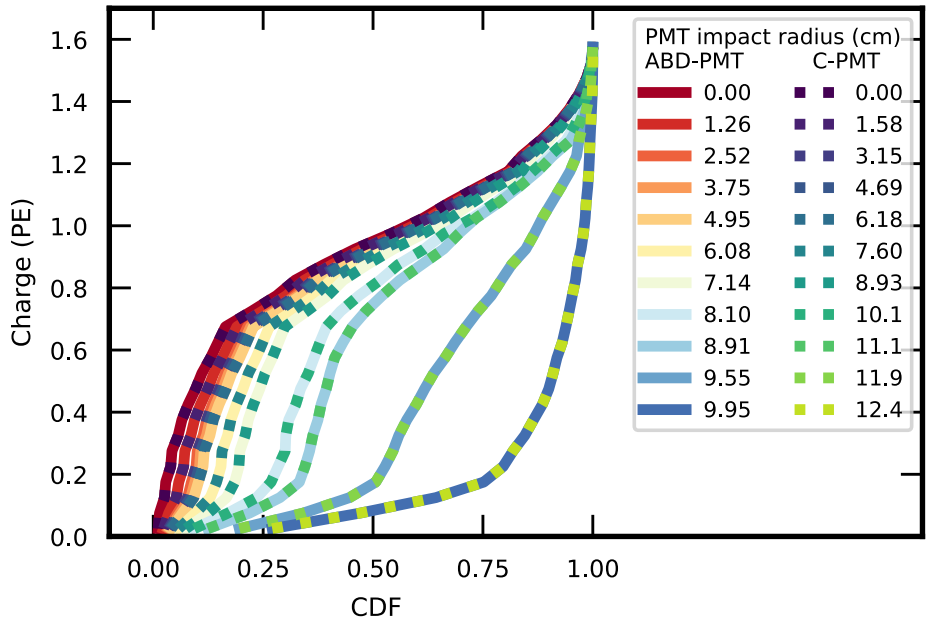

Fig. 3.7.: Cumulative distribution function of the 1 PE spectrum. The different lines indicate different impact radius, going from 0 (at the centre) to the maximum radius of the PMT surface. These curves were obtained for the 8" PMTs (shown as solid lines) and scaled to the radius of the 10" PMTs (overlapped dashed lines).

PMT Efficiency The charge detected is scaled even further to match the muon peak measured in data. An efficiency for the A, B and D PMTs of 0.8 is used, while for the C PMT an efficiency of 0.55 is applied.

Charge Resolution The charge is gaussian-smeared by a factor of 30% to mimic the charge resolution of the calibration curves used in real data.

Time Resolution The simulated time of each hit is smeared by a factor of 0.8 ns. This value is set such that the time width of the muon peak agrees with the data.

PE threshold and Calibration Maximum All hits below 0.55 PEs are discarded and anything between 0.55 and 0.65 PEs is assigned to 0.65

PEs. This helps to match a pileup at 0.65 PEs seen in data. Additionally, the maximum possible PE value that the calibration can determine is simulated using the distribution of maximum value in data. This distribution can be parametrised by a gaussian in log space with a mean value of 3.78 and sigma value of 0.13 for ABD PMTs and a mean 3.35 and sigma 0.24 for C PMTs.

PMT to PMT efficiency The PMT-per-PMT muon peak position obtained from data is used to estimate the spread of the PMT efficiency. This spread is then applied randomly to each PMT in DAQSim. The overall detector is simulated, but each PMT has an efficiency that might not match the real one.

PE Killing During the reconstruction of data, afterpulses, i.e. hits that occur soon after a high pulse hit, are vetoed. In DAQSim, values above 10000 PEs are discarded to mimic the after-pulse veto. The additional effect of removing problematic hits is mimicked in *DAQSim* by randomly discarding 1% and 2% of the ABD and C PMTs hits respectively.

Charge Scale A clear discrepancy at high values of charge is observed between data and simulations. The origin of this discrepancy is thought to be a broad pulse effect: while calibration is performed using a narrow LED pulse, showers arrive in a wider plane. Here a linear transformation in log space from 0 correction at $10^{1.25}$ PEs to a correction of 0.11 at $10^{2.25}$ PE is applied.

Noise overlap Raw data from HAWC is selected in windows of 1500 ns. If these windows of data do not satisfy the SMT, they are overlapped to the simulated showers. The addition of these noise samples improves the matching of the shower rate between data and MC, gamma-hadron separation, and angular resolution (Rosenberg, 2018).

This short description of the *DAQSim* code is meant to emphasise the fact that many features observed in data are not simulated in detail. *DAQSim* attempts to match the data and simulation by ad-hoc modifications to the timing and charge distributions, without any actual effort to simulate in detail the HAWC apparatus.

A more realistic simulation, where each PMT is modelled individually and the evolution of the detector through time is considered, is presented in Ch.6. Another major limitation of *DAQSim* is the impossibility to compare the pre-calibrated data and MC. In Ch.6 a method to obtain TOT information from the simulation is presented as a step forward towards a more realistic simulation for HAWC.

3.2 The High Energy Stereoscopic System (H.E.S.S.)

The High Energy Stereoscopic System[2] (H.E.S.S.), located in the Khomas Highland of Namibia, Africa ($23°16'18,4''$S, $16°30'0.8''$E, altitude of 1800 m.a.s.l) is the third generation of Imaging Atmospheric Cherenkov Telescopes (IACTs), and up to now the only array of IACTs with a mixed type of telescopes.

Fig. 3.8.: The H.E.S.S site in the Namibia desert. The first four telescopes (CT1,CT2,CT3 and CT4) are placed forming a squared array of 150 m length. The biggest telescope CT5 is placed at the centre of the array.

H.E.S.S began operations in the year 2004 with four Cherenkov telescopes (CTs) placed in a square array of 120 m side. Each CT uses the Daves-Cotton design (Davies et al., 1957) and consists of 380 mirrors of 30 cm radius each, forming a telescope mirror with a total area of ~ 107 m^2 and focal length of 15 m. Each CT is mounted in an altitude-azimuth setup and has a repointing speed of ~ 100 deg/min. At the focal point, a camera equipped with 960 PMTs collects the Cherenkov light of the atmospheric showers. Each PMT has a FoV of 0.16°, resulting in a total FoV of $5°$ (F. Aharonian et al., 2004).

In the year 2012, the array underwent a major upgrade, with the addition of a bigger telescope (CT5) with a surface area of ∼610 m^2, formed by 875 hexagonal mirrors with a diameter of 90 cm and focal length of 36 m (P. o. Hofverberg, 2013). The camera of CT5 consists of 2048 PMTs with a FoV of 0.067° resulting in a total FoV of $\sim 3.2°$ (Bolmont et al., 2014). The big recollection area of CT5 provides an energy threshold of ∼50 GeV (zenith

[2]https://www.mpi-hd.mpg.de/hfm/HESS/

dependent) and is perfectly suitable for the observation of transient events, due to its fast repointing speed. CT5 can re-point to any part of the sky within an average of 60 seconds (P. Hofverberg et al., 2013). This upgrade marked the start of a new era for the observatory, H.E.S.S II.

Observations with the H.E.S.S telescopes are made during astronomical darkness (~ 1000 hrs per year) where the PMTs can operate without damage. Recently, the system has been prepared to perform observations during moderate moonlight.

3.2.1 Data Acquisition System

The DAQ system is in charge of the control of the five telescopes that form H.E.S.S and the data management from the read-out of each five cameras (for a detailed explanation of the DAQ system see Balzer et al., 2014).

The DAQ allows the array to operate in multiple *SubArray* modes, making it possible to use subsets of the five telescopes simultaneously. This includes observations, calibration and maintenance runs. This feature allowed the commissioning of CT5 while the four other telescopes were taking data in a normal way.

Due to the limited time of observation hours per year, the DAQ carries out many optimisations. An auto-scheduler system is used to program all the observation runs planned for a given night. This system optimises the schedule by taking into account the observation time, zenith angle and target priority.

For the case of observations of transient events such as GRBs, the DAQ system can filter and respond to alerts received via the Gamma-ray Burst coordinates Network (GCN). When an alert is received during observation time, the DAQ is able to stop the current observation run and to control the repointing of the telescopes. To optimise in time, the interruption of the current observation is done while the telescopes are slewing, making it possible to begin a new run as soon as the target position is reached.

3.2.2 Calibration

During data taking, the analog-to-digital converter (ADC) count rate is read out for each PMT in the cameras. Two gain channels (high gain, HG and low gain, LG) are used. The signal amplitude of the detected Cherenkov photons $A^{HG(LG)}$ in units of photo-electrons is given by:

$$A^{HG} = \frac{ADC^{HG} - P^{HG}}{\gamma_e^{ADC}} \times FF \tag{3.7}$$

and

$$A^{LG} = \frac{ADC^{LG} - P^{LG}}{\gamma_e^{ADC}} \times \frac{HG}{LG} \times FF \tag{3.8}$$

where P is the pedestal value (baseline of PMT due to noise and night-sky background), FF measures the relative efficiency of a given pixel to the average of the camera, and is determined in specific calibration runs together with γ_e^{ADC}, the conversion factor of ADC counts to one photo-electron in the high gain channel. The amplification ratio HG/LG is obtained from atmospheric events.

The conversion factor from ADC counts to photo-electrons for the HG channel is determined during dedicated calibration runs using LED flashers to fire 1 PE signals onto each camera pixel in the absence of night sky background (inside a light-sealed building where the camera can be positioned). A function is fitted to the recorded ADC distribution for each pixel, under the assumption that the number of photo-electrons follows a Poisson distribution. The electronic noise (pedestal distribution) can be described with a gaussian distribution of mean P and width σ_P and the single PE response can be assumed to be Gaussian distributed. The pedestal value P is measured during observation as the baseline can change significantly at short timescales. It is obtained by averaging the ADC counts from events using parts of the camera that were not illuminated by Cherenkov light. A new averaging is done roughly every 5000 events. Pedestal information is also used to measure the night sky background (NSB) level. A more detailed description of the previous elements can be found in F. Aharonian et al., 2004.

3.2.3 Event Reconstruction

After the calibration of the events, the next step is the application of reconstruction algorithms to measure the energy and direction of the primary particle and perform the rejection of hadronic events. An image cleaning is applied to the shower images to reduce noise events. In this procedure, only pixels with a high threshold of PEs with neighbouring pixels with a low PE threshold and vice versa are kept.

Hillas Parameters

In the most basic approach, the Hillas parameters are used for the reconstruction and gamma/hadron separation (Hillas, 1985). These parameters are based on the assumption that the shape of the shower detected by each camera can be approximated as an ellipse. The parameters of the ellipse are called the *Hillas parameters* (Fig. 3.9). For each camera, the centroid position of the ellipse, and the width w, length l and the distance to the centre of the camera are measured. In addition, the total charge of the pixels in the images is recorded. To reduce the possibility of a biased reconstruction, all ellipses whose centroid is far away from the camera centre are discarded.

The assumption of ellipticity holds for gamma-ray induced showers. In the case of hadronic showers, the images in the camera tend to have a less defined structure.

The method used for gamma/hadron separation in H.E.S.S. is based on boosted decision trees (BDTs). This method uses the measurements of expected ellipticity in the shower images and other reconstructed parameters to perform the gamma/hadron separation (See Ohm et al., 2009 for more details).

Direction Reconstruction

To measure the direction of the primary particle, the Hillas parameters for the different telescopes observing an event are combined (see Fig. 3.9). In stereo observations (CT1-4) the intersection point of shower image axes (Fig. 3.10)

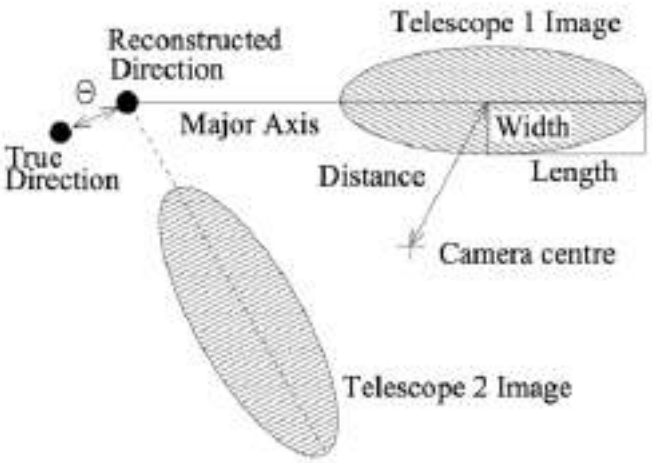

Fig. 3.9.: Diagram illustrating the determination of Hillas Parameters. The direction reconstruction is based on the inferred major axis of two telescope images. Figure obtained from F. Aharonian et al., 2006c.

provides the reconstructed direction. The θ parameter, depicted in Fig. 3.9, measures the distance between the reconstructed shower position and the source position.

The same procedure can be applied for monoscopic observations (with only CT5 participation). However, as only one image is available, the discrepancy between the reconstructed and original source direction can be considerable and sophisticated algorithms, like multi-variate analysis, are required (Parsons et al., 2016).

Energy Reconstruction

The energy reconstruction is based on lookup tables generated from the simulation. The energy is obtained from the measured image amplitude and the impact distance (the distance of the shower core location to the camera) from the telescope.

Lookup tables are generated for 20 zenith angle bands covering the whole accessible sky, seven optical efficiency bands and six off-axis angle bands. These tables are applied for each amplitude recorded in each telescope while using the impact parameter obtained in the stereoscopic approach. The energy obtained is then averaged and weighted by the uncertainty on the

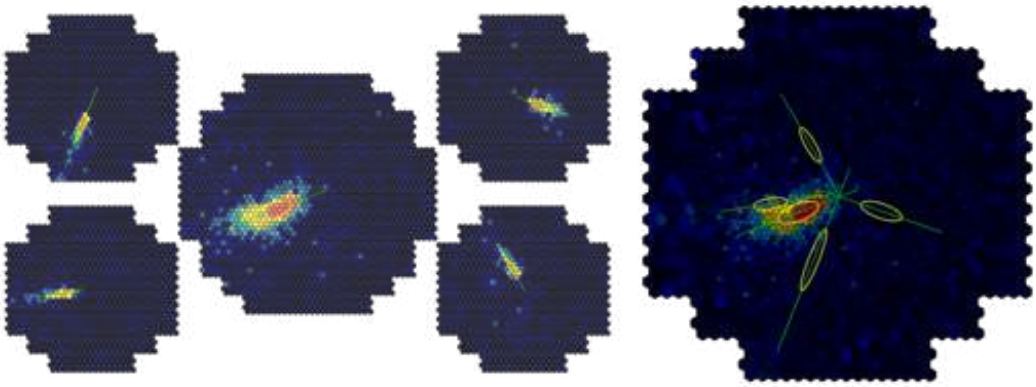

Fig. 3.10.: Camera Images for a stereo observation. The left figure shows the images as detected by the 5 telescopes of HESS for a simulated shower of a gamma-ray with energy 700 GeV. The right side shows the superposed images. The intersection point of the image axis corresponds to the reconstructed direction. Image credit: Ramin Marx, MPIK Heidelberg, and the H.E.S.S. collaboration

energy measured individually. This approach provides an energy resolution of roughly 20% (F. Aharonian et al., 2006b).

Modern Reconstruction Approaches

New reconstruction approaches have been developed based on a likelihood reconstruction method called *Model* analysis (De Naurois, 2012) and the Image Pixel-wise fit for Atmospheric Cherenkov Telescopes (ImPACT) method (Parsons et al., 2014). These two methods are based on Monte Carlo templates where the full image information (pixel-wise) recorded by the telescopes is used to perform simultaneously the energy and direction reconstruction.

The performance of the ImPACT reconstruction method compared to the Hillas method is shown in Fig. 3.11. Throughout the whole energy range of these analyses, an improvement by a factor of 2 or more in the angular and energy resolution can be seen when employing ImPACT.

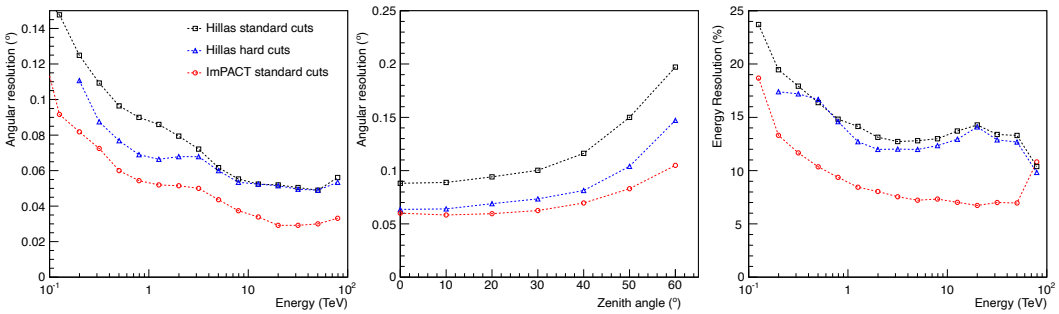

Fig. 3.11.: Performance comparison of the Hillas and ImPACT reconstruction. The left panel shows the comparison of the angular resolution as a function of simulated energy for observations at a zenith angle of 20°. The centre panel compares the angular resolution as a function of zenith angle for a power law spectrum with a photon index of -2. The right panel show the energy resolution as a function of simulated energy. Figures taken from Parsons et al., 2014.

3.2.4 Background Estimation

The background estimation methods compare the emission at a region where a source is suspected to be (ON region) to that of the surrounding regions where no emission is expected (OFF regions). Two primary methods are used for the background estimation in H.E.S.S: the ring method and the reflected background method. In these methods, nearby regions of known/expected emission (e.g. the galactic plane, extended sources) are masked and excluded from the background analysis. A summary of the different background estimation techniques can be found in Berge et al., 2007.

Ring Background Method

As shown in Fig. 3.12, in this method a ring of a given radius and thickness (OFF region) is drawn around a tested position (ON region). For point like sources in extragalactic regions (far from the galactic plane) the election of size in radius and thickness comes from a compromise between avoiding contamination from the ON into the OFF region while maintaining a good estimation of the camera acceptance. Adaptive sizes for the OFF region are employed for regions in the sky where contamination of neighbouring sources is possible.

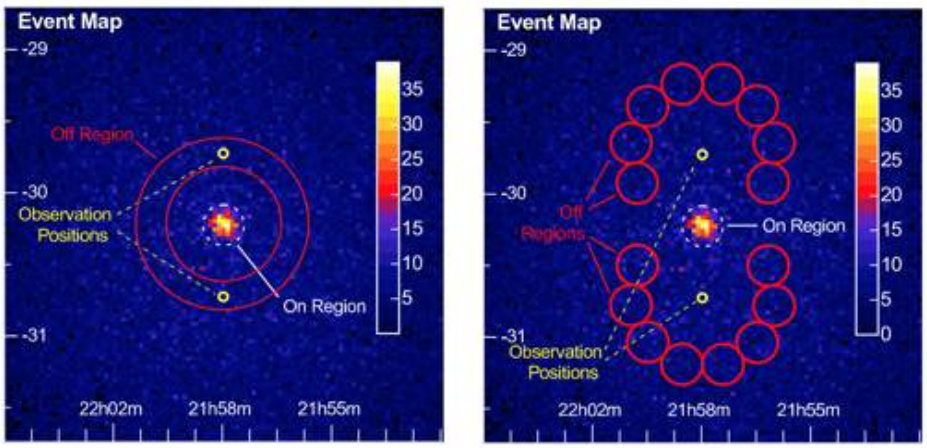

Fig. 3.12.: Illustration of the ring background and reflected background methods. The two main approaches for background estimation used in H.E.S.S. Left: Ring background method. The OFF region is a ring centred in the ON region. Right: Reflected background method. The observation is taken with an offset such that the ON region is at the same distance as the OFF regions. Figure from Berge et al., 2007.

This method is usually employed the production of sky maps and has the disadvantage that asymmetry and non-uniformity in the acceptance of the telescope needs to be properly considered.

Reflected Background Method

In this method, the source position is shifted with respect to the centre of the camera and all the OFF regions are taken symmetrically at the same angular distance (see Fig. 3.12). Since all the regions are at the same distance to the camera centre, the in-homogeneity of the instrument response is minimised, thereby, allowing the extraction of the signal without the necessity of modelling and computing it. This method is preferred when performing the extraction of data for spectral analysis.

3.2.5 Significance Calculation

The determination of significance of a source is done using the Li & Ma method as describe in Li et al., 1983. A comparison in a run-by-run basis

is done on the number of events in the ON and OFF regions extracted for example with any of the methods shown in Sec. 3.2.4. If the detector response is not the same in the ON and OFF region, a factor α is introduce to compute the number of expected background events in the ON region given the number of events in the OFF region. In the Li & Ma statistic the significance (S) of an excess $N_{ON} - \alpha N_{OFF}$ is given by Eq. 3.5.

3.2.6 Spectrum Measurement

For a given gamma-ray source, the differential energy spectrum,is determined as the number of photons in a differential interval of energy E detected per unit area and time (typically in units of $\mathrm{cm}^{-2}\mathrm{s}^{-1}\mathrm{TeV}^{-1}$):

$$F(E) = \frac{\mathrm{d}N_\gamma}{\mathrm{d}E} = \frac{1}{A_{\mathrm{eff}}} \frac{\mathrm{d}N_\gamma}{\mathrm{d}E\mathrm{d}t} \tag{3.9}$$

where A_{eff} is the effective collection area. The effective collection area is obtained from Monte Carlo simulations in which the probability of detecting a gamma-ray of a given energy, zenith and azimuth angle and distance from the array, after gamma-hadron cuts is considered. It is usually estimated by simulating a gamma-ray source with a power-law differential-energy flux with a photon index of -2.0 and retrieved via a set of lookup tables. Since the reconstructed energy of the events can differ from the real (simulated) energy, the effective area as a function of reconstructed energy is used.

For the spectrum measurement, one must take into account that some events in the ON region may come from background events. For this reason, the spectrum is obtained by extracting the number of events in the ON region relative to the OFF region considering the acceptance factor α as explained in the previous section. The Differential flux is given by:

$$F(\Delta E) = \frac{1}{t\Delta E} \left\{ \sum_{i=1}^{N_{\mathrm{ON}}(\Delta E)} \frac{1}{A_j} - \alpha(\Delta E) \sum_{j=1}^{N_{\mathrm{OFF}}(\Delta E)} \frac{1}{A_j} \right\}. \tag{3.10}$$

The resulting differential spectrum can be fit to obtain a functional form of the gamma-ray spectrum.

An improved approach for the spectrum extraction is called the forward-folding method. In this case the expected number of gamma events in a reconstructed energy range is given by

$$n_\gamma(E_{\mathrm{rec},2}, E_{\mathrm{rec},1}) = \int_{E_{\mathrm{rec},1}}^{E_{\mathrm{rec},2}} \mathrm{d}E_{\mathrm{rec}} \int_0^\infty \mathrm{d}E_{\mathrm{true}} M(E_{\mathrm{rec}}, E_{\mathrm{true}}, ...) A(E_{\mathrm{true}}, ...) \Phi(E_{\mathrm{true}}, \vec{\alpha}), \tag{3.11}$$

where M characterises the probability of reconstructing an event of an energy E_{true} at an energy E_{rec}. Both functions (or lookup tables) have a dependence on the zenith, azimuth, offset angles and telescope optical efficiency. With Φ the source spectral-shape assumption characterised by a set of parameters $\vec{\alpha}$ (e.g, photon index and spectrum normalisation). Via a log-likelihood maximisation, the parameters $\vec{\alpha}$ which better describe the detected number of ON events, while accounting for the expected and measured number of OFF events, is determined.

3.2.7 Sensitivity

The sensitivity defines the minimum flux that a source can have in order to be detectable by the experiment. It depends mainly on the spectral assumption for the source and characteristic effective area of the detector. Fig. 3.13 shows the H.E.S.S II differential flux sensitivity as a function of reconstructed energy for some characteristic telescope configurations and analysis cuts when considering an integration time of 50 hrs, requiring a detection of 5 σ. As can be seen, the addition of CT5 into the analysis provides a lower energy threshold, while at around 300 GeV the sensitivity connects to the stereo observations. CT1-4 analysis is preferred for sources of high flux or when detailed spectrum analysis is required since the performance in terms of energy and angular resolution is at the moment better than a mono analysis with CT5 or a combined analysis.

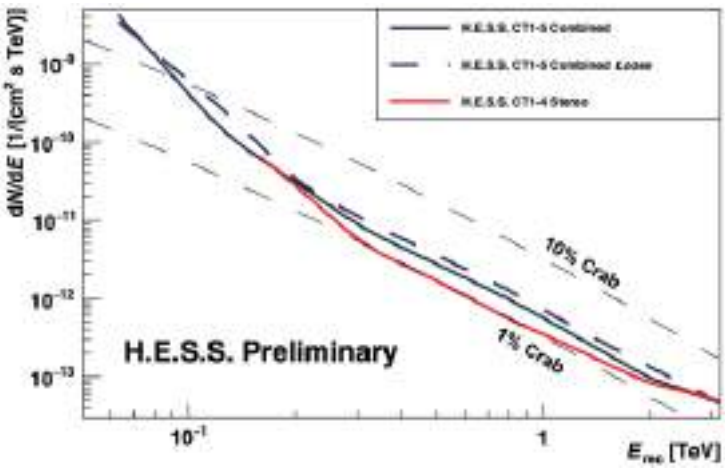

Fig. 3.13.: Differential flux sensitivity of H.E.S.S. II. The differential flux sensitivity of H.E.S.S. II calculated for an integration time of 50 hrs considering different type of telescope configurations and analysis cuts. For comparison the differential energy flux of 1% and 10% of the Crab nebula flux is shown. Figure obtained from Holler et al., 2015.

3.3 Conclusions and Outlook

In this chapter the most important notions of detection and analysis principles for HAWC and H.E.S.S. were summarised. Both achieving an order of magnitude better sensitivity compared to their predecessors.

Fig. 3.14 compares the flux sensitivity of current and planned HE and VHE observatories. The current generation of IACTs have all very similar performance for integration times of 50 hrs. Wide FoV observatories like HAWC require integration times of a couple of years to reach comparable sensitivity but outperform IACTs at the highest energies thanks to higher effective area and very good background discrimination. In the future, planned observatories like CTA (CTA Consortium, 2019) and SWGO (Albert et al., 2019) will reach an order of magnitude better sensitivity. The *Fermi*-LAT sensitivity shown in this figure is comparable to that of current VHE observatories. This provides the opportunity to study sources over more than four logarithmic decades in energy.

As can be seen from this chapter, there are several advantages and disadvantages of IACTs with respect to wide-field observatories like HAWC. Thanks to the very good angular resolution (ranging from 0.1 at the low energies

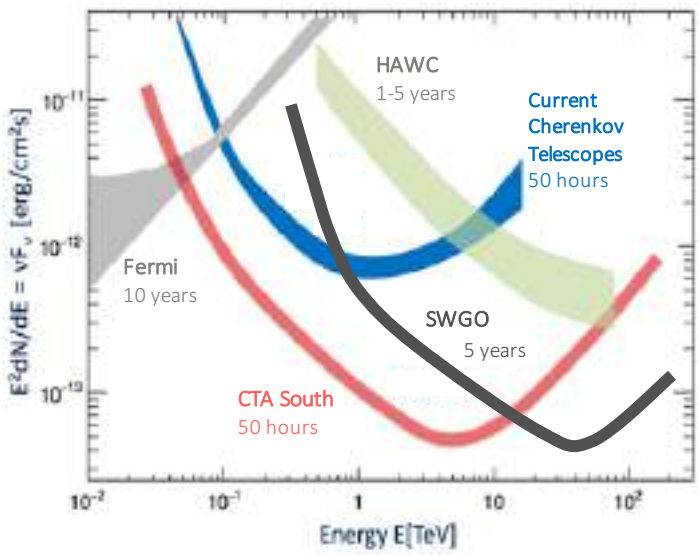

Fig. 3.14.: Differential flux sensitivity of current and future HE and VHE gamma-ray observatories. The sensitivity is shown as a function of energy. For each instrument the integration time considered for the achieved sensitivity is indicated. Figure obtained from Hinton et al., 2020.

up to 0.04 degrees at the highest energies), it is possible with H.E.S.S. to perform accurate studies in very crowded regions like the galactic plane. HAWC allows the surveying of the whole accessible sky, making it possible to identify unknown sources or sources with a spatial extension of several degrees.

In the context of transient astrophysical phenomena, HAWC is capable of monitoring a big portion of the sky instantaneously under a duty cycle of almost 100%. IACTs on the other hand, require pointing observations being held during the astronomical dark time or moderate moonlight and good weather conditions but can reach significantly lower sensitivity compared to HAWC for observations over short intervals of times. In Ch. 4 and Ch. 7 these differences will be exploited for the specific case of GRBs.

4

GRB Observations with H.E.S.S.

Contents

The isotropic localisation on the sky and transient nature of GRBs (see Ch. 2) poses challenges for instruments of a relatively small FoV and small duty cycle like H.E.S.S. (see Ch. 3.2). Specific follow-up strategies are put in place to increase the chances of detecting a GRB.

Sec. 4.1 summarises how H.E.S.S. triggers the follow-up of GRBs. In Sec. 4.2 the analysis of several GRBs observed by H.E.S.S. with these follow-up strategies is detailed along with a discussion of the most interesting observation, GRB 160310A detected by *Fermi*-LAT, given in context with the upper limits obtained with H.E.S.S. In Sec. 4.3 an extension to the follow-up strategies based on the *Swift*-BAT fluence and its predicted *Swift*-XRT afterglow flux is explained. Finally, Sec. 4.4 provides conclusions and an outlook on the GRB observation programme of H.E.S.S.

4.1 The H.E.S.S. GRB Observation Programme

The H.E.S.S GRB observation programme, being one of the key science topics of H.E.S.S, has been active since 2003, when partial operations started with the first two active telescopes. A dedicated catalogue of GRBs observed with H.E.S.S. from 2003 to 2007 can be found in Aharonian, F. et al., 2009.

The completion of the CT5 in mid-2012, which marked the second epoch for H.E.S.S, was mainly motivated by the observation of transient events like GRBs. The large collection area of CT5 and its fast slewing speed make H.E.S.S. an ideal instrument for GRB observations. The H.E.S.S. array has a narrow FoV ($\sim$3.5° for CT5) compared to all-sky experiments like HAWC, *Fermi*-LAT and *Fermi*-GBM, the latter especially built to monitor transient events and send alerts to other observatories. This together with the small duty cycle ($\sim$ 1000 h per year), requires optimised criteria to observe only the most promising GRB events.

The H.E.S.S. DAQ is connected to the IVOA (International Virtual Observatory Alliance) to receive VOEvents, which distribute GRB detection notices in a standardised format, containing the information of the issuer, time of detection, localisation of the event etc. (Hoischen, 2018). The GRB programme of H.E.S.S is part of a bigger set of efforts to detect transient phenomena, working in close coordination with the neutrino, fast radio burst, and gravitational-wave detection efforts, for which alerts are also received via the IVOA.

4.1.1 Observation Strategy

The observation of GRBs with H.E.S.S happens in a fully automatic way in the case of alerts received during observation time (*prompt* observations) or scheduled when the burst is not immediately observable (*afterglow* observations). Alerts sent by *Swift* and *Fermi* in the VOEvents are processed and filtered based on the localisation of the event (whether is observable by H.E.S.S.) and uncertainty, significance, and delay of follow-up. Besides, an

expert on call is available for every shift period as the person to decide if observations are performed and extended for several nights.

There are several criteria set to maximise the possibility of a detection without compromising the limited observation time of H.E.S.S. For instance, the $prompt$ criterion requires the source to be observable above 60° in zenith within 5 minutes. This gives the telescopes time to arrive at the target and observations can continue for a full run ($\sim$28 min), until the target falls below 60°, or be extended if the GRB expert on-call so decides. In the case of afterglow opportunities, the bursts are required to be visible with a minimum zenith angle of 45° (60° in special cases). For these observations, a time-delay dependent redshift (z) cut is made which accounts for EBL absorption of VHE gamma-rays and the characteristic exponential decay of the flux in the afterglow. Follow-ups can happen up to a maximum delay of 24 hrs:

- 24 hrs after alerter trigger if $z \leq 0.1$.
- 12 hrs after alerter trigger if $z \leq 0.3$.
- 6 hrs after alerter trigger if $z \leq 1.0$.
- 4 hrs after alerter trigger if z is unknown.

Follow-up observations of GRBs detected by *Fermi*-GBM are restricted to 45 deg in zenith. The localisation of GRBs with *Fermi*-GBM can present uncertainties that overcome the FoV of H.E.S.S. This uncertainty is correlated with the *Fermi*-GBM significance of detection since very bright bursts have in general small localisation uncertainties. A significance of more than 10 σ and a localisation uncertainty smaller than 2° are required for an alert to be considered for follow-up. A recent addition to this observation criteria (as will be detailed in Sec. 4.3) corresponds to the case of *Swift*-XRT detected GRBs, where the follow-up delay can be extended beyond 24 hrs (even if the redshift is unknown) if the X-ray brightness during the H.E.S.S. observation window exceeds $\sim 10^{-12}$ erg cm^{-2}s^{-1} (in relation to the H.E.S.S. sensitivity reached after few hours of observation). A burst is typically observed for $\sim$ 2 hrs, beginning as soon as it is within the H.E.S.S. FoV. The integration time can be extended for several more hours (even during the following nights) if the burst presents interesting/promising characteristics such as a redshift estimate, very bright X-ray emission or VHE detection. Another input

to perform deeper observations is the result of the online or real-time analysis (RTA) of H.E.S.S. performed right after the observations are concluded. In this case, observations are extended if significant emission is seen in the RTA skymaps.

4.2 The Second H.E.S.S. GRB Catalogue

A summary table of the GRBs followed up from mid-2008 to mid-2017 under the trigger criteria explained in the previous chapter can be found in Tab. 4.1. In this sample, only a few GRBs have a measured redshift, usually obtained by optical telescopes or association to the GRB host's galaxy. With a typical uncertainty of several degrees, the redshift of GRBs detected only by *Fermi*-GBM is hard to measure, since optical telescopes are unable to scan the whole region to find the optical counterpart. An extreme example is GRB 160308A listed in Tab. 4.1 with an uncertainty in localisation of 10.75°. These type of events motivated the strict cut on localisation uncertainty ($<2°$) for the follow-up of *Fermi*-GBM alerts with H.E.S.S. It is worth noting that due to the poor localisation capability of *Fermi*-GBM, the final position of some GRBs can differ by tens of degrees from the initial alert that H.E.S.S responds to. These GRBs have been dropped from the results shown here.

The following GRBs which are the subject of a dedicated H.E.S.S. publication are not discussed here: GRB 100621A (Abramowski et al., 2014) (one of the brightest GRBs ever detected in X-rays) and GRB 170817/GW170817 (the first GRB-GW association, Abdalla et al., 2020).

In Fig. 4.1 a histogram of the number of GRBs followed up each year is shown classifying them by the alerter and type of observation (afterglow or prompt). The number of GRBs observed increased after 2012 when CT5 began operations opening also the possibility to reach the target faster compared to the CT1-4 array. On average, H.E.S.S. has observed successfully 6 to 7 GRBs per year since the beginning of CT5 operations (this value excludes observations performed during bad weather conditions, false alerts, etc.), roughly equally distributed between prompt and afterglow observations. In Fig. 4.2 the GRBs locations of Tab. 4.1 are shown. As expected, no bias

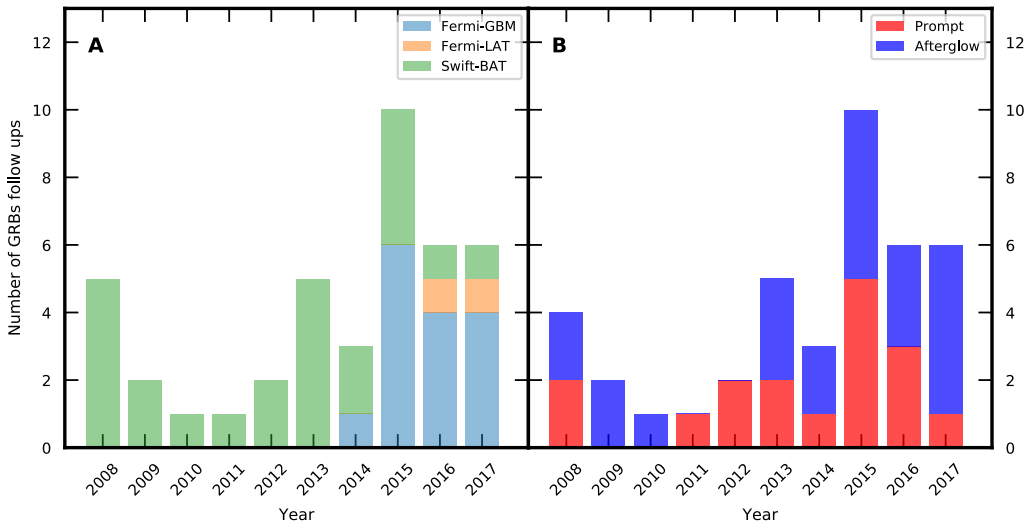

Fig. 4.1.: GRBs followed-up by H.E.S.S. from mid-2008 to mid-2017. The left panel shows the number of GRBs that were followed-up from *Fermi*-GBM (blue), *Fermi*-LAT (orange) and *Swift*-BAT (green). The right panel separates this same sample by the type of observation: prompt when the burst is immediately observable by H.E.S.S. and afterglow otherwise. In both cases an increase in the number of GRBs followed up can be seen after 2012, which marks the beginning of operations with CT5.

towards a preferred location is seen and the distribution follows the isotropic characteristic of these phenomena.

4.2.1 Unblinding and Data Analysis

To minimise the number of trials (sometimes referred to look-elsewhere effect) during the analysis of this set of GRBs, a blinding procedure is followed. To this end, a set of data quality checks and the composition of an analysis strategy must be established before one can proceed with the event reconstruction and analysis.

First, the weather quality and observations conditions are checked and taken into account to exclude bad observations from the analysis. For this, abrupt fluctuations on the trigger rate (above $\sim$30%) are identified as an indication of clouds passing by or by problems in the hardware or software during the data taking. Subsequently, the stability of the PMTs of each telescope's camera is monitored by inspecting the centre of gravity, the pedestal distribution, and

	Satellite	R.A. (J2000)	Dec. (J2000)	Position Error (deg)	T_{90} (sec)	HE	R	O	X	z	Type
GRB 080413A	*Swift*-BAT	19 h 09 m 12 s	−27° 40′ 40″	0.05<	46	×	×	✓	✓	2.433	Prompt
GRB 080804	*Swift*-BAT	21 h 54 m 40 s	−53° 11′ 05″	0.05<	34	×	×	✓	✓	2.2045	Prompt
GRB 081028A	*Swift*-BAT	08 h 07 m 35 s	+02° 18′ 29″	0.05<	269	×	×	✓	✓	3.038	Prompt
GRB 081221	*Swift*-BAT	01 h 03 m 10 s	−24° 32′ 52″	0.05<	40	×	✓	✓	✓	0.7	Afterglow
GRB 081230	*Swift*-BAT	02 h 29 m 19 s	−25° 08′ 50″	0.05<	60.7	×	×	✓	✓	-	Afterglow
GRB 090201	*Swift*-BAT	06 h 08 m 12 s	−45° 35′ 24″	0.05<	83	×	×	✓	✓	2.1	Afterglow
GRB 091018	*Swift*-BAT	02 h 08 m 45 s	−57° 32′ 54″	0.05<	4.4	×	×	✓	✓	0.971	Afterglow
GRB 100418A	*Swift*-BAT	17 h 05 m 27 s	+11° 27′ 42″	0.05<	7.0	×	✓	✓	✓	0.6235	Afterglow
GRB 110625A	*Swift*-BAT	19 h 07 m 00 s	+06° 45′ 10″	0.05<	44.5	×	×	✓	✓	-	Afterglow
GRB 120328A	*Swift*-BAT	16 h 06 m 12 s	−39° 20′ 24″	0.05<	24	×	×	×	✓	-	Prompt
GRB 120816A	*Swift*-BAT	18 h 48 m 30 s	−06° 58′ 46″	0.05<	7.6	×	×	✓	✓	-	Prompt
GRB 130206A	*Swift*-BAT/*Fermi*-GBM	09 h 21 m 30 s	−58° 09′ 36″	0.05<	50	✓	×	✓	✓	-	Afterglow
GRB 130502A	*Swift*-BAT/*Fermi*-GBM	09 h 14 m 19 s	−00° 08′ 35″	0.05<	5	×	✓	✓	✓	-	Afterglow
GRB 130515A	*Swift*-BAT/*Fermi*-GBM	18 h 53 m 41 s	−54° 16′ 51″	0.05<	0.6	×	×	×	✓	-	Prompt
GRB 131030A	*Swift*-BAT	23 h 00 m 19 s	−05° 23′ 20″	0.05<	41.1	×	×	✓	✓	1.293	Prompt
GRB 131202	*Swift*-BAT/*Fermi*-GBM	22 h 56 m 13 s	−21° 39′ 27″	0.05<	55.6	×	×	✓	✓	-	Afterglow
GRB 140818B	*Swift*-BAT	18 h 04 m 35 s	−01° 21′ 40″	0.05<	18.1	×	×	✓	✓	-	Prompt
GRB 140901A	*Fermi*-GBM	00 h 59 m 05 s	−35° 36′ 36″	2.48	0.16	×	×	✓	✓	-	Afterglow
GRB 141004A	*Swift*-BAT	05 h 06 m 55 s	+12° 49′ 59″	0.05<	3.92	×	×	✓	✓	0.573	Afterglow
GRB 150122C	*Fermi*-GBM	10 h 30 m 02 s	−31° 08′ 23″	4.07	10	×	×	×	×	-	Afterglow
GRB 150127B	*Fermi*-GBM	09 h 29 m 38 s	−03° 08′ 24″	1.0	61	×	×	×	×	-	Prompt
GRB 150227	*Fermi*-GBM	12 h 31 m 29 s	−25° 06′ 00″	6.82	10	×	×	×	✓	-	Afterglow
GRB 150301A	*Swift*-BAT	16 h 17 m 07 s	−48° 42′ 00″	0.05<	0.1	×	×	✓	✓	-	Afterglow
GRB 150415	*Fermi*-GBM	14 h 42 m 31 s	−19° 20′ 34″	3.59	8	✓	×	×	×	-	Prompt
GRB 150422A	*Fermi*-GBM	14 h 20 m 24 s	−20° 51′ 36″	1.1	37	✓	×	×	×	-	Afterglow
GRB 150428B	*Swift*-BAT	19 h 30 m 36 s	+04° 06′ 36″	0.05<	130.9	×	×	×	✓	-	Prompt
GRB 150713	*Fermi*-GBM	20 h 36 m 24 s	−62° 26′ 24″	1.56	4.1	✓	×	×	×	-	Prompt
GRB 150819A	*Swift*-BAT	02 h 49 m 19 s	+09° 46′ 48″	0.05<	50	×	×	×	✓	-	Afterglow
GRB 151205B	*Swift*-BAT	02 h 44 m 36 s	−43° 28′ 48″	0.05<	11	×	×	×	✓	-	Prompt
GRB 160308A	*Fermi*-GBM	08 h 33 m 05 s	+20° 11′ 24″	10.75	4	×	×	×	✓	-	Afterglow
GRB 160310A	*Fermi*-LAT/*Fermi*-GBM	06 h 35 m 07 s	−07° 06′ 36″	0.1	18.2	✓	×	✓	✓	-	Afterglow
GRB 160825B	*Fermi*-GBM	21 h 58 m 10 s	+08° 09′ 36′	6	4.5	×	×	×	✓	-	Afterglow
GRB 161001	*Swift*-BAT	04 h 47 m 38 s	−57° 16′ 48″	0.05<	1	✓	×	✓	✓	-	Prompt
GRB 161125A	*Fermi*-GBM	04 h 33 m 00 s	+24° 57′ 00″	4.16	20	✓	×	×	×	-	Prompt
GRB 161228A	*Fermi*-GBM	07 h 43 m 17 s	+25° 45′ 36″	3.14	27	✓	×	×	×	-	Prompt
GRB 170402	*Fermi*-GBM	20 h 31 m 36 s	−45° 54′ 00″	6	7.5	×	×	×	✓	-	Afterglow
GRB 170424A	*Fermi*-LAT	22 h 54 m 48.0 s	−45° 07′ 12″	0.45	52	✓	×	×	✓	-	Afterglow
GRB 170531B	*Swift*-BAT	19 h 7 m 34.8 s	−16° 25′ 35″	0.05<	>50	×	×	×	✓	2.366	Afterglow
GRB 170826	*Fermi*-GBM	21 h 50 m 48.0 s	−31° 48′ 00″	1.0	11	✓	×	×	×	-	Afterglow
GRB 170923A	*Fermi*-GBM	08 h 00 m 28.8 s	−35° 19′ 48″	4.89	11	✓	×	×	×	-	Prompt
GRB 170926	*Fermi*-GBM	23 h 07 m 40.8 s	−22° 40′ 12″	3.9	2	×	×	×	×	-	Afterglow

Tab. 4.1.: Properties of GRBs observed by H.E.S.S. from 2008 to mid 2017. The first column provides the name of the GRB in the standard nomenclature. The second column indicates the satellite that sent the alert to H.E.S.S. The third and fourth columns give the sky coordinates of the final GRB location in right ascension (R.A) and declination (Dec.) respectively, with its corresponding localisation uncertainty in the fifth column. The quoted localisation uncertainty is statistical only with 68% containment. T_{90}, defined as the time interval over which 90% of the total background-subtracted counts are observed by the alerter, is given in the sixth column. The following columns indicate detection at the given wavelength with a checkmark. While a cross indicates a lack of detection. The referred wavelengths are HE (high-energy), R (radio), O (optical) and X (X-ray). The second to last column indicates the measured redshift and the last column the type of follow-up performed by H.E.S.S. as explained in Sec. 4.1.1.

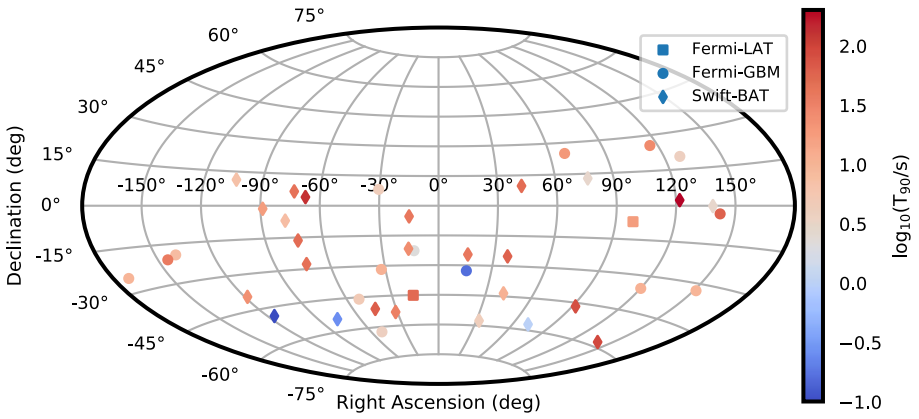

Fig. 4.2.: Distribution in the sky of GRBs followed-up by H.E.S.S. from mid-2008 to mid-2017. The squared marks indicate those GRBs whose alert was sent by *Fermi*-LAT. In the same way, circled marks indicate those detected by *Fermi*-GBM, diamond-shaped by *Swift*-BAT and star-shaped for the special case of GRB170817A/GW170817. The colour codes the value of T_{90}, blue colour corresponds to short GRBs (T_{90}<2 s) and red to long GRBs (T_{90}>2 s).

participation fraction (See Ch. 3.2.2). Having a big amount of noisy or dead channels can impact the reconstruction of the shower direction, introducing spurious signals in the significance maps. In addition to these tests, the night-sky background maps of the corresponding observation runs are produced to determine if bright stars were located around the GRB position. Bright stars are identified and masked out during the high-level analysis. After this, the strategy for the data analysis (significance and spectral analysis methods) are defined. Problematic runs identified in the previous step are excluded from the analysis and the most accurate localisation of the GRB is used.

In general, the ring background method is employed for the production of skymaps, and the reflected background method for the extraction of the spectrum. For alerts of high localisation uncertainty (typical for GRBs detected by *Fermi*-GBM), the production of skymaps is done in the first place and, if no significant emission is detected, upper limits are calculated in the whole FoV (upper-limits maps). In the case of small uncertainty in the GRB localisation, when no detection is present, differential upper limits are obtained for the GRB location assuming a power-law spectrum of photon index -2.5.

To analyse the set of GRBs presented here, a ranking was done based on the observation regime (prompt or afterglow) and MWL detection. Observations in the afterglow and prompt regime coming from *Fermi*-GBM alerts were analysed first. After this, afterglow observations of *Swift*-BAT alerts were analysed, since the delay of follow-up decreases the chance of detection. Finally, the analysis of prompt observations by *Swift*-BAT and *Fermi*-LAT, which have small localisation uncertainty and little delay of observation, was performed. This strategy was adopted to acquire experience with the less promising observations, such that when analysing the last category, all the possible limitations of the analysis were already identified and fixed.

4.2.2 Results and Discussion

Seven of the GRBs from the list of GRBs in Tab. 4.1 have been dropped due to bad weather conditions or data quality issues (identified with the procedure explained in Sec. 4.2.1) and seven are pending approval for publication. For a total of five observations, it was only possible to measure the level of significance without obtaining upper limits on their flux due to a lack of statistics (when runs had to be excluded or observations lasted for a short period of time). For 15 observations it was possible to extract upper-limits at the tested position (when the localisation uncertainty was smaller than the H.E.S.S. point-spread function, PSF), and for six observations upper-limit maps were extracted. A summary of the results can be found in Tab. 4.2. A subset of this sample has been already published in Piel et al., 2019 and a complete publication, including GRBs observed recently, is in preparation.

The distribution of significance of these results is shown in Fig. 4.3, considering only those GRBs with good localisation. Under pure statistical fluctuations, the data would follow a normal distribution. This is verified by a Gaussian fit (Fig. 4.3) which provides a mean value of $\mu = -0.05 \pm 0.19$ and a standard deviation $\sigma = 0.926 \pm 0.19$ (R^2= 0.56). Since no significant emission is present in this sample, upper limits on the gamma-ray flux were obtained. For GRBs with good localisation, the 95% confidence-level integral upper limits on the gamma-ray flux were estimated starting at the energy threshold of the analysis ($E_{\mathrm{thr.}}$, see Tab. 4.1). Flux upper-limits maps were

obtained in the case of GRBs where the localisation uncertainty is bigger than the PSF (Fig. 4.4).

For GRB 160310A (with *Fermi*-LAT detection), a more detailed analysis was performed, putting the differential flux upper limits obtained with H.E.S.S. in context with the spectrum measured by *Fermi*-LAT.

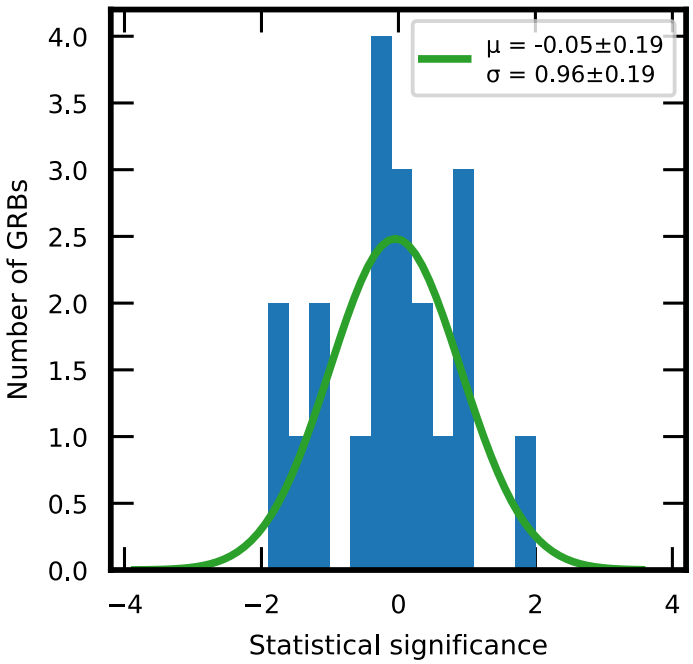

Fig. 4.3.: Distribution of significance for well localised GRBs. In blue is shown the histogram of the distribution of significance values in Tab 4.2. The green line corresponds to the fit to a gaussian model with $\mu = -0.05 \pm 0.19$ and a standard deviation $\sigma = 0.926 \pm 0.19$ with R^2=0.56.

	UTC T_{start}	Exposure Time (hrs)	CT5	Mean zenith (deg)	Kind of analysis	N_{ON}	N_{OFF}	α	Excess	Sig. (σ)	E_{th} (GeV)	Flux ULs ($cm^{-2}s^{-1}$ TeV^{-1})
GRB 080413A	2008-04-13 03:02:20	0.3	No	16.4	HESS I Loose	15	149	0.08	3.62	0.98	220	6.00×10^{-12}
GRB 080804	2008-08-04 23:25:19	0.4	No	31.3	HESS I Loose	7	91	0.08	0.13	0.05	320	1.80×10^{-12}
GRB 081028A	2008-10-28 01:05:30	0.1	No	55.7	HESS I Loose	2	13	0.09	0.98	0.82	-	-
GRB 081221	2008-12-21 19:08:02	0.9	No	26.3	HESS I Loose	21	273	0.08	-1.86	-0.38	320	4.62×10^{-12}
GRB 081230	2008-12-30 20:54:44	0.4	No	42.0	HESS I Loose	15	113	0.09	5.35	0.55	320	4.63×10^{-12}
GRB 090201	2009-02-01 21:20:25	0.8	No	32.1	HESS I Loose	13	169	0.08	-1.04	-0.27	220	3.63×10^{-12}
GRB 091018	2009-10-18 22:04:49	1.3	No	34.3	HESS I Loose	15	187	0.08	-0.37	-0.09	320	1.50×10^{-12}
GRB 100418A	2010-04-18 23:22:19	0.8	No	48.8	HESS I Loose	17	190	0.08	1.02	0.24	320	5.65×10^{-12}
GRB 120328A	2012-03-28 03:10:29	0.2	No	19.1	HESS I Loose	4	120	0.07	-4.33	-1.62	190	2.69×10^{-10}
GRB 130206	2013-02-06 20:30:40	1.7	No	39.8	HESS I Loose	26	263	0.09	2.15	0.43	-	-
GRB 130502A	2013-05-02 19:24:05	0.4	No	45.0	HESS I Loose	22	180	0.10	-4.02	0.87	320	2.19×10^{-11}
GRB 130515A	2013-05-15 01:26:25	0.4	No	32.4	HESS I Loose	15	357	0.04	-0.5	-0.12	-	-
GRB 131030A	2013-10-30 21:03:58	0.4	Yes	38.6	Mono Loose	160	1130	0.14	-1.43	-0.11	150	3.05×10^{-11}
GRB 140818B	2014-08-18 18:46:53	1.6	Yes	24.9	Mono Loose	160	1130	0.14	-1.43	-0.11	108	4.12×10^{-11}
GRB 141004A	2014-10-05 01:57:38	1.0	No	37.6	HESS I Loose	16	259	0.09	-6.60	-1.41	108	3.38×10^{-11}
GRB 150227	2015-02-27 00:12:25	1.2	Yes	5.4	Mono Loose	372	3291	0.10	36.1	1.84	-	-
GRB 151205B	2015-12-05 21:43:48	0.2	No	28.9	HESS I Loose	1	32	0.08	-1.53	-1.06	-	-
GRB 160308A	2016-03-08 19:49:30	1.3	Yes	40.5	Mono Loose	601	4443	0.14	-34.1	-1.3	200	○
GRB 160310A	2016-03-10 18:29:42	0.6	Yes	27.8	Mono Loose	54	650	0.09	-4.57	-0.58	150	4.32×10^{-11}
GRB 160825B	2016-08-25 20:43:22	1.4	Yes	35.9	Mono Loose	826	6213	0.14	-66.1	-2.1	150	○
GRB 161001	2016-10-01 01:07:16	1.2	Yes	35.0	Mono Loose	15	176	0.12	-10.3	-1.2	150	2.29×10^{-11}
GRB 161125A	2016-11-25 22:47:11	0.5	Yes	48.7	Mono Loose	164	1309	0.15	-29.6	-2.0	220	○
GRB 161228A	2016-12-28 00:47:19	0.7	Yes	54.3	Mono Loose	111	767	0.15	-2.9	-0.3	490	○
GRB 170531B	2017-05-31 22:26:43	1.2	Yes	18.0	Mono Loose	115	1363	0.10	-22.8	-1.9	98	5.93×10^{-11}
GRB 170826B	2017-08-26 21:11:00	1.8	Yes	18.3	Mono Loose	536	4471	0.14	-94.7	-3.6	130	○
GRB 170926	2017-09-26 22:30:53	1.8	Yes	25.2	Mono Loose	1173	9157	0.13	28.38	0.79	150	○

Tab. 4.2.: Results of the analysis of GRBs observed by H.E.S.S. from 2008 to mid-2017. The first column corresponds to the GRB name in the standard nomenclature. The second column is the time in UTC when H.E.S.S. started observations. The third column is the acceptance-corrected exposure time in hours. The fourth column indicates when CT5 participated in the observations. The fifth column is the mean zenith angle of the ON region. The sixth column indicates the cut configuration used for the analysis. The following columns provide the number of ON and OFF events, and α, the exposure ratio between the ON and OFF regions for the ring background method and, the excess and significance. The second to last column provides the energy threshold when upper limits are computed and the last columns provides the flux upper limits above the energy threshold. In the last column, a dash indicates that the number of ON and OFF events limits the possibility of performing a spectral analysis, while the circle indicates that upper-limit maps were extracted since the localisation uncertainty of the GRB was bigger than the PSF. These maps can be found in Fig. 4.4.

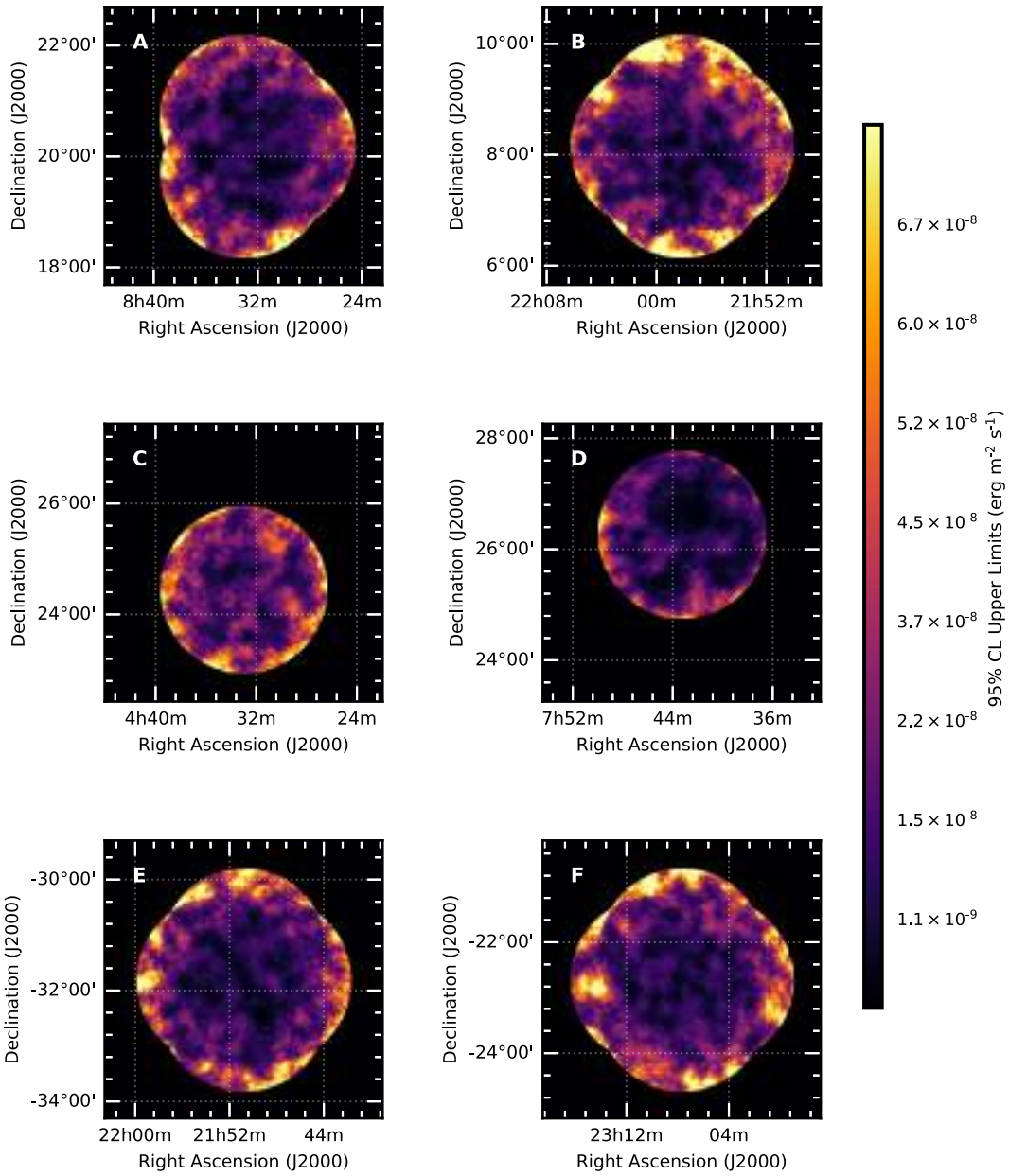

Fig. 4.4.: Upper limit maps for GRBs in Tab. 4.2 whose uncertainty is bigger than the H.E.S.S. PSF. Panel A: GRB 160808A. Panel B: GRB 160825B. Panel C: GRB 161125A. Panel D: GRB 161228A. Panel E: GRB 170226B. Panel F: GRB 170926.

GRB 160310A

GRB 160310A triggered the *Fermi*-LAT and *Fermi*-GBM on March 10th 2016 at T_0 = 00:22:58.47 (Toelge et al., 2016; Vianello et al., 2016). Although follow-up observations were performed by the *Swift* satellite and optical telescopes, only a pair of uncatalogued sources were detected without indication of fading, excluding the association of these sources with the GRB[1]. The X-ray satellited Konus-Wind was triggered at T_0-1391.997 s observing emission up to ∼4 MeV in a multi-peaked episode from T_0 + [-14 s,15 s] preceded by a faint episode starting 1510 s before T_0 which lasted for 90 s (Frederiks et al., 2016). These observations suggest that GRB 160310A is an ultra-long GRB.

This GRB was also observed by HAWC at the time of the burst onset, with a high zenith angle, without detecting significant emission (Alfaro et al., 2017). The MAGIC telescopes performed follow-up observations at T=T_0+72458 s but no upper limits have been reported until now (Berti et al., 2020).

The *Fermi*-LAT data for this GRB were downloaded and analysed using the `gtburst` software. The results were cross-checked against the published values in the *Fermi* catalogue (Ajello et al., 2019). In this publication, a value of $T_{90} = 25.9$ s (50–300 keV) is reported for the GBM detection, since GBM did not detect the pre-episode reported by the Konus Wind (Ajello et al., 2019). The detection by *Fermi*-LAT is at the ∼5 σ level (TS = 29.9) observed from 99.2 to 432.2 s after T_0. The maximum energy photon of 1.4 GeV is detected at 99.25 s after T_0. Since no temporal decay is reported in the *Fermi*-LAT catalogue, presumably due to the low statistics, in the analysis presented here the mean temporal decay index ($\alpha_{\rm LAT} = 0.99 \pm 0.04$) of the *Fermi*-LAT-detected GRBs is adopted to perform an extrapolation of the LAT detected flux to the times of the H.E.S.S. observation at T_0+17.93 hrs.

The analysis of the H.E.S.S. data provides a significance of -0.58 (See Tab. 4.2). For this analysis, differential flux upper limits assuming a photon index of -2.5 were obtained in the energy range of 0.15 to 0.73 TeV (which corresponds to the energy threshold and the limit where 10 OFF events are detected, respectively). These results together with the *Fermi*-LAT expected flux are shown in Fig. 4.5. The H.E.S.S. upper limits are consistent with a

[1]See: `https://gcn.gsfc.nasa.gov/other/160310A.gcn3`

continuation of the *Fermi*-LAT emission. It is worth mentioning that since the maximum photon detected by *Fermi*-LAT has an energy of 1.4 GeV, the extrapolation of the spectrum up to 100 GeV seems optimistic. Therefore, a dip in the spectral energy distribution at the energies between the *Fermi*-LAT and H.E.S.S cannot be ruled out.

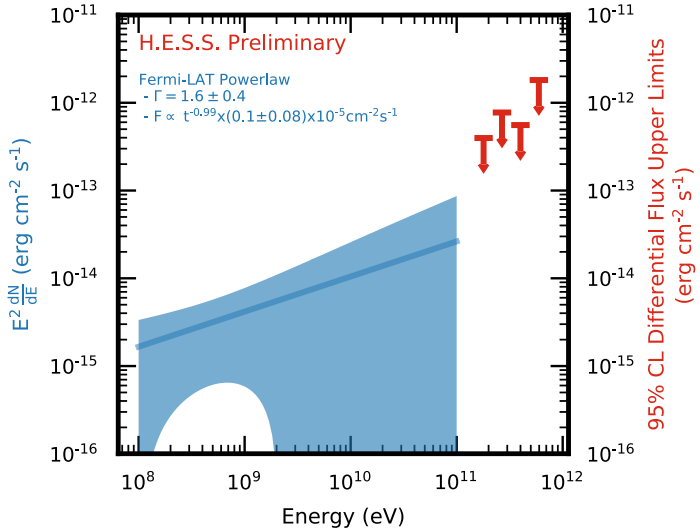

Fig. 4.5.: Spectral energy distribution of GRB 160310A. The blue butterfly shows the Fermi-LAT detected emission extrapolated to the H.E.S.S. observation time assuming a temporal decay index of 0.99. The H.E.S.S. differential flux upper limits assuming a photon index of -2.5 are shown in red.

4.3 Swift-BAT Improved Follow-up Criteria

As will be discussed in Ch. 5, VHE emission ($>$ 100 GeV) has been detected in three GRBs (GRB 180720B, GRB 190114C and GRB 190829A) and nearly as energetic in GRB 130427A (Ackermann et al., 2014). These four GRBs demonstrate the capability of these explosive phenomena to produce photons in the TeV regime. When comparing their X-ray energy flux in the energy range of 0.3–10 keV (see Fig. 4.6), these four GRBs exhibit comparable afterglow flux levels despite their diverse luminosity (due to diverse redshift values). The *Swift*-BAT follow up criteria of H.E.S.S. (see Sec. 4.1.1) was improved with these notions in mind after the detection of GRB 180720B

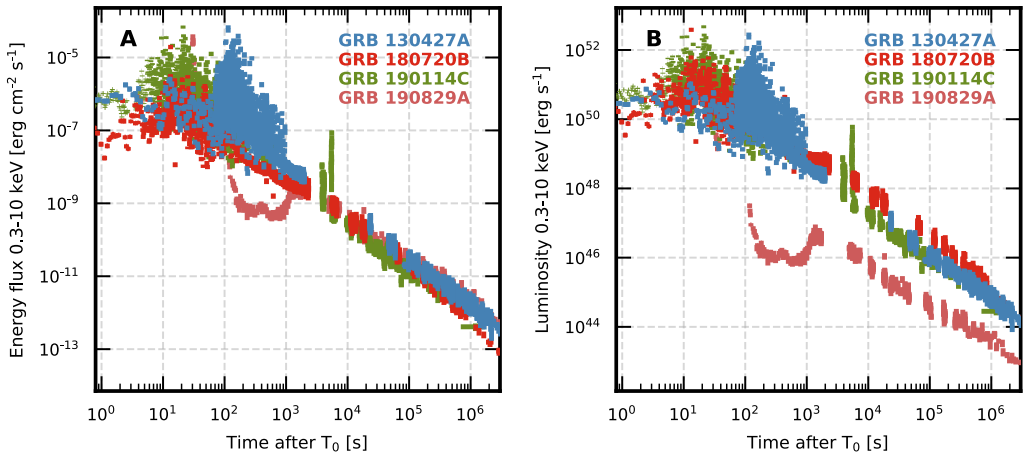

Fig. 4.6.: Energetics in the afterglow of the four GRBs with VHE emission. Panel A shows the energy flux while panel B shows the luminosity (fluence scaled by the luminosity distance) measured by *Swift*-BAT and *Swift*-XRT for GRB 130427A (blue), GRB 180720B (red), GRB 190114C (green) and GRB 190829A (salmon).

and GRB 190114C, while follow-up observations of GRB 190829A were supported by the criteria explained in this section.

In all these GRBs, the VHE emission light curve exhibits the same energy flux level as the X-ray light curve (see Ch. 5, Acciari et al., 2019). Such feature can be verified during different timescales; for GRB 190114C in the early afterglow (60 s to 100 s after T_0), for GRB 180720B in the late afterglow (10 h after T_0), GRB 130427A (up to 3×10^4 s after T_0) and GRB 190829A up to 10^5 s. On the X-ray emission side, there is evidence of a canonical afterglow light curve present in GRBs detected by *Swift*-XRT (see Ch. 2.3). In this generalisation, within times of $10^3\,\mathrm{s} < t \leq 10^4\,\mathrm{s}$, a temporal decay $1.0 < \alpha < 1.5$ characterises the GRB flux evolution ($F \propto t^{-\alpha}$). With this in mind, an empirical model was developed to estimate the late time X-ray flux-level based on the prompt emission. The estimation of the late-time flux level is then used as a further input to the follow-up strategy of H.E.S.S.

Within the first hours after a GRB detection by *Swift*-BAT, a refined analysis is distributed via a GCN circular, containing the early-time fluence of the burst. As seen in Fig. 4.7, a correlation exists between this fluence and the energy flux measured by *Swift*-XRT at later times (Gehrels et al., 2008), demonstrating the capability of this relations to predict the late-time flux

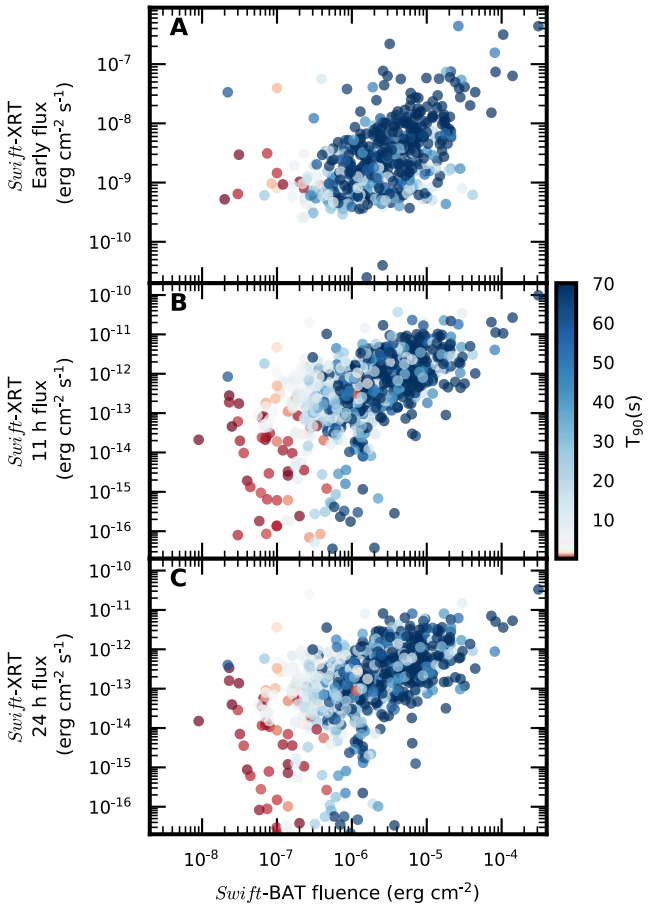

Fig. 4.7.: Correlation of the *Swift*-BAT fluence to late-times *Swift*-XRT energy flux. From top to bottom the *Swift*-XRT early flux, at 11 h after the BAT trigger and 24 h after the BAT trigger is shown. The orange points indicate short GRBs (sGRBs, $T_{90}<2$ s) while blue points indicate long ones (lGRBs, $T_{90}>2$ s). The data was downloaded from the *Swift* GRB online table: `https://swift.gsfc.nasa.gov/archive/grb_table/`.

from the measured fluence reported in the early circulars. As the purpose of this analysis is to determine the *Swift*-XRT energy flux at an arbitrary time t (where H.E.S.S. observations could be performed), the following empirical functional form is proposed to compute the *Swift*-XRT energy flux in units of erg cm^{-2} s^{-1} at a time t:

$$F_{\rm E}(t) = \frac{\mathfrak{F}}{T_{90}} \left(\frac{t}{50\rm s} \right)^{-\alpha}. \tag{4.1}$$

Where $\mathfrak{F}$ is the *Swift*-BAT energy flux in units of erg cm^{-2}, T_{90} is fixed to 1100 s when this parameter is unknown, α is the energy flux temporal decay, fixed here to -1.2 (the median value of the canonical *Swift*-XRT afterglow light curves).

To verify the prediction power of this model, the *Swift*-XRT flux at 11 and 24 h was computed with Eq. 4.1 and compared to the measured flux level reported by *Swift*-XRT. A comparison of the predicted and measured flux level at 11 h and 24 h is shown in Fig. 4.8 and Fig. 4.9 respectively.

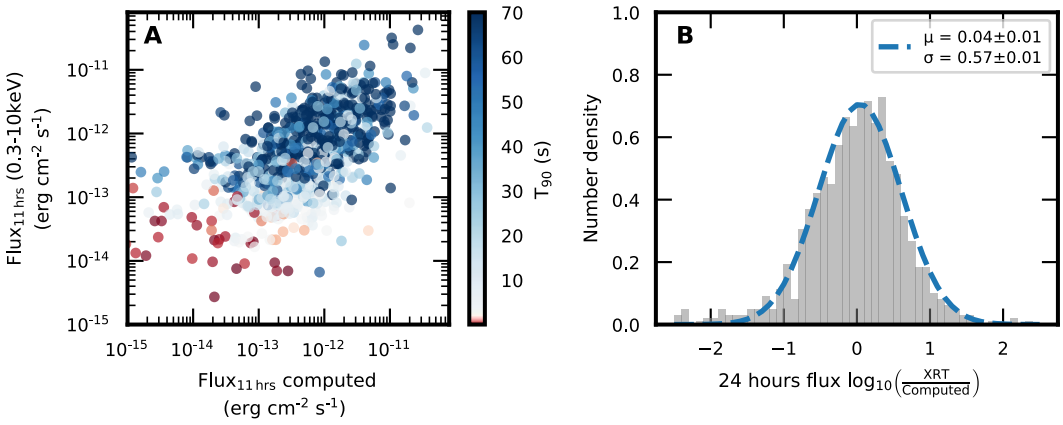

Fig. 4.8.: Relation on the computed and measured flux by *Swift*-XRT at 11 h after the GRB onset. Panel A shows a scatter plot of the *Swift*-XRT measured flux and the one calculated with Eq. 4.1 where the colour encodes the duration of the burst (T_{90}). Panel B shows the distribution of the ratio of the measured to computed energy flux. The dashed line corresponds to a Gaussian fit of mean μ and width σ with values indicated in the legend.

A Pearson's test was applied to estimate the level of correlation between the measured and predicted *Swift*-XRT flux. This test results in a value of

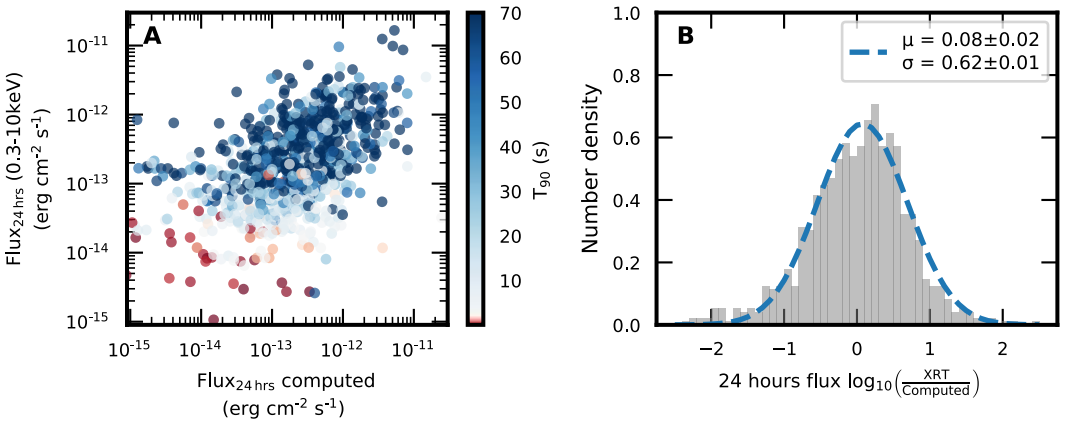

Fig. 4.9.: Relation on the computed and measured flux by *Swift*-XRT at 24 h after the GRB onset. Panel A shows a scatter plot of the *Swift*-XRT measured flux and the calculated with Eq. 4.1 where the colour encodes the duration of the burst (T_{90}). Panel B is the distribution of ratios of the measured to computed energy flux. The dashed line corresponds to a Gaussian fit of mean μ and width σ with values indicated in the legend.

0.41 (p-val $<$ 0.005) and 0.35 (p-val $<$ 0.005) for the estimation at 11 hrs and 24 hrs respectively. The correlation at 11 h is higher than at 24 h, which is expected, considering that a possible deviation of this sample from the canonical temporal decay assumed here would become more evident at later times. The level of correlation is considered when estimating the flux-level within the follow-up strategy of H.E.S.S. by extracting an uncertainty in the flux extrapolation with the level of spread obtained from panel B of Fig. 4.8 and Fig. 4.9.

Finally, these results were put in context with the upper limits obtained from the H.E.S.S. observations of some of these GRBs (see Sec. 4.2.2). The flux upper limits of *Swift*-BAT detected GRBs from Tab. 4.2 were compared to the predicted flux at the corresponding delay of observation (Fig. 4.10). Overall, the upper limits of H.E.S.S. are at a lower level than the predicted *Swift*-XRT flux. This could be explained by considering the EBL absorption of VHE photons, which would suppress the expected emission. A consideration of the redshift in this simplified model will be investigated in the future.

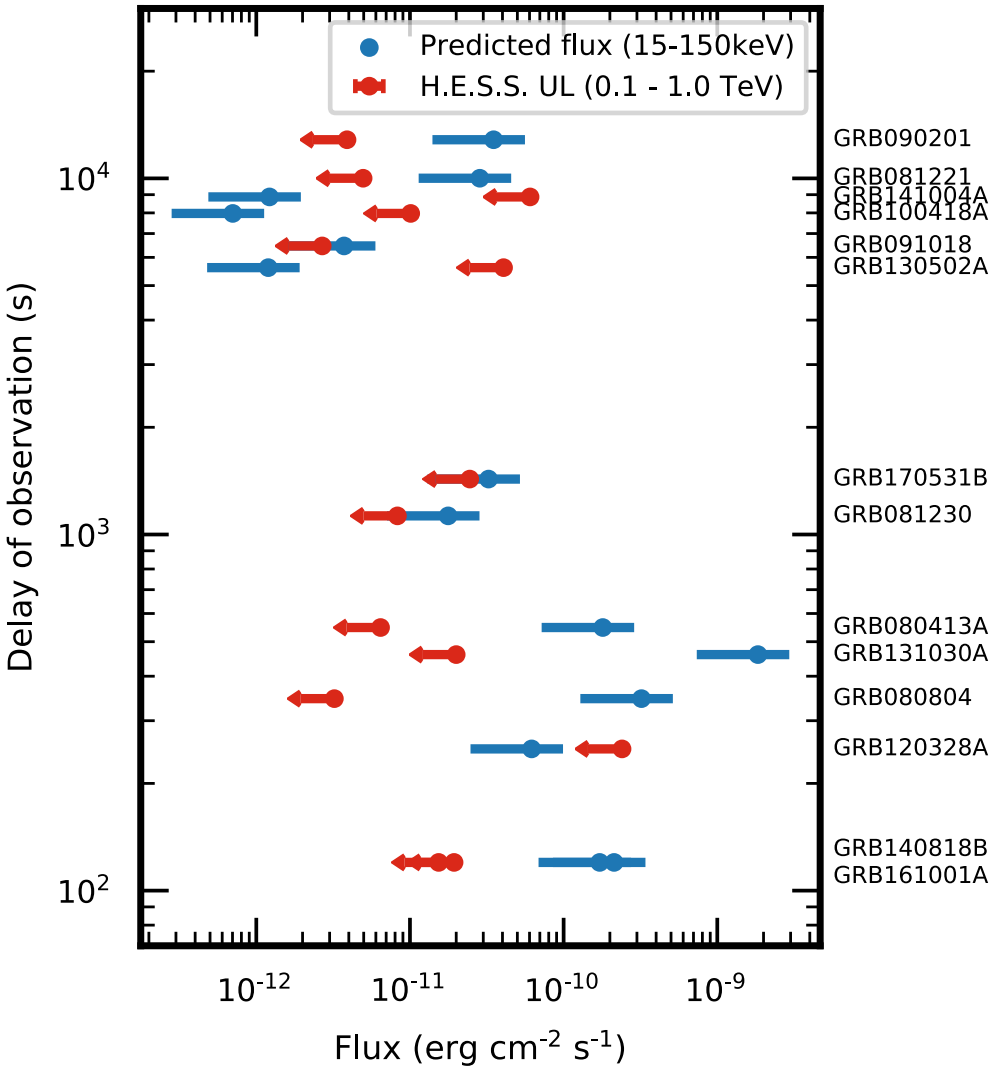

Fig. 4.10.: Comparison of the predicted XRT afterglow flux and the H.E.S.S. measured upper limits. In red the H.E.S.S. energy flux upper limits are obtained in the energy band of 0.1 to 1 TeV assuming an index of -2.0. For the corresponding delay of observation, the predicted XRT flux showing with blue dots is computed with Eq. 4.1.

4.4 Conclusions and Outlook

With an ambitious GRB observation programme, the H.E.S.S. system has followed up tens of GRB alerts from 2008 to 2018. This has been possible due to several observation criteria set in place. These criteria have evolved through the years thanks to the increased availability of multi-wavelength data and its specific application in the context of follow-ups with H.E.S.S. In addition, the deployment of CT5 has allowed a lower energy threshold in the observations and fast slewing speed which increased the chances of a detection.

In this chapter, the analysis of the GRBs observed between 2008 to 2017 was presented. The results of this analysis show no significant emission in any of the GRBs considered. The bulk of the GRBs analysed, where an estimation of the level of significance was possible, follows a normal distribution with $\mu = -0.05 \pm 0.19$, $\sigma = 0.96 \pm 0.19$, consistent with pure statistical fluctuations. Upper limits were obtained for 15 of these GRBs. The emission mechanisms responsible for the VHE emission of GRBs is still poorly understood. These upper limits, together with measurements at other wavelengths, can be used to discriminate and exclude the parameter space of the many scenarios that predict VHE emission, as exemplified with GRB 160310A.

By making use of the *Swift* table of GRB detection, an empirical model was developed to estimate the level of flux at an arbitrary time after the burst onset based on the *Swift*-BAT fluence. Since the fluence is one of the first products provided by *Swift* during a new detection, this method can be applied well in advance for GRBs in the FoV of H.E.S.S. and provides an additional follow-up criterion. Future work contemplates the extension of this tool to GRBs detected by *Fermi*-GBM and the application of a model that takes into account the redshift distribution of GRBs. The H.E.S.S. GRB programme is in constant evolution and the follow-up strategies are making more and more use of the multi-wavelength information available.

5

Detection of GRB 180720B and GRB 190829A with H.E.S.S.

Contents

Due to their extremely energetic output, and bright non-thermal emission, GRBs have been potential candidates for VHE gamma-ray emission since their discovery. Searches started during the second half of the nineties, with the Whipple, HEGRA and Milagro experiments without detections (See Atkins et al., 2004; Padilla et al., 1998). After its launch, *Fermi*-LAT provided evidence of GRBs exhibiting energetic emission and is the special case of GRB 130427A, detecting photons of up to 98 GeV (Ackermann et al., 2014). These detections added further support to the very expected VHE gamma-ray emission in GRBs. After much more than a decade of searches, within mid-

2018 to mid-2019, three GRBs were detected at VHE by IACTs. This chapter presents the detection of two GRBs using H.E.S.S[1]:

- GRB 180720B: The first GRB detected at VHEs was also detected by *Swift*-BAT, *Swift*-XRT, and *Fermi*-GBM recording extremely bright X-ray emission (see Fig 5.1). It was also detected by *Fermi*-LAT in the HE band and almost any other wavelength. Strikingly, the detection with H.E.S.S. above 150 GeV happened deep in the afterglow, with a delay of 10 hours from the burst's onset. Its redshift of 0.653 makes it a relatively local GRB, but to date, it remains one of the most distant among other GRBs detected at VHEs.
- GRB 190829A[2]: One of the nearest GRBs to date, with a redshift of 0.0785, was observed by H.E.S.S. during three consecutive nights at $\sim$4, $\sim$18 and $\sim$37 hours after the burst's onset. It exhibits fascinating characteristics, among the remarkably very bright X-ray afterglow (see Fig 5.1), and the spectral and temporal similarities between the VHE and X-ray emission.

The third GRB detected at VHEs is GRB 190114C (z = 0.564), observed with the MAGIC telescopes few minutes after the burst's onset (Acciari et al., 2019). This GRB also exhibits a bright X-ray emission. The intrinsic photon index at VHEs (after correcting for the EBL absorption), together with the *Fermi*-LAT and *Swift*-XRT observations can be explained with an SSC scenario.

5.1 GRB 180720B: First GRB Detected at VHE

The bright prompt emission of GRB 180720B triggered on July 20th 2018 the *Fermi*-GBM at 14:21:39.65 UT (Roberts et al., 2018) (T_0) and the *Swift*-BAT 5 s later (Siegel et al., 2018). *Fermi*-LAT was also triggered starting at T_0 up to $T_0 + 700$ s and detected a maximum photon energy of 5 GeV at $T_0 + 142.4$ s (Bissaldi et al., 2018). Since the detection of GRBs by *Fermi*-LAT

[1] I am a main/corresponding author of the two papers reporting these observations (see Bibliography of E. Ruiz-Velasco at the end of this thesis)
[2] Cora Parsons' GRB

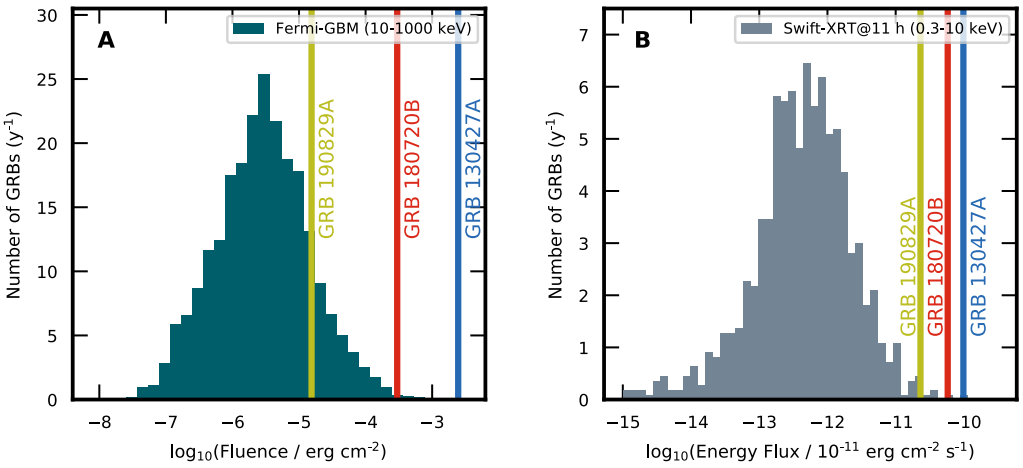

Fig. 5.1.: GRB 180720B and GRB 190829A in context with the GRB detections in the X-ray band. Panel A shows the fluence distribution in the energy range of 10–1000 keV of GRBs detected with *Fermi*-GBM. Panel B shows the distribution of the energy flux at 11 hours GRBs detected by *Swift*-XRT. In both panels, the distributions are scaled to show a rate per year.

is relatively uncommon (only 7% of the GRBs detected by *Fermi*-GBM or *Swift* have a counterpart in *Fermi*-LAT), a wide multi-wavelength follow-up campaign was triggered, including the observations with the ESO Very Large Telescope, which measured a redshift of $z = 0.653$ (Malesani et al., 2018).

In the context of the bulk of the GRBs detected in the X-ray band, this GRB presents the seventh brightest prompt emission, among over ~ 2650 GRBs detected by the *Fermi*-GBM [3] and is the second brightest afterglow (11 h after T_0) detected by *Swift*-XRT[4] (Fig. 5.1).

GRB 180720B is a long GRB, having a T_{90} duration of 48.9 ± 0.4 s (50–300 keV), which suggests a hypernova origin (see Ch. 2). This GRB has an isotropic energy release of $E^{\rm iso} = (6.0 \pm 0.1) \times 10^{53}$ erg (50–300 keV).

5.1.1 H.E.S.S. Observations and Data Analysis

Since GRB 180720B fulfilled the criteria to trigger a follow-up with H.E.S.S. (known redshift, *Fermi*-LAT detection, see Ch. 4.1.1) observations started at

[3] Up to November 2019
[4] Up to November 2019

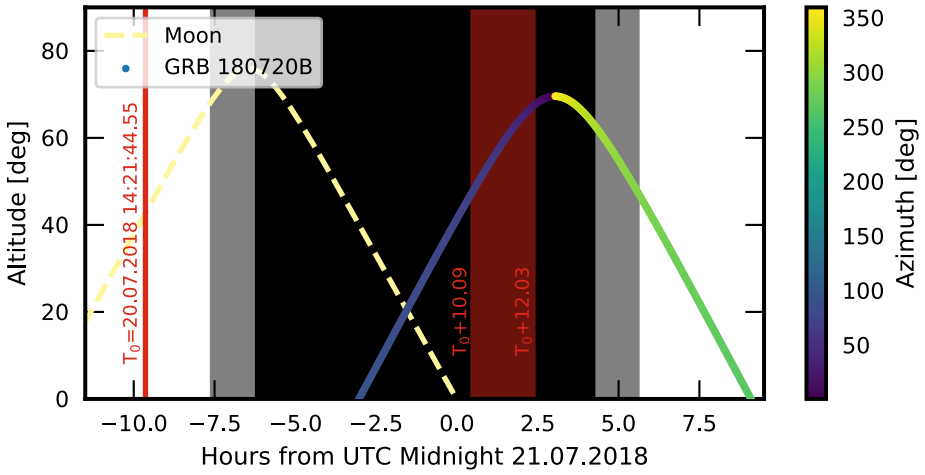

Fig. 5.2.: Navigation plot of GRB 180720B. The altitude and azimuth angle evolution are shown as a function of time for GRB 180720B at the H.E.S.S. site for the night of the first observation. The onset time T_0 is indicated with a vertical line. The dotted line indicates the transit of the Moon. The shaded red region indicates the interval in which H.E.S.S. observed the GRB with the corresponding delay from T_0.

T_0 +10.09 hrs when the burst went above 45°zenith, lasting for a total of 4 observation runs up to T_0 +12.03 hrs (Fig. 5.2).

These observations were performed with the five H.E.S.S. telescopes, in *wobble* mode with an offset of 0.5°. Low-level checks were performed on the data (see 4.2) identifying small trigger-rate drops of the order of 30% at the beginning of the observations, most likely caused by the presence of clouds. Since a low energy threshold is desired (to minimise the impact of EBL absorption), the data analysis was done using the CT5 data with the *std_ImPACT_mono* analysis configuration and the *Model_HESSII_Hybrid_Prod8* for the cross-check analysis. Additionally, due to the bright X-ray emission and HE emission detected by *Fermi*-LAT, H.E.S.S. triggered a long monitoring campaign starting at 18 days after T_0 for several days more.

Significance skymaps were extracted using the ring background method. Panel A of Fig. 5.3 shows the significance skymap of the region during the first set of observations. The gamma-ray excess seen has a statistical significance of 5.3σ. The distribution of the significance values of the skymap when including and excluding the GRB region, and the corresponding number

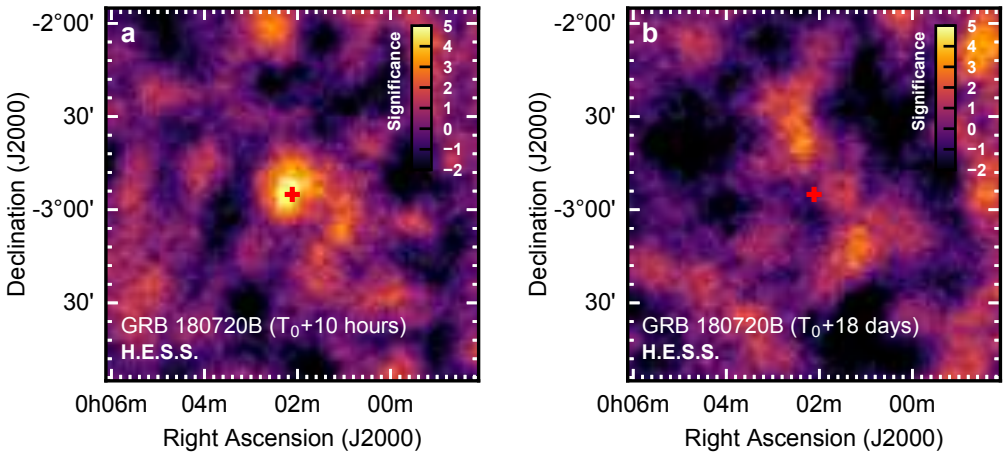

Fig. 5.3.: Very-high-energy gamma-ray maps of GRB 180720B. Significance map of the GRB 180720B field as observed by H.E.S.S. Panel a corresponds to the observation made at $T_0 + 10.1\,\mathrm{h}$ with a total observation time of 2 h. Panel b shows the same region of the sky as observed during consecutive nights between $T_0 + 18.4\,\mathrm{days}$ and $T_0 + 24.4\,\mathrm{days}$. The red cross indicates the position reported by the optical telescope ISON-Castelgrande (Schmalz et al., 2018).

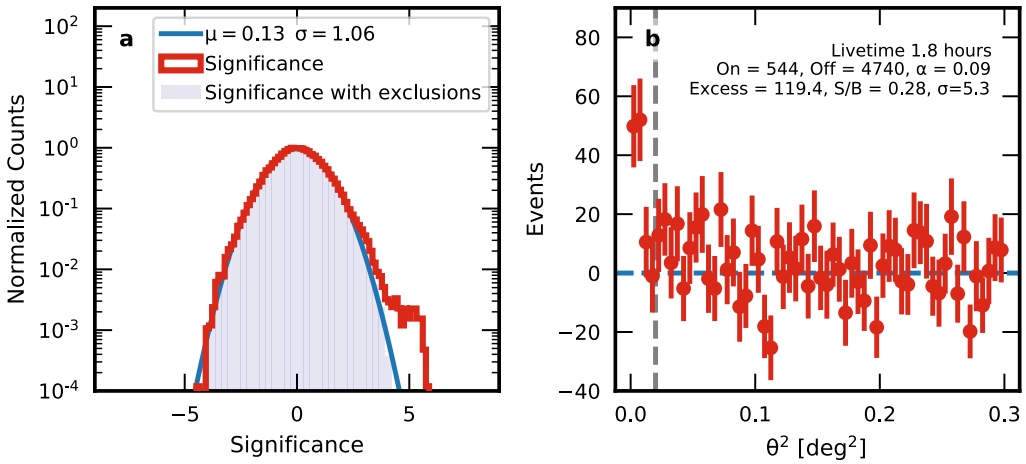

Fig. 5.4.: Significance distribution and theta squared plot of GRB 180720B. Panel a shows the significance distribution of the GRB skymap without excluding the GRB region in red. The distribution when masking the GRB region is indicated with the blue shaded area. The blue line is a Gaussian fit to this distribution with mean and sigma values shown in the label. Panel b shows the number of gamma-like events in the skymap as a function of θ^2.

of events as a function of θ^2 (see Ch. 3.2.3) is shown in Fig. 5.4.a and b respectively.

The signal position was fit with a two dimensional gaussian function and resulted in a source position $00^{\mathrm{h}}02^{\mathrm{min}}07.6^{\mathrm{s}}$ and declination $-02°56'06''$ (J2000) with a statistical uncertainty of $1.31'$. This position is consistent with the GRB position measurements at other wavelengths (Ra = $00^{\mathrm{h}}02^{\mathrm{min}}06.792^{\mathrm{s}}$, Dec = $-02°55'04.99''$) with precision of the order of arc-seconds by optical telescopes (Bissaldi et al., 2018; Schmalz et al., 2018; Siegel et al., 2018), assuring the association of this VHE emission with the GRB. The results obtained for the observations at 18 days after T_0, shown in panel B of Fig. 5.3, indicate that the GRB emission had fainted up to a level no longer detectable by H.E.S.S. and secures that the emission detected during the first observation was not produced by an unidentified steady source. This constitutes the first evidence of the presence of VHE emission in GRB afterglows.

The H.E.S.S. spectral analysis was done using the reflected background method and results in a significance of 4.6σ. The forward-folding method (see Ch. 3.2) was used to perform the spectral fit. Two types of spectra were

considered, starting with a simple power-law to characterise the emission detected at Earth:

$$F_{obs}(E) = F_{0,obs}(E/E_{0,obs})^{-\gamma_{obs}}, \tag{5.1}$$

where $F_{0,obs}$ is the flux normalisation, γ_{obs} the photon index, and $E_{0,obs}$ the reference energy. The subscript obs indicates that the parameters fit the emission observed at Earth.

Due to the EBL absorption, the photons emitted at the source get attenuated through their trajectory to the Earth. This implies that the spectrum emitted by the source will be harder than the observed one. The intrinsic spectrum was obtained by including an exponential term in the spectrum that accounts for the energy-dependent EBL absorption for a redshift z = 0.653 (Franceschini et al., 2008):

$$F_{obs}(E) = F_{int}(E) \times e^{-\tau(E,z)} = F_{0,int}(E/E_{0,Int})^{-\gamma_{int}} \times e^{-\tau(E,z)}, \tag{5.2}$$

where $\tau(E, z)$ is the energy-dependent EBL absorption coefficient for a redshift z. Additionally, to decrease the impact of the low statistics on the spectral measurement, the intrinsic spectrum was also obtained by fixing the photon index value to -2.0, which corresponds to the mean photon index observed in GRBs detected by *Fermi*-LAT (Ajello et al., 2019)

Systematic uncertainties were addressed by performing a 15% shift up and down in the reconstructed energy of the events and performing the spectral fits again, assessing the variations in the fitted parameters. This accounts for possible discrepancies in the measured Cherenkov light yield compared to simulations (Abdalla et al., 2017). Additionally, to account for systematics due to the episodes where a drop in the trigger rate was identified (21.7 min in total), these intervals were excluded and the spectral fits performed again. This results in a possible underestimation of 32% in the flux level and 4.8% in the photon index. Since these two sources of uncertainty are considered independent, a total systematic uncertainty was obtained by adding each of these systematic uncertainties in quadrature.

Spectral model	$F_0 \times 10^{-10}$ (cm^{-2} s^{-1} TeV^{-1})	γ	E_0 (TeV)
$F_0 \times \left(\frac{E}{E_0}\right)^{-\gamma}$	$2.71 \pm 0.74^{+1.43}_{-1.16}$	$3.7 \pm 1.0^{+0.2}_{-0.1}$	0.154
$F_0 \times \left(\frac{E}{E_0}\right)^{-\gamma} \times e^{-\tau(z,E)}$	$7.52 \pm 2.03^{+4.53}_{-3.84}$	$1.6 \pm 1.2^{+0.4}_{-0.4}$	0.154
$F_0 \times \left(\frac{E}{E_0}\right)^{-2} \times e^{-\tau(z,E)}$	$16.12 \pm 4.37^{+10.59}_{-9.25}$	2.0 [Fixed]	0.105

Tab. 5.1.: Intrinsic and measured spectral fits for GRB 180720B. Spectral parameters of the fits to the H.E.S.S. observed emission in the energy range 100–440 GeV. The reported uncertainties are statistical and systematic in that order.

When extracting the intrinsic spectrum, the choice of a specific EBL model may influence the values of the fit parameters (photon index and normalisation). To address such effect, the intrinsic spectrum was obtained using three additional EBL models: Domínguez et al., 2011; Finke et al., 2010; Gilmore et al., 2012. From this analysis, the maximum variation found in normalisation and index is 55.3% and 27% respectively, which is lower than the level introduced by the other systematic and statistical uncertainties of the results.

The resulting spectral fit parameters are summarised in Tab. 5.1 and the intrinsic and observed spectra with flux points are shown in Fig. 5.5. Throughout the spectral determination and systematic uncertainty estimation, the minimum energy considered for the fit is defined as the energy in which the effective area reaches 90%. The maximum energy was determined as the point at which 98% of the statistical significance of the spectrum is obtained. This corresponds to an energy range for the fitted spectra of 110 to 440 GeV.

The energy-flux of the H.E.S.S. emission was computed in the energy range of $E_{min} = 100$ GeV to $E_{max} = 440$ GeV as:

$$\mathcal{F}(E_{\mathrm{min}}, E_{\mathrm{max}}) = \int_{E_{\mathrm{min}}}^{E_{\mathrm{max}}} F_{0,\mathrm{int}}(E/E_{0,\mathrm{Int}})^{-\gamma_{\mathrm{int}}}\, E\, dE, \tag{5.3}$$

resulting in a value of $(4.82 \pm 3.30) \times 10^{-11}$ erg cm^{-2}s^{-1}.

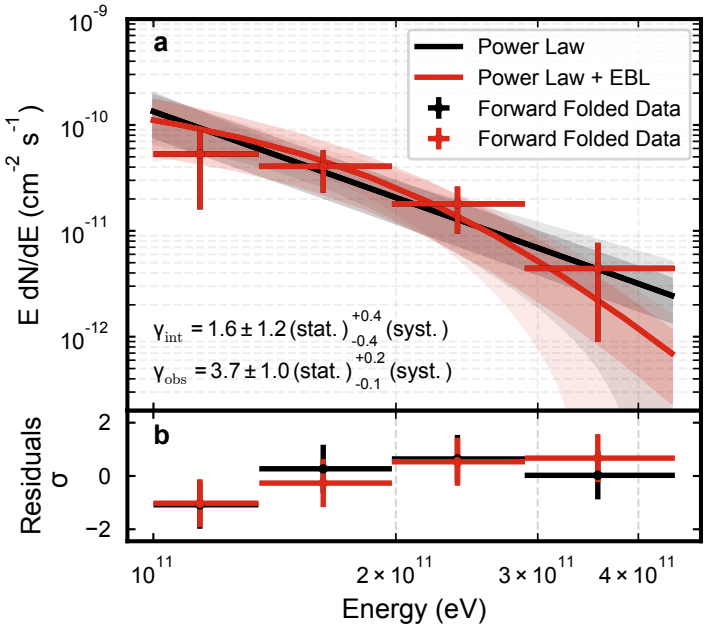

Fig. 5.5.: VHE spectral plot of GRB 180720B as detected by H.E.S.S. Panel a shows the Power Law and Power Law with EBL absorption fit envelopes to the data in black and red respectively, together with the corresponding flux points inferred with the forward folding method. Panel b shows the residuals significance of the forward folded data points to the fitted model.

5.1.2 Multi-wavelength Context

The energy-flux level of the GRB 180720B intrinsic emission measured with H.E.S.S. is shown in panel A of Fig. 5.6 together with the *Fermi*-LAT, *Fermi*-GBM, *Swift*-XRT, *Swift*-BAT and optical (r-band) energy-flux light curves. The photon index evolution of the *Swift* and *Fermi* detection, together with the H.E.S.S. intrinsic photon index are shown in panel B of this figure [5]. The initial emission is extremely bright and shows typical flares characteristic of the prompt phase of GRBs as seen in the *Fermi*-GBM and *Swift* light curve. At around 100 s, the prompt emission fades and a smooth temporal decay of the flux is seen.

The afterglow temporal decay in X-rays and optical band were fit with a model of the form $F(t) \propto t^{-\alpha}$, where α is the temporal decay index. These fits result in values of $\alpha_{XRT} = 1.29 \pm 0.01$ and $\alpha_{optical} = 1.24 \pm 0.02$. For the emission detected by *Fermi*-LAT (100 MeV-10 GeV) from $T_0 + [55\,s, 700\,s]$, the temporal-decay fit results in $\alpha_{LAT} = 1.83 \pm 0.25$. This value is $\sim 1\sigma$ away from the mean value of the distribution of temporal decay measured for long GRBs detected by *Fermi*-LAT ($\bar{\alpha}_{LAT} = 0.99 \pm 0.04$, $\sigma_{\bar{\alpha}} = 0.80 \pm 0.07$) and could potentially be in agreement with $\alpha_{optical}$ and α_{XRT}. In the same time interval the average photon-index value of the *Fermi*-LAT detection is $\gamma_{LAT} = 2.10 \pm 0.10$. For the *Swift*-XRT the average photon-index value in the afterglow is $\gamma_{XRT} \sim 2.0$ in agreement with the intrinsic photon-index value measured by H.E.S.S.

5.1.3 Discussion

The similarities seen in the optical, X-ray and HE-VHE temporal decay are one of the striking results in this GRB. The H.E.S.S. measured energy flux sits at the same level as the emission detected by the *Swift*-XRT, with a similar behaviour seen between the *Fermi*-LAT and *Swift*-BAT/XRT detections in the prompt-to-afterglow phase (See Fig. 5.6).

[5] Details on the analysis and compilation of these data is in the original publication: Abdalla et al., 2019

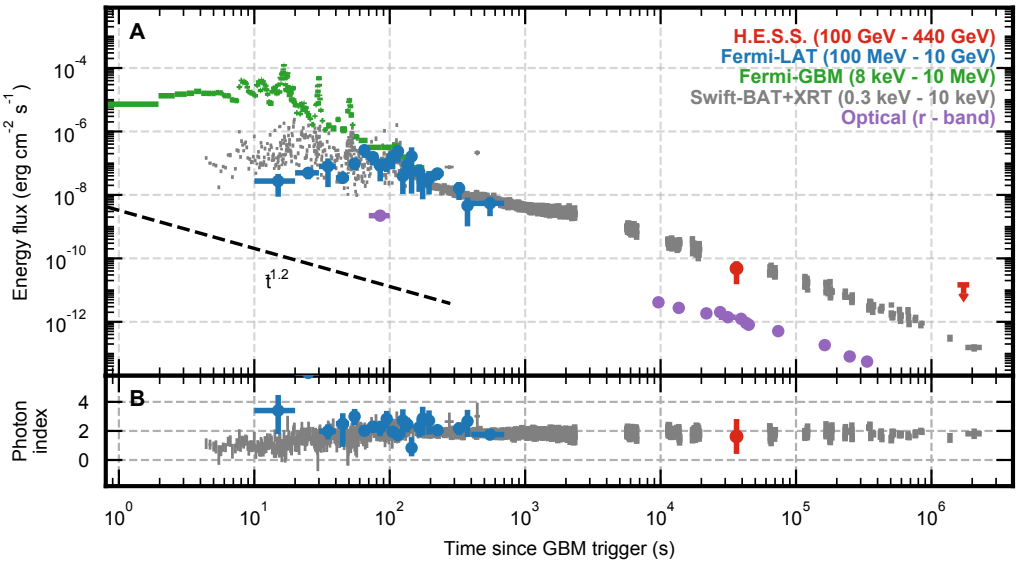

Fig. 5.6.: Multi-wavelength light curve of GRB 180720B. Panel A shows the energy-flux light curve detected by the *Fermi*-GBM using a Band spectral fit (green), and by the *Fermi*-LAT for a power-law spectrum (blue). The *Swift*-BAT detected emission from 15 keV to 150 keV is extrapolated to the XRT energy band (0.3–10 keV) to show a combined light curve (grey). The H.E.S.S. intrinsic (EBL-corrected) energy flux ($T_0 + 3.6 \times 10^3$ s) for a power-law spectrum and a 95% C.L. upper limit ($T_0 + 1.5 \times 10^6$ s) are shown in red. The black dashed line indicates a power-law temporal decay with $\alpha = -1.2$ for reference. Panel B shows the photon index evolution for the power-law fits of the *Fermi*-LAT, *Swift* and H.E.S.S. spectra. The error bars in the data points correspond to 1 σ standard deviation.

The detection of photons at T_0 +$\sim$10 h by H.E.S.S., with energies in the GeV range indicates the presence of a highly efficient non-thermal process within the forward shock of the GRB. With the highest radiation efficiency, an electron-synchrotron process seems a plausible candidate. A synchrotron emission of relativistic electrons could indeed explain the similar spectral behaviour followed by *Swift* and H.E.S.S., with a photon index value of -2 as expected from a synchrotron scenario, together with the similar temporal behaviour. A major theoretical constraint for this mechanism is the synchrotron burnoff limit $E_{\rm syn}^{\rm max} \approx 100{\rm MeV}\,\Gamma/(1+z)$ which would require values for the bulk Lorentz factor of $\Gamma \sim 13200$, which are difficult to realise, while at 10 hrs after T_0, expectations of Γ are lower than few tens. However, such limitation could be alleviated if this GRB operates as extreme accelerators where electrons in PeV energies are produced, or if the GRB environment consists of small scale magnetic turbulence, which can push this limit beyond the H.E.S.S. detected emission.

A synchrotron self-Compton (SSC) scenario could alleviate the energetic requirements and constraints of the pure synchrotron mechanism. In this case, an electron of energy E_e scatters off a target photon of energy E_t to an energy given by $\min\{E_t[E_e/(m_e c^2)]^2, \gamma E_e\}$. Thus, the presence of GeV photons becomes possible, with keV photons being up-scattered by electrons of $\sim$ 10 GeV boosted by $\Gamma \sim 10$.

In the SSC scenario, a synchrotron peak in the SED around the *Swift* detected emission would be related to the SSC peak falling within the VHE region. The ratio of the heights of the peaks will relate to the magnetic and electron energy densities (see Ch.1.2.1). However, in the SSC scenario, the KN cutoff is expected within the energy range of the H.E.S.S. detection, contradicting the broad-band temporal and spectral similarities observed. Lower fluxes and a steeper spectrum at VHEs (way steeper than the hard spectrum measured by H.E.S.S. $\gamma_{\rm int} \sim 1.6$) are expected with the presence of the KN cutoff. The detection of a hard synchrotron spectrum that goes below the keV energies could explain the delay of the KN transition. Unfortunately, the lack of multi-wavelength coverage between X-rays and the VHE band does not allow to confirm (or exclude) the presence of a second component in the SED.

5.2 GRB 190829A: Detection of Long-lasting Afterglow Emission

The onset of GRB 190829A was first detected by the *Fermi*-GBM, on the 29th of August 2019 at 19:55:53 UT (T_0), exhibiting two distinct temporal peaks in the prompt light curve from 0 s to 4 s and 50 s to 60 s (Fermi GBM Team, 2019). Since the first peak was outside the energy band of *Swift*-BAT, the *Swift* detection started with a delay of 51.5 s from T_0 detecting a re-brightening at 1000 s to 3000 s after T_0. *Swift*-BAT localised the GRB at a distance of 10 arcsec from the centre of the galaxy J025810.28-085719.2 (Sloan Digital Sky Survey, see Fig. 5.7) at a redshift $z = 0.08$ (Dichiara et al., 2019). This redshift value was subsequently confirmed by the 10.4 m GTC telescope, measuring $z = 0.0785 \pm 0.005$ (Valeev et al., 2019).

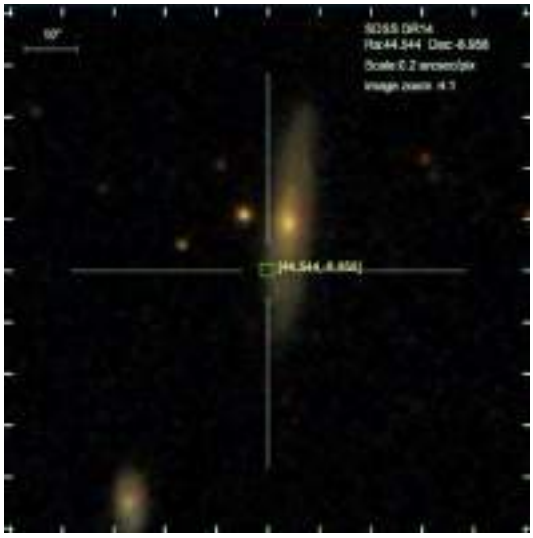

Fig. 5.7.: Location of GRB 190829A in the host galaxy. The green square indicates the location of GRB 190829A in an optical image of the host galaxy obtained from the Sloan Digital Sky Survey Data Release 14. Figure extracted from `http://skyserver.sdss.org/dr14/en/tools/chart/chartinfo.aspx`

Fermi-LAT observed the GRB region from T_0 up to T_0+1100 s without finding any significant emission, therefore reporting upper limits. The afterglow of GRB 190829A was detected in optical, NIR, X-ray and radio wavelength,

including the rise of the supernova observed in the optical and NIR at around four days after T_0. [6]

5.2.1 H.E.S.S. Observations and Data Analysis

Observations with the H.E.S.S. telescopes began on 30-08-2019 at 00:16:26 UT (T_0+4.3 hrs) and lasted for a total of 3.6 hrs. Already by the end of the first set of observations, the online analysis of H.E.S.S. showed a gamma-ray signal of significance $>5\sigma$ consistent with the GRB position. This triggered further observations on subsequent nights at T_0+27.2 hrs, for 4.7 hours, and at T_0+51.7 hrs, for another 4.7 hours.

Due to a decommissioning campaign on CT5, only data with the CT1-4 configuration was considered in this analysis. The data from these observations were analysed with the *stereo std_ImPACT* configuration using the ring background method and reflected background method for the extraction of skymaps and spectrum respectively (see Ch. 4.1.1). Crosschecks on all the results were done using the *Model* analysis. In the extracted skymaps shown in Fig. 5.8, a clear gamma-ray excess was detected by H.E.S.S in the VHE band during these observations with a statistical significance of 21σ, 5.6σ and 2.2σ respectively.

To fit the gamma-ray excess, the three sets of observation were stacked to produce an all-night skymap and the source position was fit with a point-source model convolved with the PSF of the analysis (0.07°, Parsons et al., 2014). The fit provides a source position of (R.A., Dec)=($02^{h}58^{min}11.1^{s}$, $-08°58'4.8''$) (J2000) (Fig. 5.8) with a statistical uncertainty of 11.4″. This position is 35.9″ away from the GRB position measured in the optical band with coordinates (R.A., Dec)=($02^{h}58^{min}10.58^{s}$, $-08°57'29.82''$). The H.E.S.S systematic pointing uncertainty is about 20″ per axis (Gillessen, 2004), so these positions are consistent within the uncertainties.

[6] see `https://gcn.gsfc.nasa.gov/other/190829A.gcn3` for a full compilation of GCN notices on this GRB.

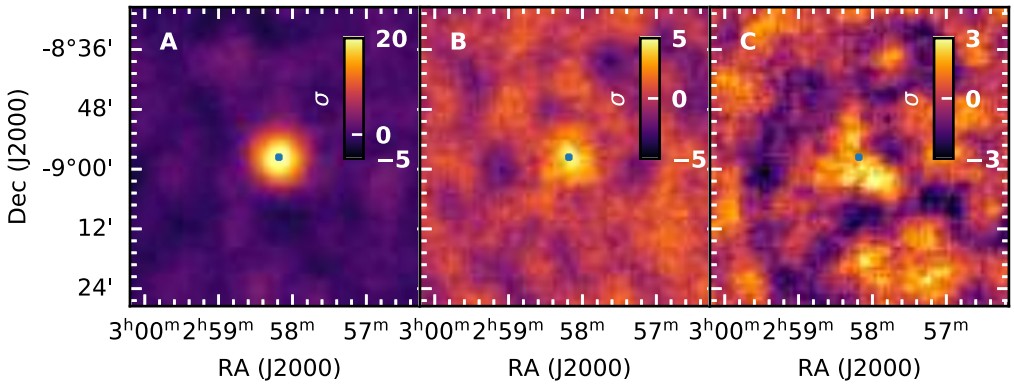

Fig. 5.8.: Significance skymaps of the H.E.S.S. observations of GRB 190829A. Panel A shows the significance skymap of the first night of observations with H.E.S.S. Panel B and C show the skymap for the second and third night respectively. These maps were obtained using the ring background method and a correlation radius of 0.07 was applied. The overlapped blue marker indicates the result of a point-source fit corresponding to R.A= $02^{\mathrm{h}}58^{\mathrm{min}}11.1^{\mathrm{s}}$ and Dec=$-08°58'4.8''$ (J2000).

Spectral Fit

The spectral fit was carried out with the *gammapy* software (Deil et al., 2017; Mohrmann et al., 2019; Nigro et al., 2019) version 0.17. In this software, a forward-folding likelihood fit (see Ch. 3.2) is performed after retrieving the reconstructed parameters of the events and detector response matrices.

For the first two observation windows, where good statistics are obtained, the detected photon spectrum was fit with a Power Law model (Eq. 5.1). Systematic uncertainties were determined by introducing a 10% shift up and down in the reconstructed energy of the events and the spectrum was fitted again. This energy variation accounts for discrepancies in the energy estimation between the two analysis chains. Additionally, a 20% uncertainty in the flux normalisation and a value of 0.09 for the photon index uncertainty were added in quadrature. These factors account for additional systematic uncertainties such as the interaction models employed for the atmospheric shower simulations, atmospheric effects, broken pixels in the cameras etc (F. Aharonian et al., 2006c).

To characterise the intrinsic gamma-ray emission, the spectrum was fitted with an EBL-attenuated power law (Eq. 5.2) with $z = 0.0785$. In addition to

the systematic uncertainties mentioned above, the choice of a specific EBL absorption model was treated as an additional systematic uncertainty. For this, the spectral fits were performed with the use of three widely-used EBL models (Domínguez et al., 2011; Finke et al., 2010; Franceschini et al., 2008) and the relative uncertainties were added in quadrature to the systematic uncertainties related to the instrument.

$dN(E)/dE = N_0 \times (E/E_0)^{-\gamma^{obs}_{\rm vhe}}$				
Interval	Time after T_0 (s)	$\gamma^{obs}_{\rm vhe}$	$N_0 \times 10^{-12}$ (TeV^{-1}cm^{-2}s^{-1})	E_0
Night 1	1.56×10^4 – 2.85×10^4	2.59 ± 0.09 (stat.) ±0.23(syst.)	13.95 ± 1.05 (stat.) ±2.92(syst.)	0.556
Night 2	9.79×10^4 – 1.15×10^5	2.46 ± 0.22 (stat.) ±0.14(syst.)	1.22 ± 0.27 (stat.) ±0.27(syst.)	0.741
Night 1-3	1.56×10^4 – 2.01×10^5	2.59 ± 0.08 (stat.) ±0.20(syst.)	5.01 ± 0.38 (stat.) ±1.04(syst.)	0.583
$dN(E)/dE = N_0 \times (E/E_0)^{-\gamma^{int}_{\rm vhe}} \times e^{-\tau}$				
Interval	Time after T_0 (s)	$\gamma^{int}_{\rm vhe}$	$N_0 \times 10^{-12}$ (TeV^{-1}cm^{-2}s^{-1})	E_0
Night 1	1.56×10^4 – 2.85×10^4	2.06 ± 0.10 (stat.) ±0.26(syst.)	22.67 ± 1.71 (stat.) ±4.84(syst.)	0.556
Night 2	9.79×10^4 – 1.15×10^5	1.86 ± 0.26 (stat.) ±0.17(syst.)	2.31 ± 0.52 (stat.) ±0.53(syst.)	0.741
Night 1-3	1.56×10^4 – 2.01×10^5	2.07 ± 0.09 (stat.) ±0.23(syst.)	8.34 ± 0.62 (stat.) ±1.78(syst.)	0.583

Tab. 5.2.: Spectral fit results of H.E.S.S. observations. The uncertainties in photon index γ and flux normalisation N_0 are statistical and systematic in that order (1 σ errors).

The results are summarised in Tab. 5.2 and shown, together with the extracted flux points from the forward-folding, in Fig. 5.9. For the first two observation windows, an index of $\gamma^{int}_{\rm vhe} = 2.06\pm0.10$ (1st night) $\gamma^{int}_{\rm vhe} = 1.86\pm0.26$ (2nd night) were obtained for the intrinsic spectra. When considering a joint spectral fit of the three observation windows, the photon index results in $\gamma^{int}_{\rm vhe} = 2.07 \pm 0.23$, indicating a remarkably stable spectrum throughout the VHE afterglow.

Temporal Evolution

To obtain a light curve of the H.E.S.S. observations, the data of the first night were split into three time intervals of equal duration (cluster 1 to 3). This results in a total of five data points for the light curve when including the observations of the second and third night. In each time interval, the intrinsic spectrum (after EBL correction) was extracted and the energy-flux level computed with Eq. 5.3. In this case $E_{\rm min}$ and $E_{\rm max}$ were set to 0.2 TeV and 4.0 TeV respectively and γ^{int} was fixed to $\gamma^{int}_{\rm vhe}$=2.07 ± 0.09 (stat.) ±0.23 (syst.)

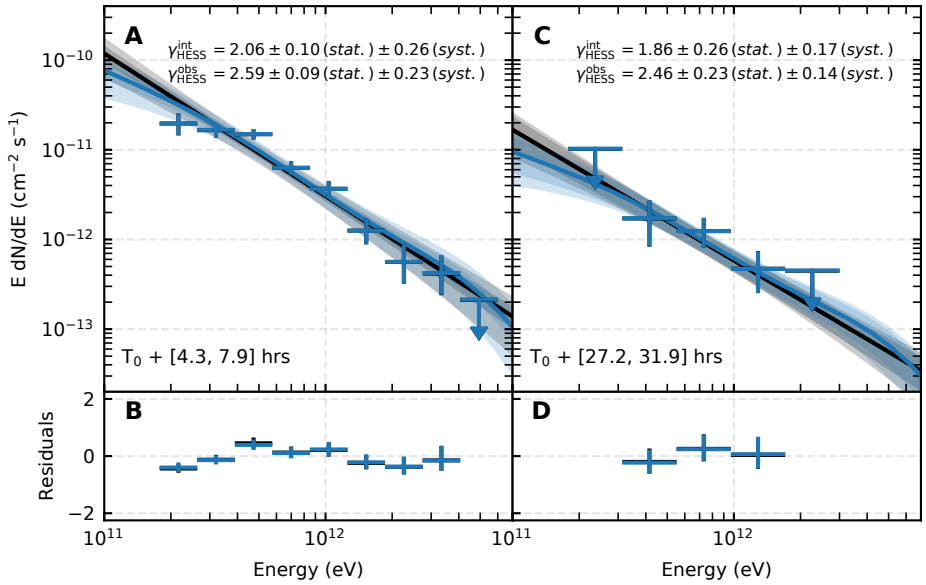

Fig. 5.9.: Spectra of the H.E.S.S. observation of GRB 190829. Panel A shows the spectral fits envelopes and flux points for the intrinsic (blue) and absorbed (black) spectrum for the first night of observation carried with H.E.S.S. The residuals computed as (data-model)/model are shown in panel B. In the same way, the results of the spectral fit and residuals for the second night of observation are shown in panel C and D.

Interval	Time after T_0 (s)	Energy Flux $\times 10^{-11}$ (erg cm^{-2} s^{-1})
Night 1, cluster 1	1.56×10^4 – 1.92×10^4	4.06 ± 0.65(stat.) ± 0.90(syst.)
Night 1, cluster 2	1.92×10^4 – 2.44×10^4	3.57 ± 0.42(stat.) ± 0.77(syst.)
Night 1, cluster 3	2.44×10^4 – 2.85×10^4	2.66 ± 0.39(stat.) ± 0.60(syst.)
Night 1	1.56×10^4 – 2.85×10^4	3.34 ± 0.28(stat.) ± 0.72(syst.)
Night 2	9.79×10^4 – 1.15×10^5	0.64 ± 0.14(stat.) ± 0.14(syst.)
Night 3	1.84×10^5 – 2.01×10^5	0.27 ± 0.13(stat.) ± 0.07(syst.)

Tab. 5.3.: Energy flux values of the H.E.S.S.-detected intrinsic VHE emission during the three consecutive nights. The photon index values are assumed to be constant with a value of 2.07 ± 0.09 as determined from the joint fit of nights 1 to 3. The energy flux level of the un-clustered Night 1 is not included in the determination of $\alpha_{\rm vhe}$ and is shown here as a reference.

corresponding to the value of the joint spectral fit from night 1 to 3 (see Tab. 5.2). The energy-flux values are summarised in Tab. 5.3.

The temporal decay evolution was fitted to a power-law model using a least-squares method and results in a temporal decay index $\alpha_{\rm vhe} = 1.09 \pm 0.05$ (Pearson's $\chi^2 = 0.31$, dof = 3).

5.2.2 Multi-wavelength Context

The H.E.S.S. energy flux evolution with the temporal decay fit is shown in Fig. 5.10 together with the detected emission with *Swift*-BAT (in the prompt phase), *Swift*-XRT (covering from 20 seconds to 11 days after T_0), and the upper-limits from the *Fermi*-LAT (see Abdalla et al., 2021 for the details on the multi-wavelength data extraction). To perform a similar estimation of the temporal decay of the detected *Swift*-XRT afterglow as in H.E.S.S., the energy-flux light curve was binned in the same time intervals defined in Tab. 5.3. The XRT temporal evolution was also fitted to the power-law model and results in a temporal decay index of $\alpha_{\rm xrt} = 1.07 \pm 0.09$ (Pearson's $\chi^2 = 2.63$, ndof = 2). This temporal decay is harder then the mean value of decay indices measured by *Swift*-XRT up to 57 hrs: $\bar{\alpha}_{\rm xrt} \sim 1.4$.

A spectral analysis of the *Swift*-XRT observations carried out during the same time period of the first and second nights of observations provide a photon-index value of $\gamma_{XRT} = 2.03 \pm 0.06$ (1st night) and $\gamma_{XRT} = 2.04 \pm 0.10$ (2nd

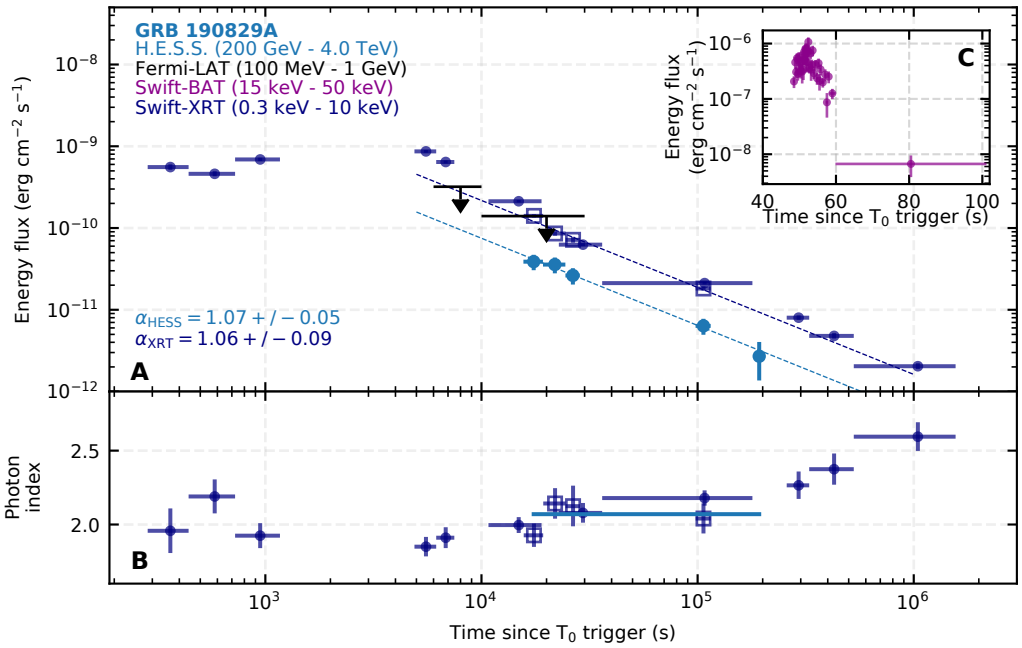

Fig. 5.10.: Multi-wavelength light curve of GRB 190829A. Panel A shows the temporal evolution of the energy flux detected by H.E.S.S. (light-blue), *Swift*-XRT with blue open squares corresponding to the same time intervals covered by H.E.S.S. and blue circles for the *Swift*-XRT detection up to 10^6 s after T_0. The *Fermi*-LAT upper limits are shown in black. Panel B shows the photon index evolution of the H.E.S.S. and *Swift*-XRT detection. Panel C shows the light curve of the prompt phase detected by *Swift*-BAT.

night). These values are very typical for GRBs measured by *Swift*-XRT (Ajello et al., 2018).

The isotropic energy of the prompt phase in the *Fermi*-GBM band (10 – 1000 keV) is $E^{\rm iso}_{\rm GBM} \approx 2 \times 10^{50}$ erg (Lesage et al., 2019). In the *Swift*-BAT energy range (15 – 150 keV) it is $E^{\rm iso}_{\rm BAT} \approx 1 \times 10^{50}$ erg with an uncertainty at the 10% level ($t < 60$ s). The isotropic energy integrated over the whole afterglow detected by *Swift*-XRT provides a value of $E^{\rm iso}_{\rm XRT} \approx 5 \times 10^{50}$ erg. This increased isotropic energy in the afterglow phase is an uncommon feature in GRBs, and is caused by the hard temporal decay index measured by *Swift*-XRT.

5.2.3 Discussion

The prompt emission of this GRB is well within the standard fluence values seen by the *Fermi*-GBM. However, its proximity makes it one of the brightest GRB afterglows detected by the *Swift*-XRT (see Fig. 5.1), which together with the hard temporal decay, might explain the detection by H.E.S.S. over an extended period of time.

The proximity of this GRB implies that intergalactic absorption of gamma-rays due to EBL does not contribute significantly to the uncertainty in the recovered spectrum. As discussed for the case of GRB 1807020B (see Sec. 5.1.3), the emission mechanisms responsible for the detected afterglow emission should correspond to the acceleration of electrons within the forward shock, with the detected gamma-ray emission coming from radiation via inverse Compton and/or synchrotron emission of the population of accelerated electrons.

The high statistical significance of the first two nights of observations with H.E.S.S., together with the small uncertainty in the gamma-gamma absorption due to the EBL, allowed to perform detailed multi-wavelength modelling of the emission (see Fig. 5.11, details can be found in the original publication: Abdalla et al., 2021). The results provide a Lorentz factor value for the emission region of $\Gamma = 4.7$ (first night) and $\Gamma = 2.6$ (second night). The modelling consisted of finding an electron distribution able to fit the emission seen in X-rays and VHE gamma-rays when considering a synchrotron and SSC radiation mechanism. Two cases were considered: first by imposing the theoretical constraint on the burn-off synchrotron limit and second, when allowing the electrons to radiate beyond this limit.

The results of the modelling when the limit is applied, predict a soft spectral index at VHEs incompatible with the H.E.S.S. detected emission. This is caused by the onset of the KN regime and a steep distribution of accelerated electrons (see blue curves of Fig. 5.11). The model involving the removal of the synchrotron energy-loss limit appears preferred, with a significance greater than 5. For this scenario, the synchrotron component spans over a broad energy range, covering from X-rays to VHE gamma-rays, with the SSC having 3 orders of magnitude lower contribution to the flux.

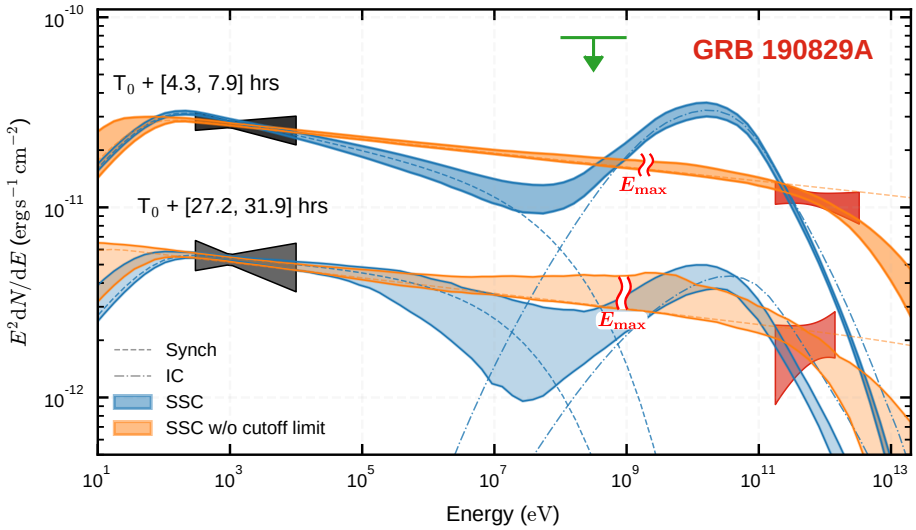

Fig. 5.11.: Multi-wavelength modelling of the GRB 190829A SED during the first two nights of observations. The red envelopes show the intrinsic emission detected by H.E.S.S. with statistical uncertainties for the first two nights of observations. The spectra with uncertainties detected by *Swift*-XRT are shown with the two envelope regions in black. The *Fermi*-LAT upper limits, coincident with the first night of observations with H.E.S.S., is shown with the green arrow. The blue and orange shaded areas show the 68% confidence intervals on the SSC model and the synchrotron model respectively. The synchrotron components of these models are indicated with dashed lines and the IC components with the double-dotted lines. For both nights, the burn-off synchrotron limit E_{max} is indicated.

The preference for the pure synchrotron mechanism would require the presence of an unknown process of high efficiency capable of taking the electrons up to PeV energies, or a scenario where a high difference in the magnetic field is present between the radiation and acceleration zone of the electrons.

Scenarios not explored, that could alleviate the discrepancy between the predicted soft photon index at VHE of the one-zone SSC scenario and the intrinsic index measured by H.E.S.S., are either a high bulk Lorenz factor or a non-power law distribution of emitting electrons. In the first case, if Γ was increased up to several hundred, the KN cut-off would be reduced, translating into a hardening of the VHE photon index and an increased flux level. However, the values of the Lorentz factor expected, and especially for the second night of observations, seem to contradict this possibility. The second case requires a hard component in the electron energy distribution at high energies, requiring extreme assumptions on the properties of the circumburst medium.

5.3 Conclusions and Outlook

In this chapter, the detection of two GRBs at VHE has been presented. The first, GRB 180720B, marked a historical benchmark, being the first detection at VHEs after decades of search. Its VHE emission is somehow expected but not at such high delays: it is the second brightest afterglow detected by *Swift*-XRT and was also detected by *Fermi*-LAT. Apart from the extreme energy release, this GRB shows rather ordinary characteristics. Its temporal decay and photon index in the X-ray band fall well within the mean values of population of long GRBs measured by *Swift*-XRT. The same applies when considering the characteristics revealed by the *Fermi*-LAT detection. After correcting for the EBL absorption, the H.E.S.S observations resulted in a hard spectrum at 10 hrs after the burst's onset. This result was placed in context with the multi-wavelength data. The synchrotron and SSC scenario of electrons accelerated in the forward shock of the GRB, were identified as the most plausible scenario to describe the multi-wavelength data. Challenges placed for both scenarios were discussed concerning the required Lorentz

factors, energetic requirements for the electrons, and their acceleration site.

The second GRB discussed in this chapter was GRB 190829A. It is a very nearby GRB with a very bright X-ray emission. Its proximity secured the detection with H.E.S.S. over three consecutive nights. The spectral index during these observations remains stable. The temporal decay and photon index are similar to data obtained by *Swift*-XRT in the same period. The bright emission detected by H.E.S.S. and small redshift allowed an accurate spectrum determination for the first two nights. The multi-wavelength modelling, with the synchrotron and SSC scenarios being tested, resulted in a significant preference for a pure synchrotron mechanism going from X-rays up to VHEs. Limitations to this scenario and possible ways in which the SSC could still operate were discussed.

Although GRBs have been the target of several observational efforts and intense multi-wavelength campaigns, the successful observations of GRBs at VHEs in the last years have revealed a lack of understanding of the processes operating in their environments. With these detections, it is being shown that current IACTs can detect the brightest and/or nearest GRBs.

As has been shown in Ch. 4.1.1, current and future VHE observatories will profit from these detections to optimise their observation criteria. As illustrated in Fig. 5.12, the GRBs detected so far lay on the two ends of the Amati relation (Eq. 2.1), indicating that very energetic or very nearby GRBs are good candidates for detecting VHE gamma-ray emission. Strikingly, their characteristics regarding spectral shape and temporal evolution in the multi-wavelength context appear rather standard. It is still an open question whether the environments in which these GRBs are generated play an important role or VHE emission is a universal feature, with detections being limited by current instrumental sensitivity. All these detections correspond to the class of long GRBs and this could be caused by their higher fluxes throughout the prompt and afterglow phase compared to short GRBs. This might indicate that short GRBs pose a bigger challenge for the observation of VHE emission. With the fourth generation of VHE observatories such as CTA, LHAASO, and SWGO, expecting to achieve an order of magnitude better sensitivity than current instruments, it is anticipated that the detection of many more GRBs, covering and testing a bigger parameter space, will become possible

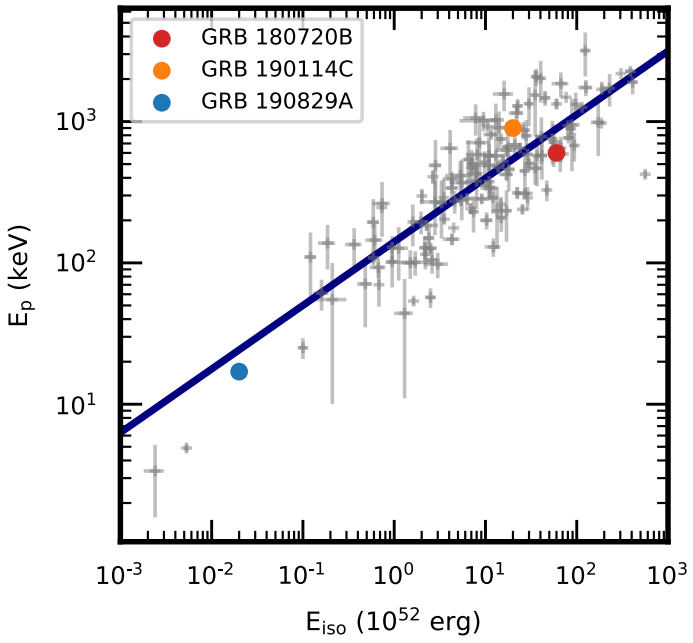

Fig. 5.12.: The GRBs detected at VHEs in the Amati relation. The location in the Amati relation for GRB 180720B, GRB 1901114C and GRB 190829A. The values of the grey data points correspond to a set of GRBs detected by INTEGRAL, Konus, *Swift* and *Fermi* taken from Tab. 1 of Y.-P. Qin et al., 2013.

6

Improving the HAWC Detector Model

Contents

A proper simulation of the HAWC detector is imperative to properly verify the energy, direction and time reconstruction algorithms of the atmospheric shower, as well as assess systematic uncertainties related to these variables. This can be achieved by simulating accurately the time and charge distributions of the detected showers in each WCD.

This chapter is aimed at improving the HAWC simulation chain by implementing a PMT-per-PMT efficiency in DAQSim (see Ch.3.1.7) and a method to simulate waveforms. In Sec. 6.1, the method for selecting muons in the HAWC data is presented. Using this method, a calibration of the efficiency of each PMT is performed and applied in the HAWC simulation chain. The implementation of this accurate efficiency measurement provides a better agreement between the real and simulated data and the possibility of accounting for the changes in the PMT efficiency with time. In Sec. 6.2, the development and results of a method to simulate analog pulses from the

PMTs are presented. This approach is meant to allow the comparison of the simulation and real data at the level of the electronics output since the current HAWC simulation chain simply does not simulate this step. To this end, a pulse shape is inferred from the calibration curves employed in the data. This is then convoluted with the single photoelectron traces produced during simulation and a TOT obtained. Sec. 6.3, concludes the chapter with an overview of future work towards a more accurate simulation of the HAWC detector.

6.1 PMT Efficiency with Muons

As discussed in Ch. 3.1.7, the PMT efficiency and acceptance can be calibrated with data by fine-tuning the charge and timing of events to match the muon and 1 PE peak distributions. The PMT photo-electron efficiency, which will be hereafter referred to as PMT efficiency, can depend on the PMT ageing, water quality, or transparency of the photo-cathode. A decrease in efficiency is expected if organic material is deposited on the PMT surface, because of damage to the PMT pulse-amplification electronics, or due to degradation in the water quality of the WCDs. Previously, the PMT efficiency was simulated by randomly sampling values from the efficiency distribution measured in the data of a specific epoch. This makes the simulated detector match the real one, but not at the level of individual PMTs. A different random seed in the simulation provides a different HAWC-like detector but no PMT-to-PMT matching.

In this section, we extend this approach by measuring the muon peak in data and simulation for each PMT to obtain the efficiency. The DAQSim code was modified to use these values. The updated code can simulate in a more precise way the individual PMT response. The PMT efficiency was measured for several epochs of the HAWC detector, to characterise the evolution of the efficiency with time.

6.1.1 Muons as a Calibration Light-Source

At the HAWC altitude, muons are minimum ionising particles with a mean energy of few GeV (Schoorlemmer et al., 2019). The ionisation energy loss in water is about 2.5 MeV per g/cm^2, and for a HAWC WCD, with 4.5 m height, muons reach the bottom of the tank losing only 2.1 GeV of energy. Assuming that their speed remains constant, a vertical muon reaches the bottom of the tank in 15 ns[1].

A muon emits ≈ 320 photons/cm (for $\lambda = 300 - 580$ nm) in the Cherenkov cone in water. Considering a vertical muon entering a WCD and impacting the central PMT, adding the geometry and area of each peripheral PMT, and considering the water absorption, this translates into a detection of ~ 12 photons/PMT in PMTs A, B and D with a time-delay of ~ 5.4 ns with respect to the C-PMT, which is expected to see several hundred of photons. By the same argument, a muon impacting a peripheral PMT will produce light in the C-PMT with a similar delay (Wood, 2015).

6.1.2 Selection of Muons in Data and Simulation

Before applying the considerations discussed in the previous section, muons are selected in data and a corresponding simulation is performed:

Data selection Muon-candidate events are selected directly from the calibrated data. The selection algorithms consist of a search for events in individual tanks that activated the four PMTs. This guarantees the selection of bright events and is motivated by the known high-light yield of muons entering the WCDs. Only those events where no other PMT within a radius of 20 meters was activated during the triggered event are considered. This ensures the selection of isolated muons rather than very bright showers, which might also trigger the four PMTs in one single tank.

[1] The energy loss due to Cherenkov radiation of these muons in water is ~ 1.36 keV per g/cm^2, which is three orders of magnitude lower than the ionisation loss.

Simulation Muons with an energy of 5 GeV are generated in GEANT4 and shot from a disk of 10 m diameter placed at 5 m above ground, arriving at a zenith angle distribution $\theta = \arctan(R/5\,\mathrm{m})$ that matches the distribution seen in data (the flux of muons rapidly decreases with zenith). The size of the ring ensures that muons arrive at as much as 63° in zenith, a range sufficient to match the rate seen in data. GEANT4 simulates the propagation of these muons in the WCD units, along with the production of Cherenkov light, until they reach the PMT surface, and DAQSim performs the smearing of charge and time to mimic the DAQ and calibration.

Taking into account the expected time for a muon to travel inside a HAWC WCD and the number of PEs to be detected, as discussed in the previous section, a set of cuts for time and charge in each PMT hit is sufficient to select the so-called muon peak (Tab 6.1). Since these cuts are defined based on the geometrical arrangement of all four PMTs, it is required that a given WCD has the four PMTs functional. The first set of cuts are defined to select muons striking the peripheral PMTs and are used to obtain the muon peak in the C-PMT, by requiring that the three peripheral PMTs detect more than 150 PEs with a time delay relative to the C-PMT of 20 ns. The second set of cuts allows to obtain the muon peak for peripheral PMTs by imposing the C-PMT to detect more than 200 PEs with a relative time delay to the peripheral ones of 15 ns. In both cases, the time delay of 5.4 ns, described previously, is relaxed to allow the selection of muons with a non-zero angle of incidence. The third set of cuts restricts the mean charge of the peripheral PMTs and serves as a high-resolution timing selection cut.

A-, B-, D-striking PMTs	C-striking PMT	C-striking (Timing)
$q_A > 150\,\mathrm{PE}$ or $q_B > 150\,\mathrm{PE}$ or $q_D > 150\,\mathrm{PE}$ and $\lvert t_C - t_A\rvert < 20\,\mathrm{ns}$ and $\lvert t_C - t_B\rvert < 20\,\mathrm{ns}$ and $\lvert t_C - t_D\rvert < 20\,\mathrm{ns}$	$q_C > 200\,\mathrm{PE}$ and $\lvert t_A - t_B\rvert < 15\,\mathrm{ns}$ and $\lvert t_A - t_D\rvert < 15\,\mathrm{ns}$ and $\lvert t_B - t_D\rvert < 15\,\mathrm{ns}$	$q_C > 200\,\mathrm{PE}$ and $\lvert t_A - t_B\rvert < 15\,\mathrm{ns}$ and $\lvert t_A - t_D\rvert < 15\,\mathrm{ns}$ and $\lvert t_B - t_D\rvert < 15\,\mathrm{ns}$ and $\frac{q_A+q_B+q_D}{3} < 20\,\mathrm{PE}$

Tab. 6.1.: Summary table of cuts for the muon hits selection This table summarises the cuts used to determine if a muon strikes the A, B or D PMTs in the first column, the C PMT in the second column. The third column lists the strict cuts for C-striking PMTs used to perform timing studies.

6.1.3 Implementation of the Method and Results

To correct the efficiency in MC using the muon peak information, the DAQSim parameters that simulate the efficiency were deactivated, and a set of simulated muons without PMT efficiency was generated as described in the previous section. The efficiency correction that should be applied for each PMT is given by the ratio between the muon peak position in data (μ) and the one in MC (μ_{mc}).

The first two sets of selection cuts in Tab. 6.1 were applied to the data and MC. A Gaussian function was fit to the muon-peak distribution of each PMT to measure μ and μ_{mc} and the efficiency was computed.

The algorithm to implement the efficiency consists of discarding PEs at a rate dictated by the obtained efficiency value. For example, considering a PMT with an efficiency of 80% that recorded 45 PE, $\sim$9 PEs are randomly discarded. The acceptance model (see Ch.3.1.7) is then applied to the resulting set of PE. These two steps constitute the full simulation of the PMT response.

Fig. 6.1 shows the location of the muon peak obtained for tank 52. The grey curve corresponds to the simulations when the PMT efficiency is not applied. The muon peak shifts to higher values since PMTs collecting more light are being simulated. The resulting muon peak location after accounting for the measured efficiency matches within statistical uncertainties the location measured in data for all four PMTs.

Panel A of Fig. 6.2 shows the measured efficiency for the 1200 PMT channels of HAWC. Panel B shows the efficiency distribution of A, B, C and D PMTs. In the GEANT4 step of the simulation, several photons are not propagated through the water to speed up the computation, since it is known that the efficiency specified by the PMT producer will be subsequently applied. The efficiency obtained with this method constitutes an additional correction to the one provided by the PMT producer. Efficiencies higher than 100% in Fig. 6.2 (roughly 3% of the total number of PMTs) indicate that in some cases the GEANT4 step of the simulation is not allowing enough photons to reach the PMT surface. Since there is no way to re-scale these simulations in a later

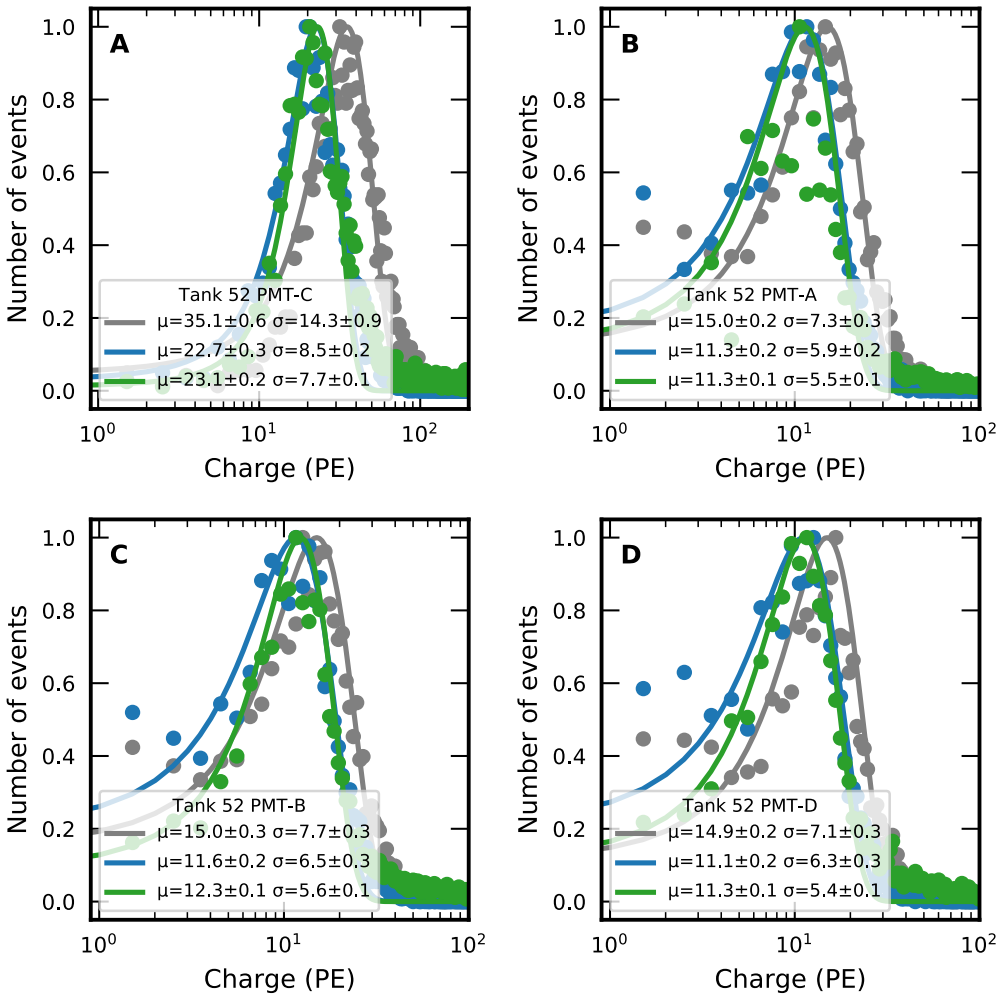

Fig. 6.1.: Muon peak locations in tank 52. Panel A shows the muon-peak location for the PMT-C of tank 52. In panel B, C and D the muon peak location is shown for the peripheral PMTs indicated in the legend. For visualisation purposes, the distributions are scaled such that the peak height corresponds to a value of 1. The grey points and curves correspond to the muon peak location in DAQSim without PMT efficiency implemented. Blue corresponds to the distribution when the efficiency is applied using the method presented here. These distributions are compared with the muon peak location in the data shown in green. The mean and sigma values of a gaussian fit to the peak are indicated in the legend of each panel.

step, inevitably the simulation for these PMTs will underestimate the light-collection in real data. This can be easily fixed by allowing more photons to reach the PMT surface in the simulation or increasing the PMT efficiency in GEANT4. However, this requires to re-run the GEANT4 simulation step, which is beyond the scope of this work.

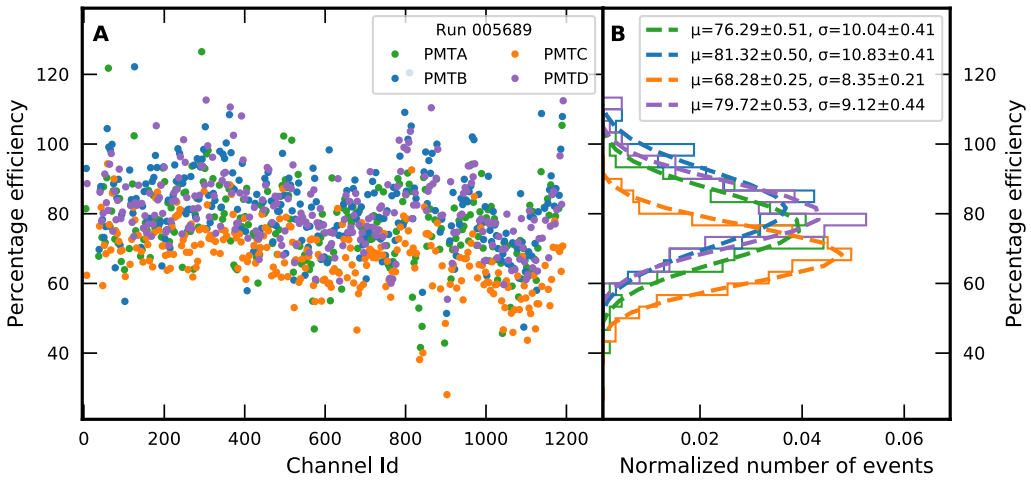

Fig. 6.2.: PMT per PMT efficiency for run 5689 Panel A shows the measured PMT efficiency for each of the 1200 channels in HAWC. The green, blue and purple data points correspond to the A, B, and D PMTs and the efficiency for the C-PMT is shown in orange. In panel B, the distribution of the efficiency values for each PMT type is shown together with a gaussian fit with parameters reported in the figure legend.

This analysis was performed for different epochs of the detector to account for degradation of the PMT efficiency. Data were selected for different calibration epochs and the PMT efficiency was measured. Fig. 6.3 shows the evolution of the width and mean value of the muon peak location for PMT A, B, D and C as a function of time. A linear model was fit to these data to identify a possible trend of efficiency degradation. No global evolution of the efficiency is seen with time, except for a marginal hint of degradation in the PMT-C efficiency. With this test, the degradation of individual PMTs cannot be ruled out and will be addressed in future investigations.

In addition to monitoring the PMT efficiency with time, this study can be used to assess systematic uncertainties when measuring source spectra. In the standard method of HAWC, the PMT efficiency of a specific epoch is used for the generation of baseline instrument-response functions, while the

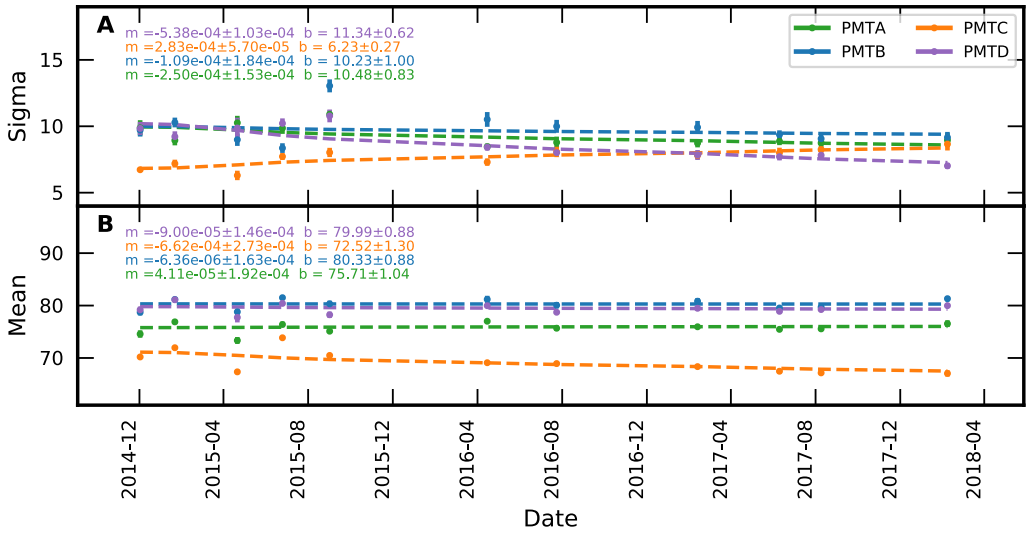

Fig. 6.3.: Temporal evolution of the efficiency parameter. The PMT efficiency is shown as a function of time. Each data point corresponds to a measurement done in between two calibration epochs. The sigma and mean values shown in panel A and B are obtained with a Gaussian fit as shown in Fig. 6.2. The dashed lines show a linear fit to the sigma and mean values. The values of the slope m and b (the y-intercept) are indicated in the figure.

data is, in most cases, integrated over the whole time of HAWC operations (currently close to 5 years). The use of a single PMT-efficiency epoch can under/over-estimate the light-yield of the detected showers, which impacts directly the estimation of the energy of the showers and the effective area of the detector.

6.2 Waveform Simulation

In the standard HAWC simulation (HAWCsim and DAQSim), the time-over-threshold is not simulated. A simulation of the electronics in HAWC was implemented but never adopted in the standard chain. This simulation was based on laboratory measurements of the PMT gain, dark current, rise/fall time of the pulses, the transformation of the pulses through cables (cable length, impedance, capacitance, attenuation etc.) and the front-end-boards (FEB) characteristics. The simulation resulted in a slow and computationally

intensive task, making it hard to replicate the experimental data due to the large number of parameters.

In DAQSim, the time stamp of each PMT hit is obtained from the arrival time of the first photon impacting the photon cathode. The fact that this time is different at the PMT output or that the first photon might not suffice to reach the first threshold is not considered. Moreover, the number of PE in DAQSim is simply a smeared sum of the number of PEs obtained from HAWCSim. In real data, the effect of the time spread of the arrival of the PEs can increase the TOT duration, making the charge calibration a rather complex procedure. A TOT value does not have a unique correspondence to a charge: for example, two small hits separated in time can cause a large TOT; this is also the reason why two thresholds are used in the DAQ system of HAWC (see Sec. 3.1.2). The simulation chain of HAWC should be able to replicate the ambiguities and the effects of the analog-to-digital processing of the signal and of the TOT-to-charge conversion, with the derivation of timing and charge proceeding identically as for data. This section presents WaveSim, a method that simulates TOTs and therefore addresses these problems. A waveform for each PMT is generated (explained in Sec. 6.2.1) using the timing and charge calibrations curves that are applied to data. These are then convolved with the time of arrival of each simulated PE hitting the PMTs to obtain a simulated waveform. The TOT technique can be applied to these pulses to obtain simulated data in the same format as real data.

6.2.1 Single PE Pulse Shape Reconstruction

A pulse shape was inferred from the charge calibration curves, measured with the laser system of HAWC (see Ch. 3.1.3), by relating a voltage level to its corresponding TOT duration. When employing the charge calibration curves, it is worth noting that the inferred pulse is expected to have a different shape when using one or the other of the two calibration curves, since two different gains of amplification are used in the electronics. For this study, the HiTOT calibration curve was used to derive the pulse shape.

As illustrated in Fig. 6.4, the method consist of sampling the TOT duration from the charge calibration curve and setting this as a pulse width at the

equivalent charge level. Using the slewing calibration curves, the width is then displaced by the slewing time corresponding to the TOT sampled.

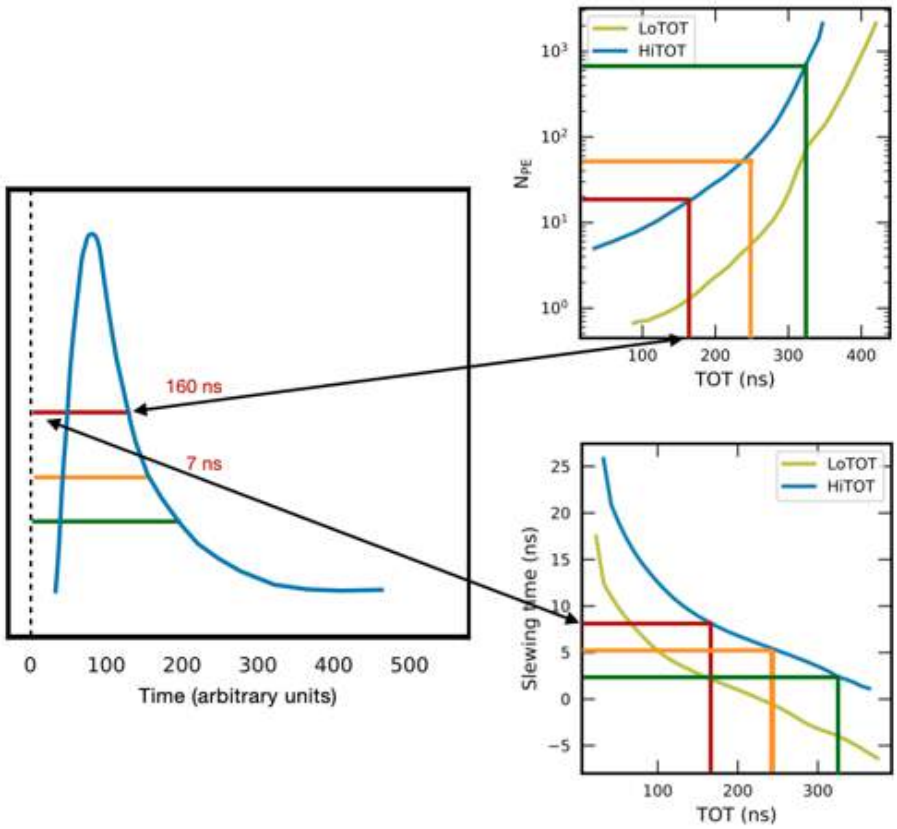

Fig. 6.4.: Illustration of the procedure to obtain a pulse shape. The upper-right panel shows an example of a charge calibration curve. Values of TOT are sampled from the HiTOT curve and placed at a corresponding pulse height for the pulse reconstruction as shown in the left panel. The time of each pulse level is displaced with the slewing time, as shown in the lower-right panel of the figure.

The calibration curves do not cover the whole interval of TOT duration that is required to reconstruct the pulse shape. The blue points in Fig. 6.6 show the segment of a pulse that corresponds to the values inferred from the calibration curves. In the initial segment of the pulse, a linear extrapolation is used to remove the out layers depicted in panel A of Fig. 6.5, where a sudden drop of the curves is seen. This is completed with the use of an exponential cutoff for the final segment of the pulse as shown in cyan in Fig. 6.6. The pulse shape considered for WaveSim is obtained by combining these segments and performing a quadratic spline interpolation as shown in green colour. In the same figure, some examples of different pulse shapes generated with

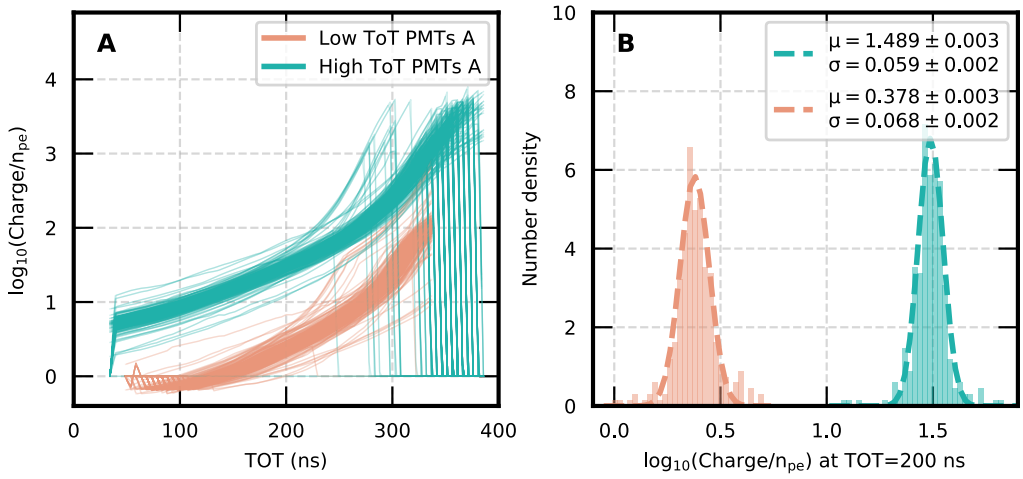

Fig. 6.5.: Charge calibration curves. Panel A shows the calibration curves of all A-PMTs in the calibration run 5213. Panel B shows the distribution of the number of photoelectrons that correspond to a TOT duration of 200 ns.

this method are shown. One pulse shape was reconstructed for each PMT to reflect the differences seen in the calibration curves (Fig. 6.5).

For the construction of these pulse shapes, a binning in time of 0.09765 ns was used, corresponding to the time resolution of the time-to-digital (TDC) converter of HAWC[2]. The conversion of the N_{PE} units of the calibration curves to a voltage was done by finding a scaling factor that made the pulse width at the FEB low threshold (set at 7.1 mV) correspond to the LoTOT duration of 1 PE.

To verify the procedure, charge calibration curves were inferred from the pulse shapes by applying a convolution with an impulse of various amplitudes covering the charge range of the laser calibration curves. The duration at the LoTOT and HiTOT was measured, as the time that the pulse spent above 7.1 mV and 113.5 mV respectively, corresponding to the thresholds set in the FEBs. An example of the resulting calibration curves is shown in panel A of Fig. 6.7 compared to the corresponding curve from the laser system. In panel B the distribution for the 1200 PMTs of the charge ratio at 200 ns between the calibration curves from the laser system and the simulated pulses is shown. On average an (over)underestimation of 10% is seen for the (Lo)HiTOT. This discrepancy is attributed to the fact that only the HiTOT

[2] 1 TDC count represents 25/256 = 0.09765 ns.

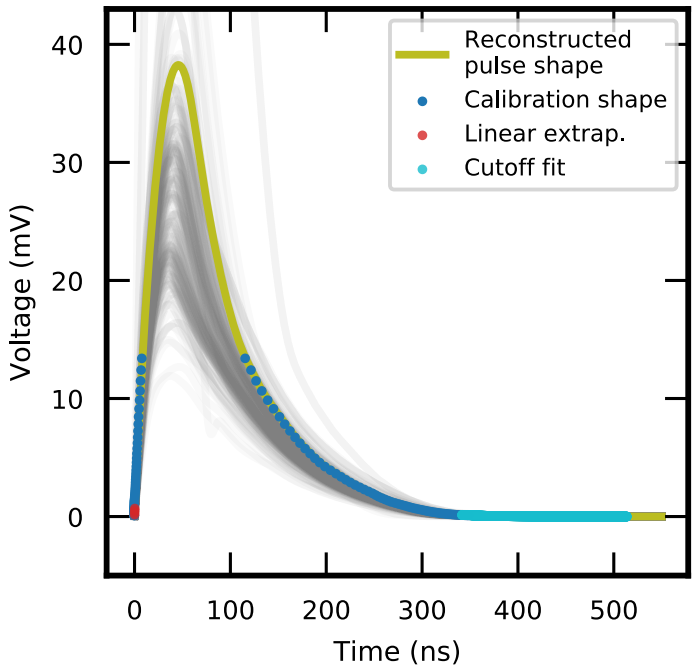

Fig. 6.6.: Examples of reconstructed pulses. The green shows the reconstructed pulse shape of a specific PMT. The segments inferred from the calibration curves, linear extrapolation and a cutoff fit are shown in dark-blue, red and light blue respectively. The grey lines show examples of other reconstructed pulses.

charge curves are used for inferring the pulse shape and the scaling factor to mV is obtained from the point in the LoTOT curve of 1 PE. This does not represent a limitation to the procedure, since the effect of this discrepancy can be corrected by employing these reconstructed curves for the calibration of the simulated data.

6.2.2 Trace and TOT Simulation

The HAWC simulated data was employed to generate signal traces. The *HAWCsim* package provides the time of arrival of individual PEs to each PMT from the simulated showers. For each PMT, the acceptance model (see Ch. 3.1.7) and the PMT efficiency (obtained as described in Sec. 6.1) was applied to include the simulation of the PMT response. To simulate the time jitter, the arrival-time of the PEs was spread by sampling random values

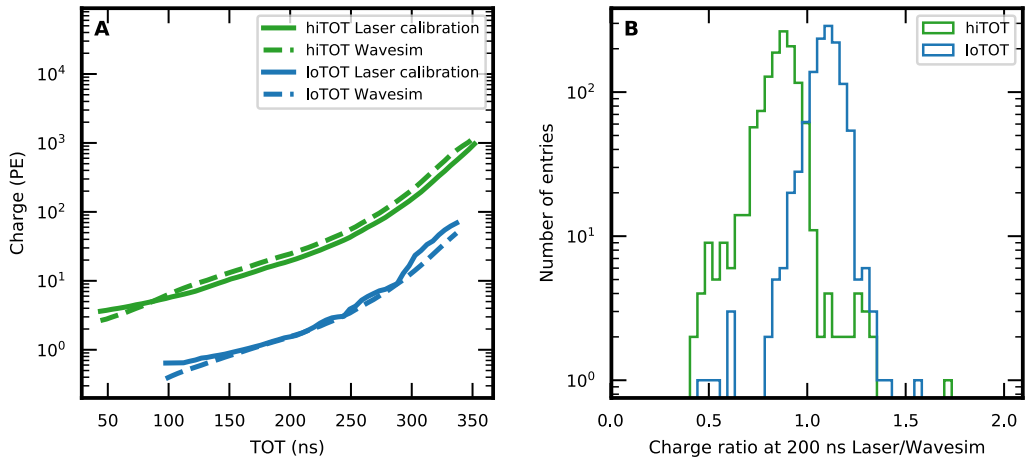

Fig. 6.7.: Comparison of charge calibration curves from the laser system and the inferred pulse-shapes. Panel A shows an example of a calibration curve inferred from the WaveSim pulse shapes compared to the corresponding calibration curves used for the pulse reconstruction (from the laser calibration). Panel B shows the distribution for the 1200 PMTs of the calibrated charge ratio between the WaveSim and Laser system for a Lo/HiTOT duration of 200 ns.

from a gaussian distribution with a width of 1.02 ns and 1.44 ns for the A, B, D-PMTs and C-PMTs, respectively. These are the values reported for the transit time spread of the PMTs by the manufacturer (*Large Photo Cathode Area PMTs* 2019). The resulting time of each PE was used to construct a trace consisting of single impulses with the corresponding PE amplitude after the PMT acceptance was applied. The convolution with the pulse shape was applied to this trace to obtain the analog signal. The digital output is obtained by constructing a rectangular pulse with the Lo and HiTOT duration. A logical OR is applied to the HiTOT duration and combined with the LoTOT rectangular pulse, equivalent to the procedure done by the DAQ system in real data. An example of the resulting traces is shown in Fig. 6.8, with the low and high thresholds for the TOT indicated by the dashed horizontal lines. Panel B of this figure shows the logical pulses obtained when applying the TOT.

To compare this implementation with DAQSim, showers with a proton as a primary particle with an energy of 10 TeV were simulated with DAQSim and with the method presented here. The charge calibration was applied to the triggered data obtained from WaveSim (DAQSim provides directly the

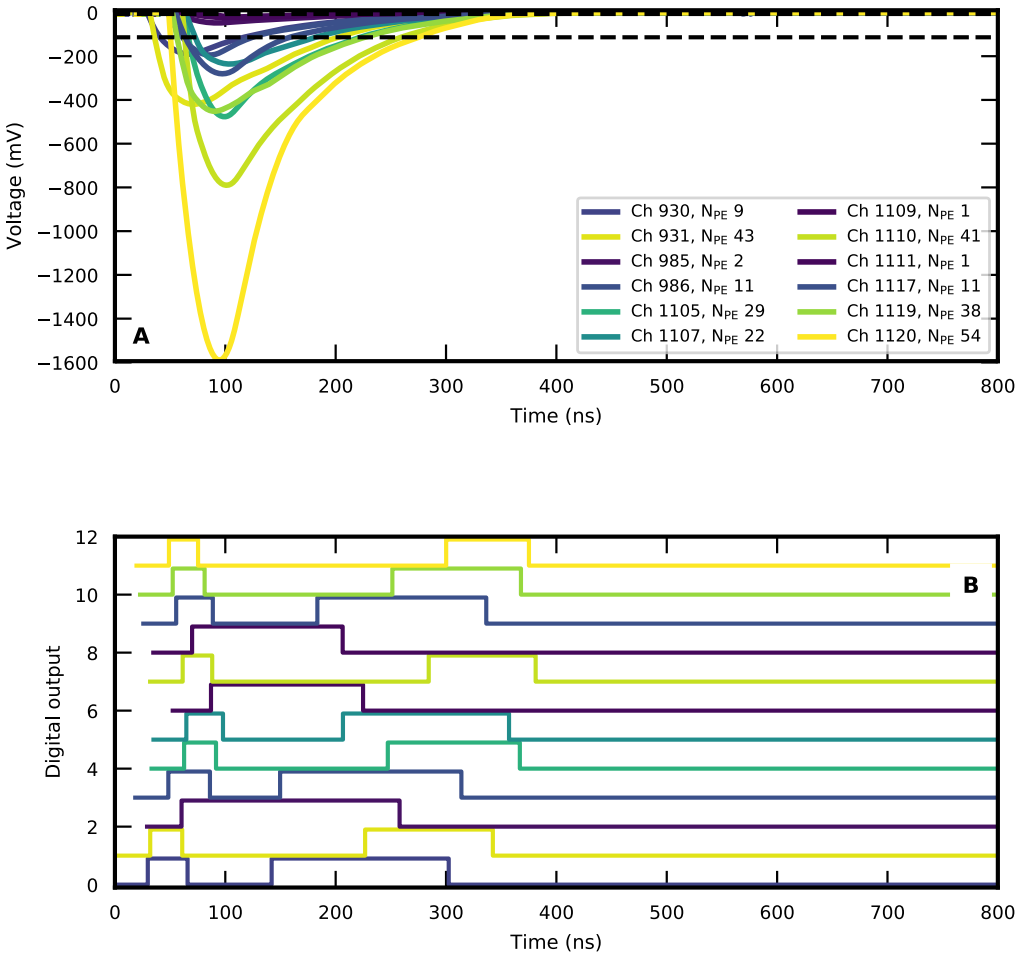

Fig. 6.8.: Examples of waveform simulations and edges Panel A shows some examples of waveforms obtained from a simulated shower. The dashed lines show the trigger level for the TOT measurement set at 7.1 mV and 113.5 mV. The figure label indicates the channel id and number of PEs impacting the photocathode. In panel B the corresponding digital pulse is shown.

simulated charge). In Fig. 6.9, the calibrated charge for each PMT is plotted against the number of PE received at the photo-cathode. It can be seen that DAQSim performs better in the region of low number of PEs (N_{PE}), where WaveSim considerably overestimates the charge, while in the region above $\sim$10 PE, less spread in the estimated charge is seen with WaveSim. At the moment, the origin of the discrepancy at low charge is unknown and future explorations are required to understand this behaviour. It is important to note that the HAWCSim estimated N_{PE} in Fig. 6.9 does not include the PMT response (acceptance and efficiency). The incorporation of this will spread and displace the N_{PE} values. However, the comparison remains valid, since the same PMT acceptance model is applied for DAQSim and WaveSim.

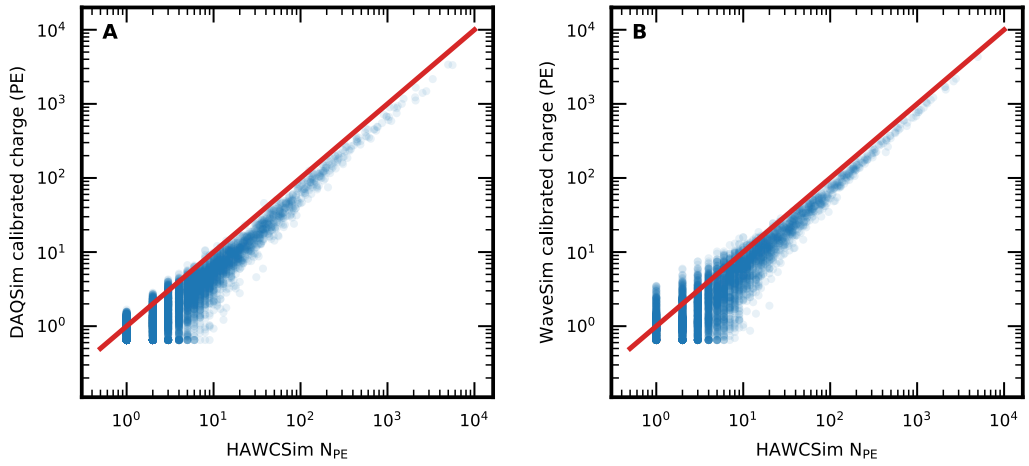

Fig. 6.9.: Calibrated charge for simulations as a function of number of PE in HAWCSim. The blue points show the calibrated charge for DAQSim (panel A) and WaveSim (panel B) as a function of the number of incident photons to the photo-cathode obtained from HAWCSim. The red line shows a one-to-one correspondence.

6.2.3 Data-MC Comparison

A set of proton showers with an energy spectrum of the form $E^{-2.5}$ were simulated using HAWCSim and WaveSim. The standard multiplicity trigger of HAWC is applied to these data. This trigger consists of storing the data from -500 ns to 1000 ns if at least 28 hits are found in a window of 150 ns. The simulated data contain the TOT duration and time stamps of the edges

for each PMT that was activated during the simulated shower, identical to the parameters stored in real data.

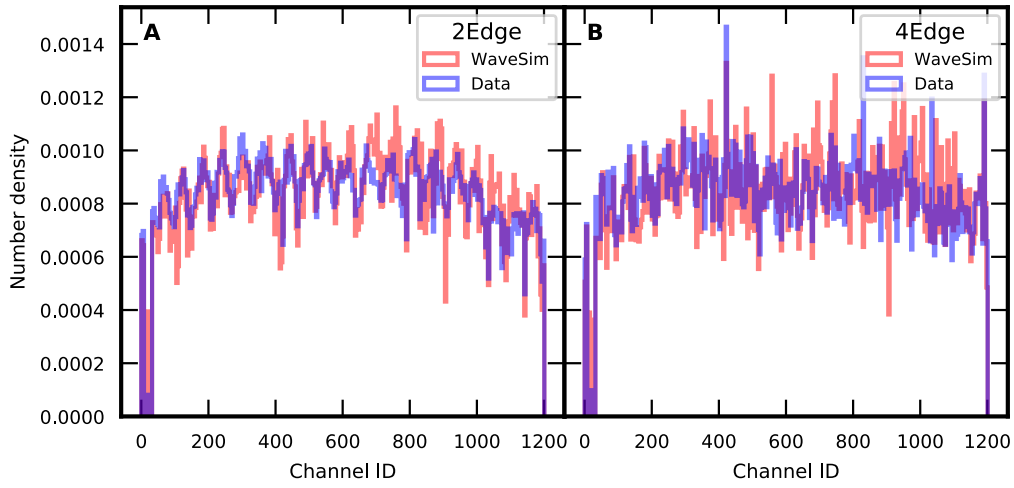

Fig. 6.10.: Participation fraction for simulated showers with WaveSim and data. The participation fraction between data (blue) and WaveSim (red) is shown for 2Edge and 4Edge hits in panel A and B respectively. The data is plotted in 300 bins to group each PMT participation with its corresponding tank. A total of 5×10^5 showers were used to obtain each distribution.

The parameters obtained from the simulation of showers with WaveSim were compared to real data. All distributions obtained from WaveSim are weighted with a factor $E^{-0.2}$ to recover the cosmic-ray spectrum, which dominates the energy distribution seen in data $\sim E^{-2.7}$. The obtained parameters can be separated as 2Edge hits (if only the low threshold is crossed) and 4Edge hits (when also the second threshold is crossed). Fig. 6.10 compares the 2Edge and 4Edge participation fraction. WaveSim is capable of reproducing the overall structure seen in the participation fraction, with a slightly bigger spread probably attributable to the lack of noise simulation, together with the possible mis-reconstruction of the waveforms for some channels that can result in lower/higher rates than required.

In Fig. 6.11 the distributions of TOT values for data and WaveSim are shown. Some of these distributions show a good agreement between data and WaveSim, especially the LoTOT durations. The distribution of the time_{01}, which measures the time that the pulse takes to go from the first to the second threshold, shows a significant discrepancy. It is suspected

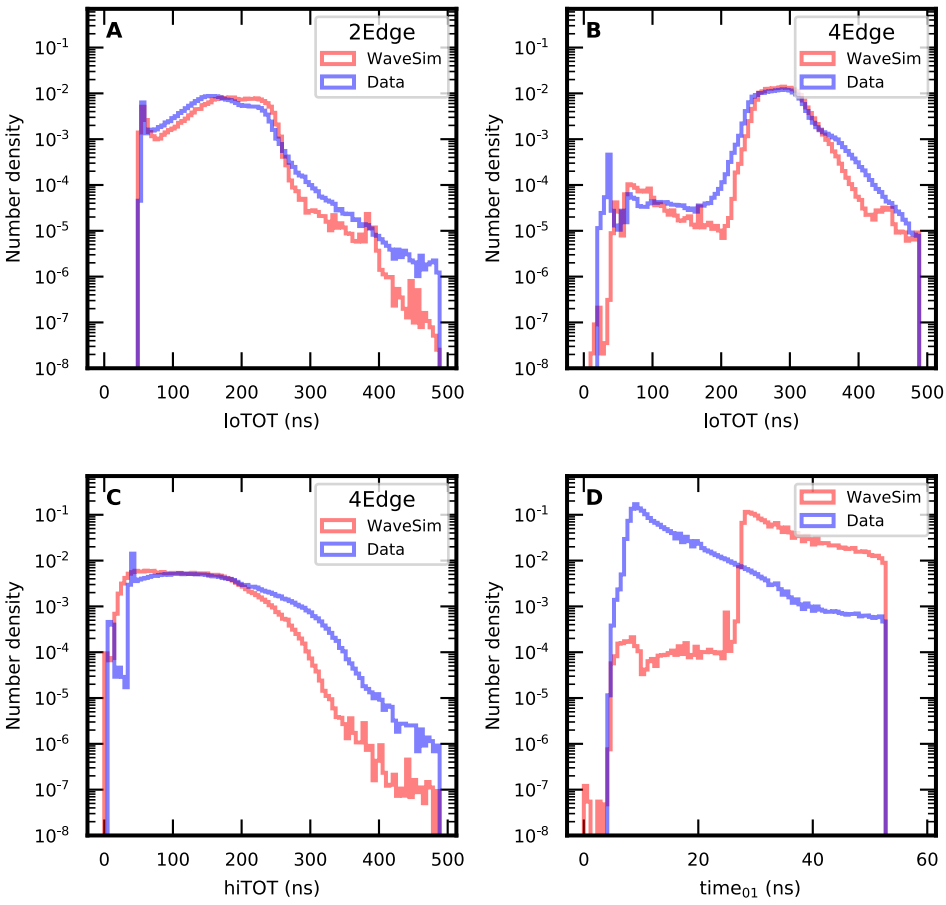

Fig. 6.11.: Triggered parameters for simulated showers with WaveSim and data Panel A shows the distribution of LoTOT durations for 2Edge hits for data in blue and WaveSim in red. In panel B the distributions of LoTOT duration for 4Edge hits are shown. Panel C shows the distributions of HiTOT durations and panel D shows the parameter time$_{01}$ explained in the text. A total of 5×10^5 showers were used to obtain each distribution.

that this discrepancy arises from an artificial shift applied in the traces from real data to guarantee the proper identification of edges. The step in the procedure that applies this shift needs to be identified and removed from the simulation chain. It is expected that this discrepancy will impact events of high amplitude, where pulses rise faster and have lower values of time_{01}. The discrepancies seen in the HiTOT distribution correspond to the region of pulses with long HiTOT values, where the convolution of individual peaks is not able to widen enough the pulse. Moreover, in these regions, the shape of the pulse might be modified by the onset of saturation effects and such behaviour is not being simulated.

Showers simulated with WaveSim and real data were reconstructed using the standard reconstruction chain of HAWC. Showers were also simulated with DAQSim with the standard simulation parameters. During reconstruction, the TOT measurements are converted to a calibrated charge. The calibration curves obtained from the pulse shape analysis were used to calibrate the WaveSim events.

In Fig. 6.12 the comparison of the distribution of calibrated time and charge of individual PMT hits is shown. In either DAQSim or WaveSim, the time distribution of the events does not seem to replicate the data accurately, except for the region closer to the trigger time. In the case of WaveSim, this can be attributed to a lack of simulation of noise hits, which would increase the rate of late and early hits. The calibrated charge, however, shows a relatively good agreement. Discrepancies in WaveSim are significant for high values of the charge, attributable to the discrepancy seen in the HiTOT distribution compared to data (panel C of Fig. 6.11).

Fig. 6.13 compares the distributions of the reconstructed zenith and azimuth angle and the reconstructed core location of the showers. Although some of the TOT and timing distributions from WaveSim present discrepancies, these do not seem to impact the distribution of the reconstructed arrival location and direction of the showers. In the case of the zenith and azimuth distributions, this occurs since the timing of the events is well matched in the region where they contribute to the fit of the direction (See panel A of Fig. 6.12). The core location is also reconstructed accurately since the reconstructed charge of the PMTs hits, used for fitting the core location, shows an underestimation that would simply scale the overall simulated charge

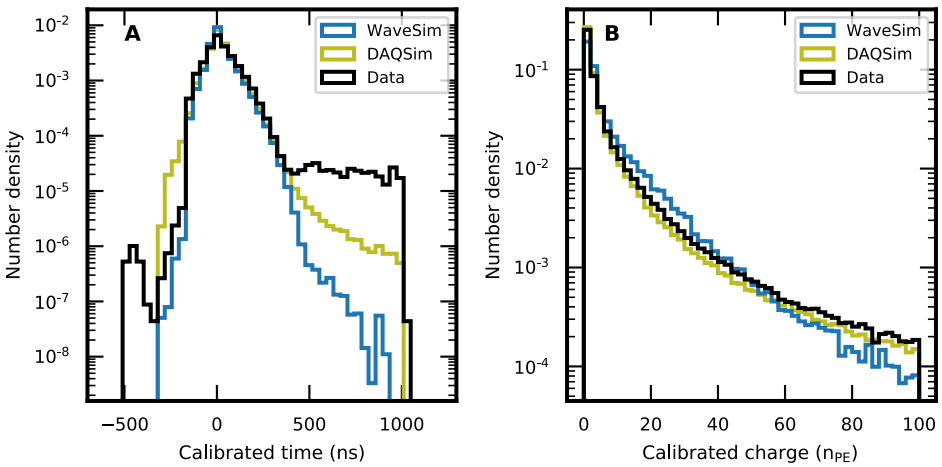

Fig. 6.12.: Comparisons of the distribution of calibrated charge and time. Panel A shows the distribution of calibrated time. Panel B shows the distribution of calibrated charge. In both panels, these distributions are drawn for WaveSim in blue, DAQSim in green and data in black.

of the shower (See panel B of Fig. 6.12). The resulting good agreement motivates further analysis and development for WaveSim.

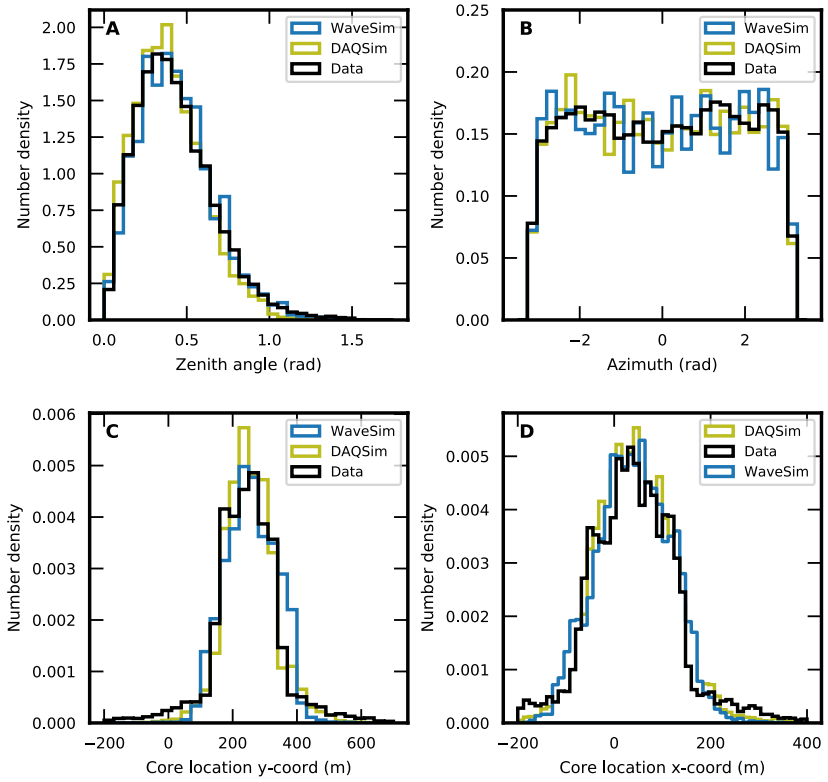

Fig. 6.13.: Distribution of the reconstructed parameters for data and simulation. Panel A and B show the distribution of reconstructed zenith and azimuth angle of the measured (black) and simulated showers (Wavesim in blue, DAQSim in green). In panel B the azimuth distribution is shown. The core location in the y and x coordinates is shown in panel C and D respectively. The core location is measured from a point of reference in the outer part of the array. The peak of both distributions corresponds to the geometrical centre of the array.

6.3 Conclusions and Outlook

In this chapter, two studies that aim at alleviating the deficiencies of DAQSim were presented. The efficiency of the PMTs was measured and applied to the simulations. This implementation was verified by comparing the 1 PE and muon peak position in data and MC, showing a great improvement compared to the previous approach, where the efficiency was randomly sampled from distributions. With this new model, the DAQSim simulations are one step closer to precisely reproduce the real data at a PMT-per-PMT level.

The PMT efficiencies were measured for different epochs of the detector. Overall, no degradation with time is seen but might constitute a second-order correction in the future. This method can be applied as a monitor of the degradation of the PMTs due to ageing or other effects that might translate into a shift in the muon peak location, such as water quality degradation or leak of light into the tanks. The application of the measured PMT efficiency into simulations has been adopted by the HAWC collaboration to derive the baseline detector response and used to estimate systematic uncertainties in the study of source spectra (see eg. Abeysekara et al., 2019). Currently, these measurements are used to degrade the efficiency in simulations and could be used instead to calibrate the detector for real data. This is a topic for future work since it would require the reconstruction of all data, which is beyond the scope of this work.

The second part of this chapter focused on the development of a method that opens for the first time the possibility of comparing at the lowest level the data and MC and can replicate the effects in timing and charge calibration introduced by the TOT technique and the pulse generation. WaveSim provides an important tool for the verification of the simulation and calibration at the lowest possible level, which is clearly needed to perform simulations reliably. A major limitation in DAQSim is the lack of a simulation of the slewing effect in pulses. In WaveSim this can be properly simulated since the time-spread of the arrival of individual PE is properly included. This is important for the reconstruction and assessment of the shower curvature in data and MC. Currently, in the HAWC analysis, corrections in data are made with a shower curvature model obtained from a clean gamma-ray sample of the Crab nebula, but this correction is not required in the simulation. This

makes clear that a one-to-one comparison between data and MC is currently not possible with the simulation chain of HAWC.

Since the pulse is reconstructed for each PMT individually, the method presented here also addresses the differences in the response of each PMT and could be used for run-wise simulations, which would provide better control on the systematic uncertainties in the analysis of sources.

In future work, the discrepancies seen in the TOT distributions between data and WaveSim are to be addressed. These discrepancies are most likely generated by a not sufficiently accurate simulation of the rising time and width of the reconstructed pulses. A better approach requires inferring the pulse shape using the information of the Lo and HiTOT calibration curves and simulate saturation effects. This will allow to capture the different effects from the two amplification channels of the DAQ system. Future work will also focus on the implementation of an algorithm capable of injecting coherent noise in the simulated showers. The approach used in DAQSim for this is a simple overlap of noise hits. In WaveSim, the implementation of the noise should happen at the waveform or TOT level. In this way, noise hits might combine with shower hits to form single pulses.

Despite some limitations, WaveSim is a big step further from the current non-existing simulation of the electronics, in contrast with the ad-hoc tunning of timing and charge used in DAQSim. Although the method is not complete, all the ingredients are present and detailed studies will continue to identify and correct the sources of discrepancy between data and MC.

7

GRB Observations with HAWC

Contents

In contrast to GRB observations with IACTs, where the re-pointing of the telescopes is required within the limited dark time, HAWC operates day and night, and stores the data of the whole instantaneously observable sky. Thanks to its large FoV ($\sim$2 sr) and high duty cycle ($\gtrsim$95%), HAWC is optimal for independent searches of GRB signals. It can be also used for the follow-up and monitoring of known GRBs thanks to the possibility to perform searches in the archival data, with an almost arbitrary duration. This chapter describes such a search with a method developed to estimate an optimal integration window for GRBs in the HAWC FoV. The method considers the evolution of a GRB signal transiting in the sky, together with a detailed determination of the instrument response.

Sec.7.1 gives a summary of the status of previous GRB searches of HAWC. In Sec.7.2 the method to estimate the optimal integration window for GRBs in the HAWC FoV is presented. Sec.7.3 presents the results of the searches for GRB emission applying the optimised search method described previously. In Sec. 7.4 upper limits to the VHE emission are obtained and in Sec.7.5 the results are placed in context with the satellite data and prospects for GRB detections with HAWC are discussed. Sec.7.6 concludes this chapter and an overview of future improvements to the method and other possible applications are provided.

7.1 Previous GRBs Search Strategies in HAWC

Three methods are used in the previous GRB searches on the HAWC data: an unbiased search for hotspots in the sky, which does not rely on GRB detections by other instruments; a search on the archival data for GRBs detected by other instruments; and a search in the scaler system of HAWC. A summary of the HAWC GRB programme can be found in Lennarz et al., 2017.

7.1.1 Real-time Search

For the near real-time search in the online triggered data, simplified algorithms for the reconstruction and very broad selection cuts are applied to ensure a fast analysis (Abeysekara et al., 2017b). The sky is scanned in the search for emission using a sliding square window of 2.3° side in steps of 0.11°. The emission is integrated over four time intervals, thought to characterise the typical duration of peaks seen in the GRB light curves, of 0.1 s, 1.0 s 10 s and 100 s with a sliding time window of width 10% of the integration time. This sliding procedure ensures a 90% overlap in space and time respectively. The emission of each region is statistically compared to an estimate of the expected background counts obtained over a period of 1.5 hrs from the data. Because of the large number of spatial and temporal bins employed, this blind search is highly penalised by the roughly $\sim 10^{12}$ number of trials. In Fig. 7.1 an example of a GRB candidate found by the online monitor over the 100 s search window is shown. The excess counts have a significance of more than 3σ, but once corrected for the number of trials due to the different tested timescales, it becomes consistent with a statistical fluctuation.

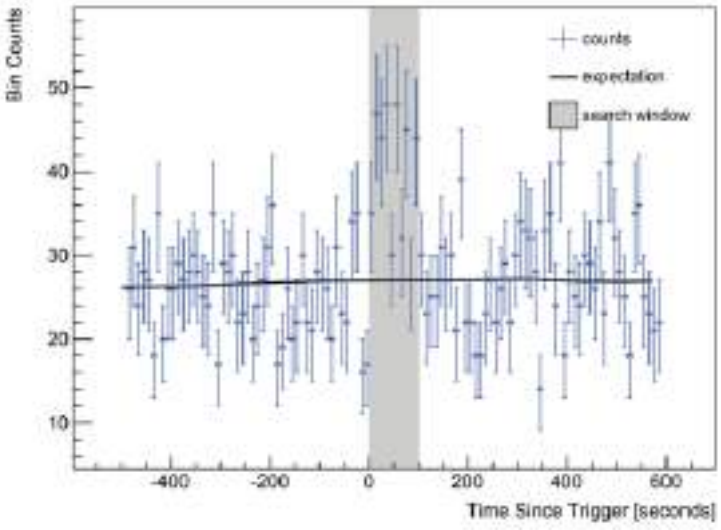

Fig. 7.1.: Counts as a function of time for a blind GRB search in HAWC. The number of counts in a time interval (grey shaded area) where a $> 3\sigma$ excess is found in the HAWC data. Since the search happens over several time and spatial windows, after accounting for trials, the significance of this excess is consistent with background. Figure reproduced from Lennarz et al., 2017.

The number of trials in this type of search decreases when considering GRBs detected by other instruments, communicated to HAWC via the GCN Network. In this case, the spatial window is fixed to the location of the alert. If the T_{90} is reported, the time windows are set to 1, 3 or 10 times the T_{90} for long GRBs, and 1, 6 and 20 seconds for short GRBs, otherwise a window of 1, 20 and 300 seconds is used (Wood, 2018).

7.1.2 Search in the Scalers System

HAWC is also able to search for GRBs with the DAQ scaler system, which stores the stream of hits detected by the HAWC PMTs. Since events are dominated by cosmic rays, a constant rate for each PMT is expected. The search for GRB emission with the scaler system consists of monitoring the PMT counting rate in fixed time intervals, searching for a significant increase coincident with a GRB detection by other instruments. The energy threshold for these searches is only restricted by the capability of primary particles to generate shower detectable at the HAWC altitude (few GeVs). The scaler system was used to search for VHE emission from GRB 130427A when only 30 WCDs of HAWC were operating. With only 10% of the whole array, no significant emission was found and the inferred upper limits were not very constraining. However, when considering the sensitivity of this analysis for the whole array, GRB 130427A and other GRBs with very bright emission could be easily detected (Abeysekara et al., 2015).

7.1.3 Archival Data Search

An offline search for emission is performed in the position in the sky and time coincident with GRBs previously detected by satellites. This search provides a better sensitivity compared to the online analysis since the full reconstruction and event selection cuts are applied. An ON/OFF method (see Ch. 3.2.4) is used to estimate the number of background and signal events. The OFF regions are shifted in right ascension with a displacement that corresponds to multiples of the search duration, such that each OFF region navigates through the same zenith angles as the ON region. The number of events in

the ON and OFF regions is corrected for a sinusoidal behaviour seen in the all-sky rate due to atmospheric tide effects. The corrected number of ON and OFF events are used to estimate the significance of detection, assuming a Poisson distribution. The search duration is typically the burst duration T_{90} (Alfaro et al., 2017) or a multiple of T_{90} with sliding windows when searching for delayed or extended emission (Becerril et al., 2017).

So far, these methods have not lead to a GRB detection and upper limits have been reported as shown in Fig.7.2.

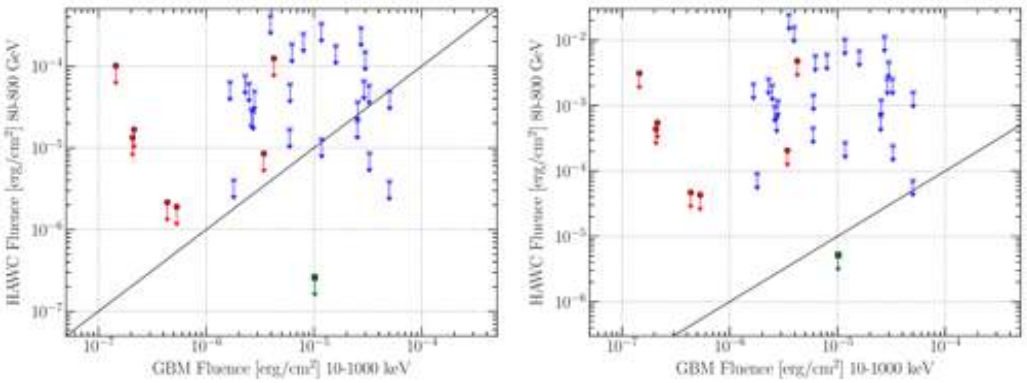

Fig. 7.2.: Comparison between the HAWC fluence upper limits and *Fermi*-GBM fluence. The left and right panels correspond to the HAWC 90% confidence level upper limits assuming a redshift of $z = 0.3$ and $z = 1.0$ respectively for a search over the T_{90} duration for GRBs detected by *Fermi*-GBM inside the HAWC FoV. The red circles show short GRBs, long GRBs are shown with the blue asterisks and the green square shows GRB 170206A (one of the brightest short GRBs detected by *Fermi*-GBM). Figure reproduced from Alfaro et al., 2017

7.1.4 Summary

In the first and last approach described here, where a detailed analysis is performed over the triggered data, the time window used for the search corresponds to the duration of the GRB prompt emission T_{90} or a fixed time interval, and neglect the specific characteristics of the HAWC instrument; a detector which is background-dominated at low energies in very short timescales (smaller than typical T_{90} values) and is almost background free for several hours or days at the highest energies. The method presented in what follows addresses the limitations of these type of analyses by accounting for

the detector response together with a hypothesis of the flux evolution of a typical GRB.

7.2 Optimal Search Window for GRBs

When considering steady sources, in a counting experiment like HAWC, the source significance increases approximately with the square root of time. In contrast, for sources like GRBs, whose emission rapidly decays after the termination of the prompt phase, at some point in the search window a maximum significance is reached.

7.2.1 Description of the Model

The model presented here takes into account the duration of the GRB prompt emission, the background rate and the delay of the observation to obtain the optimal search window for GRBs. A description of a GRB flux is used motivated by the similarities seen between the X-ray and VHE emission in recent GRB detections. This consists of a plateau of duration T_{90} followed by a decay of the signal of the form $1/t$, corresponding to the decay seen in *Fermi*-LAT GRBs (Ajello et al., 2019). In addition, the source can be inside the HAWC after a certain delay Δt, or instantaneously: $\Delta t = 0$. To model the source behaviour, the duration T_{90}, the integration time of the signal, and the delay Δt are expressed in terms of the inverse of the background rate (Bkg_R). The flux level of the simulated signal is then increased iteratively until an integration time that provides a $5\,\sigma$ detection is found. Since the background level is known, the significance is calculated with the Cash statistics (Cash, 1979). Fig. 7.3 shows an example of this method. The duration of the plateau phase is set to $T_{90}\times Bkg_R = 0.5$, while the observation delay is set to $\Delta t\times Bkg_R = 0.1$. The significance reaches a maximum at 1.87 s$\times Bkg_R$ and decreases rapidly.

In Fig.7.4 a scan of the parameter space for this optimisation is shown, as a function of T_{90} and constant Δt relative to the background rate, and for a constant T_{90} as a function of Δt. The optimal time is highly dependent

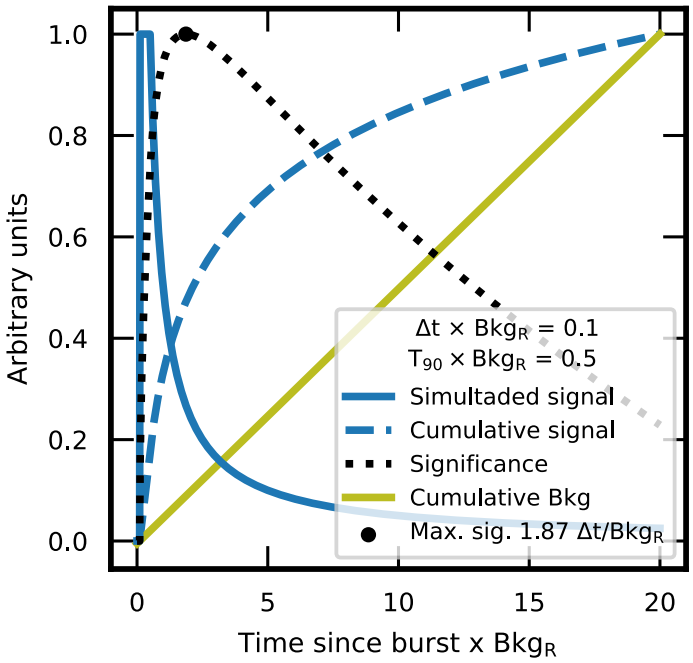

Fig. 7.3.: Example of the optimal integration time for a GRB-like signal. The number of signal events shown with the blue solid line is simulated with a plateau phase of a duration of 0.5/Bkg$_{\mathrm{R}}$ followed by $1/t$ decay of the signal. The blue dashed line corresponds to the cumulative number of signal events and the cumulative number of background events is shown in green. The dashed black line shows the evolution of the statistical significance. The black point on this line indicates the maximum significance reached at 1.87 s$\times$Bkg$_{\mathrm{R}}$ from the delay of observation set to 0.1$\times$Bkg$_{\mathrm{R}}$. All these curves are scaled to a maximum value of 1.0 for visualisation purposes.

on these variables when one considers bursts occurring instantaneously in the FoV. The optimal time increases asymptotically when the observations happen in the decay phase of the flux and is no longer dictated by T_{90}.

An empirically derived parametric function which provides the optimal integration time $\mathrm{O}(\mathrm{T}_{90}, \Delta t)$ of the form

$$\mathrm{O}(\mathrm{T}_{90}, \Delta t) = \left((9\Delta t \times \mathrm{Bkg}_{\mathrm{R}})^2 + \left(\frac{9}{2} \mathrm{T}_{90} \times \mathrm{Bkg}_{\mathrm{R}} \right)^2 \right)^{\frac{3}{10}},$$

models this behaviour and is also shown in Fig.7.4.

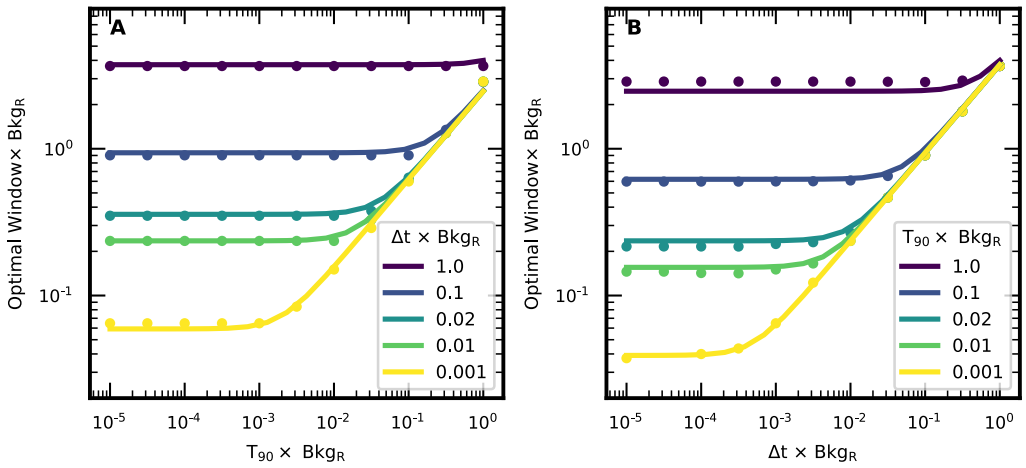

Fig. 7.4.: Optimisation of integration time for a GRB-like source. Panel A shows the optimal time window as a function of T_{90} for the different values of Δt indicated in the figure legend. In panel B the optimal time is shown as a function of Δt for fixed values of T_{90}.

7.2.2 HAWC Response to a Transiting Source

This section treats this optimisation problem with a realistic assessment of the HAWC detector's response together with values of T_{90} and observation delay of GRBs from the *Swift*-XRT/BAT and *Fermi*-LAT catalogues. Only GRBs that happen inside the FoV of HAWC or become observable after a maximum delay of 12 hrs are considered. *Fermi*-GBM GRBs are not considered in this study, since they require an extension to the method presented here to account for their typically larger localisation uncertainty compared to the PSF of HAWC. The analysis of *Fermi*-GBM GRBs will be the subject of future studies.

In HAWC the characterisation of the expected number of signal and background events for a source transiting in the sky is highly influenced by the zenith angle of observation. As will be shown in this section, for a given analysis bin $\mathcal{B}$ (see Ch. 3.1.4), the effective area decreases by more than an order of magnitude at a zenith angle of observation of 45.0° compared to 0.0°. This influences the signal of a gamma-ray source and the hadronic background.

To characterise the HAWC detector response to a GRB, the flux evolution of the source was simulated as described in Sec. 7.2. A power-law with EBL absorption is considered as the spectral shape of the GRB signal. The

signal is then followed in its navigation through the sky by converting the right ascension, declination and time to local coordinates (zenith and azimuth) which, convoluted with the effective area of the detector provides the expected number of signal events. The background rate is measured from data and integrated over the source navigation to obtain the total number of expected background events. The detailed procedure is as follows:

GRB sample The *Swift*-BAT/XRT[1] and *Fermi*-LAT[2] catalogues were obtained from the online pages, which will be referred to as the GRB sample in this study. In each catalogue, the onset time, fluence, duration of T_{90}, redshift (if it is known), and equatorial coordinates of the detected GRBs is specified. Only those GRBs observable in the HAWC FoV within a maximum delay of observation of 12 hrs and whose transit goes below 45° in zenith angle are considered. For the case of Swift, this sample ranges from March 2015 (when HAWC was inaugurated) to March 2019. For *Fermi*-LAT GRBs, it ranges from March 2015 up to the end of the second *Fermi*-LAT catalogue on July 2018.

GRB navigation Using the equatorial coordinates of each GRB in the sample, the navigation through the sky in local coordinates (zenith, azimuth) is obtained from the start of the burst T_0 up to their point where the source goes above 45° in zenith. The time of appearance of the GRB in the HAWC field of view (Δt) is stored together with the zenith bins where the source transits with a binning in time of 1 second. In Fig. 7.5 the navigation plot of GRB 150323A is shown as an example.

Effective area The effective area is computed by binning the simulated data over zenith bins from 0° to 45° in steps of 0.5° over an energy range of $10^{0.5}$ GeV to 10^{6} GeV, employing the standard event binning ($\mathcal{B}$) and gamma/hadron separation cuts of HAWC (see Ch. 3.1.4). The zenith and energy-dependent effective area for each $\mathcal{B}$ bin are stored in a lookup table and values for an arbitrary zenith angle value are obtained by linear interpolation between adjacent zenith bin curves. Fig. 7.6 shows the effective area under this zenith binning for $\mathcal{B} = 4$.

[1] Swift GRB online database: `https://swift.gsfc.nasa.gov/archive/grb_table/`
[2] *Fermi*-LAT Second Gamma-Ray Burst Catalog database: `https://heasarc.gsfc.nasa.gov/W3Browse/fermi/fermilgrb.html`

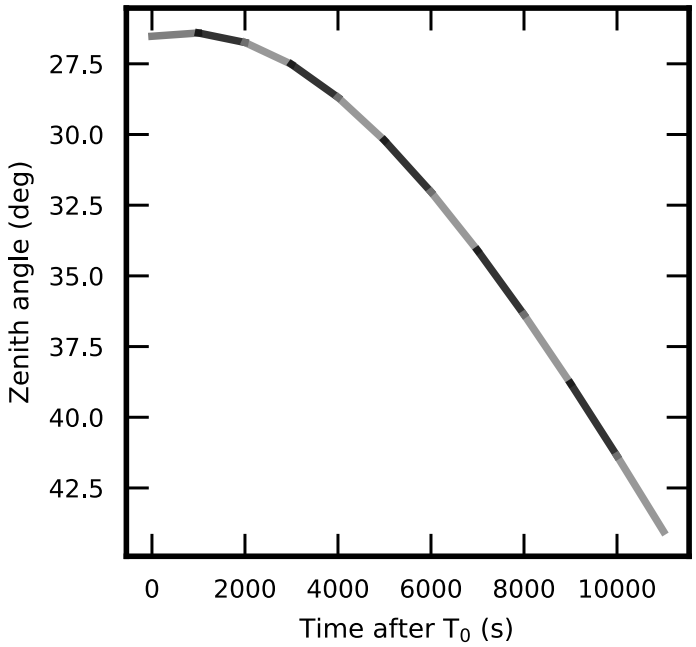

Fig. 7.5.: Navigation plot for GRB 150323A. The evolution of the zenith angle of observations as a function of time for GRB 150323A (R.A.=128.17°, Dec=45.44°) whose onset happens while being inside the HAWC FoV. The source reaches maximum culmination at $\sim 26°$ in zenith and starts to fall going below 45° at $11354\,\mathrm{s}$ after T_0. In the analysis, the navigation is binned over intervals of one second, here a binning of $1000\,\mathrm{s}$ is used for visualisation purposes.

Expected signal The expected signal is computed by determining the signal rate in each zenith bin of the GRB navigation. For this, the effective area in the mean value of each zenith band where the GRB is transiting is retrieved. Assuming a photon spectrum $F(E)$ with units of $\mathrm{erg}^{-1}\mathrm{cm}^{-2}\mathrm{s}^{-1}$, for each $\mathcal{B}$ bin, the signal rate in each energy interval $\mathrm{d}E$ is given by

$$dN(\theta) = \int_E A_{\mathrm{Eff}}(\theta, E) \times F(E) dE.$$

, where A_{Eff} is the effective area. This rate is summed over the effective area energy range to obtain the total expected rate per $\mathcal{B}$ bin and zenith band. The rate is multiplied by the time the source spends in each zenith band (fixed to 1 s) to obtain the total number of expected signal counts per $\mathcal{B}$ bin. The photon spectrum is assumed with a power-law

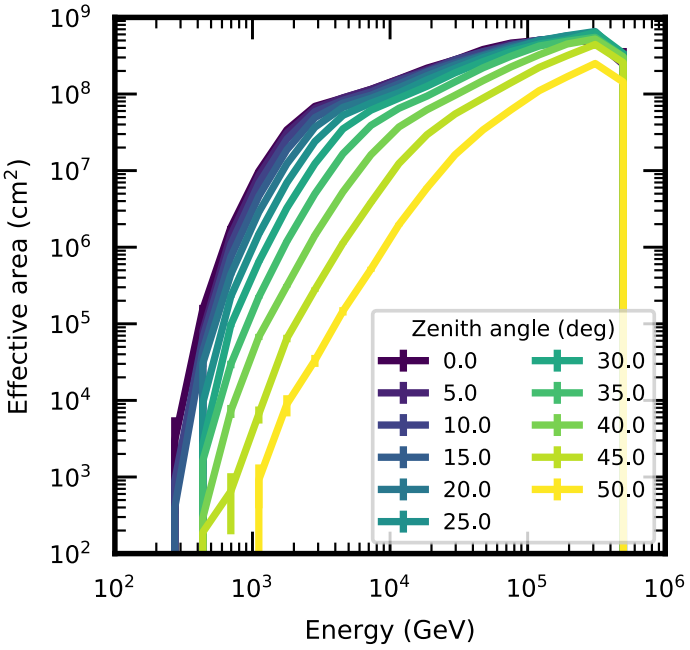

Fig. 7.6.: Effective area as a function of zenith angle. An example of the effective area evolution as a function of zenith angle for $\mathcal{B} = 4$. The different curves represent the different zenith angles as indicated in the figure label.

of index -2 with EBL attenuation (Franceschini et al., 2008). This index value corresponds to the mean index measured by *Fermi*-LAT (Ajello et al., 2019). For the EBL attenuation, two sets of analysis are done based on different assumptions for the redshift. One where all GRBs with no redshift measurement are set to $z = 0.1$ and the other, where the measured redshift of the GRB is applied. In the latter, if no redshift measurement is provided, a value of $z = 2.0$ and $z = 0.5$ is used for long and short GRBs respectively.

Background rate The background rate was obtained by producing skymaps in local coordinates. Known VHE sources like the Crab, Geminga/Monogem, Markarian 421, Markarian 501 and the galactic plane are masked so that they do not contribute to the overall rate (Martinez-Castellanos, 2016). The gamma/hadron cuts and $\mathcal{B}$ binning are applied to these events and the skymaps are split into zenith bands. The number of events within a band is scaled by the area of the band (in deg^2) and the total integration time of the data to obtain a background rate per

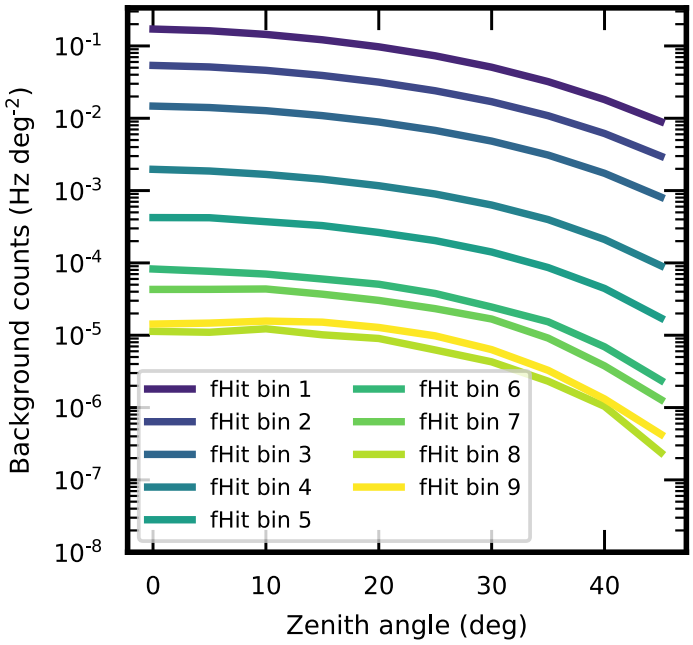

Fig. 7.7.: Background rate per zenith angle. The number of background counts per unit time and area is shown as a function of zenith angle for the nine $\mathcal{B}$ bins ($\mathcal{B}$) in HAWC.

unit area. The values are stored in a lookup table and can be retrieved for an arbitrary zenith angle using a linear interpolation.

To allow a good determination of the background rate, a total integration time of 239 hrs for the local maps was used under a zenith binning from 0.0° to 45° in steps of 5°.

Expected background A linear interpolation of the background rate as a function of zenith is applied to obtain the background rate per $\mathcal{B}$ bin in each zenith band of the source navigation (Fig. 7.7). The rate is scaled by the PSF area of each $\mathcal{B}$ bin (Abeysekara et al., 2017a) and multiplied by the time that the source spends in each zenith band to obtain the $\mathcal{B}$-wise expected background counts in each zenith band of the GRB transit.

Expected Signal Counts from the Crab Nebula.

To verify the procedure, one transit through the HAWC sky of the Crab Nebula was considered. The expected number of signal events was computed with the prescription explained by considering a power-law spectrum of the form

$$\frac{\mathrm{d}N}{\mathrm{d}E} = 2.51 \times 10^{-13} \left(\frac{E}{7\,\mathrm{TeV}}\right)^{-2.63} \frac{1}{\mathrm{TeV\,cm^2\,s}}$$

Panel A of Fig.7.8 shows the resulting expected number of signal events compared to the published HAWC data on the Crab observations (Abeysekara et al., 2017a). The ratio of the number of expected events between this work and the public HAWC measurements is shown in panel B. The discrepancy seen in the low $\mathcal{B}$ bins is expected, since the actual spectrum of the Crab is better described with a log-parabola function, so lower counts are expected in the low $\mathcal{B}$ bins. Other discrepancies are the result of the fact that the simulated signal in this work is obtained by considering only one transit, using one detector response. It is important to note furthermore that the systematic uncertainties of the reported Crab observations are within the discrepancy seen from this study.

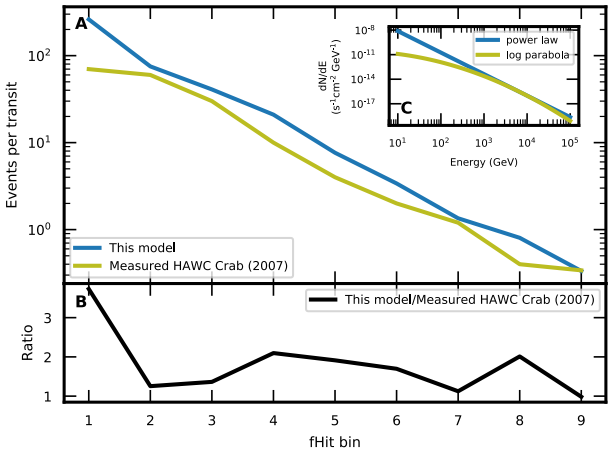

Fig. 7.8.: Expected and measured signal counts from the Crab Nebula. Panel A shows the number of measured excess events per transit obtained from Abeysekara et al., 2017a, indicated in green, and the expected excess events from this work in blue. Panel B shows the ratio of these two curves. In panel C the spectrum of the Crab nebula is compared to the one assumed here.

7.2.3 Sensitivity of the Optimal Time Window Method

The GRB sample obtained from the *Swift*-BAT/XRT and *Fermi*-LAT catalogues was used to simulate GRB-like sources transiting in the HAWC sky. For each GRB, the expected cumulative number of signal and background events was obtained as described in Sec.7.2.2.

For each $\mathcal{B}$ bin, the optimal integration window was estimated by successively scaling the required normalisation of the flux until the time interval that provides the 5 σ detection was found, as described in Sec. 7.2. For GRBs with high redshift and/or big delay of observation, the required normalisation can easily reach extreme values. For example, at an energy of 3 TeV (the mean energy value of $\mathcal{B} = 5$), the EBL absorption coefficient for redshift 2.0 is 1.02×10^{-30}. To avoid reaching extreme scaling factors of the signal in such cases, a limit on the optimal normalisation at 100 GeV was set to a value of 1×10^{10} erg^{-1}cm^{-2}s^{-1}. This threshold is usually reached for the high $\mathcal{B}$ bins, where the background starts to dominate on timescales longer than the typical time of a GRB transit. If this limit is reached, the optimal integration window is set to the whole available observation time.

In Fig. 7.9, the obtained parameters are shown for the case of GRB 150323A (with navigation plot shown in Fig.7.5) when assuming a redshift value of 0.1. This GRB has a T_{90} duration of 149.6 s and a delay of observation $\Delta t = 0$ and is visible for a total of 11354 s. The maximum optimal integration time increases rapidly with the $\mathcal{B}$ bin and reaches a maximum of about 6000 s. The required normalisation in each $\mathcal{B}$ bin is modulated by the detector response and the EBL attenuation starting to dominate for high $\mathcal{B}$ bins. The maximum sensitivity is reached for $\mathcal{B} = 3$ where the best compromise of these factors is reached.

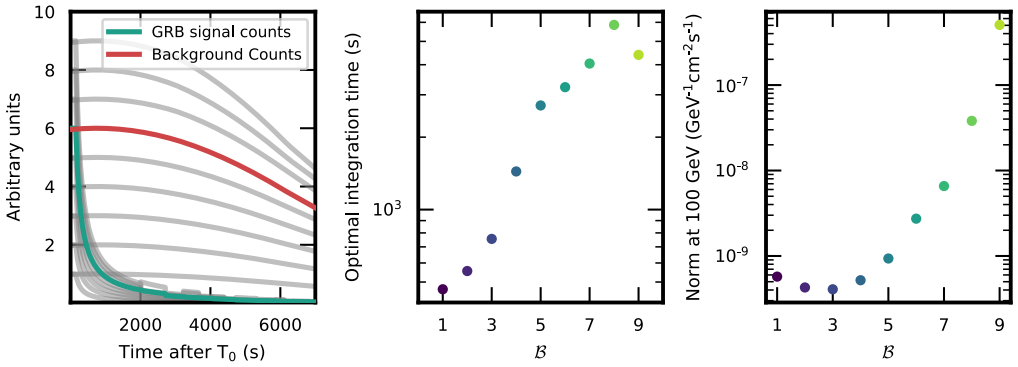

Fig. 7.9.: Example of the optimisation results for GRB 150323A. The left panel shows the expected signal counts for GRB 150323A (T_{90} = 149.6 s) and background counts as a function of time for the nine $\mathcal{B}$ bins with the curves highlighted in colour corresponding to $\mathcal{B} = 6$. The centre panel shows the optimal integration time for the 9 $\mathcal{B}$ bins. The right panel shows the required normalisation for a 5σ detection at 100 GeV for the power-law spectrum with EBL at redshift 0.1 for each of the nine $\mathcal{B}$ bins.

To illustrate the effect of the different parameters that rule this optimisation, the required fluence in the HAWC band was compared to the X-ray fluence. Since an E^{-2} spectrum was assumed for the intrinsic emission, the energy flux is proportional to the logarithmic energy interval chosen. Using the spectrum normalisation upper limit, a required fluence was computed in an energy range equivalent to the number of logarithmic decades used by *Swift*-BAT (one logarithmic decade, 15–150 keV) or *Fermi*-GBM (two logarithmic decades, 10–1000 keV). This corresponds to an energy range of 100–1000 GeV and 100-10000 GeV for the HAWC required fluence for the *Swift* and *Fermi*-LAT GRBs respectively.

The results in each $\mathcal{B}$ bin for the GRBs detected by *Swift*-BAT happening in the FoV of HAWC (prompt observations) and assuming a redshift of $z = 0.1$ are shown in Fig. 7.10. The required level of signal increases with $\mathcal{B}$ due to the spectral steepening and higher EBL absorption at higher energies. Short GRBs require smaller integration times than long GRBs since their emission reaches the $1/t$ decay phase faster. In the high $\mathcal{B}$ bins, the integration time is dictated only by the total time that the burst is observable. In Fig. 7.11 the results for GRBs becoming observable at later times (afterglow observations) are shown. In this case, since the observations happen after the end of the plateau T_{90} phase, the required fluence for HAWC is highly dominated by the way the source transits, as a high dependency on the mean zenith angle of observation is seen. In the same way as to prompt observations, an increase in the required fluence is seen with increasing $\mathcal{B}$. The results of GRBs detected by *Fermi*-LAT and when using the known/assumed redshift can be found in App. A.

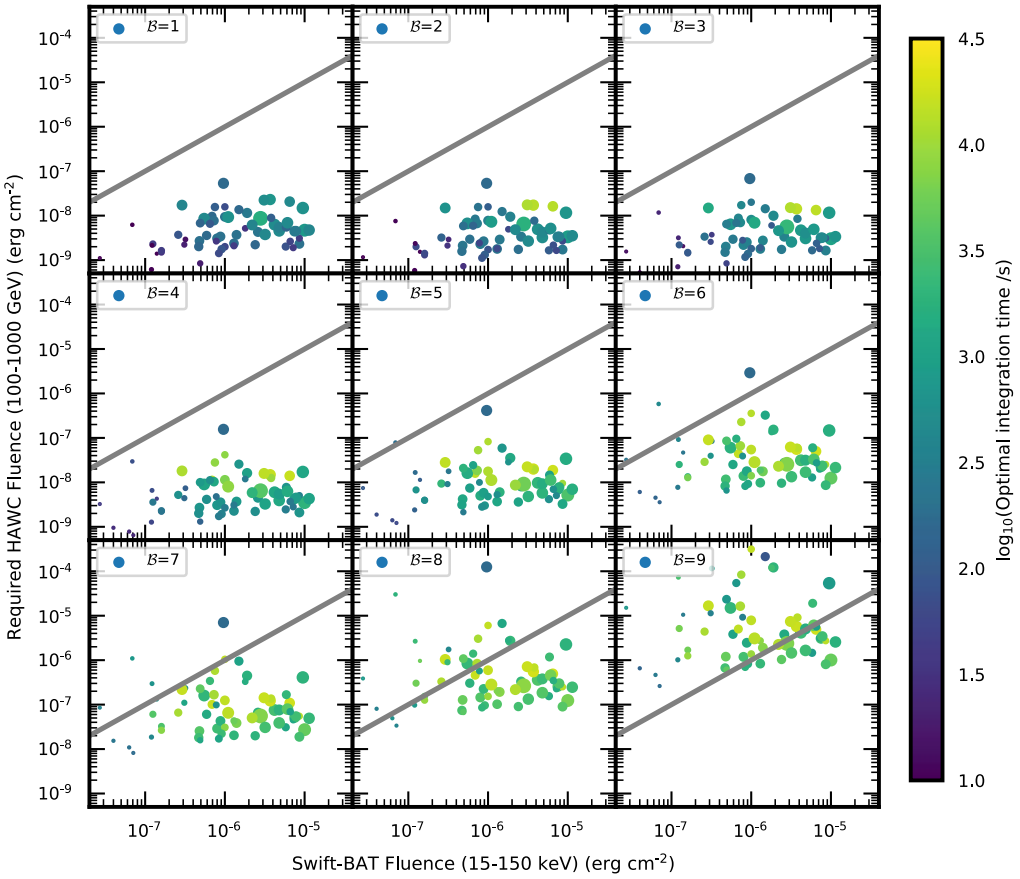

Fig. 7.10.: Required GRB fluence for 5 σ detection with HAWC for prompt observations and assumed redshift z=0.1. Each panel shows for each $\mathcal{B}$ the relationship between the required GRB fluence for a 5 σ detection with HAWC in the energy range of $100 - 1000$ GeV and the measured fluence with *Swift*-BAT in the energy range from $15 - 150$ keV. The colour of each point encodes the required integration time obtained from the optimisation and the size of the point is proportional to T_{90}. The grey line corresponds to equal fluence. This sample corresponds to GRBs happening inside the FoV of HAWC, $\Delta t = 0$ s.

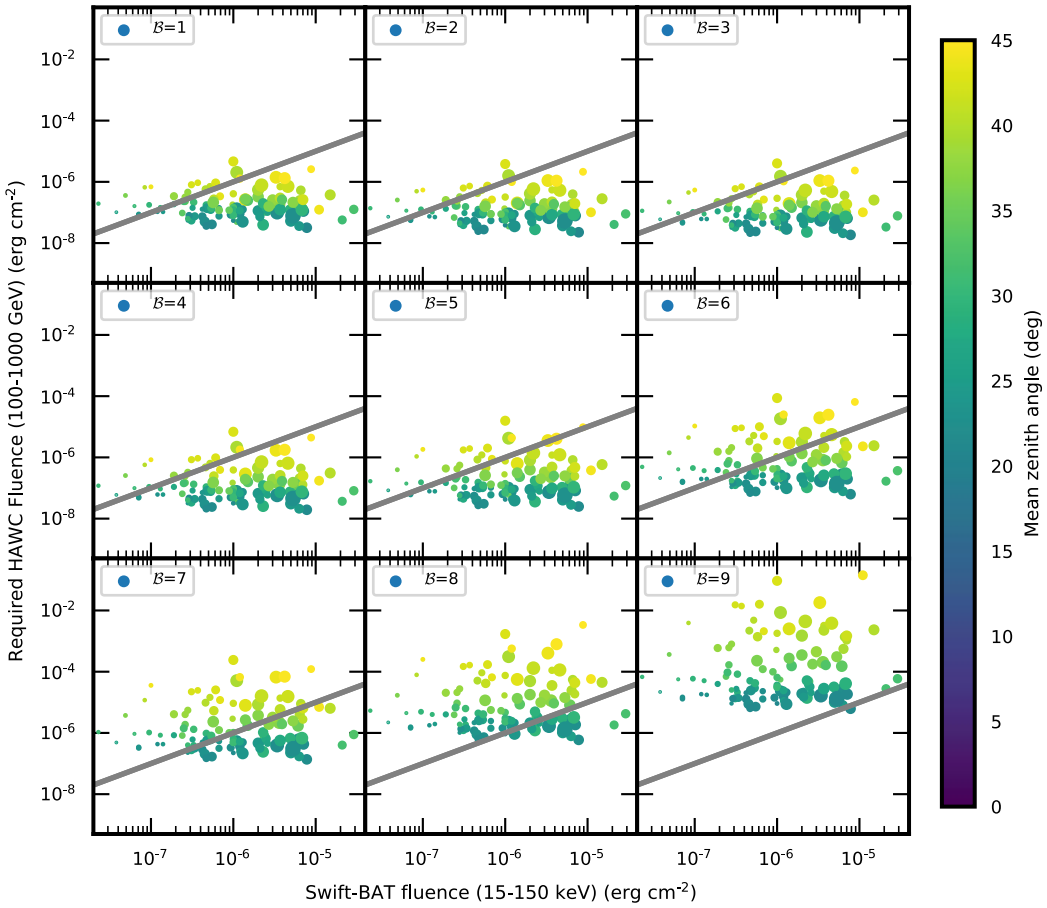

Fig. 7.11.: Required GRB fluence for 5 σ detection with HAWC for afterglow observations and assumed redshift z=0.1. Each panel shows, for each $\mathcal{B}$, the relationship between the required GRB fluence for a 5 σ detection with HAWC in the energy range of $100 - 1000$ GeV and the measured fluence with *Swift*-BAT in the energy range from $15 - 150$ keV. The colour of each point encodes the mean zenith angle of the observations with HAWC and the size of the point is proportional to T_{90}. The grey line corresponds to equal fluence. This sample corresponds to GRBs observed with a $\Delta t > 10$ s.

7.3 Search for Emission in the HAWC Data

Here, the methods developed in the previous section are applied for the search of emission in the HAWC data over the optimal integration time for each GRB.

7.3.1 Ring Background Method and Significance Estimation

The ring background method (see Ch. 3.2.4) was employed for the search of VHE gamma-ray emission in the GRB sample. To account for the different optimal integration times and PSF values, one search is performed for each $\mathcal{B}$. The ON region radius is set to the corresponding PSF size of the $\mathcal{B}$ bin as described in Sec. 7.2.2. The inner and outer radius of the OFF region is set 1° and 1.7° away from the ON region respectively. If with this configuration, no events in the OFF regions are found, the outer radius size is increased in steps of 0.2° until at least 2 events in the OFF region are detected allowing for a maximum outer radius size of 20°. With this method, the number of ON and OFF events (n_{ON}, n_{OFF}) are counted over the integration time.

To monitor and verify the stability of this method, a control region, located at the opposite azimuth angle in the local sky and transiting over the same zenith bands was used to measure ON and OFF events with the same region sizes and integration times as the GRB region.

The Li&Ma method, which estimates the probability that the measured number of ON events contains some signal assuming a Poisson regime (Eq.3.6), was used to measure the statistical significance of the results with α the ratio of the ON region to the OFF region size. This method provides the test statistics (TS), with the significance of detection given by $\sigma = \sqrt{TS}$

7.3.2 Results

The HAWC reconstructed data falling in the optimal time for each GRB in the sample were retrieved. For each GRB, the ON region was placed at the location given by the GRB catalogue (Swift-BAT or Fermi-LAT location) with the OFF regions and control regions set as described above. The $\mathcal{B}$ binning scheme and gamma-hadron separation cuts were applied to the data.

Fig. 7.12 shows the significance distribution for each $\mathcal{B}$ bin in the search for emission over the GRB sample (*Swift*-BAT and *Fermi*-LAT GRBs) for the case

of known redshift values. The results for the case of $z = 0.1$ are shown in App. A.

A total significance was computed by taking $\sqrt{\sum TS_i}$, where TS_i is the TS value of the i-th $\mathcal{B}$ bin. If the excess of events is negative, i.e $n_{\mathrm{ON}} - \alpha n_{\mathrm{OFF}} < 0$, the negative of TS_i is used. The distribution of the total significance in the case of known redshift and $z = 0.1$ is shown in Fig. 7.13. A normal significance distribution is expected, while the bi-modal behaviour is induced by the high $\mathcal{B}$ bins. In these bins, there are usually no ON events, because of the expected low rate of these bins and the small ON region sizes. The significance rapidly increases if even one event is detected in the ON region.

No significant emission ($5 > \sigma$) is detected in any of these two searches (redshift set to $z = 0.1$ or known/assumed redshift), when considering the significance in each $\mathcal{B}$ bin or when measuring a total significance, and the distributions are consistent with statistical fluctuations. The strongest candidate for emission is found for GRB 170115A with a total significance value of 4.5 σ in both types of searches. The onset of this GRB happened inside the FoV of HAWC, it has a T_{90} measured by *Swift*-BAT of 48.0 s and is observed by HAWC with an initial zenith angle of 5.5°, making it a strong candidate for detection.

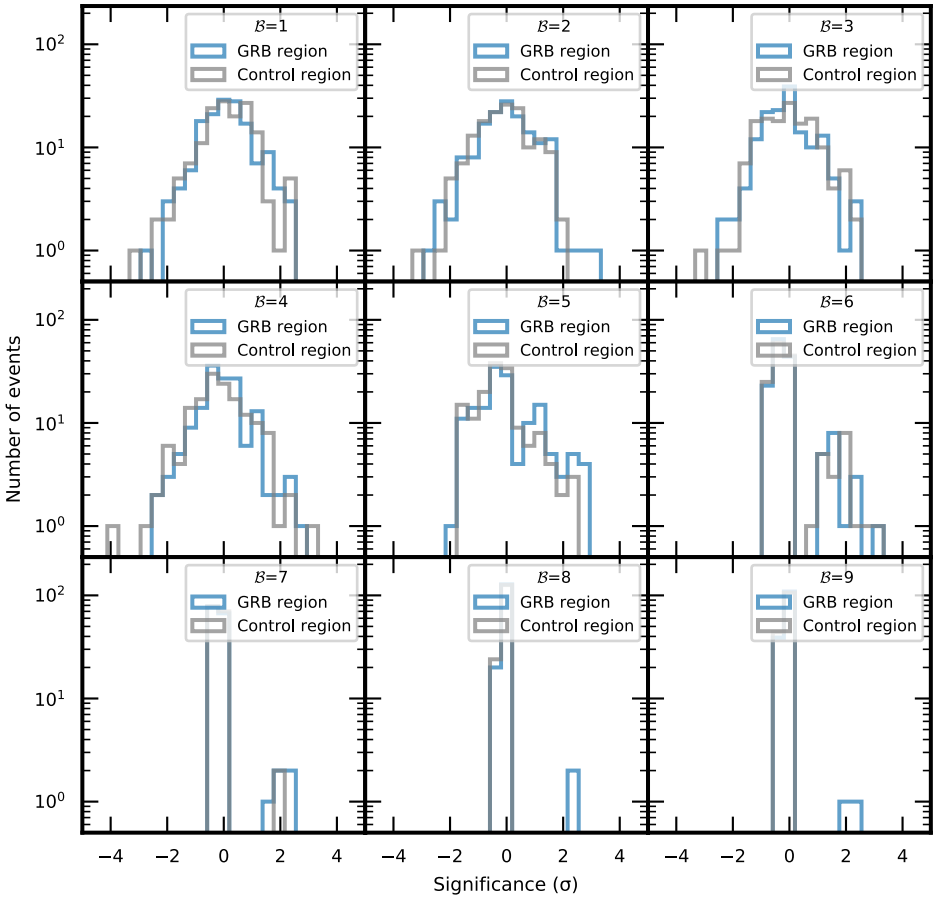

Fig. 7.12.: Significance distribution from the GRB searches with HAWC on each individual $\mathcal{B}$ bin. Each panel shows the significance distribution for the whole GRB sample applying the known redshift value, or assumed according to the T_{90} duration, as explained in the text. The grey distribution corresponds to the control region and in the blue to the GRB tested position.

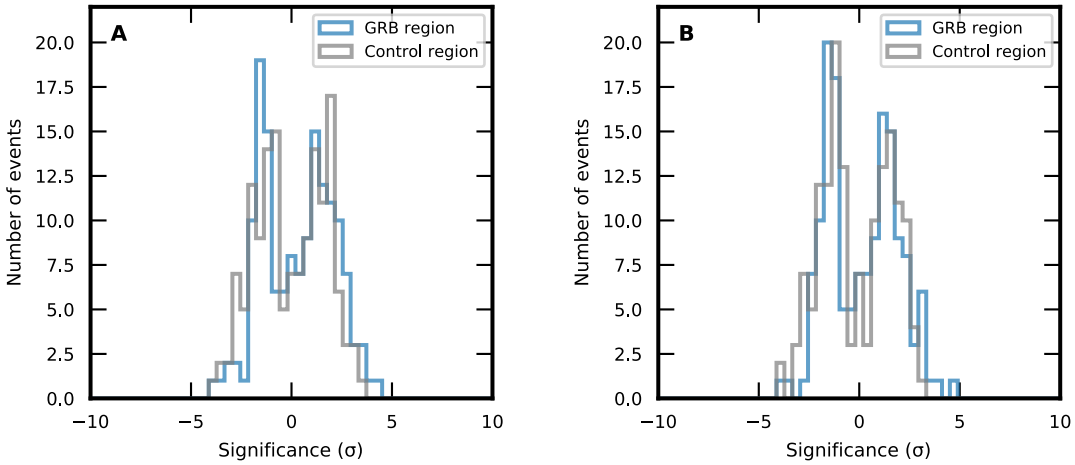

Fig. 7.13.: Distribution of the total significance for GRBs observed by HAWC. Distribution of significance when combining the value of each $\mathcal{B}$ (see Fig. 7.12) shown in panel A and B for measured/inferred redshift and for redshift assumed to be $z = 0.1$ respectively. The grey line corresponds to the control regions and the blue line to the GRB regions.

7.4 Upper Limits on the VHE Emission.

Since no significant detection was found in the sample, upper limits on the VHE emission are set.

7.4.1 Poisson Likelihood for the Estimation of Upper Limits

The number of detected ON and OFF events ($n_{\rm ON}$ and $n_{\rm OFF}$, respectively) obtained in Sec.7.3 were use to construct a Likelihood profile. Following the same approach as De Naurois, 2012, in Poisson statistics, the conditional probability of detecting $n_{\rm ON}$ and $n_{\rm OFF}$ events given a known signal and background level n_γ and $n_{\rm bkg}$ is given by:

$$P(n_{\rm ON}, n_{\rm OFF}|n_\gamma, n_{\rm bkg}) = \frac{(n_\gamma + \alpha n_{\rm bkg})^{n_{\rm ON}}}{n_{\rm ON}!} e^{-(n_\gamma + \alpha n_{\rm bkg})} \times \frac{n_{\rm bkg}^{n_{\rm OFF}}}{n_{\rm OFF}!} e^{-n_{\rm bkg}} \quad (7.1)$$

For the case of unknown expected background, $n_{\rm bkg}$ can be treated as a nuisance parameter and therefore the partial derivative of P with respect to $n_{\rm bkg}$ will be zero at the best fit:

$$\frac{\partial P}{\partial n_{\rm bkg}} = 0,$$

leading to the quadratic equation in $n_{\rm bkg}$

$$\frac{\alpha\, n_{\rm ON}}{n_\gamma + \alpha\, n_{\rm bkg}} + \frac{n_{\rm OFF}}{n_{\rm bkg}} - (\alpha + 1) = 0,$$

with solution:

$$n_{\rm bkg} = \frac{C + D}{2\alpha(\alpha + 1)},$$

where $C = \alpha(n_{\rm ON} + n_{\rm OFF} - (\alpha + 1)n_\gamma$, and $D^2 = C^2 + 4(\alpha + 1)\,\alpha\, n_{\rm OFF}\, n_\gamma$.

When $n_{\rm bkg}$ is treated as a nuisance parameter, the probability is Eq. 7.1 is left with n_γ as the only free parameter. By taking $-2\log(P)$, the likelihood ratio, the null hypothesis that no source exists (and therefore n_γ is consistent with background) is compared against the alternative hypothesis where n_γ describes an additional source. This tests statistic (TS) is called WStat (*Appendix B: Statistics in XSPEC* 2021) and according to Wilks theorem, WStat follows a χ^2 distribution with n_γ the only degree of freedom.

7.4.2 Application to the GRB Sample

Based on the statistical value for n_γ, the upper side of the 95% confidence interval (2σ) was used to infer an upper limit on the GRB signal.

The WStat curve was constructed for each set of $n_{\rm ON}$, $n_{\rm OFF}$ and α measured for each GRB with the ring background method. Nine curves are constructed, one for each $\mathcal{B}$ bin measurement. The expected counts n_γ is related to the normalisation of the assumed spectrum by computing the expected number of events in each $\mathcal{B}$ under the same spectral assumptions used for the search of emission (power-law with EBL attenuation). In Fig. 7.14 the nine curves computed for the results obtained for GRB 150323A are shown as an example. In these figures, the high $\mathcal{B}$ present skewed curves due to the limited number of events in the ON and OFF regions. The total WStat curve, which computes the statistic for the nine $\mathcal{B}$ together is given by:

$$\mathrm{WStat}_{\rm tot} = -2\sum_{\mathcal{B}} \log(P_{\mathcal{B}}), \tag{7.2}$$

with P given by Eq. 7.1. Curves inferred when zero events are detected in the ON and OFF regions for a $\mathcal{B}$ bin are excluded from this sum. Overall, the skewed curves due to low statistics do not contribute significantly to the final WStat curve.

The upper limit on the flux is computed by finding the spectrum normalisation that provides a certain difference Δ(TS) from the minimum in the WStat curve. Choosing a confidence level (CL) of 95% for this study corresponds to a $\Delta(TS)$=3.84. An example is shown in Fig. 7.15 for the case of GRB 150323A resulting in an upper limit of 8×10^{-11} GeV^{-1}cm^{-2}s^{-1}.

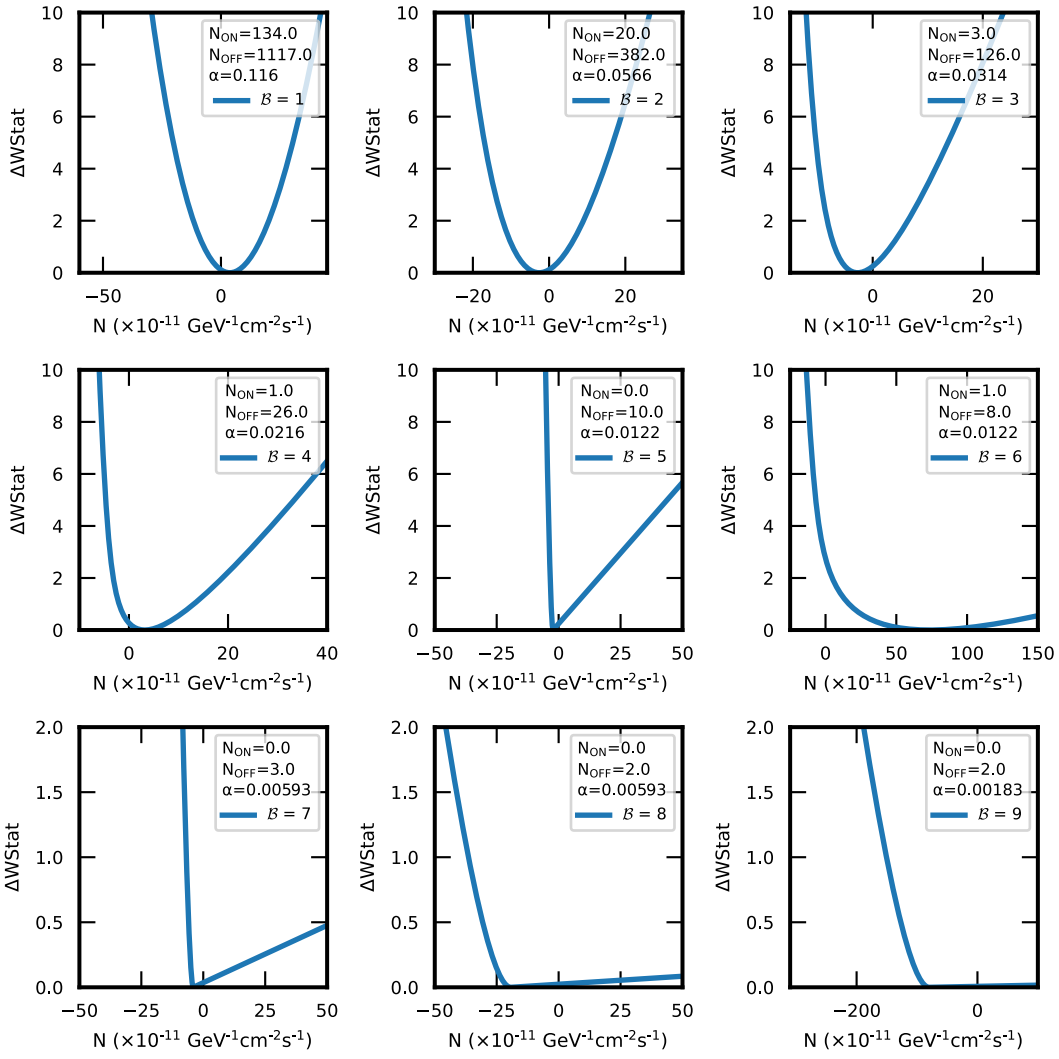

Fig. 7.14.: WStat curves for each $\mathcal{B}$ bin from the results on GRB 150323A. The nine panels show the WStat constructed for each $\mathcal{B}$ bin using Eq. 7.1 and the values of n_{ON}, n_{OFF} and α indicated in each panel's legend.

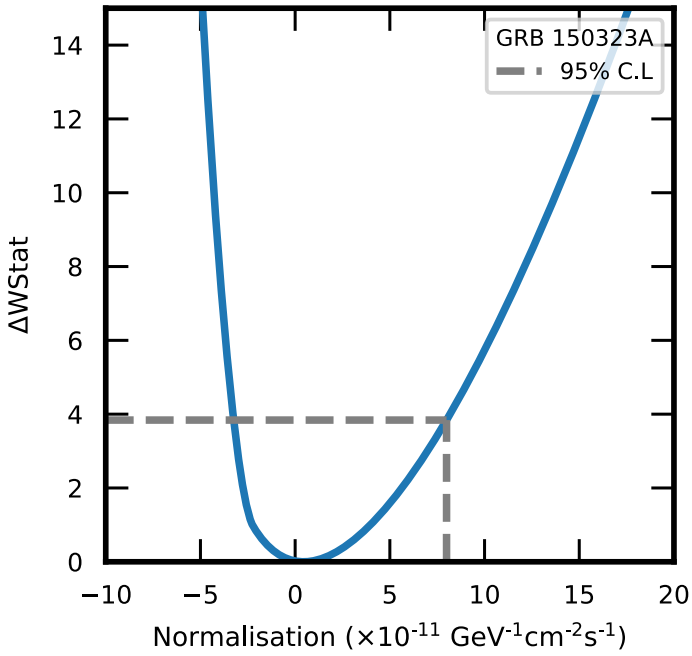

Fig. 7.15.: Combined WStat curve for GRB 150323A. The WStat as a function of spectrum normalisation at 100 GeV is shown for the case of GRB 150323A in blue. The dashed grey lines show the location of the normalisation value that corresponds to a 95% confidence level.

7.4.3 Results

Irrespective of the observation delay and integration time, the obtained ULs correspond to the flux during the simulated plateau phase of duration T_{90}. Fig. 7.16 shows the comparison of the fluence upper limits obtained with HAWC, with the energy range as described in Sec. 7.2.3, and the fluence measured with *Swift*-BAT and *Fermi*-GBM for *Fermi*-LAT detections, in the case of known redshift or redshift inferred from the T_{90} duration. In these figures, the seven most constraining upper-limits, defined as those whose HAWC fluence upper-limit is closer to the X-ray fluence, are annotated and the values on the fluence upper limits, X-ray fluence, T_{90}, integration time of the search, and redshift are summarised in Tab. 7.1.

In Fig. 7.17 the fluence upper limits from HAWC for GRBs without a redshift measurement are shown when assuming a redshift $z = 0.1$ for all of them compared to the *Swift*-XRT and *Fermi*-GBM measurement.

	Name	T_{90} (s)	z	Int. time (s)	*Swift*-BAT flu. 15-150 keV (erg cm^{-2})	HAWC flu. 95% CL U.L 100-1000 GeV (erg cm^{-2})
1	GRB 171205A	189.4	0.0368	15520.5	3.6×10^{-6}	3.2×10^{-6}
2	GRB 160804A	144.2	0.736	6837.5	1.1×10^{-5}	1.4×10^{-5}
3	GRB 150323A	149.6	0.593	7517.5	6.1×10^{-6}	2.0×10^{-5}
4	GRB 160821A	10.0	-	8453.5	7.2×10^{-6}	2.3×10^{-5}
	Name	T_{90} (s)	z	Int. time (s)	*Fermi*-GBM flu. 10-1000 keV (erg cm^{-2})	HAWC flu. 95% CL U.L 100-10000 GeV (erg cm^{-2})
5	GRB 171120A	44.1	-	11914.5	1.61×10^{-5}	1.03×10^{-4}
6	GRB 160625B	453.4	1.406	21377.5	6.43×10^{-4}	5.12×10^{-3}
7	GRB 170214A	122.9	2.53	3822.5	1.77×10^{-4}	2.45×10^{-3}

Tab. 7.1.: Fluence upper limits obtained with HAWC on selected GRBs. The first column corresponds to the number label for the seven GRBs annotated in Fig. 7.16.

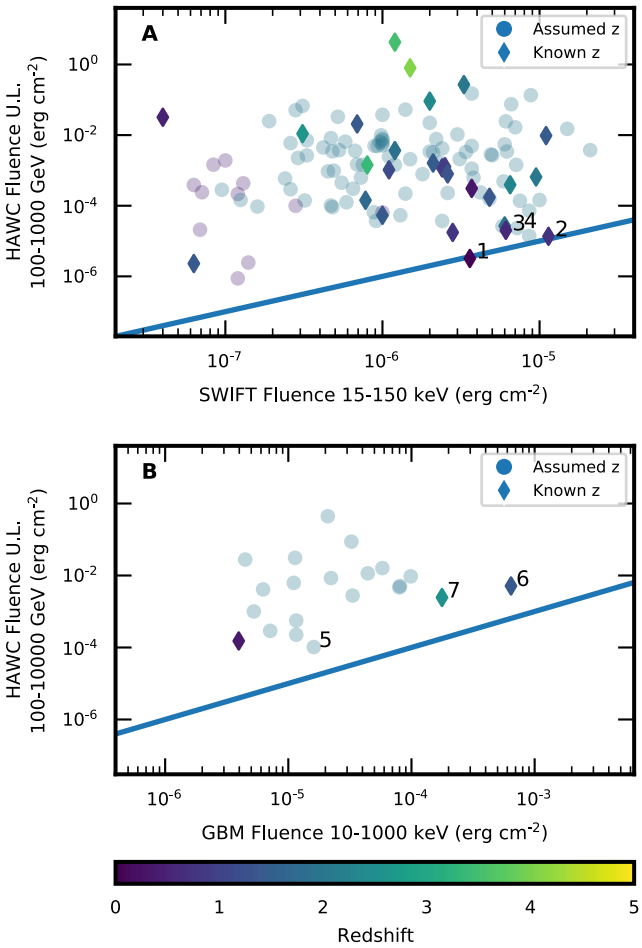

Fig. 7.16.: Comparison between the HAWC fluence upper-limit and the X-ray fluence for GRBs observable by HAWC. Panel A shows the 95% C.L. upper limits of HAWC versus the measured *Swift*-BAT fluence. Panel B shows the HAWC fluence ULs versus the *Fermi*-GBM measurement for *Fermi*-LAT GRBs. The colour encodes the redshift value used. GRBs with measured redshift are indicated with a diamond. GRBs without redshift measurement are shown with circles. In the latter case, a value of z=0.5 and z=2.0 was used for long and short GRBs respectively.

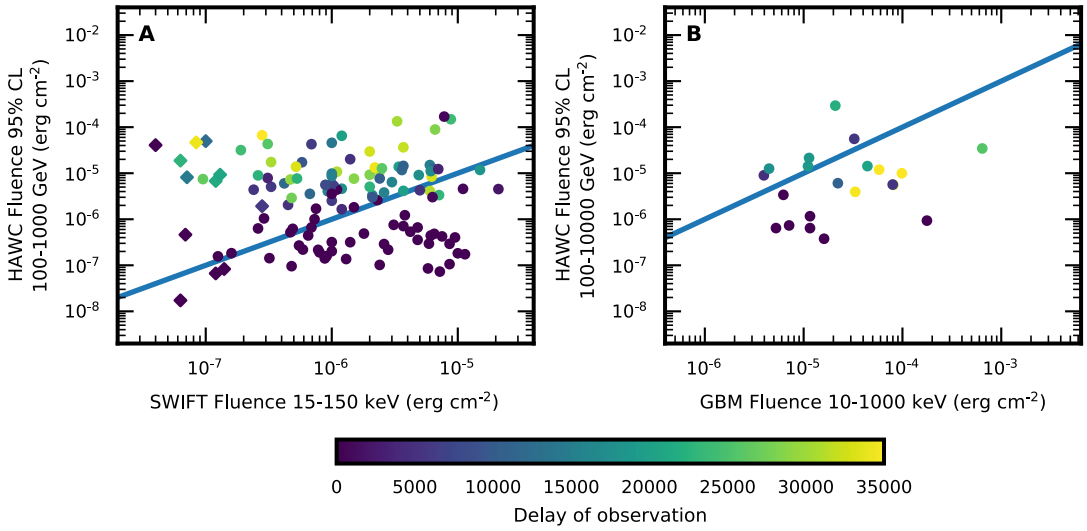

Fig. 7.17.: Comparison between the HAWC fluence ULs and the X-ray fluence for GRBs observable by HAWC assuming a redshift z=0.1. Panel A shows the case of *Swift*-BAT GRBs and panel B for *Fermi*-LAT detected GRBs. The colour encodes the delay of observation with short GRBs shown in diamond shape and long GRBs with a circle. The HAWC ULs are at the 95% CL. Only GRBs without redshift measurement are considered for these figures.

7.5 Discussion

7.5.1 Specific GRBs

Some of the results presented in the previous section were selected to provide a more detailed discussion on the ULs set by HAWC given their interesting multi-wavelength context. The case of GRB 160623A, the longest HE emission detected by *Fermi*-LAT, and the case of GRB 150323A, with strong upper limits set by VERITAS, are presented here.

GRB 160623A

GRB 160623A was first detected by *Fermi*-GBM. It was also detected by *Fermi*-LAT, when it went in the FoV 400 s after the GBM trigger, for a total of 35000 s. In this interval, photons above 1 GeV were detected, making it the GRB with the longest HE duration in the *Fermi*-LAT catalogue (Ajello et al., 2019). The

Gran Telescopio Canarias measured a redshift of $z = 0.367$ (*Composite GCN List for GRB 160623A* 2016). Follow-up observations were triggered by *Swift*-XRT and started at $\sim 3 \times 10^4$ s. The CALET gamma-ray burst monitor detected emission starting ~ 1 min before the *Fermi*-GBM trigger. This GRB was also detected by Konus-Wind and by optical telescopes. A deep monitoring of the afterglow in the radio wavelength was performed. With this data, it has been inferred that the radio and X-ray afterglow can be described with a two jet component, consisting of a collimated jet giving rise to the X-ray emission and a relativistic cocoon surrounding it that provides the radiation detected in the radio wavelength (Chen et al., 2020).

The HAWC observation started at 4807 s after the GBM trigger and lasted for 20086 s, corresponding to the maximum integration reached with $\mathcal{B} = 7$. Fig. 7.18 shows the energy-flux light curve reported by *Fermi*-GBM, *Fermi*-LAT, *Swift*-XRT[3] and the HAWC upper-limit. The integral flux detected by *Fermi*-LAT was converted to an energy flux using the measured temporal decay $\alpha = 1.25 \pm 0.09$ ($F \propto t^{-\alpha}$, Fig. 9 in Ajello et al., 2019). The HAWC upper-limit do not strongly constrain the expected VHE emission or a continuation of the *Fermi*-LAT spectrum, but they are still relevant since they are contemporaneous to the *Fermi*-LAT detection.

GRB 150323A

This GRB has one of the most constraining UL found with HAWC (the third element of Tab.7.1). It triggered first the *Swift*-BAT. It was also detected by *Swift*-XRT, Konus-Wind and by optical telescopes, with the Keck telescope measuring a redshift of $z = 0.593$ (*Composite GCN List for GRB 150323A* n.d.). This GRB was followed-up by VERITAS from 270 s after T_0 up to 170 min after T_0. For maximum sensitivity, the observation with VERITAS was analysed up to 40 min after T_0 as suggested from a Monte Carlo simulation which accounts for the typical IACTs background rate and a $1/t$ decay assumption of the GRB flux (Abeysekara et al., 2018). These observations did not provide any significant detection. VERITAS reported a 99% confidence level integral

[3]The *Swift*-XRT light curve was retrieved from `https://www.swift.ac.uk/burst_analyser/00020666/`

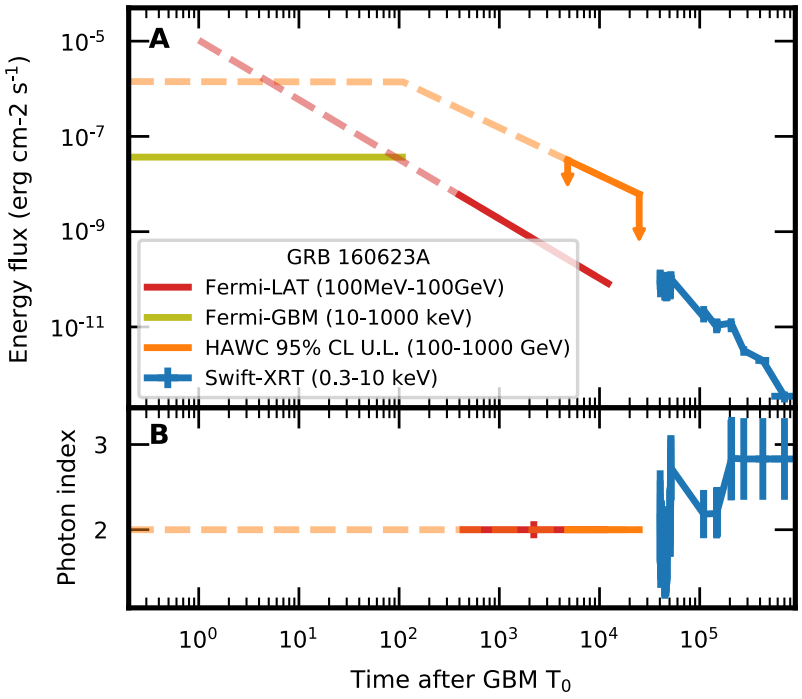

Fig. 7.18.: Multi-wavelength light curve of GRB 160623A. Panel A shows the energy flux light curve measured by *Swift*-XRT (blue) and as inferred from the *Fermi*-GBM fluence (green) and from the *Fermi*-LAT integral flux, obtained from 401.5 s to 35069.0 s after the GBM (red). The HAWC upper limits from the observation in the interval of 4807-24893 s are shown in orange. Panel B shows the measured photon index by *Fermi*-LAT in the corresponding integration window, by Swift-XRT, and the photon index assumed for the HAWC UL.

upper-limit from 140 GeV to 30 TeV of $1.6 \times 10^{-7}\,\mathrm{m^{-2}s^{-1}}$ that allow strong constraints on the GRB circumburst medium to explain the non-detection.

This GRB was immediately observable by HAWC, and the optimisation of the integration time provides a coverage of up to 7555 s after the *Swift*-BAT trigger when the burst sets in the sky. It is observable with a mean zenith angle of 40°. Fig. 7.19 shows the ULs obtained by HAWC in contrast with the UL set by VERITAS and the *Swift* light curve. Although the HAWC UL contemporaneous to the VERITAS observations are roughly 5 orders of magnitude less constraining, this analysis allows the prompt emission phase to be covered with HAWC and set upper limits on the prompt emission peaks.

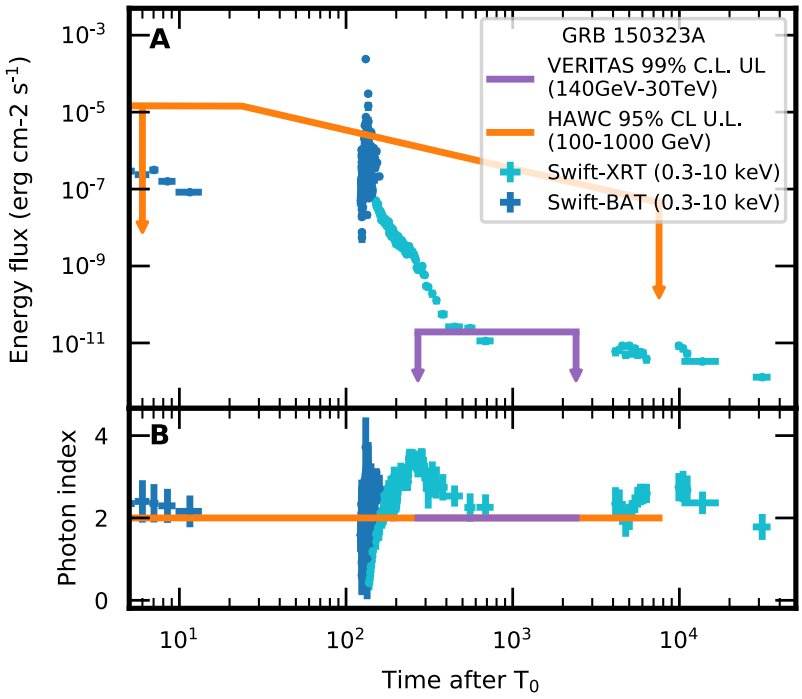

Fig. 7.19.: Multi-wavelength light curve of GRB 150323A. Panel A shows the energy flux evolution of GRB 150323A as observed by *Swift*-BAT (cyan) and *Swift*-XRT (blue). The HAWC 95% confidence level upper limit is shown in orange. The VERITAS upper-limits Abeysekara et al., 2018 are shown in purple. Panel B indicates the corresponding measured photon index for the *Swift* observations and the assumed photon index of 2.0 used for the VERITAS and HAWC upper limits.

7.5.2 HAWC Detection Prospects

To characterise the detection capabilities of HAWC, upper limits for the GRB sample were obtained by assuming a redshift value of $z = 0.3$, $z = 0.5$ and $z = 0.7$ for all GRBs without redshift measurement, in addition to these obtained for $z = 0.1$, discussed throughout this chapter and shown in Fig. 7.17.

GRBs with potential detection are defined here as those whose fluence upper limits from HAWC are lower than the fluence in the X-ray band. Panel A of Fig. 7.20 shows the HAWC efficiency for potential detection as a function of redshift. The expected number of GRBs observable by HAWC in the corresponding redshift binning is shown in panel B of this figure. An upper and lower limit of the expected number of events is indicated. The lower range corresponds to the distribution of redshift values for all GRBs detected by *Swift* scaled by the 16 years of *Swift* operations. The upper range is obtained by considering that only 27% of the GRBs detected by *Swift* have a redshift measurement and assumes that these GRBs without redshift estimation follow the same redshift distribution. An additional factor is added to account for the observation efficiency of HAWC, i.e. 30% and 34% of the total number of GRBs detected by *Fermi*-LAT and *Swift*-BAT are seen by HAWC in the same time interval of this sample (3.3 and 4 years respectively).

The expected number of GRBs per year from *Fermi*-LAT and *Swift*-BAT with a potential detection with HAWC is obtained by folding the HAWC efficiency (panel A of Fig. 7.20, assuming an equal efficiency for neighbouring redshift values) with the expected redshift distribution (panel B of Fig. 7.20) and is shown in Fig.7.21.

Assuming that all GRBs happen in a small redshift, it demonstrates that HAWC should be able to detect relatively nearby GRBs provided a good navigation in the sky and a small delay of observation. However, GRBs do not exhibit a euclidean distribution. Taking this point into consideration, the expectation of GRBs with potential detection reduces substantially. It is important to consider that very nearby GRBs are expected to have a redshift measurement in the great majority of cases, therefore the upper interval of the first two bins of Fig. 7.21 is likely an overestimate. Crudely one can

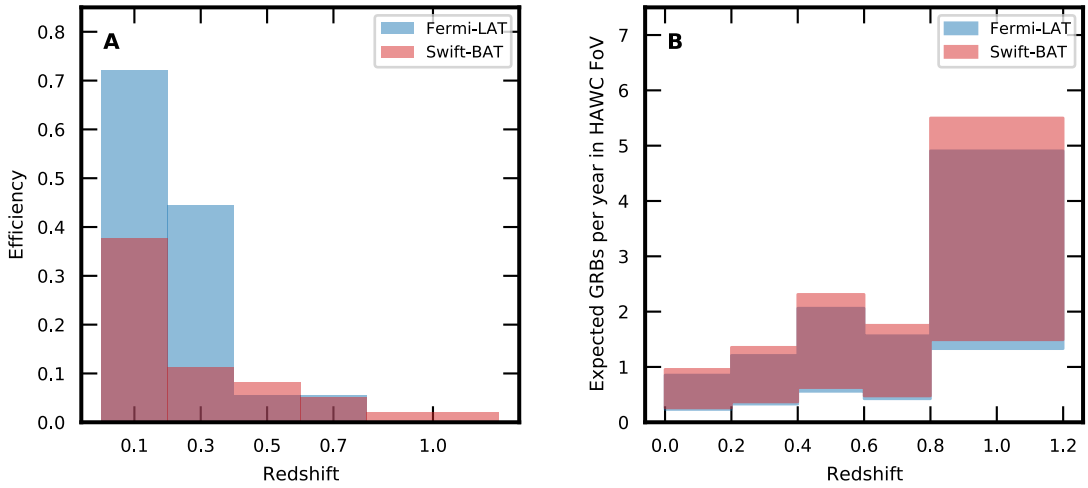

Fig. 7.20.: HAWC Efficiency and expected GRBs in the redshift binning. Panel A shows the portion of GRBs observed by HAWC with potential detection assuming a fixed redshift for the *Fermi*-LAT and *Swift*-BAT sample in blue and red respectively. Panel B shows the interval of expected GRBs per year in the HAWC FoV under the same redshift binning as panel A.

consider a constant expectation of 0.1 and 0.17 GRBs per year, obtained as the mean of the upper and lower expected rate, in each redshift bin for the potential detection by HAWC of *Swift*-BAT and *Fermi*-LAT GRBs. This expectation corresponds to two GRBs in the interval of 4 years for *Swift*-BAT GRBs and 3 GRB in a 3.3 years interval for *Fermi*-LAT GRBs, in agreement with the results shown in Fig. 7.16. Additionally, HAWC will require 10 years of observations to reach the expectation of observing a GRB at redshift < 0.2 with a high detection potential.

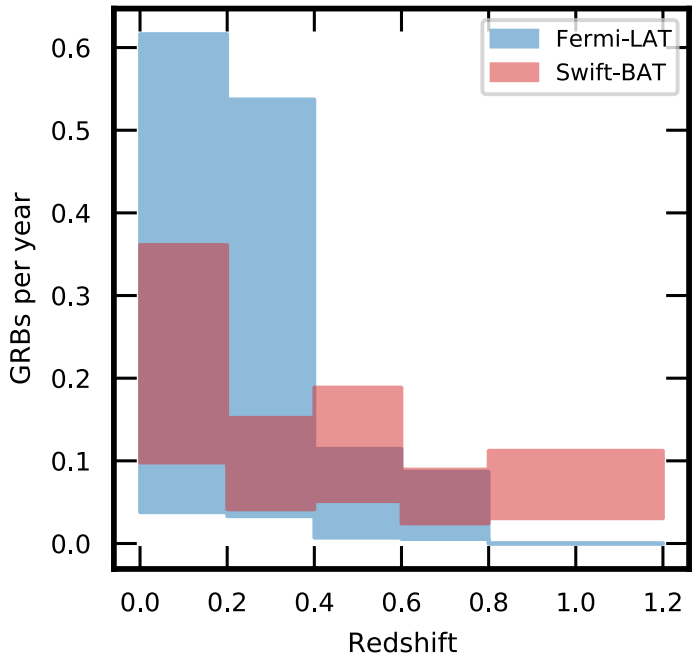

Fig. 7.21.: Expected GRBs with potential detection in HAWC per year. In red and blue the interval of the expected number of GRBs per year, for *Swift*-BAT and *Fermi*-LAT GRBs respectively, as a function of redshift is shown.

7.6 Conclusions and Outlook

In this chapter the development of a method to accurately estimate the optimal integration time for the analysis of GRBs with HAWC was presented. This method relies on the assumption that the VHE GRB flux evolves similarly as the X-ray light curves, in line with the finding of recent VHE detections, and incorporates the detector response to properly estimate the best integration window for the search for emission.

The set of GRBs detected by *Fermi*-LAT and *Swift*-XRT that are observable with HAWC with up to 18 hrs of delay were used for this study. This totals to 127 and 21 GRBs respectively for an interval of 3.3 years and 4.0 years. No significant emission is detected in this set, except for a $4.5\,\sigma$ excess for GRB 170115A, observed in favourable conditions. Improvements to the HAWC reconstruction, binning and gamma/hadron separation have been carried out in the past months by the collaboration and are expected to improve the sensitivity at all energies. A re-analysis of the data for GRB 170115A with these improved algorithms will be carried out in the future.

Strong upper limits were set for at least seven of these GRBs with known redshift. It was shown that GRBs of long T_{90} and low redshift constitute the best candidates for a detection with HAWC, with an additional dependency on the observation conditions imposed by their location (zenith navigation and duration of transit). The power of this optimal time window method was demonstrated for two specific GRBs: GRB 160623A and GRB 150323A.

The results presented here are hard to compare with previous results obtained with HAWC since there is no direct resemblance in either the integration windows, the set of GRBs used or the method for measuring the significance.

The best scenario for GRB searches will emerge when incorporating the strengths of previous methods into this new method. The possibility of simulating a delayed onset of the VHE emission for the method presented here will be explored in future work. This will resemble the sliding windows used in the previous searches with HAWC and assess the well-known delay onset seen in GRBs detected by *Fermi*-LAT. Corrections due to atmospheric

tide effects could be incorporated, as well as an accurate simulation of the detector with the methods presented in Ch. 6.

Future work contemplates the application of this method to GRBs detected by *Fermi*-GBM. These observations constitute an additional challenge to the method since the localisation uncertainty of these GRBs is typically bigger than the PSF of HAWC. A tiling strategy to obtain the optimal integration time and for the search of emission could be used in this cases, with the penalty of an increased number of trials.

For the HAWC detection prospects, it was shown that assuming a nearby distance for this set of GRBs, HAWC could potentially detect several of them per year. An assumption of redshift of z=0.7, which might be a marginal but realistic assumption for long GRBs suffices for a more conservative rate of detection of 1 GRB per year. However, these expectations are reduced when considering the redshift distribution of GRBs detected by *Swift*-BAT, resulting in an expectation of 0.5 GRBs per year with redshift smaller than ~ 1.0 for either *Swift*-BAT or *Fermi*-LAT detections. A combination of good zenith angle of observation and proximity seems required to achieve a GRB detection with HAWC and makes clear that future generation of observatories like SWGO, where one order of magnitude better sensitivity and a lower energy threshold is expected, could secure the detection of more distant/less bright GRBs with less observational constraints.

Finally, it is worth highlighting that the optimal time method could be easily extended to searches of other types of transient events like AGN flares and follow-up of gravitational wave alerts etc., and it could be applied to other present and future observatories. In these cases, the assumption on the flux evolution and spectral shape can be adapted on a case by case basis, potentially being obtained from observations at other wavelengths and fed to the method developed in this chapter.

Bibliography

Aartsen, M. G. et al. (June 2016). “An all-sky search for three flavours of neutrinos from gamma-ray bursts with the IceCube neutrino observatory”. In: *The Astrophysical Journal* 824.2, p. 115. URL: https://doi.org/10.3847/0004-637x/824/2/115 (cit. on p. 31).

Abbott, B. P. et al. (Oct. 2017). “Multi-messenger Observations of a Binary Neutron Star Merger”. In: *The Astrophysical Journal Letters* 848.2, p. L12. URL: http://stacks.iop.org/2041-8205/848/i=2/a=L12 (cit. on p. 31).

Abdalla, H. et al. (2019). “A very-high-energy component deep in the gamma-ray burst afterglow”. In: *Nature* 575.7783, pp. 464–467. URL: https://doi.org/10.1038/s41586-019-1743-9 (cit. on p. 104).

Abdalla, H. et al. (Apr. 2017). “Gamma-ray blazar spectra with H.E.S.S. II mono analysis: The case of PKS 2155-304 and PG 1553+113”. In: *Astronomy & Astrophysics* 600, A89, A89 (cit. on p. 101).

Abdalla, H. et al. (May 2020). “Probing the Magnetic Field in the GW170817 Outflow Using H.E.S.S. Observations”. In: *The Astrophysical Journal* 894.2, p. L16. URL: https://doi.org/10.3847/2041-8213/ab8b59 (cit. on p. 78).

Abdalla, H. et al. (2021). “Revealing X-ray and gamma ray temporal and spectral similarities in the GRB 190829A afterglow”. In: *Science (accepted)* (cit. on pp. 112, 114).

Abeysekara, A. U. et al. (June 2017a). In: 843.1, p. 39. URL: https://doi.org/10.3847/1538-4357/aa7555 (cit. on pp. 55, 152–154).

Abeysekara, A. U. et al. (Apr. 2018). “A Strong Limit on the Very-high-energy Emission from GRB 150323A”. In: *The Astrophysical Journal* 857.1, p. 33. URL: https://doi.org/10.3847/1538-4357/aab371 (cit. on pp. 170, 172).

Abeysekara, A. U. et al. (Aug. 2019). “Measurement of the Crab Nebula Spectrum Past 100 TeV with HAWC”. In: *The Astrophysical Journal* 881.2, p. 134. URL: https://doi.org/10.3847/1538-4357/ab2f7d (cit. on pp. 54, 139).

Abeysekara, A. U. et al. (Feb. 2015). "Search for gamma-rays from the unusually bright GRB 130427A with the HAWC Gamma-ray Observatory". In: *The Astrophysical Journal* 800.2, p. 78. URL: https://doi.org/10.1088/0004-637x/800/2/78 (cit. on p. 144).

Abeysekara, A. U. et al. (July 2017b). "The HAWC Real-time Flare Monitor for Rapid Detection of Transient Events". In: *The Astrophysical Journal* 843.2, p. 116. URL: https://doi.org/10.3847/1538-4357/aa789f (cit. on p. 143).

Abramowski, A. et al. (May 2014). "Search for TeV Gamma-ray Emission from GRB 100621A, an extremely bright GRB in X-rays, with H.E.S.S." In: *Astronomy and Astrophysics* 565, A16, A16 (cit. on p. 78).

Acciari, V. A. et al. (2019). "Teraelectronvolt emission from the gamma-ray burst GRB 190114C". In: *Nature* 575.7783, pp. 455–458. URL: https://doi.org/10.1038/s41586-019-1750-x (cit. on pp. 31, 88, 96).

Ackermann, M. et al. (2014). "Fermi-LAT Observations of the Gamma-Ray Burst GRB 130427A". In: *Science* 343.6166, pp. 42–47. URL: http://science.sciencemag.org/content/343/6166/42 (cit. on pp. 87, 95).

Agostinelli, S. et al. (2003). "GEANT4: A Simulation toolkit". In: *Nuclear Instruments and Methods* A506, pp. 250–303 (cit. on p. 59).

Aharonian, F. et al. (2009). "HESS observations of bursts in 2003-2007". In: *Astronomy & Astrophysics* 495.2, pp. 505–512. URL: https://doi.org/10.1051/0004-6361:200811072 (cit. on p. 76).

Aharonian, F. A. (2004). *Very high energy cosmic gamma radiation : a crucial window on the extreme Universe*. World Scientific Publishing Co (cit. on p. 9).

Aharonian, F. et al. (2006a). "A low level of extragalactic background light as revealed by gamma-rays from blazars". In: *Nature* 440.7087, pp. 1018–1021. URL: https://doi.org/10.1038/nature04680 (cit. on p. 19).

Aharonian, F. et al. (2004). "Calibration of cameras of the H.E.S.S. detector". In: *Astroparticle Physics* 22.2, pp. 109–125. URL: http://www.sciencedirect.com/science/article/pii/S0927650504001227 (cit. on pp. 63, 65).

Aharonian, F. et al. (2006b). "Observations of the Crab Nebula with H.E.S.S". In: *Astronomy & Astrophysics* 457, pp. 899–915 (cit. on p. 68).

Aharonian, F. et al. (Oct. 2006c). "Observations of the Crab Nebula with H.E.S.S." In: *Astronomy & Astrophysics* 457, pp. 899–915 (cit. on pp. 67, 109).

Ajello, M. et al. (June 2019). "A Decade of Gamma-Ray Bursts Observed by Fermi-LAT: The Second GRB Catalog". In: *Astrophysical Journal* 878, 52, p. 52 (cit. on pp. 43, 86, 101, 146, 151, 169, 170).

Ajello, M. et al. (Aug. 2018). “Investigating the Nature of Late-time High-energy GRB Emission through Joint Fermi/Swift Observations”. In: *Astrophysical Journal* 863.2, 138, p. 138 (cit. on p. 113).

Albert, A. et al. (Feb. 2019). “Science Case for a Wide Field-of-View Very-High-Energy Gamma-Ray Observatory in the Southern Hemisphere”. In: arXiv: 1902.08429 [astro-ph.HE] (cit. on p. 73).

Alfaro, R. et al. (July 2017). “Search for very-high-energy emission from Gamma-ray Bursts using the first 18 months of data from the HAWC Gamma-ray Observatory”. In: *The Astrophysical Journal* 843.2, p. 88. URL: https://doi.org/10.3847/1538-4357/aa756f (cit. on pp. 86, 145).

Alves Batista, R. et al. (June 2019). “Open questions in cosmic-ray research at ultrahigh energies”. In: *Frontiers in Astronomy and Space Sciences* 6, p. 23. URL: https://www.frontiersin.org/article/10.3389/fspas.2019.00023 (cit. on pp. 9, 10).

Amati, L. (Oct. 2006). “The $E_{p,i}$-E_{iso} correlation in gamma-ray bursts: updated observational status, re-analysis and main implications”. In: *Monthly Notices of the Royal Astronomical Society* 372.1, pp. 233–245. eprint: https://academic.oup.com/mnras/article-pdf/372/1/233/5781510/mnras0372-0233.pdf. URL: https://doi.org/10.1111/j.1365-2966.2006.10840.x (cit. on p. 42).

Amsler, C. et al. (Sept. 2008). “Review of Particle Physics”. English (US). In: *Physics Letters, Section B: Nuclear, Elementary Particle and High-Energy Physics* 667.1-5, pp. 1–6 (cit. on p. 5).

Ando, S. et al. (Dec. 2008). “GeV Emission from Prompt and Afterglow Phases of Gamma-Ray Bursts”. In: *The Astrophysical Journal* 689.2, pp. 1150–1160. URL: https://doi.org/10.1086/592486 (cit. on p. 43).

Appendix B: Statistics in XSPEC (2021). https://heasarc.gsfc.nasa.gov/xanadu/xspec/manual/XSappendixStatistics.html. Accessed: 2021-01-01 (cit. on p. 164).

Atkins, R. et al. (Feb. 2004). “Limits on Very High Energy Emission from Gamma-Ray Bursts with the Milagro Observatory”. In: *The Astrophysical Journal* 604.1, pp. L25–L28. URL: https://doi.org/10.1086/383414 (cit. on p. 95).

Auger, P. et al. (July 1939). “Extensive Cosmic-Ray Showers”. In: *Reviews of Modern Physics* 11 (3-4), pp. 288–291. URL: https://link.aps.org/doi/10.1103/RevModPhys.11.288 (cit. on p. 4).

Ayala Solares, H. A. et al. (2016). “The Calibration System of the HAWC Gamma-Ray Observatory”. In: *PoS* ICRC2015, p. 997 (cit. on p. 52).

Balzer, A. et al. (2014). “The H.E.S.S. data acquisition system”. In: *Journal of Physics: Conference Series* 513.1, p. 012003. URL: http://stacks.iop.org/1742-6596/513/i=1/a=012003 (cit. on p. 64).

Band, D. et al. (Aug. 1993). “BATSE observations of gamma-ray burst spectra. I - Spectral diversity”. In: *Astrophysical Journal* 413, pp. 281–292 (cit. on p. 29).

Becerril, A. D. et al. (2017). “Triggered searches of delayed or extended VHE GRB emissions with HAWC”. In: *AIP Conference Proceedings* 1792.1, p. 070003 (cit. on p. 145).

Bell, A. (2013). “Cosmic ray acceleration”. In: *Astroparticle Physics* 43. Seeing the High-Energy Universe with the Cherenkov Telescope Array - The Science Explored with the CTA, pp. 56–70. URL: http://www.sciencedirect.com/science/article/pii/S0927650512001272 (cit. on p. 6).

Berezinsky, V. (June 2013). “UHECR: Signatures and models”. In: *European Physical Journal Web of Conferences*. Vol. 53. European Physical Journal Web of Conferences, p. 01003 (cit. on p. 6).

Berge, D. et al. (May 2007). “Background modelling in very-high-energy γ-ray astronomy”. In: *Astronomy & Astrophysics* 466, pp. 1219–1229 (cit. on pp. 69, 70).

Berger, E. (2014). “Short-Duration Gamma-Ray Bursts”. In: *Annual Review of Astronomy and Astrophysics* 52.1, pp. 43–105. eprint: https://doi.org/10.1146/annurev-astro-081913-035926. URL: https://doi.org/10.1146/annurev-astro-081913-035926 (cit. on p. 41).

Berti, A. et al. (2020). “Searching for GRBs at VHE with MAGIC: the status before CTA”. In: *PoS* ICRC2019, p. 634 (cit. on p. 86).

Bissaldi, E. et al. (July 2018). “GCN22980 - GRB 180720B: Fermi-LAT detection”. In: *GCN Circulars* (cit. on pp. 96, 100).

Bloom, J. S. et al. (June 2001). “The Prompt Energy Release of Gamma-Ray Bursts using a Cosmological k-Correction”. In: *The Astronomical Journal* 121.6, pp. 2879–2888. URL: https://doi.org/10.1086/321093 (cit. on p. 42).

Bolmont, J. et al. (2014). “The camera of the fifth H.E.S.S. telescope. Part I: System description”. In: *Nuclear Instruments and Methods in Physics Research Section A: Accelerators, Spectrometers, Detectors and Associated Equipment* 761, pp. 46–57. URL: http://www.sciencedirect.com/science/article/pii/S0168900214006469 (cit. on p. 63).

Bothe, W. et al. (Nov. 1929). “Das Wesen der Höhenstrahlung”. In: *Zeitschrift fur Physik* 56.11-12, pp. 751–777 (cit. on p. 4).

Burlon, D. et al. (2008). “Precursors in Swift Gamma Ray Bursts with redshift”. In: *Astrophysical Journal Letters* 685, p. L19 (cit. on p. 33).

Cash, W. (Mar. 1979). “Parameter estimation in astronomy through application of the likelihood ratio.” In: *Astrophysical Journal* 228, pp. 939–947 (cit. on p. 146).

Chen, W. J. et al. (Mar. 2020). “Two-component Jets of GRB 160623A as Shocked Jet Cocoon Afterglow”. In: *The Astrophysical Journal* 891.1, p. L15. URL: https://doi.org/10.3847/2041-8213/ab76d4 (cit. on p. 170).

Cherenkov, P. A. (Aug. 1937). “Visible Radiation Produced by Electrons Moving in a Medium with Velocities Exceeding that of Light”. In: *Physical Review* 52 (4), pp. 378–379. URL: https://link.aps.org/doi/10.1103/PhysRev.52.378 (cit. on p. 24).

Chincarini, G. et al. (Dec. 2007). “The First Survey of X-Ray Flares from Gamma-Ray Bursts Observed bySwift: Temporal Properties and Morphology”. In: *The Astrophysical Journal* 671.2, pp. 1903–1920. URL: https://doi.org/10.1086/521591 (cit. on p. 37).

Composite GCN List for GRB 150323A (n.d.). https://gcn.gsfc.nasa.gov/other/150323A.gcn3 (cit. on p. 170).

Composite GCN List for GRB 160623A (2016). https://gcn.gsfc.nasa.gov/other/160623A.gcn3 (cit. on p. 170).

Cronin, J. W. et al. (Jan. 1997). “Cosmic rays at the energy frontier.” In: *Scientific American* 276, pp. 32–37 (cit. on p. 5).

CTA Consortium (2019). *Science with the Cherenkov Telescope Array*. World Scientific Publishing Co (cit. on p. 73).

Davies, J. M. et al. (Apr. 1957). “Design of the quartermaster solar furnace”. In: *Solar Energy* 1.2-3, pp. 16–22 (cit. on p. 63).

De Angelis, A. (Dec. 2010). “Domenico Pacini, uncredited pioneer of the discovery of cosmic rays”. In: *Nuovo Cimento Rivista Serie* 33.12, pp. 713–756 (cit. on p. 4).

de Gouveia Dal Pino, E. M. et al. (2015). “Particle Acceleration by Magnetic Reconnection”. In: *Magnetic Fields in Diffuse Media*. Ed. by A. Lazarian et al. Vol. 407, p. 373 (cit. on p. 38).

De Naurois, M. (Mar. 2012). “Very High Energy astronomy from H.E.S.S. to CTA. Opening of a new astronomical window on the non-thermal Universe”. Habilitation à diriger des recherches. Université Pierre et Marie Curie - Paris VI. URL: https://tel.archives-ouvertes.fr/tel-00687872 (cit. on pp. 23, 68, 163).

Deil, C. et al. (Jan. 2017). “Gammapy - A prototype for the CTA science tools”. In: *35th International Cosmic Ray Conference (ICRC2017)*. Vol. 301. International Cosmic Ray Conference, p. 766 (cit. on p. 109).

Dichiara, S. et al. (Aug. 2019). “GRB 190829A: Swift detection of a burst consistent with a galaxy at z=0.08”. In: *GRB Coordinates Network* 25552, p. 1 (cit. on p. 107).

Domínguez, A. et al. (Jan. 2011). “Extragalactic background light inferred from AEGIS galaxy-SED-type fractions”. In: *Monthly Notices of the Royal Astronomical Society* 410.4, pp. 2556–2578. URL: https://doi.org/10.1111/j.1365-2966.2010.17631.x (cit. on pp. 18, 19, 102, 110).

Dwek, E. et al. (2013). “The extragalactic background light and the gamma-ray opacity of the universe”. In: *Astroparticle Physics* 43. Seeing the High-Energy Universe with the Cherenkov Telescope Array - The Science Explored with the CTA, pp. 112–133. URL: http://www.sciencedirect.com/science/article/pii/S0927650512001752 (cit. on p. 18).

Fermi GBM Team (Aug. 2019). “GRB 190829A: Fermi GBM Final Real-time Localization”. In: *GRB Coordinates Network* 25551, p. 1 (cit. on p. 107).

Fermi, E. (Apr. 1949). “On the Origin of the Cosmic Radiation”. In: *Physical Review* 75 (8), pp. 1169–1174. URL: https://link.aps.org/doi/10.1103/PhysRev.75.1169 (cit. on p. 6).

Finke, J. D. et al. (Feb. 2010). “Modeling the extragalactic background light from stars and dust”. In: *Astrophysical Journal* 712.1, pp. 238–249. URL: https://doi.org/10.1088%2F0004-637x%2F712%2F1%2F238 (cit. on pp. 102, 110).

Franceschini, A. et al. (Sept. 2008). “Extragalactic optical-infrared background radiation, its time evolution and the cosmic photon-photon opacity”. In: *Astronomy & Astrophysics* 487, pp. 837–852 (cit. on pp. 20, 101, 110, 151).

Franceschini, A. et al. (July 2017). “The extragalactic background light revisited and the cosmic photon-photon opacity”. In: *Astronomy & Astrophysics* 603, A34, A34 (cit. on p. 18).

Frederiks, D. et al. (Mar. 2016). “GCN19167 - Konus-Wind observation of GRB 160310A (possible ultra-long GRB?)” In: *GCN Circulars* (cit. on p. 86).

Funk, S. (July 2005). “A new population of very high-energy gamma-ray sources detected with H.E.S.S. in the inner part of the Milky Way”. PhD thesis (cit. on p. 7).

Gehrels, N. et al. (2008). “Correlations of Prompt and Afterglow Emission in Swift Long and Short Gamma Ray Bursts”. In: *Astrophysical Journal* 689, p. 1161 (cit. on p. 88).

Gillessen, S. (July 2004). “Sub-Bogenminuten-genaue Positionen von TeV-Quellen mit H.E.S.S.” PhD thesis. Ruprecht-Karls-Universität Heidelberg (cit. on p. 108).

Gilmore, R. C. et al. (May 2012). “Semi-analytic modelling of the extragalactic background light and consequences for extragalactic gamma-ray spectra”. In: *Monthly Notices of the Royal Astronomical Society* 422.4, pp. 3189–3207. URL: https://doi.org/10.1111/j.1365-2966.2012.20841.x (cit. on pp. 18, 102).

Greisen, K. (1960). “Cosmic Ray Showers”. In: *Annual Review of Nuclear Science* 10.1, pp. 63–108. eprint: https://doi.org/10.1146/annurev.ns.10.120160.000431. URL: https://doi.org/10.1146/annurev.ns.10.120160.000431 (cit. on p. 55).

Greisen, K. (1952). “Progress in Cosmic Ray Physics. J. G. Wilson, Ed. Amsterdam: North-Holland Pub.; New York: Interscience, 1952. 557 pp.” In: *Science* 115.2990, pp. 426–427. eprint: http://science.sciencemag.org/content/115/2990/426.2.full.pdf. URL: http://science.sciencemag.org/content/115/2990/426.2 (cit. on p. 21).

He, H. (July 2019). “Status and First Results of the LHAASO Experiment”. In: *PoS(2019)* 36, p. 693 (cit. on p. 6).

Heck, D. et al. (1998). *CORSIKA: a Monte Carlo code to simulate extensive air showers.* (Cit. on p. 59).

Hillas, A. M. (Aug. 1985). “Cerenkov light images of EAS produced by primary gamma”. In: *International Cosmic Ray Conference* 3 (cit. on p. 66).

Hinton, J. et al. (Feb. 2020). “Multi-messenger astronomy with very-high-energy gamma-ray observations”. In: *Proceedings of TAUP2019* 1468. Ed. by M. Nakahata, p. 012096. URL: https://doi.org/10.1088/1742-6596/1468/1/012096 (cit. on p. 74).

Hofverberg, P. o. (Jan. 2013). “Commissioning and Initial Performance of the H.E.S.S. II Drive System”. In: *International Cosmic Ray Conference*. Vol. 33. International Cosmic Ray Conference, p. 3092 (cit. on p. 63).

Hofverberg, P. et al. (July 2013). “Commissioning and initial performance of the H.E.S.S. II drive system”. In: *33rd International Cosmic Ray Conference*, p. 0926 (cit. on p. 64).

Hoischen, C. (2018). “Multi-Messenger Astronomy with H.E.S.S: the Starburst Galaxy NGC253 and the Search for Short Time-Scale Transients”. PhD thesis. Universität Potsdam, p. 135 (cit. on p. 76).

Holler, M. et al. (2015). “Observations of the Crab Nebula with H.E.S.S. Phase II”. In: *34th International Cosmic Ray Conference (ICRC2015)*. Proceedings of Science (PoS), p. 847. URL: https://www.scopus.com/inward/record.uri?partnerID=HzOxMe3b&scp=84988697060&origin=inward (cit. on p. 73).

Hörandel, J. R. (2013). “Early Cosmic-Ray Work Published in German”. In: *AIP Conf. Proc.* 1516.1. Ed. by J. F. Ormes, pp. 52–60 (cit. on p. 4).

Inoue, S. et al. (2013). “Gamma-Ray Burst Science in the Era of the Cherenkov Telescope Array”. In: *Astroparticle Physics* 43, pp. 252–275 (cit. on p. 42).

Jackson, J. D. (1998). *Classical Electrodynamics*. Wiley (cit. on p. 25).

Joshi, V. et al. (June 2019). “A template-based γ-ray reconstruction method for air shower arrays”. In: *Journal of Cosmology and Astroparticle Physics* 2019.01, pp. 012–012. URL: https://doi.org/10.1088/1475-7516/2019/01/012 (cit. on p. 55).

Kamata, K. et al. (1958). “The Lateral and the Angular Structure Functions of Electron Showers”. In: *Progress of Theoretical Physics Supplement* 6, pp. 93–155 (cit. on p. 21).

Klebesadel, R. W. et al. (June 1973). “Observations of Gamma-Ray Bursts of Cosmic Origin”. In: *Astrophysical Journal Letters* 182, p. L85 (cit. on p. 28).

Kouveliotou, C. et al. (Aug. 1993). “Identification of Two Classes of Gamma-Ray Bursts”. In: *Astrophysical Journal Letters* 413, p. L101 (cit. on p. 32).

Large Photo Cathode Area PMTs (2019). TPMH1376E01. Rev. D. Hammamatsu Photonics K.K. URL: https://www.hamamatsu.com/resources/pdf/etd/LARGE_AREA_PMT_TPMH1376E.pdf (cit. on p. 131).

Lennarz, D. et al. (2017). “The HAWC GRB programme”. In: *AIP Conference Proceedings* 1792.1, p. 050033. eprint: https://aip.scitation.org/doi/pdf/10.1063/1.4968979. URL: https://aip.scitation.org/doi/abs/10.1063/1.4968979 (cit. on pp. 142, 143).

Lesage, S. et al. (Aug. 2019). “GRB 190829A: Fermi GBM detection”. In: *GRB Coordinates Network* 25575, p. 1 (cit. on p. 113).

Li, T.-P. et al. (Sept. 1983). “Analysis methods for results in gamma-ray astronomy”. In: *Astrophysical Journal* 272, pp. 317–324 (cit. on pp. 58, 70).

Longair, M. S. (Feb. 2011). *High Energy Astrophysics* (cit. on pp. 6, 24).

Malesani, D. et al. (July 2018). “GCN22996 - VLT/X-shooter redshift”. In: *GCN Circulars* (cit. on p. 97).

Marandon, V. et al. (July 2019). “Latest news from the HAWC outrigger array”. In: International Cosmic Ray Conference 36, 736, p. 736 (cit. on p. 48).

Martinez Castellanos, I. (2019). “Search for gamma-ray counterparts of gravitational wave events and other transient signals with HAWC”. PhD thesis. Maryland U. (cit. on p. 51).

Martinez-Castellanos, I. (June 2016). “Background calculation for low statistics analysis bins”. HAWC internal documents (cit. on p. 151).

Matthews, J. (2005). “A Heitler model of extensive air showers”. In: *Astroparticle Physics* 22, pp. 387–397 (cit. on p. 20).

Meegan, C. A. et al. (1992). “Spatial distribution of gamma-ray bursts observed by BATSE”. In: *Nature* 355.6356, pp. 143–145. URL: https://doi.org/10.1038/355143a0 (cit. on p. 39).

Mohrmann, L. et al. (Oct. 2019). “Validation of open-source science tools and background model construction in gamma-ray astronomy”. In: *Astronomy & Astrophysics* 632 (cit. on p. 109).

Nava, L. et al. (2017). “Constraints on the bulk Lorentz factor of Gamma-Ray Burst jets from Fermi/LAT upper limits”. In: *Monthly Notices of the Royal Astronomical Society* 465.1, pp. 811–819 (cit. on p. 42).

Nigro, C. et al. (May 2019). “Towards open and reproducible multi-instrument analysis in gamma-ray astronomy”. In: *Astronomy & Astrophysics* 625, A10, A10 (cit. on p. 109).

Nikishov, A. I. (Aug. 1961). “Absorption of high energy photons in the universe.” In: *Zhur. Eksptl. Teoret. Fiz.* Vol: 41 (cit. on p. 18).

Nousek, J. A. et al. (2006). “Evidence for a canonical GRB afterglow light curve in the Swift/XRT data”. In: *Astrophysical Journal* 642, pp. 389–400 (cit. on p. 35).

Ohm, S. et al. (June 2009). “γ/hadron separation in very-high-energy γ-ray astronomy using a multivariate analysis method”. In: *Astroparticle Physics* 31, pp. 383–391 (cit. on p. 66).

Paciesas, W. S. et al. (June 1999). “The Fourth BATSE Gamma-Ray Burst Catalog (Revised)”. In: *Astrophysical Journal, Supplement* 122.2, pp. 465–495 (cit. on p. 40).

Padilla, L. et al. (Sept. 1998). “Search for gamma-ray bursts above 20 TeV with the HEGRA AIROBICC Cherenkov array”. In: *Astronomy & Astrophysics* 337, pp. 43–50 (cit. on p. 95).

Parsons, R. et al. (Apr. 2014). “A Monte Carlo Template based analysis for Air-Cherenkov Arrays”. In: *Astroparticle Physics* 56 (cit. on pp. 68, 69, 108).

Parsons, R. et al. (2016). “HESS II Data Analysis with ImPACT”. In: *PoS* ICRC2015, p. 826 (cit. on p. 67).

Piel, Q. et al. (July 2019). “Gamma-Ray Burst observation at Very High Energy with H.E.S.S.” In: *36th International Cosmic Ray Conference (ICRC2019)*. Vol. 36. International Cosmic Ray Conference, p. 761 (cit. on p. 82).

Piran, T. (June 1999). “Gamma-ray bursts and the fireball model”. In: *Physics Reports* 314.6, pp. 575–667 (cit. on p. 32).

Preece, R. D. et al. (Jan. 2000). “The BATSE Gamma-Ray Burst Spectral Catalog. I. High Time Resolution Spectroscopy of Bright Bursts Using High Energy Resolution Data”. In: *Astrophysical Journal Supplements* 126.1, pp. 19–36 (cit. on p. 34).

Pretz, J. et al. (Apr. 2018). *DAQSim- Code an Parameter Tuning*. HAWC internal memo. `https://private.hawc-observatory.org/hawc.umd.edu/internal/db/2397_02.pdf` (cit. on p. 59).

Pretz, J. (2016). “Highlights from the High Altitude Water Cherenkov Observatory”. In: *PoS* ICRC2015, p. 025 (cit. on p. 3).

Qin, Y.-P. et al. (Mar. 2013). “Statistical classification of gamma-ray bursts based on the Amati relation”. In: *Monthly Notices of the Royal Astronomical Society* 430.1, pp. 163–173 (cit. on p. 118).

Qin, Y. et al. (Jan. 2013). “A Comprehensive Analysis of Fermi Gamma-Ray Burst Data. III. Energy-dependent T_{90} Distributions of GBM GRBs and Instrumental Selection Effect on Duration Classification”. In: *Astrophysical Journal* 763.1, 15, p. 15 (cit. on p. 32).

Rieger, F. M. et al. (Oct. 2005). “Particle Acceleration in Gamma-Ray Burst Jets”. In: *Astrophysical Journal Letters* 632.1, pp. L21–L24 (cit. on p. 39).

Roberts, O. J. et al. (July 2018). “GCN22981 - GRB 180720B: Fermi-GBM observation”. In: *GCN Circulars* (cit. on p. 96).

Rosenberg, M. (Oct. 2018). “Data Noise Technical Note”. HAWC internal documents (cit. on p. 61).

Schmalz, S. et al. (July 2018). “GCN23020 - ISON-Castelgrande observation of GRB 180720B”. In: *GCN Circulars* (cit. on pp. 99, 100).

Schönfelder, V. (2001). *The Universe in Gamma Rays*, p. 407 (cit. on p. 9).

Schoorlemmer, H. et al. (May 2019). “Characteristics of extensive air showers around the energy threshold for ground-particle-based γ -ray observatories”. In: *European Physical Journal C* 79.5, 427, p. 427 (cit. on p. 121).

Siegel, M. H. et al. (July 2018). “GCN22973 - GRB 180720B: Swift detection of a burst”. In: *GCN Circulars* (cit. on pp. 96, 100).

Tanabashi, M. et al. (Aug. 2018). “Review of Particle Physics”. In: *Physical Review D* 98 (3), p. 030001. URL: https://link.aps.org/doi/10.1103/PhysRevD.98.030001 (cit. on p. 11).

The Pierre Auger collaboration (2015). “The Pierre Auger Cosmic Ray Observatory”. In: *Nuclear Instruments and Methods in Physics Research Section A: Accelerators, Spectrometers, Detectors and Associated Equipment* 798, pp. 172–213. URL: http://www.sciencedirect.com/science/article/pii/S0168900215008086 (cit. on p. 6).

Toelge, K. et al. (Mar. 2016). “GCN19161 - GRB 160310A: Fermi GBM observation”. In: *GCN Circulars* (cit. on p. 86).

Valeev, A. F. et al. (Aug. 2019). “GRB 190829A: 10.4m GTC spectroscopy”. In: *GRB Coordinates Network* 25565, p. 1 (cit. on p. 107).

Vianello, G. et al. (Mar. 2016). “GCN19158 - GRB 160310A: Fermi-LAT detection”. In: *GCN Circulars* (cit. on p. 86).

Wagner, R. M. (2006). “Measurement of very high energy gamma-ray emission from four blazars using the MAGIC telescope and a comparative blazar study”. Dissertation. München: Technische Universität München (cit. on p. 2).

Wakely, S. et al. (2018). *TevCat An online catalog for Very High Energy Gamma-Ray Astronomy*. URL: http://tevct.uchicago.edu (visited on Sept. 7, 2018) (cit. on p. 16).

Wood, J. (Apr. 2015). “Identifying Atmospheric Muon Signatures in HAWC Data”. HAWC internal documents (cit. on p. 121).

Wood, J. (2018). “Results from the first one and a half years of the HAWC GRB program”. In: *PoS* ICRC2017, p. 619 (cit. on p. 144).

Zhang, B. (2006). “Gamma-ray burst afterglows”. In: *Advances in Space Research* 40, pp. 1186–1198 (cit. on p. 36).

Zhang, B. (2018). *The Physics of Gamma-Ray Bursts*. Cambridge University Press (cit. on pp. 14, 28, 42).

Zhang, B. and Mészáros, P. (Sept. 2001). “High-Energy Spectral Components in Gamma-Ray Burst Afterglows”. In: *Astrophysical Journal* 559.1, pp. 110–122 (cit. on p. 44).

Bibliography of E. Ruiz-Velasco

Publications

Listed are the publications where I am a corresponding author, excluding collaboration-wide publications.

- Abdalla, H., **Ruiz-Velasco, E.**, et al. A very-high-energy component deep in the γ-ray burst afterglow. Nature 575, 464–467 (2019).
- Abdalla, H., **Ruiz-Velasco, E.**, et al. Revealing X-ray and gamma ray temporal and spectral similarities in the GRB 190829A afterglow. accepted for publication in Science (2021)

See `https://orcid.org/0000-0001-6939-7825` for a full list of publications.

In preparation

- Abdalla, H., **Ruiz-Velasco, E.**, et al. Ten years of GRB observations with the H.E.S.S. telescopes. *Prepared for submission* in Astronomy & Astrophysics.
- La Mura, G., Barres de Almeida, U., Conceição, R., De Angelis, A., Longo, F., Pimenta, M., Prandini, E., **Ruiz-Velasco, E.** Tomé, B. Gamma-Ray Burst detection prospects for next generation ground-based VHE facilities. *Prepared for submission* in Monthly Notices of the Royal Astronomical Society.

Conference proceedings

- Hinton, J. and **Ruiz-Velasco, E.** Multi-messenger astronomy with very-high-energy gamma-ray observations. 2020 Journal of Physics: Conference Series, 1468, 012096.
- **Ruiz-Velasco, E.** The H.E.S.S. detection of GRB 180720B and GRB 190829A. Proceedings of TMEX 2020, Quy Nhon, Vietnam.
- Piel, Q., Arcaro, C. H. E., Ashkar, H., Bissaldi, E., Böttcher, M., Carosi, A., Egbert, K., Hoischen, C., Holler, M., O'Brien, P., Parsons, R., Prokoph, H., Pühlhofer, G., Rowell, G., **Ruiz-Velasco, E.**, Seglar-Arroyo, M., Wagner, S., Schüssler, F. Gamma-Ray Burst observation at Very High Energy with H.E.S.S.. 36th International Cosmic Ray Conference, Jul 2019, Madison, United States. pp.761

Conference contributions

- **Ruiz-Velasco, E.** Highlights from the H.E.S.S GRB observation program. TeVPA 2019, Sidney, Australia.
- **Ruiz-Velasco, E.** The detection of VHE emission in the deep afterglow of GRB 180720B, *Plenary talk* TeVPA 2019, Sidney, Australia.
- **Ruiz-Velasco E.** Discovery of Late-Time Very High Energy Emission from a Gamma-ray Burst Afterglow, *Invited talk* First CTA science symposium, 2019, Bologna, Italy.
- **Ruiz-Velasco E.** The H.E.S.S. detection of GRB 180720B deep in the afterglow phase and other news. *Invited talk* 16th Rencontres du Vietnam: Theory meeting experiment: Particle astrophysic and cosmology, 2020, Quy Nhon, Vietnam.

Acknowledgements

Foremost, I want to thank my supervisor Prof. Dr. Jim Hinton for all your clever ideas and help. Many thanks to Dr. Harm Schroolemmer, Dr. Daniel Parsons, and Dr. Vincent Marandon for reading the thesis and your input. Thanks for your huge support and patience which together with Jim's supervision certainly made this thesis possible. Thanks to the H.E.S.S, Collaboration, especially Prof. Stefan Wagner for refereeing this thesis, Dr. Andrew Taylor for the collaboration and leadership with the GRB detections, and the members of the GRB group. Thanks to the HAWC Collaboration, especially to Dr. John Pretz and Dr. Andrew Smith for fruitful discussion regarding the HAWC simulations. Thanks to the members of the gammapy and astropy project for building and maintaining many of the tools used in this work. Many thanks to my previous supervisors Dr. Andres Sandoval and Dr. Ernesto Belmont for all the support received during my bachelor's degree, I will always be in debt.

Thanks to all the members of the non-thermal astrophysics group at MPIK for the extremely cheerful atmosphere, and for the collaborative spirit that holds in the group. Thanks to Dr. Brian Reville for checking parts of the thesis, and Dr. Simon Sailer and Dr. Felix Werner for translating the abstract. Thanks to Ruth Crespo for the support during my arrival and stay in the group. Many thanks to those how became friends with me outside the work atmosphere. Special thanks to Alvaro Pastor and Hazal Gokzu for the evenings of beers and music over the last few months of lockdowns and thesis stress. To Edgar C. Cortez and Janathan M. Juarez for your friendship.

Thanks to Dr. Emilio Meschi for balancing the challenges of these years with your weird humour and company. Many thanks for proofreading the whole thesis.

Gracias a mi papá Sostenes Miguel Ruiz Calderon y a mi mamá Elena Romero Perez por apoyarme en esta y todas las etapas de mi vida. Gracias a mis hermanos Leonardo Daniel Sanchez Romero, Mariana Ruiz Romero (y Olivia) y Miguel Ruiz Velasco. A toda mi familia y a mis grandes amigos, pero sobre todo a Atahualpa T. Vado.

And citing a famous American rapper: "Last but not least, I wanna thank me..."

List of Figures

List of Tables

A

Results on the GRB Searches with HAWC

A.0.1 Significance Distribution for the Ring Background Search

Redshift z=0.1

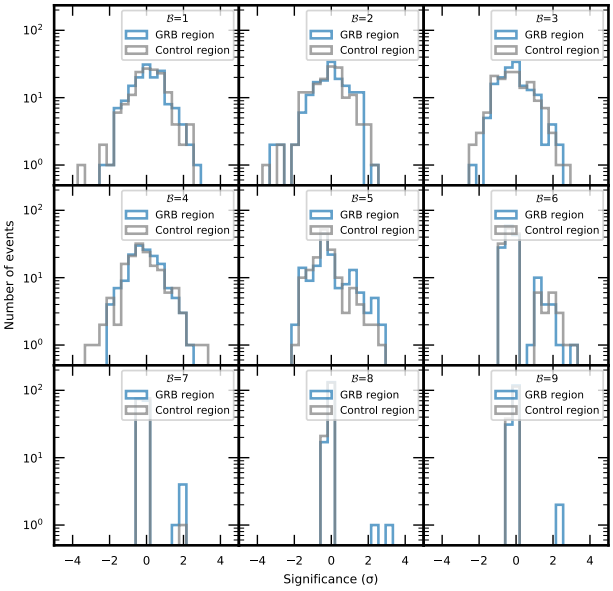

Fig. A.1.: **Significance distribution for each $\mathcal{B}$ bin assuming a redshift z=0.1.**

A.0.2 Optimal Integration Time of the Swift Sample

The figures corresponding to z=0.1 can be found in the main text.

Redshift Free

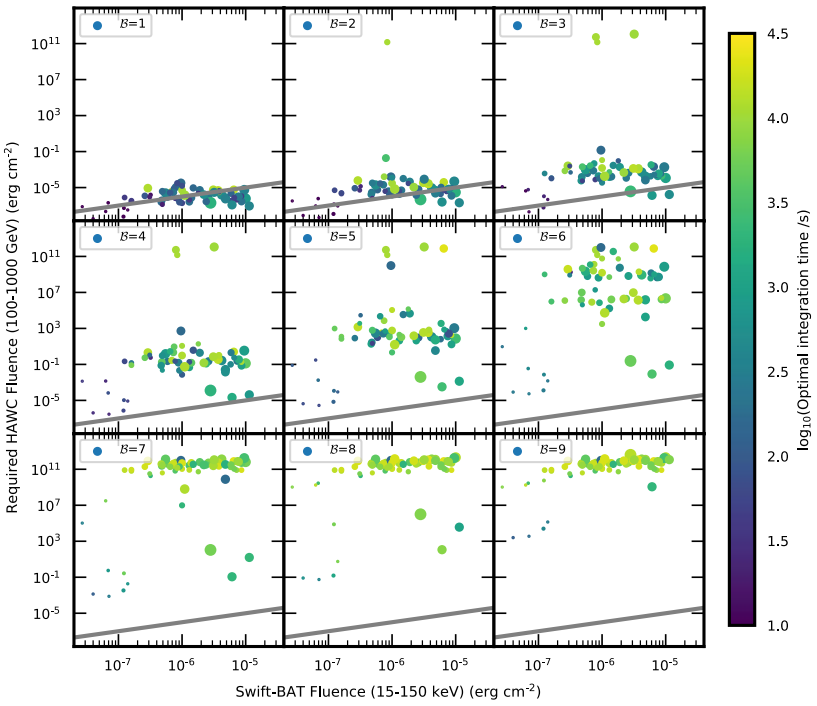

Fig. A.2.: Required GRB fluence for 5 σ detection with HAWC for prompt observations and redshift known. Each panel shows for each $\mathcal{B}$ the relationship between the required GRB fluence for a 5 σ detection with HAWC in the energy range of $100 - 1000$ GeV and the measured fluence with *Swift*-BAT in the energy range from $15 - 150$ keV. The colour of each point encodes the required integration time obtained from the optimisation and the size of the point is proportional to T_{90}. The grey line corresponds to equal HAWC and *Swift* fluence. This sample corresponds to GRBs happening inside the FoV of HAWc, Δt<10 s. If redshift is unknown the value is set to 0.5 and 2.0 for long and short GRBs respectively.

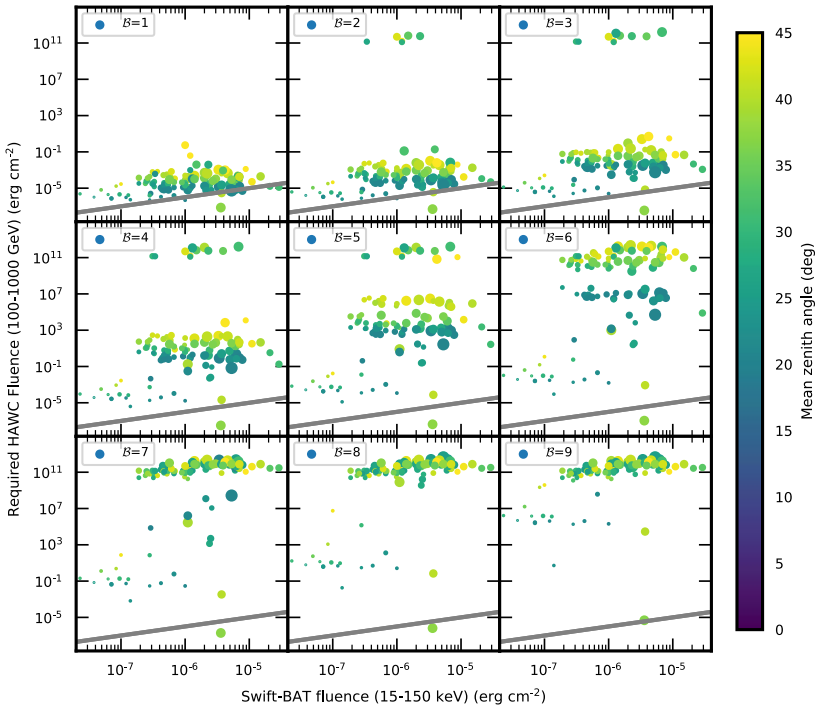

Fig. A.3.: Required GRB fluence for 5 σ detection with HAWC for afterglow observations and redshift known. Each panel shows, for each $\mathcal{B}$, the relationship between the required GRB fluence for a 5 σ detection with HAWC in the energy range of $100 - 1000$ GeV and the measured fluence with *Swift*-BAT in the energy range from $15 - 150$ keV. The colour of each point encodes the mean zenith angle of the observations with HAWC and the size of the point is proportional to T_{90}. The grey line corresponds to the identity line. This sample corresponds to GRBs observed with a $\Delta t > 10$ s. If redshift is unknown the value is set to 0.5 and 2.0 for long and short GRBs respectively.

A.0.3 Optimal Integration Time of the Fermi-LAT Sample

Redshift Free

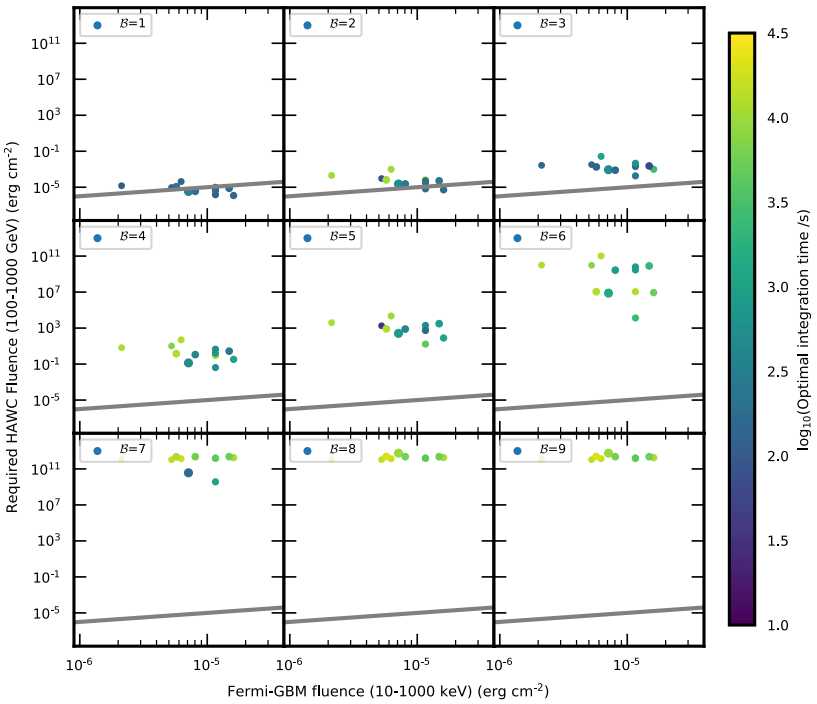

Fig. A.4.: Required GRB fluence for 5 σ detection with HAWC for prompt observations and redshift known. Each panel shows for each $\mathcal{B}$ the relationship between the required GRB fluence for a 5 σ detection with HAWC in the energy range of $100 - 10000$ GeV and the measured fluence with *Fermi*-GBM in the energy range from $10 - 10000$ keV. The colour of each point encodes the required integration time obtained from the optimisation and the size of the point is proportional to T_{90}. The grey line corresponds to equal HAWC and *Fermi* fluence. This sample corresponds to GRBs happening inside the FoV of HAWc, $\Delta t < 10$ s. If redshift is unknown the value is set to 0.5 and 2.0 for long and short GRBs respectively.

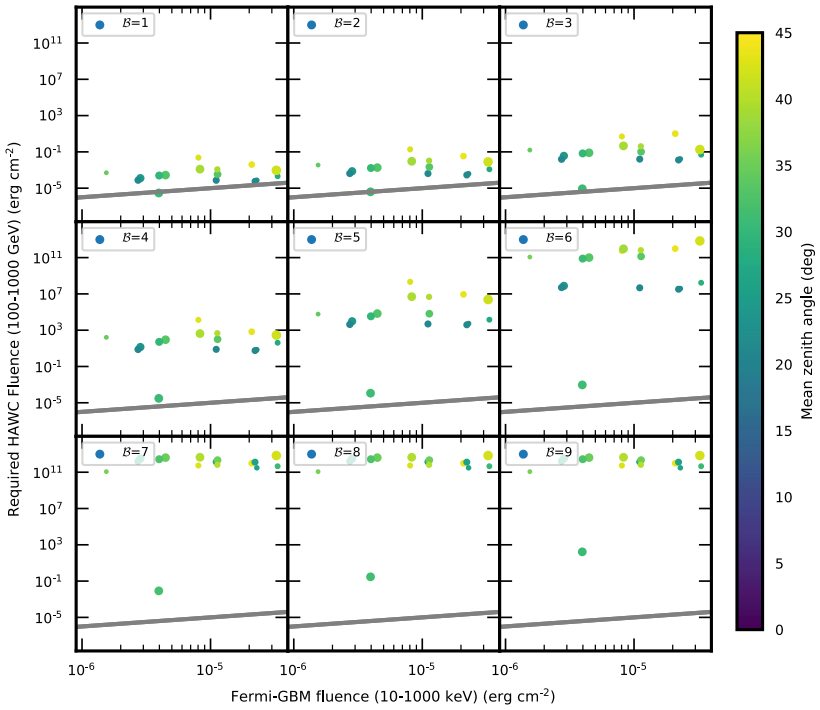

Fig. A.5.: Required GRB fluence for 5 σ detection with HAWC for afterglow observations and redshift known. Each panel shows, for each $\mathcal{B}$, the relationship between the required GRB fluence for a 5 σ detection with HAWC in the energy range of $100 - 1000$ GeV and the measured fluence with *Fermi*-GBM in the energy range from $10 - 10000$ keV. The colour of each point encodes the mean zenith angle of the observations with HAWC and the size of the point is proportional to T_{90}. The grey line corresponds to the identity line. This sample corresponds to GRBs observed with a $\Delta t > 10$ s. If redshift is unknown the value is set to 0.5 and 2.0 for long and short GRBs respectively.

Redshift z=0.1

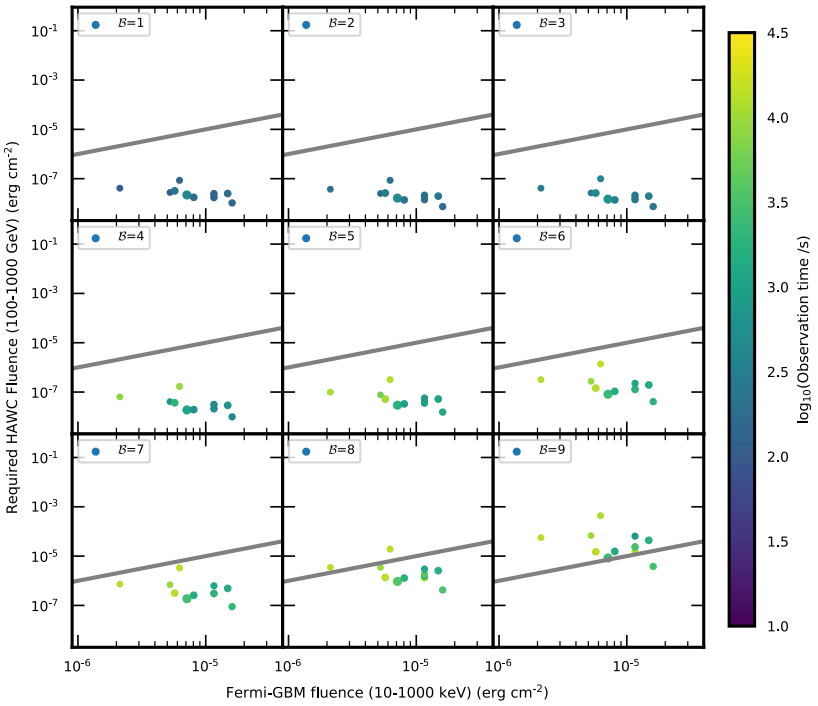

Fig. A.6.: Required GRB fluence for 5 σ detection with HAWC for prompt observations and redshift z=0.1. Each panel shows for each $\mathcal{B}$ the relationship between the required GRB fluence for a 5 σ detection with HAWC in the energy range of $100 - 1000$ GeV and the measured fluence with *Fermi*-GBM in the energy range from $10 - 10000$ keV. The colour of each point encodes the required integration time obtained from the optimisation and the size of the point is proportional to T_{90}. The grey line corresponds to equal HAWC and *Fermi* fluence. This sample corresponds to GRBs happening inside the FoV of HAWc, $\Delta t < 10$ s.

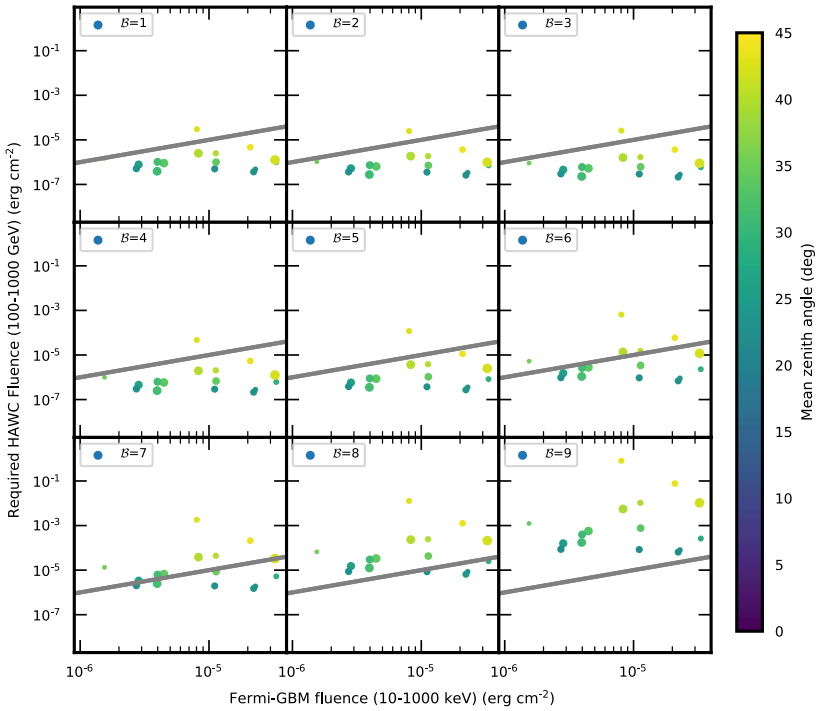

Fig. A.7.: Required GRB fluence for 5 σ detection with HAWC for afterglow observations and redshift z=0.1. Each panel shows, for each $\mathcal{B}$, the relationship between the required GRB fluence for a 5 σ detection with HAWC in the energy range of $100 - 1000$ GeV and the measured fluence with *Fermi*-GBM in the energy range from $10 - 10000$ keV. The colour of each point encodes the mean zenith angle of the observations with HAWC and the size of the point is proportional to T_{90}. The grey line corresponds to the identity line. This sample corresponds to GRBs observed with a $\Delta t > 10$ s.

Colophon

This thesis was typeset with LaTeX 2$_\varepsilon$. It uses the *Clean Thesis* style developed by Ricardo Langner. The design of the *Clean Thesis* style is inspired by user guide documents from Apple Inc.

Download the *Clean Thesis* style at `http://cleanthesis.der-ric.de/`.